Numerical Modeling of Rotating Neutron Stars and the Equation of State of Superdense Matter

Farrell, Delaney

2024

UNIVERSITY OF CALIFORNIA,
IRVINE

Numerical Modeling of Rotating Neutron Stars and the Equation of State of Superdense Matter

DISSERTATION

submitted in partial satisfaction of the requirements
for the degree of

DOCTOR OF PHILOSOPHY

in Computational Science

by

Delaney Farrell

Dissertation Committee:
Professor Fridolin Weber, Chair
Professor Pierre Baldi
Professor David Buote
Professor Calvin Johnson
Professor Daniel Whiteson

2024

DEDICATION

To my family, friends, and kitty girls.

”A society has no chance of success if its women are uneducated.”
- Khaled Hosseini, *A Thousand Splendid Suns*

TABLE OF CONTENTS

LIST OF FIGURES

LIST OF TABLES

ACKNOWLEDGMENTS

I would first like to thank my advisors, Fridolin Weber and Daniel Whiteson, for their support and guidance throughout my PhD. Fridolin, thank you for taking a chance on me, answering my never-ending questions, and giving me the freedom to explore a wide range of topics and projects. Daniel, thank you for introducing me to new ideas and shaping me into an independent researcher. I feel as though I've grown in insurmountable ways under the mentorship of you both, and for that, I am truly grateful.

I am also extremely grateful to my other committee members: Calvin Johnson, Pierre Baldi, and David Boute. The support I have received from you all over the years is incredible and I'm very grateful to have had such strong guidance.

I would like to acknowledge my deepest gratitude to the Computational Science Research Center (CSRC) at SDSU. Specifically, my thanks go to Jose Castillo for supporting me as a student and leader, to Satchi Venkataraman for always believing in me, and to Parisa Plant for keeping the program going and helping me at every step.

I also would like to express how grateful I am to the students in the CSRC for supporting me academically and personally. Thank you to my cohort and the SIAM Student Chapter for giving me a sense of community, and specifically to Angel Boada Velazco and Johnny Corbino Delgado for ensuring I passed my courses during my first year in the program.

Finally, I would like to thank my friends, family, and especially Hunter for all the support when I needed it the most.

This work received funding from the National Science Foundation under Grant No. PHY-2012152. I was also financially supported at SDSU through the University Graduate Fellowship and CORE Fellowship. Special thanks as well to the CSRC for providing additional financial support through the ASSICS Scholarship under NSF Grant No. 1930546, which was a pleasure to participate in.

Portions of Chapter 2 of this dissertation are a reprint of material that has been accepted for publication as "Relativistic Brueckner-Hartree-Fock Calculations for Cold and Hot Neutron Stars" in the Astrophysical Journal, used with permission from IOP Publishing. The coauthor listed in this publication is Fridolin Weber, who directed and supervised research which forms the basis for the dissertation.

Portions of Chapter 3 of this dissertation are a reprint of the material as it appears in "Differential rotation in compact objects with hyperons and delta isobars" in Astronomische Nachrichten, used with permission from Wiley-VCH GmbH. The coauthors listed in this publication are Fridolin Weber, Jia Jie Li, and Armen Sedrakian. Fridolin Weber directed and supervised research which forms the basis for the dissertation.

Portions of Chapter 5 of this dissertation are a reprint of the material as it appears in "Deducing Neutron Star Equation of State Parameters directly from Telescope Spectra with Uncertainty-Aware Machine Learning" in the Journal of Cosmology and Astroparticle Physics, used with permission from IOP Publishing. The coauthors listed in this publication are Pierre Baldi, Jordan Ott, Aishik Ghosh, Andrew W. Steiner, Atharva Kavitkar, Lee Lindblom, Daniel Whiteson, and Fridolin Weber. Daniel Whiteson directed and supervised research which forms the basis for the dissertation.

Portions of Chapter 6 of this dissertation are a reprint of the material as it appears in "Deducing Neutron Star Equation of State from Telescope Spectra with Machine-Learning-Derived Likelihoods" in the Journal of Cosmology and Astroparticle Physics, used with permission from IOP Publishing. The coauthors listed in this publication are Pierre Baldi, Jordan Ott, Aishik Ghosh, Andrew W. Steiner, Atharva Kavitkar, Lee Lindblom, Daniel Whiteson, and Fridolin Weber. Daniel Whiteson directed and supervised research which forms the basis for the dissertation.

VITA

Delaney Farrell

EDUCATION

Doctor of Philosophy in Computational Science **2024**
University of California, Irvine and San Diego State University *San Diego, California*

Bachelor of Science in Physics **2019**
San Diego State University *San Diego, California*

RESEARCH EXPERIENCE

Graduate Research Assistant **2019–2024**
San Diego State Univeristy *San Diego, California*

Graduate Research Assistant **2020–2024**
University of California, Irvine *Irvine, California*

Defense Science and Technology Intern **2022**
Lawrence Livermore National Laboratory *Livermore, California*

TEACHING EXPERIENCE

Teaching Assistant **2019-2020**
San Diego State University *San Diego, California*

REFEREED JOURNAL PUBLICATIONS

Relativistic Brueckner-Hartree-Fock Calculations for Cold and Hot Neutron Stars **2024**
Farrell, D. and Weber, F.
The Astrophysical Journal, Accepted.

Neural Simulation-Based Inference of the Neutron Star Equation of State directly from Telescope Spectra **2024**
Brandes, L., Modi, C., Ghosh, A., Farrell, D., Lindblom, L., Heinrich, L., Steiner, A. W., Weber, F., & Whiteson, D.
Journal of Cosmology and Astroparticle Physics, Pending.

Deducing Neutron Star Equation of State from Telescope Spectra with Machine-Learning-Derived Likelihoods **2023**
Farrell, D., Baldi, P., Ott, J., Ghosh, A., Steiner, A. W., Kavitkar, A., Lindblom, L., Whiteson, D., & Weber, F.
Journal of Cosmology and Astroparticle Physics, 2023(12):022, 2023.

Deducing Neutron Star Equation of State Parameters directly from Telescope Spectra with Uncertainty-Aware Machine Learning **2023**
Farrell, D., Baldi, P., Ott, J., Ghosh, A., Steiner, A. W., Kavitkar, A., Lindblom, L., Whiteson, D., & Weber, F.
Journal of Cosmology and Astroparticle Physics, 2023(02):016, 2023.

Phases of Hadron-Quark Matter in (Proto) Neutron Stars **2019**
Weber, F., Farrell, D., Spinella, w., Malfatti, G., Orsaria, M. G., Contrera, G., and Maloney, I.
Universe, 5(7), 169.

Neutrino Emissivity in the Color Superconducting Quark-Hadron-Mixed Phase **2019**
Freeman, A., Farrell, D., Weber, F., Spinella, W., Orsaria, M. G., & Contrera G.
Astronomische Nachrichten, p. 139-144, Vol. 340, 2019.

REFEREED CONFERENCE PUBLICATIONS

Differential Rotation in Compact Objects with Hyperons and Delta Isobars **2024**
Farrell, D., Weber, F., Li, J. J., & Sedrakian, A.
Astronomische Nachrichten, p. e20230160, Vol. 345, 2024.

Structure and Stability of Differentially Rotating Compact Stellar Objects **2023**
Farrell, D., Negreiros, R., & Weber, F.
Astronomische Nachrichten, p. e20230010, Vol. 344, 2023.

Deducing the EOS of Dense Neutron Star Matter with Machine Learning **2023**
Farrell, D., Baldi, P., Ott, J., Ghosh, A., Steiner, A. W., Kavitkar, A., Lindblom, L., Whiteson, D., & Weber, F.
Astronomische Nachrichten, p. e20230009, Vol. 344, 2023.

Proto-Neutron Star Matter **2022**
Alp, A., Farrell, D., Weber, F., Malfatti, G., Orsaria, M. G., & Ranea-Sandoval, I. F.
Journal of Physics: Conference Series, Col. 2340, no. 1, p. 012013.

REFEREED BOOK CHAPTERS

Fast Pulsars, Neutron Stars, and Astrophysical Strange Quark Matter Objects **2024**
Farrell, D., Weber, F., Orsaria, M. G., Ranea-Sandoval, I. F., Canullán, M., Negreiros, R., Katayama, T., and Wagaman, I.
"Pulsar Astronomy: Unrevealing Compact Stars with China's New Facilities", *World Scientific*, 55 pages, In Press.

Hot Neutron Star Matter and Proto Neutron Stars **2023**
Farrell, D., Alp, A., Weber, F., Spinella, W., Malfatti, G., Orsaria, M. G., & Ranea-Sandoval, I. F.
"New phenomena and new states of matter in the Universe: from Quarks to Cosmos," *World Scientific*, p. 199-259.

ABSTRACT OF THE DISSERTATION

Numerical Modeling of Rotating Neutron Stars and
the Equation of State of Superdense Matter

By

Delaney Farrell

Doctor of Philosophy in Computational Science

University of California, Irvine, 2024

Professor Fridolin Weber, Chair

Neutron stars harbor dense nuclear matter in density and temperature regimes inaccessible in terrestrial laboratory experiments. Understanding the interior of these stars and determining the equation of state of such matter has been a forefront area of nuclear and astrophysics research for decades, as the properties of neutron star matter are of key importance in comprehending the early Universe, laboratory and particle physics, and other astrophysical phenomena like supernovae and stellar mergers.

In this work, the determination of the equation of state of dense neutron star matter and neutron star structure is approached in several ways. The first is through theoretical modeling carried out in the framework of relativistic quantum field theory at both zero and finite temperatures. The calculated equation of state models are then used to compute the properties of neutron stars using Einstein's theory of general relativity. Special emphasis is placed on the structure and stability of differentially rotating compact objects, which may exist on short timescales following extreme astrophysical events like binary neutron star mergers.

The second approach to determining the equation of state of dense neutron star matter is based on machine learning, utilizing X-ray spectra and observable properties such as mass and radius of neutron stars. A novel inference of the equation of state directly from

simulated high-dimensional spectra of observed stars is compared with a calculation of the full likelihood of the equation of state parameters, accomplished by replacing intractable elements of the likelihood with machine learning models trained on samples of simulated stars.

Chapter 1

Superdense Matter and Neutron Stars

1.1 Introduction

A longstanding area of interest in nuclear and astrophysics is the exploration of the properties of matter existing at extreme densities, pressures, and temperatures. Understanding the properties of such matter, described succinctly by its equation of state (EOS), may better our understanding of various research fronts: the early Universe, compact objects, laboratory physics explored with particle colliders, and other extreme astrophysical phenomena like core-collapse supernovae and stellar mergers. A phase diagram of the Universe is shown in Figure 1.1; terrestrial laboratories with particle colliders like the Large Hadron Collider (LHC) [12], Relativistic Heavy Ion Collider (RHIC) [13], the Facility for Antiproton and Ion Research (FAIR) [14], and the Nuclotron-based Ion Collider fAcility (NICA) [15] probe dense matter at high temperatures. On the other extreme, neutron stars contain one of the densest forms of matter in the Universe, characterized by temperatures that are less than 10^{10} K (or around 1 MeV), effectively registering as zero temperature on the nuclear scale. The conditions within a neutron star cannot be replicated in terrestrial laboratories, making

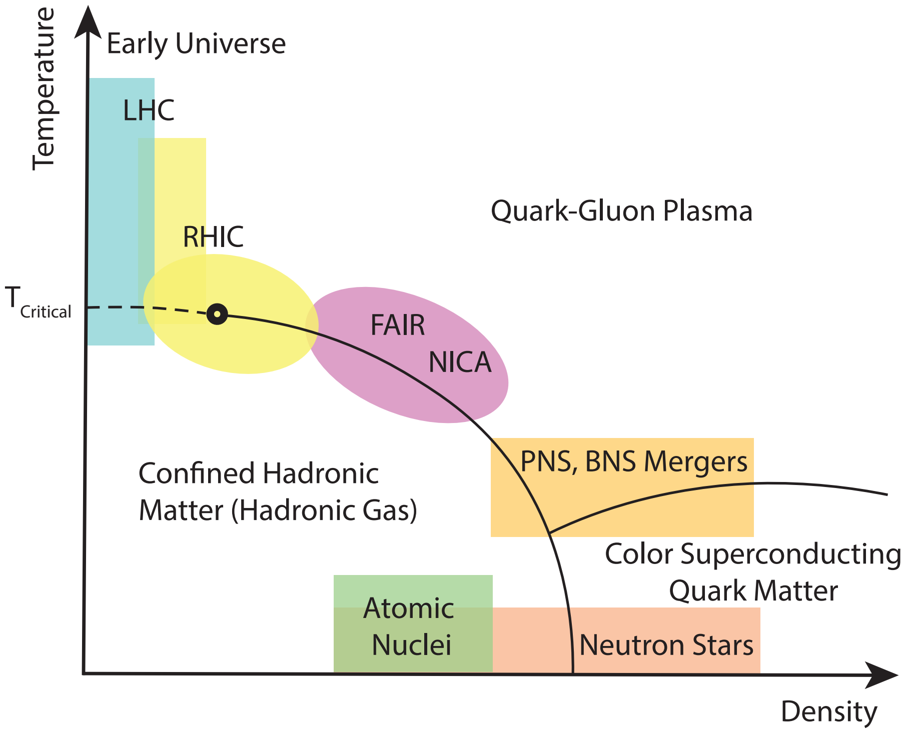

Figure 1.1: Phase diagram of the hot and dense matter, where the critical temperature T_{Critical} is $\approx 160 - 170$ MeV. The light blue is representative of experiments at the Large Hadron Collider (LHC), the yellow is the Relativistic Heavy Ion Collider (RHIC), and the purple is the Facility for Antiproton and Ion Research (FAIR) and the Nuclotron-based Ion Collider fAcility (NICA). Additionally shown are the regimes for proto-neutron stars (PNS), binary neutron star (BNS) mergers, atomic nuclei, and neutron stars. Similar diagrams can be found in Refs. [1–3].

them unique naturally-occurring laboratories to study matter in extreme conditions [16–21]. A newly born neutron star, also known as a proto-neutron star (PNS), and stellar binary mergers containing neutron stars are also incredibly dense but are much hotter than a neutron star, existing in a regime closer to being probed by particle colliders [22]. Determining the EOS of both cold and hot superdense matter remains a forefront area of research, even after decades of theoretical, experimental, and observational endeavors.

A neutron star is formed from the iron core of a massive star - one 8 to 25 times the mass of our sun, $M_\odot$. When the iron core of such a star surpasses the so-called Chandrasekhar limit (1.4 $M_\odot$), gravity overcomes the balance of forces within the star resulting in a core-collapse supernova, where the star expels much of its matter and leaves behind a neutron star. Neutron stars are the densest observed stellar objects, typically harboring masses within the range of 1 to 2 solar masses ($M_\odot$) and radii spanning from 10 to 15 km. Their high mass and small radius result in immense gravitational forces within the star, compressing the matter in the innermost regions to densities up to an order of magnitude higher than nuclear saturation density (2.5×10^{14} g/cm^3). The high mass and extreme densities encountered within these stars warp the geometry of spacetime considerably, so modeling of neutron stars must be carried out in the framework of Einstein's theory of general relativity. Beyond their extreme densities, neutron stars may also be rotating rapidly and possess very strong magnetic fields. To date, the fastest rotating neutron star, also known as a pulsar, is PSR J1748–2446ad with a rotational frequency of 716 Hz [23]. Pulsars may also fall into a class of neutron stars referred to as magnetars, which rotate at slow frequencies but have extremely high magnetic fields (on the order of 10^{14} - 10^{15} G on their surface). Pulsars emit beamed radiation in the form of radio, X-ray, and gamma rays which can be detected by radio telescopes like the Parkes telescope [24] and FAST (Five hundred meter Aperture Spherical Telescope) [25], or X-ray telescopes like NICER (Neutron star Interior Composition Explorer) [26], the Chandra X-ray Observatory [27], and XMM-Newton [28].

In this dissertation, a variety of numerical techniques are used to explore the properties of rotating neutron stars and superdense matter. The following sections give a theoretical introduction to each topic explored and the motivation to study them.

1.2 Equation of State

The essential physics of matter within a neutron star can be succinctly summarized by the equation of state (EOS), which describes the pressure-density relation within the star. Because the matter within the core of a neutron star exists in a low-temperature, high-

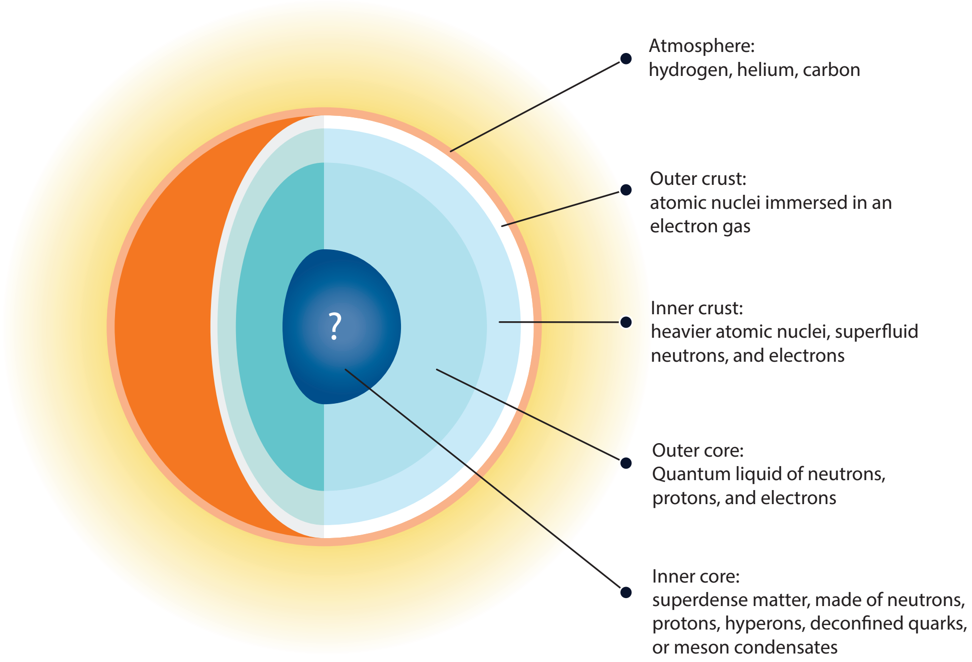

Figure 1.2: The layered structure of a neutron star.

density regime that cannot be replicated in laboratories or particle colliders, the EOS of dense neutron star matter must instead be described by theoretical models that vary widely due to particle composition and mathematical frameworks used to model such matter.

Figure 1.2 shows the composition of each region of a neutron star, which is believed to have a layered structure. Theoretical modeling the EOS of neutron star matter is a formidable task, as the density within a neutron star ranges from a few grams per cubic centimeter at the surface to around 10^{15} g/cm^3 at the core. The least dense portions of a neutron star are its surface and outer crust region, where matter is compressed to densities up to 10^6 g/cm^3. The surface region is comprised of ordinary atomic nuclei (such as ^{56}Fe) and non-relativistic electrons; this is the region that emits thermal radiation that telescopes like NICER or the Chandra X-ray Observatory can observe. In the outer crust, at densities on the order of $10^6 - 10^{11}$ g/cm^3, electrons become relativistic and form a relativistic electron gas. Additionally, the atomic nuclei grow more neutron-rich because of the inverse β-reaction while forming a Coulomb lattice. In the inner crust, which has densities in the range $10^{11} - 10^{14}$ g/cm^3, atomic nuclei grow extremely neutron-rich to the point neutrons begin to drip out of the nuclei and populate free states; the neutron-rich nuclei form clusters in a lattice and are then immersed in a gas of relativistic electrons and neutrons [29–33].

The high-density region of a neutron star, its core, is composed of a relativistic Fermi liquid of neutrons and protons. The liquid is extremely neutron-rich while maintaining a certain fraction of protons, electrons, and muons to maintain chemical or β-equilibrium [34]:

$$\mu_B = \mu_n + q_B(\mu_e - \mu_{\nu_e}), \tag{1.1}$$

where μ_B is the chemical potential of baryons B, neutrons (μ_n), electrons (μ_e), and electron neutrinos (μ_{ν_e}), while q_B is the baryon electric charge. Neutron star matter additionally fulfills electric charge neutrality. The dense, neutron-rich matter in the core may reach densities of up to 10 times nuclear saturation density, and as nuclear boundaries at such high densities begin to overlap, the matter is expected to transition into non-nucleonic or ”exotic” states of matter. These states can take several forms: the onset of quark degrees of freedom and deconfined quark matter [35–43] which may occur in color superconducting phases [16, 18, 44, 45], boson condensates formed by pions or kaons [46–59], or the formation of other matter with a high degree of strangeness carried by hyperons [60–65].

While the matter within the core of a neutron star cannot be replicated in terrestrial laboratories, properties of laboratory neutron-rich nuclei can be used to define the EOS for the crust (up to order 10^{11} g/cm^3). The crust regions are thin, contributing very little to the bulk properties of the star like its mass; below 10^{11} g/cm^3, the crust only contributes 10^{-5} $M_\odot$ to the mass. Today, two commonly used EOS models for the crust include Baym-Pethick-Sutherland [66] and Baym-Bethe-Pethick [67] (BPS-BBP), or Harrison-Wheeler [68] and Negele-Vautherin [69] (HW-NV).

The EOS of dense neutron star matter is modeled as a many-body problem that can be solved theoretically using different nuclear many-body theories which broadly fall into two categories: phenomenological or *ab initio* [70–73]. Phenomenological models, based on density functional theories with effective nucleon-nucleon (NN) interactions, are constructed to reproduce the empirical saturation properties of finite nuclei and symmetric nuclear matter (SNM) while adhering to constraints extracted from nuclear physics and astrophysics [74–76]. A popular method of constructing phenomenological models is the relativistic mean field (RMF) approximation, also referred to as the relativistic Hartree approximation. This methodology is expanded on in the relativistic Hartree-Fock (RHF) theory, where an exchange contribution (i.e. the Fock contribution) is added such that the final states of each of the two baryons propagating in the many-body medium are interchanged [70].

In contrast to the effective NN interactions used in phenomenological models, *ab initio* methods use realistic NN interactions which are determined by nucleon-nucleon scattering data and the properties of the deuteron. These NN interactions are characterized by a repulsive core at short distances, a strong attraction in an intermediate range, and are dominated by the one-pion exchange at large distances. *Ab initio* methods of this kind include the quantum Monte Carlo method [77–79], the self-consistent Green's function method [80], and Brueckner-Hartree-Fock approaches [81–89]. Most *ab initio* calculations are constructed in a non-relativistic framework, which can simulate the saturation behavior of symmetric nuclear matter (SNM) using high-precision, realistic NN interactions [90]. To reproduce the saturation properties of nuclear matter, non-relativistic calculations need to include three-body interactions, which makes calculations to extend the theory to heavier nuclei very difficult. On the other hand, relativistic *ab initio* methods, like the relativistic Brueckner-Hartree-Fock (RBHF) approximation, more closely reproduce empirical data than non-relativistic calculations [83, 91]. Unlike the RMF or RHF approximations, the RBHF approximation couples the propagation of baryons to the many-body background and encapsulates dynamical correlations between baryons, computed using a relativistic scattering (T) matrix.

Solving the nuclear many-body problem in a relativistic framework is considerably more tedious (both theoretically and numerically) than non-relativistic methods as a self-consistent spinor basis with positive and negative energy states is necessary. Because of this, studies carried out using the RBHF approximation have historically been relatively rare in the literature. However, there is a growing body demonstrating that variations of the RBHF approximation are successful in reproducing the empirical saturation properties of SNM, including the works of Refs. [83, 85, 89, 92–95]. Additionally, the vast majority of models of neutron star matter are calculated at zero temperature which is suitable for certain classes of neutron stars, but there is a vested interest within the nuclear astrophysics community to carry out calculations at higher temperatures to model newly born neutron stars (proto-neutron stars), core-collapse supernovae, and stellar merger events.

1.3 Rotation and Stellar Structure

The structure of a neutron star, including macroscopic properties like the mass and radius, can be deduced from observation (a topic explored more in Section 1.4) or modeled theoretically in the framework of Einstein's theory of general relativity. The stellar equations for neutron stars are derived from Einstein's field equation, which is written as ($\mu, \nu = 0, 1, 2, 3$):

$$G^{\mu\nu} = 8\pi T^{\mu\nu}(\epsilon, P(\epsilon)), \tag{1.2}$$

where $G^{\mu\nu}$ is the Einstein curvature tensor and $T^{\mu\nu}$ is the energy-momentum tensor. The energy-momentum tensor contains the EOS (i.e. the energy density ϵ and pressure $P(\epsilon)$) as an input, meaning the stellar structure equations serve as a mapping between the EOS of neutron star matter and macroscopic properties.

The simplest form of stellar structure equations is the Tolman-Oppenheimer-Volkoff equation, which models non-rotating, spherically symmetric objects in hydrostatic equilibrium [96, 97]. In this case, the stellar structure simplifies to an ordinary differential equation that describes the pressure gradient within the star. For rotating stars, the calculations become considerably more complicated. Rapid rotation deforms the structure of the star, which is discussed more in Chapters 2 and 3. Additionally, rotation drags along the local inertial frames inside and outside of the star so that they co-rotate, also known as frame-dragging, which must be accounted for in the calculations [70, 98].

The vast majority of rotating neutron stars exhibit rigid body or uniform rotation, wherein the entire star rotates as a singular entity, maintaining a consistent rotation rate. However, following extreme astrophysical events like core-collapse supernovae or binary neutron star mergers, a neutron star may rotate differentially as opposed to uniformly. A newly formed proto-neutron star may experience some degree of differential rotation following a core-collapse supernova, but the phenomena would be short-lived. Hydrodynamical forces in the form of Ekman pumping and turbulent mixing will dampen any differential rotation in the star within a few days [70]. Another avenue for a star to experience differential rotation is following a binary neutron star merger event, where complex hydrodynamic motions come into play during coalescence [99]. The resulting remnant star following the collision may either promptly collapse into a black hole, or form a hypermassive neutron star depending on the dynamics of the binary prior to merging. A hypermassive remnant star is likely stabilized by thermal pressure and differential rotation on short, dynamical timescales. Modeling differential rotation in neutron stars can provide a better understanding of the structure and stability of these objects, an important task in the new era of multi-messenger astronomy.

There are only very few independent numerical codes that solve the stellar structure equations for uniformly rotating stars, some of which are open-source like *RNS* [100] and *XNS* [101]. These codes follow different numerical schemes to varying accuracy; a full review can be found in Ref. [102]. Currently (to the best of my knowledge), there exists only one open-source numerical code that models differential rotation in neutron stars, which is included as a module of the Einstein Toolkit [103]. This module is a black box, which limits the capability to customize, alter, or fine-tune the numerical scheme. Independent studies of differential rotation in neutron stars have been conducted in the literature [104–109]. Like those for uniform rotation, the numerical codes for differential rotation follow different schemes, but many use the same linear rotation law, which is explored more in Chapters 3 and 4.

1.4 Observation

Observation has long served as an avenue for furthering our understanding of neutron stars and superdense matter. In the last two decades, there has been an increasing amount of high-quality, new data from X-ray and gamma-ray telescopes, including precisely timed observations of pulsars [110]. Today, over 3,000 pulsars have been discovered, and their discoveries have provided valuable constraints on various neutron star properties like mass and radius, cooling [111], and magnetic fields [112]. As we move into an era of new-generation X-ray telescopes, these constraints on neutron star properties and EOS are expected to tighten even further. These discoveries will also aid in our understanding of other astrophysical phenomena like core-collapse supernovae, r-process nucleosynthesis, and gravitational wave emission [110].

The emission from a neutron star is directly influenced by macroscopic stellar properties such as mass and radius, which are determined by the star's underlying EOS. Therefore, in principle, the EOS (which also determines such stellar properties) can be inferred from observations of stellar emission. In practice, crucial elements of the likelihood are not tractable, preventing straightforward inference. For example, while the mass and radius can be calculated from the EOS using the stellar structure equations, the equations cannot be trivially inverted [113–119]. The task is further complicated by the small number of neutron star observations and the relatively large uncertainty of the individual measurements. Instead, the current state-of-the-art methods to place constraints on stellar properties use statistical inference to fit emissions to theoretical models.

In this section, we discuss how physical properties like mass, radius, and tidal deformability are deduced from spectral emission and gravitational waves, as well as how these properties in turn place constraints on the nuclear EOS. For each property, the current state-of-the-art inference methods are given, and a new inference method, machine learning, is introduced as well.

1.4.1 Neutron Star Masses and the Equation of State

The mass of neutron stars is perhaps the most precisely measured neutron star property, especially those coming from radio pulsar timing of neutron star masses in compact binaries [1]. Observed values of masses of neutron stars [120] are extremely valuable measurements as they test theories of nuclear matter and therefore provide constraints on the (nuclear) EOS. A notable example of such a constraint resulted from the observation of massive neutron stars. For several decades the canonical mass of a neutron star was thought to be around 1.4 $M_{\odot}$, but recent observations of heavier neutron stars (≥ 2 $M_{\odot}$) have widened the range of masses that must be accounted for with theoretical EOS models. Heavy neutron stars directly challenge theoretical models of dense nuclear matter in quantum chromodynamics (QCD) if exotic degrees of freedom are taken into account. Observations of massive stars enforced the requirement that EOS models for neutron star matter must produce maximum stable masses of at least 2 $M_{\odot}$. Such models are referred to as "stiff" meaning they have a larger pressure for a given density than a "soft" model, so observations of massive neutron stars ruled out many softer theoretical EOS models. An example of such a massive neutron star is the millisecond pulsar MSP J0740+6620 with a measured mass of $2.14^{+0.10}_{-0.09}$ $M_\odot$, making it one of the heaviest millisecond pulsars observed thus far [121].

Radio pulsars, or highly magnetized, rotating neutron stars, that exist in binary stellar systems generate radio pulses that can be precisely tracked as a method of determining the binary's mass [110]. Radio pulsars have long-term rotational stability, allowing for very precise timing measurements of orbital motion. The binary mass function, $f(M_1, M_2, i)$, can be derived from measurements of five Keplerian parameters: the binary period P_b, the projection of the pulsar's orbital semimajor axis a on the line of sight $x \equiv a_i \sin i$, the orbital eccentricity e, and time T_0 and longitude ω_0 of periastron ω [70]. The formula for the mass function is given as:

$$f(M_1, M_2, i) \equiv \frac{(M_2 \sin i)^3}{(M_1 + M_2)^2} = \frac{P_b v_1^3}{2\pi G} = \frac{4\pi^2 x^3}{G P_b^2}, \tag{1.3}$$

where G is Newton's gravitational constant and $v_1 = (2\pi/P_b)x$ is the orbital velocity of star M_1 along the line of sight. Other relativistic effects, like the transverse Doppler effect and gravitational redshift, can also be used to determine the pulsar and companion's masses in a binary system [70, 110].

Alongside other parameters, mass can also be inferred from stellar emission using other observational techniques like waveform modeling, where a Bayesian inference approach is employed to analyze X-ray waveform oscillations emitted by pulsars [5, 122]. X-ray oscillations can be observed from accretion-powered pulsars, thermal emission of rotation-powered (or non-accreting) pulsars, or some thermonuclear bursts on accreting neutron stars [1]. It is believed that the X-ray oscillations are emitted from a "hot spot" on the star's surface, or a region of the stellar surface that is both hotter than its surroundings and offset from the rotational pole of the star. The pulse profile, or waveform, from the hot spot combined with general relativistic effects like light bending and Doppler boosting, can be used to determine the mass and radius of the source. Pulse waveform modeling was pioneered using data from X-ray telescopes like ROSAT and XMM-Newton, but the methodology has become more popular recently with observations from NICER, which has extraordinary absolute timing accuracy when determining the pulse profile of isolated neutron stars and those in binary systems [5]. For example, NICER data was used to determine estimations for the mass and radius of the isolated millisecond pulsars PSR J0030+0451 [5, 123] and PSR J0740+6620 (together with XMM-Newton data) [124, 125]. The latter study showed that although having a mass $\sim 40\%$ larger, the radii of PSR J0740+6620 and PSR J0030+0451 are of the same order [123, 125]. This finding is all the more interesting when considering that the determination of neutron star radius has historically been more difficult than mass, which is discussed further below.

1.4.2 Radius

Historically, direct measurements of neutron star radius do not exist, and inference of radius using various techniques provides large uncertainties when compared to precise mass measurements. Current methods for determining radius commonly rely on the spectroscopic measurements of surface emission to either measure apparent angular size or look for effects of the emission on neutron star spacetime [1, 110]. These methods broadly fall into one of two categories: spectroscopic or timing measurements.

Spectroscopic measurements from either the surface emission of quiescent low-mass X-ray binary (LMXB) systems or from thermonuclear bursts can be used to constrain the mass-radius relation. If it is assumed that the surface spectrum is a diluted blackbody and the source of the spectrum is at a known distance D, the mass-radius (M-R) relation of a slowly spinning neutron star can be defined as:

$$R^2\left(1-\frac{2GM}{Rc^2}\right)^{-1}=\frac{FD^2f_c^4}{\sigma T_c^4}, \tag{1.4}$$

where F is the measured flux, σ is the Stefan-Boltzmann constant, and T_c and f_c are the color temperature and color-correction factor, respectively [1]. The color temperature is assumed to be larger than the star's effective temperature, defined as $T_c = f_c T_{\text{eff}}$. The color-correction factor f_c is dependent on both the assumed atmospheric composition and effective surface gravity, where $f_c \approx 1.3-2$ [1]. Under the same assumed conditions, the observed or apparent radius R_{obs} can be defined as:

$$R_{\text{obs}}=R\left(1-\frac{2GM}{Rc^2}\right)^{-1/2}. \tag{1.5}$$

The above approximation is reliant on several assumptions and exact measurements and thus may not hold in various instances. In the case of strong magnetic fields, for example, the assumptions of a specific atmospheric composition and a constant surface temperature may be incorrect [110]. For rotating neutron stars that are rotating rapidly (i.e. not spinning slowly), spin-dependent corrections must be applied to the observed angular size as a Schwarzschild metric can not describe the spacetime due to frame dragging [110]. Additional complications to the approximation are introduced if there is uncertainty when measuring the exact distance D to the star.

Some uncertainties can be alleviated by choosing sources with low magnetic fields or those that exist in globular clusters of known distances, which is why thermal emission from sources like LMXBs in quiescence is at the forefront of constraining the neutron star mass-radius relation. The observed thermal spectrum can be fit to a well-motivated theoretical model dependent on the assumed atmosphere of the neutron star in a process called spectral fitting. Many of these theoretical models assume quiescent LMXBs have pure hydrogen atmospheres as the companion stars are hydrogen-rich, but other atmospheric compositions like helium and carbon have also been explored in the literature [126].

As mentioned in the section above, the mass-radius relation can also be explored through X-ray timing techniques like waveform modeling, spin measurements, and asteroseismology. While further explanation of these techniques will not be discussed explicitly, the reader can find more information at [1, 5, 125, 127].

1.4.3 Tidal Deformability and Gravitational Waves

The tidal deformability of compact objects is an important physical quantity for gravitational-wave (GW) astronomy. The main reason is that it determines the pre-merger GW signal in binary neutron star merger events. Working up to linear order, the tidal deformability λ is given by [128]:

$$\lambda = -\frac{\varepsilon_{ij}}{Q_{ij}}, \tag{1.6}$$

where ε_{ij} denotes the external gravitation field produced by the external source and Q_{ij} is the induced mass-quadrupolar moment of the given object. In addition, λ is related to the second Love number, k_2, and the radius of the compact object, R, by [128]:

$$\lambda = \frac{2}{3} k_2 R^5. \tag{1.7}$$

Finally, the dimensionless tidal deformability, Λ, is defined by [128]:

$$\Lambda = \frac{\lambda}{M^5}, \tag{1.8}$$

where the M denotes the gravitational mass of the compact star. For details on how theoretical calculations related to this quantity are performed, the interested reader can refer to Refs. [128, 129] and references therein.

The detection by LIGO and Virgo observatories of the gravitational waves emitted during event GW170817, a binary neutron star merger (see, for example, [130] and references therein) together with its electromagnetic counterpart (see, for example, [131], and references therein) allow to estimate the possible masses, radius and dimensionless tidal deformability of the merging objects. Additionally, the dimensionless tidal deformability of a canonical neutron star was estimated to be $\Lambda_{1.4} = 190^{+390}_{-120}$ at a 90% level with no strong restrictions to the EOS are imposed [130].

1.4.4 Machine Learning

In recent years, the application of machine learning to scientific problems has exploded, including the application to the inference of neutron star properties and the EOS. Machine learning has been used previously for data analysis in the natural sciences [132], increasing the power of valuable data [133] while naturally propagating uncertainties [134]. Applications in particle physics have used larger and deeper neural networks powered by advances in hardware processing to tackle more complex and higher-dimensional tasks [135, 136]. In astrophysical contexts such as regression of neutron star parameters where the likelihood is not tractable and analytical inversion is not feasible, simulation-based inference techniques [137] have been explored. For example, recent work from Fujimoto *et al* [6, 7] demonstrated regression of neutron star matter EOS from mass-radius pairs, where networks are trained on samples of simulated stars and uncertainties are drawn from an ad-hoc Gaussian model. Morawski [8] also performed regression from mass-radius pairs to EOS assuming Gaussian uncertainty and attempted to reduce EOS parameterization dependence. Soma *et al* [138] regressed both EOS and mass-radius information through a set of connected modes: density values are used to determine pressure values using a deep neural network, and the regressed pressure values are then used to generate mass-radius pairs using a generative deep learning model. Ferreira [9] instead regressed EOS from radius and tidal deformation information using support vector machines (SVMs) and deep neural networks (DNNs).

1.5 Projects

This thesis is comprised of three main projects, involving the modeling of dense neutron star matter at zero and finite temperatures, the modeling of differential rotation in neutron stars, and using machine learning to deduce the EOS of neutron star matter from observed X-ray spectra. In detail:

Project 1: In the next chapter of this thesis, Chapter 2, we numerically model the EOS of neutron star matter using the RBHF formalism. Calculations are carried out at zero temperature to describe conventional neutron stars, as well as at finite temperatures up to 70 MeV which can be used to model proto-neutron stars or binary neutron star mergers. The EOS models are then used to calculate the bulk properties of both non-rotating and uniformly rotating neutron stars.

Project 2: As shown throughout the literature, the calculated properties of uniform and differential rotation depend not only on the mathematical framework used to solve Einstein's field equations but also on the underlying EOS [70, 102, 104, 105, 139]. In Chapter 3, we numerically model differential rotation in neutron stars to explore the structure and stability of hypermassive stars, using modern EOS models that include strange matter. In Chapter 4, we extend the calculations to matter at finite temperatures, specifically using models constructed using the RBHF formalism described in Chapter 2. For the differentially rotating stellar models constructed at finite temperatures, we classify models as stable or unstable to excitation of the dynamical bar-mode instability and provide examples of the physical structures of unstable models.

Project 3: The vast majority of published studies that use machine learning techniques to determine the EOS of neutron star matter from observed stellar properties (like mass and radius) make simplifications to handle uncertainties in the regression task. None begin directly with stellar emission from which the observed properties are derived. In Chapter 5, we demonstrate regression of EOS directly from simulated X-ray spectra from neutron stars without collapsing to intermediate states of observable properties like mass and radius, and where uncertainty due to unknown values of other stellar parameters is fully propagated. In Chpater 6, we instead infer EOS from simulated X-ray spectra by constructing an otherwise intractable likelihood by replacing the intractable elements with neural networks trained on samples of simulated stars.

1.6 Notation and Abbreviations

This section provides information on the notation and mathematical conventions used in this thesis.

Modeling neutron stars is carried out in the framework of Einstein's theory of general relativity. In this framework, the coordinates of an event are generally written as x^μ where Greek indices (μ in this case) take values from 0 to 3 corresponding to four dimensions. The first, x^0, is the time coordinate, and the last three, x^1, x^2, and x^3, are the space coordinates. Additionally, equations shown throughout this thesis use Einstein's summation notation, where any index that is repeated in a product is summed over.

Table 1.1: Common abbreviations used throughout this thesis.

Abbreviation	**Meaning**
EOS	equation of state
SNM/ANM	symmetric/asymmetric nuclear matter
OBE	one boson exchange
PNM	pure neutron matter
PNS	proto-neutron star
BNS	binary neutron star, in the context of BNS merger events
CST	Cook-Shaprio-Teukolsky, differential rotation algorithm [104]
RBHF	relativistic Brueckner-Hartree-Fock
RHF	relativistic Hartree-Fock
RMF	relativistic mean field
ML	machine learning
NN	neural network

For the context of this work, the metric tensor $g_{\mu\nu}$ is defined as [97]:

$$g_{\mu\nu} = \begin{pmatrix} -1 & 0 & 0 & 0 \\ 0 & 1 & 0 & 0 \\ 0 & 0 & 1 & 0 \\ 0 & 0 & 0 & 1 \end{pmatrix} \tag{1.9}$$

in matrix notation. The equations appear throughout the text using geometrized units, where the gravitational constant G, the speed of light c, and Planck's constant $\hbar$ are all set to 1. The Dirac matrices used are in the Bjorken-Drell notation [140, 141].

In many of the chapters, bulk properties of neutron stars like mass and radius are calculated. If not otherwise specified, the mass M will always refer to the gravitational mass, and the radius R refers to the equatorial radius.

Several abbreviations are commonly used throughout the text, which can be found in Table 1.1. These abbreviations will be mentioned and redefined at the first use in each chapter.

Chapter 2

Modeling Neutron Star Matter with the Relativistic Brueckner-Hartree-Fock Formalism

This chapter presents text and results from work in collaboration with Fridolin Weber that has been accepted for publication in the Astrophysical Journal.

2.1 Introduction

There is a particular interest in the fields of nuclear and astrophysics to learn and model the equation of state (EOS) of nuclear matter under extreme conditions. For superdense nuclear matter, far beyond its saturation point, this knowledge is paramount to the study of neutron stars whose core densities can reach an order of magnitude higher than saturation density. However, the unique internal conditions within a neutron star are well beyond the reach of our terrestrial laboratories, namely due to the extreme densities exhibited in the inner regions of the star and because the matter is highly isospin-asymmetric ($N \neq Z$) [20, 142]. Some experimental constraints on neutron star matter have come from ultra-relativistic heavy-ion collisions (as conducted at the RHIC [143], the LHC [144], and FAIR [145]), which probe the nature of hot, symmetric nuclear matter. Extremely neutron-rich matter has more recently been probed in studies of neutron skin or giant monopole and dipole resonances, but these studies are limited in nature [146]. Unfortunately, these experiments currently lack the temperature and density constraints present within the core of a neutron star - meaning the dense matter encountered within a neutron star cannot yet be replicated by experiment. Other promising avenues to constraining the knowledge of the equation of state of neutron star matter come from multi-messenger astronomy; vital constraints have come from telescopes like the Neutron Star Interior Composition Explorer (NICER) [147] and NASA's Chandra Observatory [148], or more recently, from the gravitational wave observatories LIGO [149] and Advanced Virgo [150].

As mentioned in Chapter 1, the vast majority of theoretical EOS models for neutron star matter, especially those calculated using a relativistic framework like the relativistic Brueckner-Hartree-Fock (RBHF) approximation, are done at zero temperature. However, finite temperature EOS models are vital to understanding various astrophysical phenomena like core-collapse supernovae, binary neutron star mergers, and proto-neutron stars. In this chapter, we extend the RBHF approximation in full Dirac space to finite temperatures. For asymmetric nuclear matter (ANM), we produce EOS models for dense neutron star matter at both zero and finite temperatures, which are then used to calculate bulk properties of both rotating and non-rotating neutron stars. This chapter is organized as follows: the theoretical framework of the RBHF theory and the modifications for the inclusion of temperature are shown in Section 2.2. The theoretical framework for calculating properties of neutron stars, rotating and non-rotating, is discussed in Section 2.3. Section 2.4 shows the calculated results, including properties of nuclear matter at zero and finite temperature, and the resulting bulk properties of neutron stars. Section 2.5 presents the summary of the work.

2.2 Theoretical Framework

The general theory for modeling nuclear matter in the RBHF approximation is outlined in extensive detail in Refs. [70, 83]; the information presented in this chapter follows directly from the aforementioned references. Nuclear matter at supranuclear densities can be described from the framework of nuclear physics as a complex, many-body system whose dynamics are governed by the Lagrangian density:

$$\mathcal{L} = \mathcal{L}_N + \sum_M (\mathcal{L}_M + \mathcal{L}_{MN}), \tag{2.1}$$

where $\mathcal{L}_N$ denotes the Lagrangian of non-interacting nucleons and $\mathcal{L}_M$ is the Lagrangian of different free meson fields $M = \sigma, \omega, \rho, \pi, \phi, \delta, \eta$. $\mathcal{L}_{MN}$ describes the interaction between nucleons and mesons; a complete description of the interaction Lagrangians is given in Eqs. (2.3) - (2.12) in Ref. [83]. The interactions caused by various meson fields in the proposed relativistic model are taken into account by an effective relativistic single-particle potential or self-energy [151]. The vital distinction of RBHF theory is that nucleons in this system are treated as effective Dirac particles, which can be described by the relativistic Dirac equation:

$$(i\gamma^\mu \partial_\mu - m)\Phi = \sum_M \Gamma_M \, \Phi \,, \tag{2.2}$$

where γ^μ are the Dirac matrices, m is the particle mass, Φ represents the spinors, and Γ_M are the meson-nucleon vertices.

2.2.1 Green's Functions

The equations of motion for the various particle fields within the many-body system are derived from the Euler-Lagrange equation and solved using the Martin-Schwinger hierarchy of coupled Green's functions [152]. The Green's functions, denoted by G_n, are defined as ground-state ($|\Phi_0\rangle$) expectation values of time-ordered field operators and contain information vital to the structure of the many-body system [70, 83]. To describe the propagation of n nucleons relative to the many-body background, the $2n$-point Green's function is defined as:

$$G_n(1...n, 1'...n') = i^n\langle\Phi_0 \mid T(\psi_{\xi_1}(x_1)...\psi_{\xi_n}(x_n)\ \bar{\psi}_{\xi_1}(x_1)...\bar{\psi}_{\xi_n}(x_n)) \mid \Phi_0\rangle\,, \tag{2.3}$$

where the integers 1 to n denote the spacetime coordinates $(x_1^0, \vec{x}_1)\ldots(x_n^0, \vec{x}_n)$ with corresponding spin-isospin coordinates $\xi_1 \ldots \xi_n$. The nucleon fields are represented by ψ. $\hat{T}$ is the time-ordering operator, which is defined such that the operators are ordered in time according to the values of their associated time parameters. For example, if $t_1 < t_2 < \ldots < t_n$, the operators are arranged in ascending order of time.

The RBHF approximation accounts for dynamical two-body correlations by using a six-point Green's function, which is factorized into products of four- and two-point functions (shown schematically in Figure 2.1). Therefore the nucleonic three-body force is reduced to an effective two-body force by averaging over the third nucleon in the medium [153]. Figure 2.1 shows ingoing (un-primed) particles entering a medium, scattering, and exiting in outgoing (primed) states. Here, Green's functions G act as particle propagators from ingoing to outgoing states. Within the approximation, the four-point Green's function preserves the dynamical two-body correlations and the third body (particle 3 in the schematic) only contributes as a spectator. The key differentiation between the RBHF approximation and other many-body approximations like the relativistic mean-field (RMF) and Hartree-Fock (RHF) approximations is the inclusion of dynamical correlations within the scattering or T-matrix, as will be discussed below. For both RMF and RHF, particles propagate independently from each other in the medium, meaning dynamical correlations are ignored. Both approximations factor the four-point Green's function into products of two-point functions, where RHF

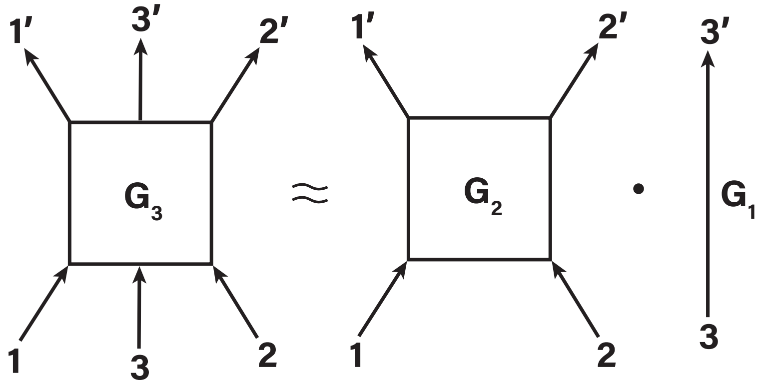

Figure 2.1: A schematic for the factorization of the six-point Green's function G_3 in the RBHF approximation. G_3 is factorized into a product of four-point (G_2) and two-point (G_1), where the dynamical two-body correlations are held in G_2. Ingoing states are unprimed, and outgoing are primed (see text for more detail).

expands on RMF by including an "exchange" or Fock contribution.

2.2.2 Coupled System of Many-Body Equations

To describe the properties of a dense, many-body system, the formal structure of the RBHF approach is to solve a highly nonlinear, coupled system of equations. This approach first begins with solving for G_1 for all nucleons using the Dyson equation, which in position space is defined as:

$$G_1 = G_1^0 + G_1^0 \, \Sigma \, G_1 \,, \tag{2.4}$$

where G_1^0 represents the free nucleon Green's function and the influence of the surrounding nucleons is expressed by the nucleon self-energy, Σ. Under the Fourier transformation, the Dyson equation is represented as:

$$[\not{p} - m - \Sigma(p)] \, G_1(p) = 1 \,, \tag{2.5}$$

where $\not{p} = \gamma^\mu p_\mu = \gamma^\mu g_{\mu\nu} p^\nu = \gamma^0 p^0 - \sum_{i=1}^{3} \gamma^i p^i$ and γ^0 and γ^i are the Dirac matrices. Once the 2-point G_1 function is solved for, the in-medium scattering matrix, here referred to as the T-matrix, is solved for. It is given by a Bethe-Salpeter-type integral equation:

$$\mathrm{T}{=}\, V + \textstyle\int V \, \Lambda \, T \, , \tag{2.6}$$

where Λ is the intermediate nucleon-nucleon propagator, which takes the form of the Brueckner propagator in the RBHF approach (discussed further in Section 2.2.7). V is representative of repeated sums of two-particle interactions given by a one-boson-exchange (OBE) potential, which describes the interaction among two nucleons in terms of the exchange of scalar, pseudo-scalar, and vector mesons. It can be written as a sum over meson (M) contributions:

$$\langle 1\, 2 \,|\, V \,|\, 3,\, 4 \rangle = \sum_{M} \langle 1\, 2 \,|\, V_M \,|\, 3,\, 4 \rangle \, , \tag{2.7}$$

where the numbers 1 to 4 denote time and space (or momentum). In the same vein, Eq. (2.6) can be written as:

$$\langle 1\, 2 \,|\, T \,|\, 1',\, 2' \rangle = \langle 1\, 2 \,|\, V \,|\, 1'\, 2' - 2'\, 1' \rangle + \langle 1\, 2 \,|\, V \,|\, 3,\, 4 \rangle \, \Lambda(3\, 4, 5\, 6) \, \langle 5\, 6 \,|\, T \,|\, 1',\, 2' \rangle . \tag{2.8}$$

which constitutes a four-dimensional integral equation. In momentum space, the integral equation is given as:

$$T(P; p, p') = V(p - p') + \int \frac{d^4 p''}{(2\pi)^4} \, V(p - p'') \, \Lambda \left(\frac{P}{2} + p'', \frac{P}{2} - p'' \right) T(P; p'', p') \, , \tag{2.9}$$

where the momenta p, p', and p'' denote the relative four-momenta in the final, initial, and intermediate state, respectively, and P is the total momenta. The matrix elements of the OBE potential V serve as an input to solve the matrix elements of T. The last coupled equation in the formal scheme is for the self-energy or mass operator Σ, given by an explicit sum over matrix elements in terms of the T-matrix and the two-point Green's function:

$$\Sigma(1,\,2) = -i\langle 1\,4\,|\,T\,|\,5\,2\rangle\, G_1(5,\,4). \tag{2.10}$$

In momentum space, Σ is written as:

$$\Sigma(p) = \frac{i}{(2\pi)^4}\int d^4p' \left[\left\langle \frac{p-p'}{2}\middle|\hat{T}(p+p')\middle|\frac{p-p'}{2}\right\rangle - \left\langle \frac{p-p'}{2}\middle|T(p+p')\middle|\frac{p'-p}{2}\right\rangle\right] G_1(p'). \tag{2.11}$$

The system of coupled equations follows an iterative process to determine solutions to the above equations. To begin, the self-energy Σ can be first calculated using a simplified approximation like the RHF approach. These calculated values are then used in the first step to determine the spectral functions Ξ (Eqs. (2.30) and (2.32)) and single particle energies ω (Eq. (2.31)). The T-matrix equations can be then solved to determine new values for Σ to be used in the next iterative step until convergence is achieved. Once converged, properties of nuclear matter (symmetric and asymmetric) which define the equation of state can be calculated.

2.2.3 Self-Consistent Basis

The integral equation that determines the T-matrix, Eq. (2.6), has 256 elements with respect to spin indices, making the computation extremely complicated. A method to simplify the numerical process is to introduce a complete basis of particles (Φ_λ) and antiparticles (θ_λ), where $\lambda = \pm 1/2$ are the helicity eigenvalues. The complete basis decouples the integral equations and makes the two-body propagator Λ diagonal, thereby breaking the self-energy

Σ into scalar Σ_s, vector Σ_v, and time-like Σ_0 components:

$$\Sigma(p) = \Sigma_s(p)\mathbb{1} + \Sigma_v(p) \left(\frac{\vec{p}}{|\vec{p}|} \cdot \vec{\gamma}\right) + \Sigma_0(p)\,\gamma^0 \,, \tag{2.12}$$

where $\mathbb{1}$ is the 4×4 unity matrix. From Eq. (2.12), the particle spinors obey:

$$[p_0 - \Sigma_0(p)]\gamma^0 - \vec{\gamma} \cdot \hat{p}[|\vec{p}| + \Sigma_v(p)] - [m + \Sigma_s(p)]\Phi_l(p) = 0\,, \tag{2.13}$$

where $\hat{p} = \vec{p}/|\vec{p}|$ is the momentum unit vector. The particle spinors are thus a solution of Eq. (2.13):

$$\Phi_\lambda(p) = \left[\frac{\epsilon(p)}{2m^*(p)}\right]^{1/2} \begin{bmatrix} 1 \\ \frac{2\lambda p^*(p)}{\epsilon(p)} \end{bmatrix} \otimes |\lambda\rangle\,, \tag{2.14}$$

where $m^* = m + \Sigma_s(p)$ is the effective mass, $p^* = |\vec{p}| + \Sigma_v(p)$ is the effective momentum, and $\epsilon(p) = E(p) - \Sigma_0 + m^*$. The quantities m^* and p^* are self-consistent and determine the particle spinors, which is why the basis can be referred to as self-consistent as well.

In Eq. (2.14), the quantity $|\lambda\rangle$ is representative of the eigenstates of the helicity operator $\hat{h}$:

$$\hat{h} = s \cdot \frac{p}{|p|} = \frac{1}{2}\sigma \cdot \frac{p}{|p|}\,, \tag{2.15}$$

where:

$$\frac{1}{2}\sigma \cdot \frac{p}{|p|}|\lambda\rangle = \lambda|\lambda\rangle\,, \tag{2.16}$$

with eigenvalues $\lambda = \pm 1/2$ [70]. Here, σ are the Pauli matrices and $p/|p| = \hat{p}$ is the momentum unit vector. The particle spinors obey the following:

$$\frac{1}{2}\sigma \cdot \hat{p}\, \Phi_\lambda(p) = \lambda \Phi_\lambda(p). \tag{2.17}$$

The anti-particle spinors are defined as:

$$\theta_\lambda(p) = \left[\frac{\epsilon(p)}{2m^*(p)}\right]^{1/2} \begin{bmatrix} \frac{2\lambda p^*(p)}{\epsilon(p)} \\ 1 \end{bmatrix} \otimes |\lambda\rangle\,, \tag{2.18}$$

and can be neatly defined in terms of the particle spinors by the relation:

$$\theta_\lambda(p) = \gamma^5 \Phi_\lambda(p)\,, \tag{2.19}$$

just with negative energy and reversed momentum and helicity [70, 83]. The symbol $\gamma^5 = -i\gamma^0\gamma^1\gamma^2\gamma^3$ is comprised of the Dirac matrices. The particle and anti-particle spinors obey standard orthogonality:

$$\begin{aligned} \bar{\Phi}_\lambda(p)\, \Phi_{\lambda'}(p) &= \delta_{\lambda\lambda'}\,, \\ \bar{\theta}_\lambda(p)\, \theta_{\lambda'}(p) &= \delta_{\lambda\lambda'}\,, \\ \bar{\Phi}_\lambda(p)\, \theta_{\lambda'}(p) = \bar{\theta}_{\lambda'}(p)\Phi_\lambda(p) &= 0. \end{aligned} \tag{2.20}$$

2.2.4 Spectral Function

An elegant technique used to make the many-body equations numerically tractable and to calculate the key quantities of many-body systems is to utilize the spectral representation of the G_1 function [83]. G_1 can then be defined in Fourier space at zero temperature as:

$$G_1(p) = \int d\omega\, \frac{\Xi(\omega, \vec{p})}{\omega - (p^0 - \mu)(1 + i\eta)}\,, \tag{2.21}$$

where Ξ is the spectral function dependent on the single particle energy ω. The quantity μ is the chemical potential of a nucleon, and η is used to circumvent a singularity occurring as the integral is carried out in the complex plane. Within the self-consistent basis $\{\Phi_\lambda,\, \theta_\lambda\}$, the matrix elements for the particle and anti-particle spectral functions are given by the following equations. The matrix elements for the particle contribution are given by:

$$\langle\Phi_\lambda(\omega_1,\vec{p})|\,\Xi_1(\vec{p})\,|\Phi_\lambda(\omega_1,\vec{p})\rangle = \delta_{\lambda\lambda'} n_1(\vec{p})\,, \tag{2.22}$$

$$\langle\theta_\lambda(\omega_1,\vec{p})|\,\Xi_1(\vec{p})\,|\theta_\lambda(\omega_1,\vec{p})\rangle = \delta_{\lambda\lambda'}\,\mathcal{O}\left[\frac{\partial\Sigma}{\partial\omega}\right]\,, \tag{2.23}$$

$$\langle\Phi_\lambda(\omega_1,\vec{p})|\,\Xi_1(\vec{p})\,|\theta_\lambda(\omega_1,\vec{p})\rangle = \langle\theta_\lambda(\omega_1,\vec{p})|\,\Xi_1(\vec{p})\,|\Phi_\lambda(\omega_1,\vec{p})\rangle = \delta_{\lambda\lambda'}\,\mathcal{O}\left[\frac{\partial\Sigma}{\partial\omega}\right]\,, \tag{2.24}$$

where ”1” denotes the particle (positive energy) contribution. Similarly, the matrix elements for the anti-particle contribution are given by:

$$\langle\theta_\lambda(\omega_2,\vec{p})|\,\Xi_2(\vec{p})\,|\theta_\lambda(\omega_2,\vec{p})\rangle = \delta_{\lambda\lambda'} n_2(\vec{p})\,, \tag{2.25}$$

$$\langle\Phi_\lambda(\omega_2,\vec{p})|\,\Xi_2(\vec{p})\,|\Phi_\lambda(\omega_2,\vec{p})\rangle = \delta_{\lambda\lambda'}\,\mathcal{O}\left[\frac{\partial\Sigma}{\partial\omega}\right]\,, \tag{2.26}$$

$$\langle\Phi_\lambda(\omega_2,\vec{p})|\,\Xi_2(\vec{p})\,|\theta_\lambda(\omega_2,\vec{p})\rangle = \langle\theta_\lambda(\omega_2,\vec{p})|\,\Xi_2(\vec{p})\,|\Phi_\lambda(\omega_2,\vec{p})\rangle = \delta_{\lambda\lambda'}\,\mathcal{O}\left[\frac{\partial\Sigma}{\partial\omega}\right]\,, \tag{2.27}$$

where "2" denotes the antiparticle (negative energy) contribution. The function $n(\vec{p})$ is defined as:

$$n_i(\vec{p}) = \left[\frac{m^*}{|W - \left(m^* \frac{\partial \Sigma_S}{\partial \omega} + p^* \frac{\partial \Sigma_V}{\partial \omega} + W \frac{\partial \Sigma_0}{\partial \omega}\right)|} \right]_{p_0 = \omega_i(\vec{p})} , \tag{2.28}$$

where, for $\omega_i(\vec{p})$, $i = 1, 2$ for particles and antiparticles, respectively.

Once the matrix values of Ξ are determined in the self-consistent basis, the spectral function can be decomposed into scalar Ξ_s, vector Ξ_v, and time-like Ξ_0 components:

$$\Xi(\omega, \vec{p}) = \Xi_s(\omega, \vec{p}) + \Xi_v(\omega, \vec{p})(\vec{p} \cdot \vec{\gamma}) + \Xi_0(\omega, \vec{p})\gamma^0 . \tag{2.29}$$

Ξ is comprised of contributions from both particles and antiparticles in the many-body system, which is shown explicitly in the expression:

$$\Xi(\omega, \vec{p}) = \mathrm{sign}[\omega_1 - \Sigma_0(\omega_1, \vec{p})]\, \Xi_1 \delta(\omega + \mu - \omega_1) + \mathrm{sign}[\omega_2 - \Sigma_0(\omega_2, \vec{p})]\, \Xi_2 \delta(\omega + \mu - \omega_2) , \tag{2.30}$$

The single-particle energies, ω_1 for particles and ω_2 for antiparticles, are defined as (i = 1,2):

$$\omega_i = \Sigma_0(\omega_i, \vec{p}) + (-1)^{i+1} \sqrt{(m + \Sigma_s(\omega_i, \vec{p}))^2 + (\vec{p} + \Sigma_v(\omega_i, \vec{p})^2} , \tag{2.31}$$

and are used to find the scalar, vector, and time-like components of A for both particles and antiparticles (i = 1,2):

$$\begin{aligned}
\Xi_{i,\,s}(p) &= \frac{m + \Sigma_s(p)}{|\frac{\partial F}{\partial \omega_i}(p)|} \cdot \mathrm{sign}(\omega_i) , \\
\Xi_{i,\,v}(p) &= \frac{p + \Sigma_v(p)}{|\frac{\partial F}{\partial \omega_i}(p)|} \cdot \mathrm{sign}(\omega_i) , \\
\Xi_{i,\,0}(p) &= \frac{\omega_i - \Sigma_0(p)}{|\frac{\partial F}{\partial \omega_i}(p)|} \cdot \mathrm{sign}(\omega_i) ,
\end{aligned} \tag{2.32}$$

where $p = |\vec{p}|$ and

$$F(\omega) = (m + \Sigma_s(\omega, p))^2 + (p + \Sigma_v(\omega, p))^2 - (\Sigma_0(\omega, p) - \omega)^2. \tag{2.33}$$

2.2.5 Self-Energy (Mass-Operator)

As shown in the previous sections, the self-energy Σ becomes diagonal with the definition of the self-consistent basis. To calculate the scalar, vector, and time-like components of Σ shown in Eq. (2.10), the components are first calculated in the self-consistent basis. The components are given by $\Sigma_{\Phi\Phi}(p) = \langle \Phi_\lambda(p) \,|\, \Sigma(p) \,|\, \Phi_\lambda(p) \rangle$, with $\Sigma_{\theta\theta}$ and $\Sigma_{\Phi\theta}$ defined similarly.

The scalar, vector, and time-like components of Σ are expressed in the self-consistent basis as:

$$\begin{aligned}
\Sigma_s(p) &= \frac{1}{2}[\Sigma_{\Phi\Phi}(p) - \Sigma_{\theta\theta}(p)]\,, \\
\Sigma_v(p) &= p^*(p) - |\vec{p}|\,, \\
\Sigma_0(p) &= \frac{1}{2}\frac{W(p)}{m^*(p)}\left[\Sigma_{\Phi\Phi}(p) + \Sigma_{\theta\theta}(p) - \frac{p^*(p)}{m^*(p)}\,\Sigma_{\Phi\theta}(p)\right]\,,
\end{aligned} \tag{2.34}$$

where $W(p) = (m^*(p)^2 + p^*(p)^2)^{1/2}$. Equations (2.34) can also be rearranged and solved for $\Sigma_{\Phi\Phi}$, $\Sigma_{\theta\theta}$, and $\Sigma_{\Phi\theta}$. The above equations show the momentum-dependent self-energies computed in the full basis, but this procedure can also be made less complicated by using momentum-averaged self-energies (still as a self-consistent calculation). The results shown in Section 2.4 will compare the full momentum dependence calculations to momentum-averaged calculations.

The determination of the components of Σ in the self-consistent basis requires the knowledge of the particle-particle scattering amplitude and the particle-antiparticle scattering amplitude, which are contained in the T-matrix [70]. Thus, the self-energy components obey the following equations:

$$\begin{aligned}\Sigma_{\Phi\Phi}(p) = \frac{1}{2}\sum_{B}\int \frac{d^3p}{(2\pi)^3}[\langle \Phi_\lambda(p), \Phi_{\lambda'}(p')| \, T \, |\Phi_\lambda(p), \Phi_{\lambda'}(p')\rangle - \\ \langle \Phi_\lambda(p), \Phi_{\lambda'}(p')| \, T \, |\Phi_{\lambda'}(p'), \Phi_\lambda(p)\rangle] \, n_1^B(p')\Theta(p_F^{B'} - p')\,,\end{aligned} \tag{2.35}$$

$$\begin{aligned}\Sigma_{\theta\theta}(p) = \frac{1}{2}\sum_{B}\int \frac{d^3p}{(2\pi)^3}[\langle \theta_\lambda(p), \theta_{\lambda'}(p')| \, T \, |\theta_\lambda(p), \theta_{\lambda'}(p')\rangle - \\ \langle \theta_\lambda(p), \theta_{\lambda'}(p')| \, T \, |\theta_{\lambda'}(p'), \theta_\lambda(p)\rangle] \, n_1^B(p')\Theta(p_F^{B'} - p')\,,\end{aligned} \tag{2.36}$$

$$\begin{aligned}\Sigma_{\theta\Phi}(p) = \frac{1}{2}\sum_{B}\int \frac{d^3p}{(2\pi)^3}[\langle \theta_\lambda(p), \Phi_{\lambda'}(p')| \, T \, |\Phi_\lambda(p), \Phi_{\lambda'}(p')\rangle - \\ \langle \theta_\lambda(p), \Phi_{\lambda'}(p')| \, T \, |\Phi_{\lambda'}(p'), \Phi_\lambda(p)\rangle] \, n_1^B(k')\Theta(p_F^{B'} - p')\,,\end{aligned} \tag{2.37}$$

where B sums protons and neutrons and Θ is the Heaveside step function evaluated at the Fermi momentum p_F.

2.2.6 One-Boson-Exchange (OBE) Interaction

The RBHF approximation is considered "parameter-free" due to the use of meson-exchange potentials created from scattering data and properties of the deuteron. The RBHF approximation can also be referred to as the relativistic ladder approximation as two-particle scattering processes, where the meson exchange occurs, are summed infinitely to calculate dynamical two-body correlations. This process is shown schematically in Figure 2.2. The OBE potential V depends on the nature of nucleon-meson couplings, shown visually with the red vertices Γ in the diagram. For numerical stability, these vertices are replaced with form factors F that are adapted for the specified OBE model (see Ref. [70] for an in-depth explanation). For the context of this work, we use three potentials constructed by Brock-

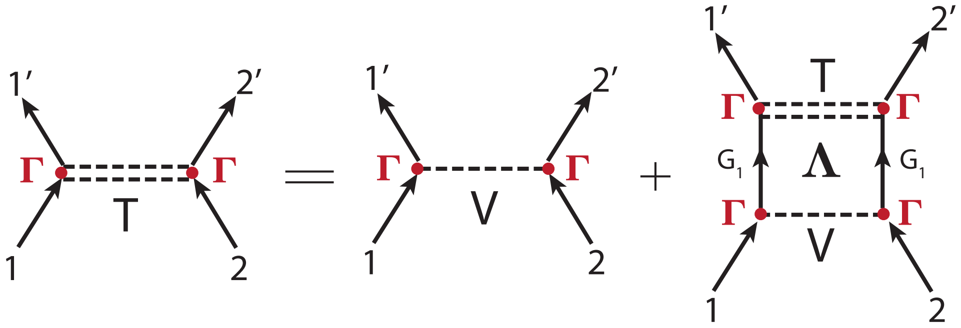

Figure 2.2: The graphical representation of the T-matrix scattering equation. The single dashed line shows the scattering of two particles via the OBE potential V, and the summation occurs in the repeated scattering. The propagator Λ, given by the product of two-point Green's functions G_1, describes the propagation of intermediate particle states. Ingoing states are unprimed, and outgoing states are primed.

mann and Machleidt [85], known colloquially as the Bonn potentials (denoted by A, B, and C). The values for the coupling constants and cut-off masses in these three potentials are given in Appendix B. They use the following form factor:

$$F(p, p') = \frac{\Lambda_\alpha^2 - m_M^2}{\Lambda_\alpha^2 + (p' - p)^2}\,, \tag{2.38}$$

where m_α is the meson mass of meson type α (scalar, pseudovector, and vector) and Λ_α is the corresponding cut-off mass.

The determination of the matrix elements of V, computed for scalar, pseudovector, and vector mesons, has the form $\langle \Phi_{\lambda_1'}(p_1'), \Phi_{\lambda_2'}(p_2')|\, V_\alpha\, |\Phi_{\lambda_1}(p_1), \Phi_{\lambda_2}(p_2)\rangle$, which can be written in short-hand notation as:

$$\langle \lambda_1'\lambda_2' p'|\, V_\alpha\, |\lambda_1\lambda_2 p\rangle = \langle \Phi_{\lambda_1'}(p_1'), \Phi_{\lambda_2'}(p_2')|\, V_\alpha\, |\Phi_{\lambda_1}(p_1), \Phi_{\lambda_2}(p_2)\rangle\,, \tag{2.39}$$

for each meson type α. Similar redefinitions are made for the mixed particle-antiparticle matrix elements:

$$\begin{aligned}
\langle\lambda_1'\lambda_2'p'|\, U_\alpha\, |\lambda_1\lambda_2 p\rangle &= \langle\theta_{\lambda_1'}(p_1'), \Phi_{\lambda_2'}(p_2')|\, V_\alpha\, |\Phi_{\lambda_1}(p_1), \Phi_{\lambda_2}(p_2)\rangle, \\
\langle\lambda_1'\lambda_2'p'|\, W_\alpha\, |\lambda_1\lambda_2 p\rangle &= \langle\theta_{\lambda_1'}(p_1'), \Phi_{\lambda_2'}(p_2')|\, V_\alpha\, |\Phi_{\lambda_1}(p_1), \theta_{\lambda_2}(p_2)\rangle, \\
\langle\lambda_1'\lambda_2'p'|\, Z_\alpha\, |\lambda_1\lambda_2 p\rangle &= \langle\theta_{\lambda_1'}(p_1'), \Phi_{\lambda_2'}(p_2')|\, V_\alpha\, |\theta_{\lambda_1}(p_1), \Phi_{\lambda_2}(p_2)\rangle.
\end{aligned} \tag{2.40}$$

The matrix elements for scalar mesons ($\alpha = s$), for example, then take the form:

$$\begin{gathered}
\langle\lambda_1'\lambda_2'p'|\, V_s\, |\lambda_1\lambda_2 p\rangle = -g_s^2\Delta_S^0(p,p')S(p',p) \times \\
\left(1 - \frac{4\lambda_1'\lambda_1 p_1'^{*} p_1^*}{\epsilon_1'\epsilon_1}\right)\left(1 - \frac{4\lambda_2'\lambda_1 p_2'^{*} p_2^*}{\epsilon_2'\epsilon_2}\right)\langle\lambda_1'\lambda_2'|\, \mathbb{1}\, |\lambda_1\lambda_2\rangle\,,
\end{gathered} \tag{2.41}$$

$$\begin{gathered}
\langle\lambda_1'\lambda_2'p'|\, U_s\, |\lambda_1\lambda_2 p\rangle = -g_s^2\Delta_S^0(p,p')S(p',p) \times \\
\left(\frac{2\lambda_1' p_1'^{*}}{\epsilon_1'} - \frac{2\lambda_1 p_1^*}{\epsilon_1}\right)\left(1 - \frac{4\lambda_2'\lambda_1 p_2'^{*} p_2^*}{\epsilon_2'\epsilon_2}\right)\langle\lambda_1'\lambda_2'|\, \mathbb{1}\, |\lambda_1\lambda_2\rangle\,,
\end{gathered} \tag{2.42}$$

$$\begin{gathered}
\langle\lambda_1'\lambda_2'p'|\, W_s\, |\lambda_1\lambda_2 p\rangle = -g_s^2\Delta_S^0(p,p')S(p',p) \times \\
\left(\frac{2\lambda_1' p_1'^{*}}{\epsilon_1'} - \frac{2\lambda_1 p_1^*}{\epsilon_1}\right)\left(\frac{2\lambda_2' p_2'^{*}}{\epsilon_2'} - \frac{2\lambda_2 p_2^*}{\epsilon_2}\right)\langle\lambda_1'\lambda_2'|\, \mathbb{1}\, |\lambda_1\lambda_2\rangle\,,
\end{gathered} \tag{2.43}$$

$$\langle\lambda_1'\lambda_2'p'|\, Z_s\, |\lambda_1\lambda_2 p\rangle = -\langle\lambda_1'\lambda_2'p'|\, V_s\, |\lambda_1\lambda_2 p\rangle\,, \tag{2.44}$$

where $\Delta_S^0(p,p')$ is the free meson field equation, $\epsilon = m^* + W$, and S is:

$$S(p',p) = \frac{1}{4}\left[\frac{\epsilon_1'}{m_1^{*\prime}}\frac{\epsilon_1}{m_1^*}\frac{\epsilon_2'}{m_2^{*\prime}}\frac{\epsilon_2}{m_2^*}\right]^{1/2}. \tag{2.45}$$

Similar relations for the pseudovector and vector meson matrix elements are detailed in [70].

2.2.7 The Brueckner Propagator

The generalized mathematical formalism described throughout this text can use any relativistic propagator, but the Brueckner propagator has been shown in the literature to produce saturation properties closest to their empirical values [83, 85, 89, 93, 95]. At zero temperature, the Brueckner propagator is defined as:

$$\Lambda(\vec{p}, \vec{p}\,', E) = 2\pi \frac{\Theta(|\vec{p}| - p_F)\,\Theta(|\vec{p}\,'| - p_F)}{E - \omega_1(|\vec{p}|) - \omega_1(|\vec{p}\,'|)}\,, \tag{2.46}$$

Here, the step functions, represented by $\Theta(|\vec{p}| - p_F)$, account for the Pauli exclusion principle, ensuring that intermediate scattering states lie outside the nucleon Fermi sea, characterized by the Fermi momentum p_F. As will be discussed in Section 2.2.10, the step functions are modified for finite temperatures. The quantity ω_1 denotes the single-nucleon energy and is defined as:

$$\omega_1(|\vec{p}|) = \Sigma_0(|\vec{p}|) + \left\{[m + \Sigma_s(|\vec{p}|)]^2 + [|\vec{p}| + \Sigma_v(|\vec{p}|)]^2\right\}^{1/2}. \tag{2.47}$$

In this expression, $\Sigma_0(|\vec{p}|)$, $\Sigma_s(|\vec{p}|)$, and $\Sigma_v(|\vec{p}|)$ represent momentum-dependent self-energies arising from the scalar, vector, and time-like components (see Eq. (2.12)) of the nucleon-nucleon interaction, respectively. The quantity m stands for the nucleon rest mass.

The use of the Brueckner propagator in the mathematical framework described above results in the RBHF approximation. While the results demonstrated in this work use the Brueckner propagator, other notable propagators that have been explored in the literature are the Λ^{00} which is comprised of two free two-point Green's functions G_1^0 are therefore not coupled to the medium:

$$\Lambda^{00}(\vec{p}, \vec{p}') = i\, e^{i\eta p_0}\, G_1^0(\vec{p}')\, G_1^0(\vec{p})\,, \tag{2.48}$$

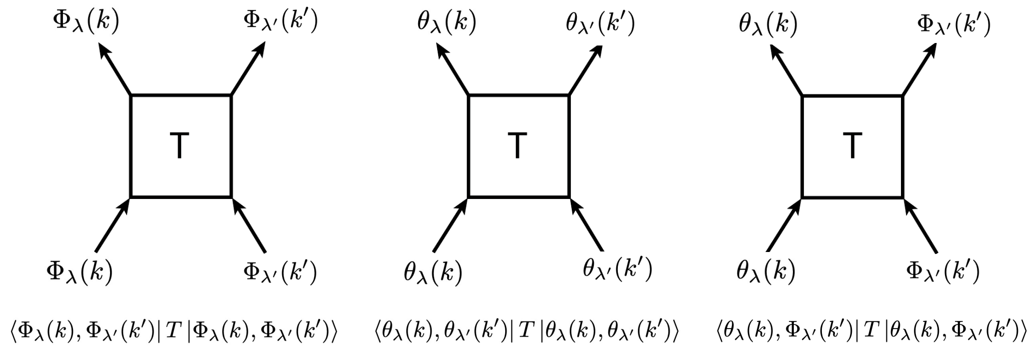

Figure 2.3: A schematic for the particle-particle, antiparticle-antiparticle, and particle-antiparticle T-matrix amplitudes shown in the direct terms of $\Sigma_{\Phi\Phi}$, $\Sigma_{\theta\theta}$, and $\Sigma_{\theta\Phi}$ (Eqs. (2.35), (2.36), and (2.37)), where $\Phi_\lambda(k)$ denote the particle spinors and $\theta_\lambda(k)$ denote the antiparticles spinors.

and the Λ^{10}, which additionally takes into account the full two-point Green's function G_1:

$$\Lambda^{10}(\vec{p},\vec{p}') = \frac{i}{2}[e^{i\eta p_0'}G_1^0(\vec{p})\,G_1(\vec{p}') + e^{i\eta p_0}G_1(\vec{p})\,G_1^0(\vec{p}')]. \tag{2.49}$$

As shown in [70, 83, 93], the Λ^{00} propagator creates too much energy per nucleon (over-binding) at saturation, and the Λ^{10} creates too little (under-binding) at saturation.

2.2.8 T-matrix Elements

The scattering amplitudes seen in Eqs. (2.35), (2.36), and (2.37) are depicted visually in Fig. 2.3. To calculate the matrix elements of Σ in the self-consistent basis, the elements of the T-matrix must first be solved.

The integral equations for the scattering amplitudes of the T-matrix contain particle and antiparticle states in the initial and final scattering states, but do not contain intermediate antiparticle states as they are excluded in the OBE potentials [70]. Therefore, the initial and final states are computed in the full particle-antiparticle basis, but the intermediate states are determined by the intermediate propagator $\tilde{\Lambda}$:

$$\tilde{\Lambda}(p,p') = \langle \Phi_\lambda(p)\Phi_{\lambda'}(p')|\, \Lambda(p,p')\, |\Phi_\lambda(p)\Phi_{\lambda'}(p')\rangle \,, \tag{2.50}$$

which is only computed in the particle basis. Using the intermediate propagator, the integral equation for the particle spinors takes the form:

$$\begin{aligned}\langle \Phi_{\lambda_1}\, \Phi_{\lambda_2}; p|\, T(P) - V\, |\Phi_{\lambda_1'}\, \Phi_{\lambda_2'}; p'\rangle = \int \frac{d^4p''}{(2\pi)^4}\, [\langle \Phi_{\lambda_1}\, \Phi_{\lambda_2}; p|\, V\, |\Phi_{\lambda_3}\, \Phi_{\lambda_4}; p''\rangle \\ \tilde{\Lambda}\left(\frac{P}{2} + p'', \frac{P}{2} - p''\right) \times \langle \Phi_{\lambda_3}\, \Phi_{\lambda_4}; p''|\, T(P)\, |\Phi_{\lambda_1'}\, \Phi_{\lambda_2'}; p'\rangle.\end{aligned} \tag{2.51}$$

A useful simplification to the calculation of the elements of the T-matrix is to use its partial wave expansion with an angle-averaged propagator. A more in-depth mathematical breakdown of the partial wave expansion can be found in Appendix A.

2.2.9 Properties of Nuclear Matter at Zero Temperature

When employing the spectral representation described in Section 2.2.4, the properties of nuclear matter can then be determined by the self-energy Σ and spectral function Ξ (described in greater detail in [70, 83]). Once a self-consistent solution to the coupled system of equations is found, bulk properties of symmetric nuclear matter (SNM) can be calculated and compared to empirical values at zero temperature. Using the spectral decomposition of the 2-point function G_1, the number density ρ of the system follows from:

$$\rho = \frac{4}{(2\pi)^3} \int d^3p\, \Xi_0(\omega, \vec{p})\Theta(p_F - p)\,, \tag{2.52}$$

where Ξ_0 is the time-like component of the spectral function. The step function Θ is evaluated at the Fermi momentum p_F. Note that the step function Θ is modified in the case of finite temperatures, which will be discussed below in Section 2.2.10. The energy per nucleon E/A of the system is expressed as:

$$\begin{aligned} E/A(\rho) = \frac{1}{4\pi^3} \int d^3p \; & [2(m\Xi_s(p) - p\Xi_v(p)) + \Sigma_s(p)\Xi_s(p) \\ & -\Sigma_v(p)\Xi_v(p) + \Sigma_0(p)\Xi_0(p)) \, \Theta(|p_F - p|) \,. \end{aligned} \tag{2.53}$$

Once the energy per nucleon and number density of the system are calculated, the compressibility K of the matter:

$$K(\rho) = 9\rho^2 \left(\frac{\partial^2 E/A(\rho)}{\partial \rho^2} \right) , \tag{2.54}$$

and the pressure P:

$$P(\rho) = \rho^2 \left(\frac{\partial E/A(\rho)}{\partial \rho} \right) , \tag{2.55}$$

can be computed at zero temperature. The total energy density ϵ of the system follows from the energy per nucleon as:

$$\epsilon(\rho) = (E/A(\rho) + m) \, \rho \,, \tag{2.56}$$

where m is the nucleon mass.

In the case of asymmetric nuclear matter (ANM), an asymmetry parameter α which defines the asymmetry between the number of neutrons and protons in the system can be defined as:

$$\alpha = \frac{\rho_n - \rho_p}{\rho}, \tag{2.57}$$

where ρ_n is the density of neutrons and ρ_p is the density of protons. In the case of SNM, $\alpha = 0$, and for pure neutron matter, $\alpha = 1$. For ANM, the energy per nucleon can be expressed as a power series dependent on the total density of the system ρ and the asymmetry parameter α [95]:

$$E/A(\rho,\alpha) = E/A(\rho,0) + E_{\text{sym}}(\rho)\alpha^2 + \mathcal{O}(4)\,. \tag{2.58}$$

E_{sym} is the nuclear symmetry energy, which is defined as:

$$E_{\text{sym}}(\rho) = \frac{1}{2}\frac{\partial^2 E/A(\rho,\alpha)}{\partial\alpha^2}\bigg|_{\alpha=0}\,, \tag{2.59}$$

and can be approximated as $E_{\text{sym}}(\rho) \approx E/A(\rho,1) - E/A(\rho,0)$ [154].

2.2.10 Extensions to Finite Temperatures

For finite temperatures, the formal structure of solving the many-body problem in the RBHF approximation is the same as for zero temperature. The Green's function formalism is modified, where the 2-point Green's function G_1 in Eq. (2.21) is instead expressed as [70, 83, 93]:

$$G_1(p) = \int d\omega \left[\frac{\Xi(\omega,\vec{p})}{\omega - (p^0-\mu)(1+i\eta)}\right] - 2i\pi\,\text{sign}(p^0-\mu)\,\frac{\Xi(p^0-\mu,\vec{p})}{e^{\beta|p^0-\mu|}+1}\,, \tag{2.60}$$

with $\beta = 1/k_BT$, where k_B is the Stefan-Boltzmann constant and T is the temperature. While the formal structure of the spectral function Ξ is unaltered when compared to zero temperature, Ξ has an implicit temperature dependence from G_1.

In the case of finite temperatures, the properties described in Section 2.2.9 are also modified to include a temperature dependence. This is achieved by replacing the step functions Θ

seen in Eqs. (2.52) and (2.53) with Fermi-Dirac distribution functions $f(\vec{p})$:

$$f_1(\vec{p}) = \frac{1}{e^{\beta(\omega_1(\vec{p})-\mu)} + 1}\,, \tag{2.61}$$

$$f_2(\vec{p}) = \frac{1}{e^{\beta(-\omega_2(\vec{p})+\mu)} + 1}\,, \tag{2.62}$$

where "1" indicates the particle contribution and "2" indicates the antiparticle contribution. We remember that at finite temperatures, the behavior of nuclear matter undergoes an important modification, attributed to thermal nucleonic excitations surpassing the Fermi surface. Contrary to absolute zero conditions where all states within the Fermi sea ($|\vec{p}| < p_F$) are fully occupied, higher temperatures induce partial occupancy due to thermal excitations of particles and antiparticles. This phenomenon significantly impacts various thermodynamic attributes of dense stellar matter, including the equation of state and the entropy of hot neutron star matter. Both particle and antiparticle distributions adhere to modified Fermi-Dirac statistics, resulting in alterations in state occupancy for both species, both below and above the Fermi surface, as expressed by Eqs. (2.61) and (2.62).

At zero temperature, nucleons propagate in the many-body system, filling particle and antiparticle states within the Fermi sea ($|p| < p_F$). The inclusion of temperature in the system results in states outside of the Fermi sea filled (i.e. states with momenta $|p| > p_F$) by particles (and antiparticles) with corresponding hole (anti-hole) states in the Fermi sea. This phenomenon is seen for particles in Figure 2.4. As $T \to 0$, the Fermi-Dirac distribution for particles becomes:

$$f_1(\vec{p}) \to \Theta(\mu - \omega_1(\vec{p}))\,, \tag{2.63}$$

and for antiparticles, $f_2(\vec{p}) \to 0$.

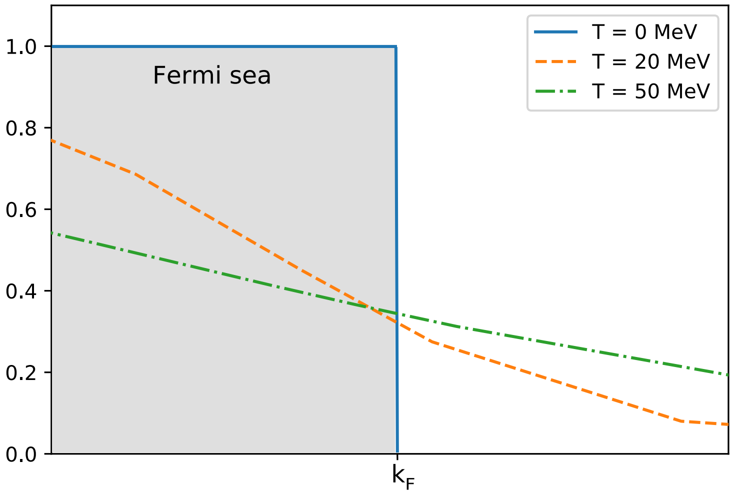

Figure 2.4: The depletion of single-particle states with the inclusion of temperature. At zero temperature, the Fermi-Dirac distribution becomes a step function Θ, as described in Eq. (2.63). Higher temperatures smear the boundary, resulting in filled states outside the Fermi sea.

For finite temperatures, the pressure is instead calculated with the free energy F per nucleon, which is defined as:

$$F(\rho, T) = U(\rho, T) - TS(\rho, T)\,, \tag{2.64}$$

where U is the internal energy (equal to the energy per nucleon E/A with the thermal contribution) and S is the entropy of the system [92]. The entropy is given by:

$$S(\rho, T) = \frac{-1}{(2\pi)^3 \rho} \int d^3p \left[(1 - f(\vec{p})) \ln(1 - f(\vec{p})) + f(\vec{p}) \ln(f(\vec{p}))\right], \tag{2.65}$$

where f is the Fermi-Dirac distribution. Both particles and antiparticles contribute to S, but the antiparticle contribution is very small ($f_2 << f_1$). Therefore, Eq. (2.65) can be approximated with only the particle contribution, or $f = f_1$. Once the entropy S, and subsequently the free energy F, are calculated, the pressure is derived as:

$$P(\rho, T) = \rho^2 \frac{\partial F(\rho, T)}{\partial \rho}. \tag{2.66}$$

2.3 Theoretical Framework for Calculating Neutron Star Properties

The equation of state (EOS) of neutron star matter is described as a relationship between the pressure P and energy density ϵ of the many-body system within. This holds true for the majority of neutron stars, which can be described as zero temperature on the nuclear scale (or just a few MeV). However, following extreme events like a core-collapse supernova or a binary neutron star merger, the system's temperature is much higher (on the order of 50-100 MeV) and therefore plays a critical role in the EOS. The RBHF formalism is used to calculate the EOS of asymmetric nuclear matter within a neutron star at both zero and finite temperatures. Once an EOS model has been defined, the structural properties of a neutron star can be calculated in the framework of Einstein's theory of general relativity.

2.3.1 Non-Rotating Compact Stars

For non-rotating compact stars, the stellar structure is described by the Tolman-Oppenheimer-Volkoff (TOV) equation (where $G = c = 1$):

$$\frac{dP(r)}{dr} = -\frac{(\epsilon(r) + P(r))(m(r) + 4\pi r^3 P(r))}{r^2 \left(1 - \frac{2m(r)}{r}\right)}, \tag{2.67}$$

that describes the pressure gradient within the star as a function of the radius r. The mass m contained in a sphere of radius r can be found with:

$$\frac{dm}{dr} = 4\pi r^2 \epsilon(r)\,, \tag{2.68}$$

where, at the origin, $m(0) = 0$. Using a specified model for the EOS, a star's mass and radius can be determined by first choosing a central value for density ϵ_C with a corresponding pressure value P_C, and integrating Eqs. (2.68) and (2.67) until pressure vanishes, signifying the total radius R of the star.

2.3.2 Rotating Compact Stars

The stellar structure of rotating compact stars is more complicated than that of non-rotating stars for several reasons, as mentioned in Chapter 1. Non-rotating stars are assumed to be spherically symmetric, so their stellar structure depends solely on the radial coordinate. However, rapid rotation can deform the star's shape by flattening at the pole and expanding in the equatorial direction; to account for this deformation, the stellar structure equations must also include a dependence on the polar coordinate θ. While spherical symmetry is broken in rotating stars, the assumptions of stationary rotation, axial symmetry, and reflection symmetry still hold, leaving the stellar structure equations independent from time t and the azimuthal angle ϕ. The metric of a rotating neutron star can thus be written as:

$$ds^2 = -e^{2\nu(r,\theta)}dt^2 + e^{2\psi(r,\theta)}(d\phi - \omega(r,\theta)\,dt)^2 + e^{2\mu(r,\theta)}d\theta^2 + e^{2\lambda(r,\theta)}dr^2\,, \tag{2.69}$$

where the metric functions (ν, ψ, μ, and λ) are dependent on the radial r and polar θ coordinates, as well as implicitly on the star's rotational frequency Ω. The term ω is indicative of an additional complication from rotation: the general relativistic effect of frame dragging, where ω is the angular velocity of the local inertial frames being dragged in the direction of the star's rotation.

The absolute upper limit for a neutron star's rotational frequency is the mass-shedding limit, set by the Kepler frequency Ω_K. This frequency can be defined in terms of the metric functions ψ and ν, and frame-dragging term ω as:

$$\Omega_K = \frac{\omega'}{2\psi'} + e^{\nu-\psi}\left[\frac{\nu'}{\psi'} + \left(\frac{\omega'}{2\psi'}e^{\psi-\nu}\right)\right]^{1/2} + \omega\,, \tag{2.70}$$

evaluated at the equator, where mass-shedding occurs when the angular velocity reaches Ω_K at the star's equator, and the prime indicates a partial derivative with respect to the radial coordinate r. In general, rotating stars can be more massive than non-rotating stars, as rotation stabilizes the star against gravitational collapse. The mass-shedding limit sets the maximum allowed mass of a (uniformly) rotating neutron star, which can be 20% higher than non-rotating stars for very stiff EOS models [155].

Due to the complications introduced by rotation, there exists no analytical solution for solving the system of equations deriving the stellar structure of relativistic rotating objects. Instead, numerical methods are employed; an in-depth review of different schemes can be found in Ref. [102]. In this chapter, models for rotating stars at the Kepler frequency are computed using Hartle's perturbative rotation formalism [156]. In the next chapters, we introduce another numerical scheme referred to as Cook-Shapiro-Teukolsky (CST) [104], which will be modified to account for differential rotation.

2.4 Results

The saturation properties of dense SNM and ANM are calculated at zero and finite temperatures. For this investigation, calculations are carried out using the three OBE potentials constructed by Brockmann and Machleidt [85], known colloquially as the Bonn potentials (denoted by A, B, and C). The calculated EOS models are then used to determine the bulk properties of neutron stars.

2.4.1 Properties of Dense Nucleonic Matter at Zero Temperature

The Bonn potentials have previously been shown to produce values for the bulk properties of SNM at zero temperature that are in good agreement with empirical values [70, 85, 93, 95]. For both the full momentum-dependence and the momentum-averaged calculations, values for the saturation density ρ_0, energy per nucleon E/A, Fermi momentum p_F, compressibility K, effective nucleon mass m^*/m, and symmetry energy E_{sym} are given in Table 2.1. The corresponding empirical values are shown for comparison but it is worth noting the empirical values for the saturation properties vary across the literature.

The saturation density, ρ_0, is found in a recent study to be within the range 0.155 ± 0.005 fm^{-3} [157]. This value directly correlates to the Fermi momentum p_F via:

$$\rho_0 = \frac{2p_F^3}{3\pi^2}\,, \tag{2.71}$$

leading its empirical value to be ≈ 1.32 fm^{-1}. The energy per nucleon E/A is also given in Ref. [157] as -16 ± 1 MeV but has been found with different bounds throughout the literature. For the compressibility K, Ref. [158] provides a historical overview of the empirical range from a variety of theoretical approaches, which is shown to be as low as 100 and as high as 370 depending on the reference. However, more recent studies like that of Ref. [159] provide a more narrow uncertainty band on K, 240 ± 20 MeV. For the effective nucleon mass m^*/m, analyses of the isoscalar nucleon mass provide the range 0.8 ± 0.1, but there is less consensus of the isovector nucleon mass with values ranging as low as 0.6 and as high as 0.93 [160]. Ref. [161] provides values for the symmetry energy E_{sym} using different semi-classical methods but finds a consensus centered around 32 MeV.

Table 2.1: Saturation properties of symmetric nuclear matter (SNM) at zero temperature for different approximations using the Bonn potentials (A, B, and C). The first approximation is carried out using the full basis and a momentum-dependent (Momentum-Dep.) self-energy and the second uses the full basis and a momentum-averaged (Momentum-Avg.) self-energy. Empirical values are shown in the last row, where the ± indicates a range of values (see text for references).

Self-Energy Σ	Potential	ρ_0 (fm^{-3})	E/A (MeV)	p_F (fm^{-1})	K (MeV)	m^*/m	E$_{\text{sym}}$ (MeV)
Momentum-Dep.	A	0.17	-14.08	1.36	281.64	0.675	32.07
	B	0.16	-12.99	1.33	246.77	0.701	29.67
	C	0.15	-12.30	1.30	227.99	0.725	27.26
Momentum-Avg.	A	0.17	-15.45	1.36	265.54	0.657	33.44
	B	0.16	-14.33	1.33	241.40	0.685	31.01
	C	0.16	-13.63	1.33	225.31	0.692	28.86
Empirical Value		0.155 ± 0.005	-16 ± 1	1.32	240 ± 20	0.8 ± 0.1	32

For both momentum-dependence and the momentum-averaged calculations, the Bonn potential A results are the closest to the empirical value for the binding and symmetry energies, a finding that is consistent with other implementations of the RBHF approximation at zero temperature.

We next investigate ANM produced by the RBHF approximation to produce an equation of state for neutron star matter. For ANM, results are shown for the full iteration procedure using the momentum-dependent Σ. Following the theoretical description in Section 2.2.9, the energy per nucleon E/A of ANM, defined in Eq. (2.58), becomes dependent on the asymmetry parameter α. When $\alpha = 0$, there are an equal number of protons and neutrons within the system (SNM), and when $\alpha = 1$, the system is pure neutron matter (PNM). In Figure 2.7, energy per nucleon as a function of density for varying values of α are shown, along with the (non-relativistic) calculated results from Ref. [4], known colloquially as APR.

In the high-density regime of a neutron star, the asymmetry between neutrons and protons is believed to be ≈ 0.8. Using the energy per nucleon E/A with $\alpha = 0.8$ and the corresponding number density ρ, the pressure P and energy density ϵ can be calculated using Eqs. (2.55) and (2.56), respectively. The EOS models for the Bonn potentials A, B, and C following this

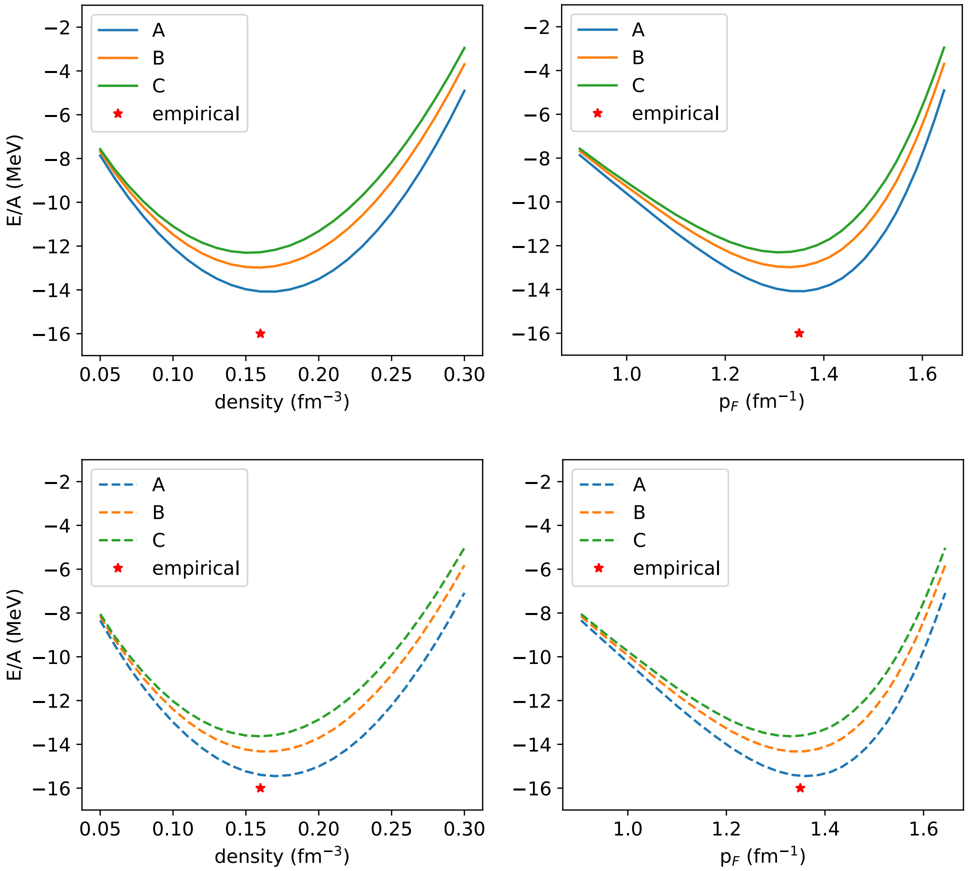

Figure 2.5: The energy per nucleon E/A for the three Bonn potentials (A, B, and C) compared to density ρ on the left and Fermi momentum p_F on the right. The top row with solid lines shows the momentum-dependent self-energy approximation completed in the full basis, and the bottom row with dashed lines is the momentum-averaged approximation.

procedure are displayed in Figure 2.8. Despite the differences in the saturation properties of the three potentials, the resulting EOS models remain very similar.

2.4.2 Properties of Dense Nucleonic Matter at Finite Temperature

We extend the calculations of nuclear matter in the RBHF approximation to finite temperatures, specifically for $T = 10$, 30, 50, and 70 MeV. Modifications to the numerical scheme are introduced to be consistent with the mathematical framework described in Section 2.2.10.

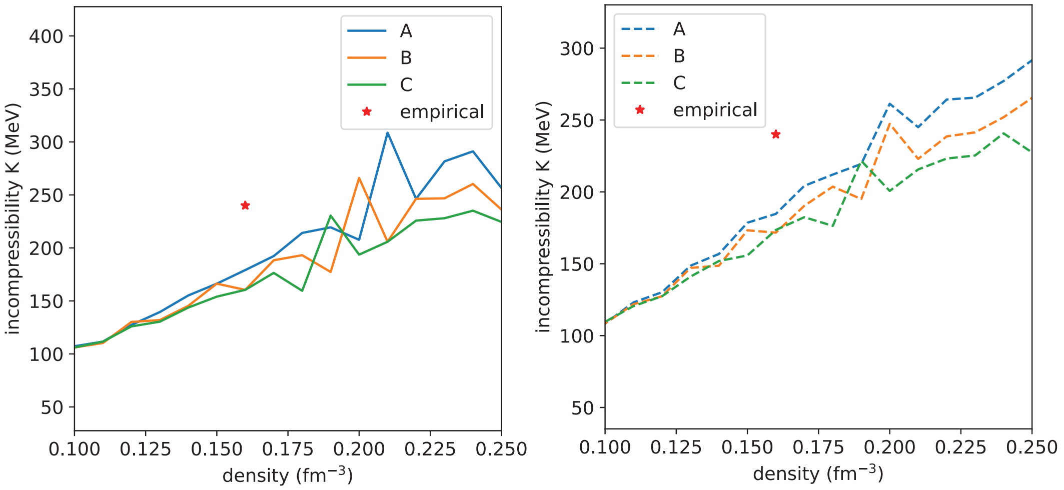

Figure 2.6: The compressibility K for the three Bonn potentials (A, B, and C) compared to density ρ. The approximation using momentum-dependent self-energy is shown on the left with solid lines and the approximation using momentum-averaged self-energy is shown on the right with dashed lines.

Due to the additional complexity of the algorithm, we find solutions to be more stable numerically, especially at higher temperatures, using the momentum-averaged self-energy approximation.

The binding energies per nucleon E/A for four different temperatures are shown in Figure 2.9, calculated using the Bonn B potential. Each meson provides a thermal contribution to the energy per nucleon, which grows larger as the temperature increases. For finite temperatures, the energy per nucleon is used to calculate the free energy per nucleon F/A, given in Eq. (2.64). When using the RBHF approximation at temperatures ≥ 50 MeV, we find the Bonn B potential provided the most stable results. The free energies of SNM and PNM from the Bonn B potential for four temperatures are displayed in Figure 2.10.

Pressure is calculated from F/A using Eq. (2.66). As for zero temperature, the pressure and energy density are calculated with the asymmetry parameter $\alpha = 0.8$ for neutron star matter. The EOS, pressure vs. energy density, for varying temperatures are shown in Figure 2.11. Higher temperatures at low densities introduce some level of numerical noise, as seen in

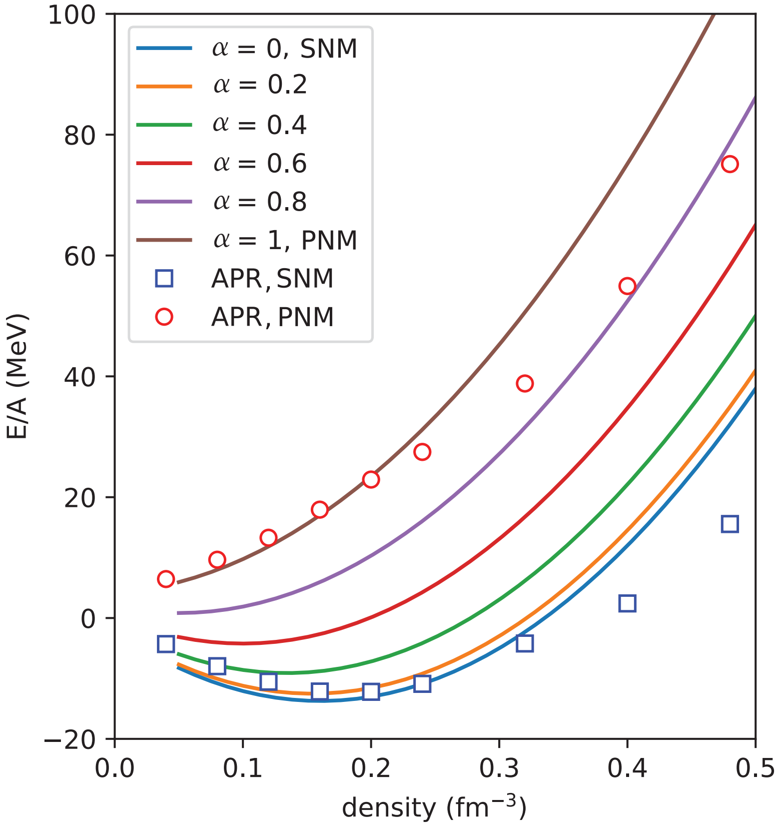

Figure 2.7: Energy per nucleon per nucleon E/A vs. density for asymmetric nuclear matter (ANM) calculated with the Bonn A potential at zero temperature. Shown are varying values of the asymmetry parameter α ranging from 0 (SNM) to 1 (PNM), and compared to the APR method [4] shown with blue squares (SNM) and red circles (PNM).

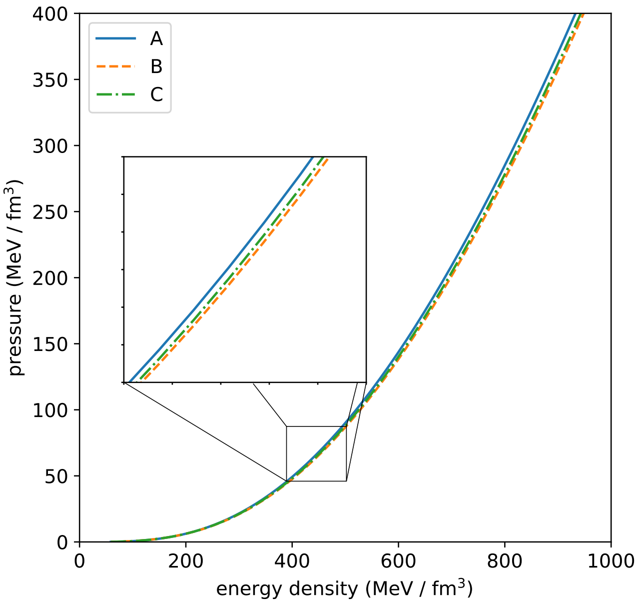

Figure 2.8: Pressure as a function of energy density for all three Bonn potentials (A, B, and C) for asymmetric nuclear matter with $\alpha = 0.8$ (see text for more details).

Figure 2.11.

2.4.3 Neutron Star Properties

Once models have been defined for the EOS of neutron star matter at both zero and finite temperatures, bulk properties like mass and radius can be solved numerically.

At zero temperature, EOS models resulting from both the momentum-dependent and momentum-averaged self-energy calculations are used. To compute rotating and non-rotating stellar models, an EOS that describes the neutron star from the core to the crust must be specified. The RBHF approximation is used for the high-density region. For the crust, we use Harrison and Wheeler (HW) [68] for the outer crust, and Negele and Vanutherin (NV) [69] for the inner. Mass-radius relations for non-rotating (dashed lines) and rotating (solid lines) stars are shown in Figure 2.12, resulting from calculations that use the momentum-dependent

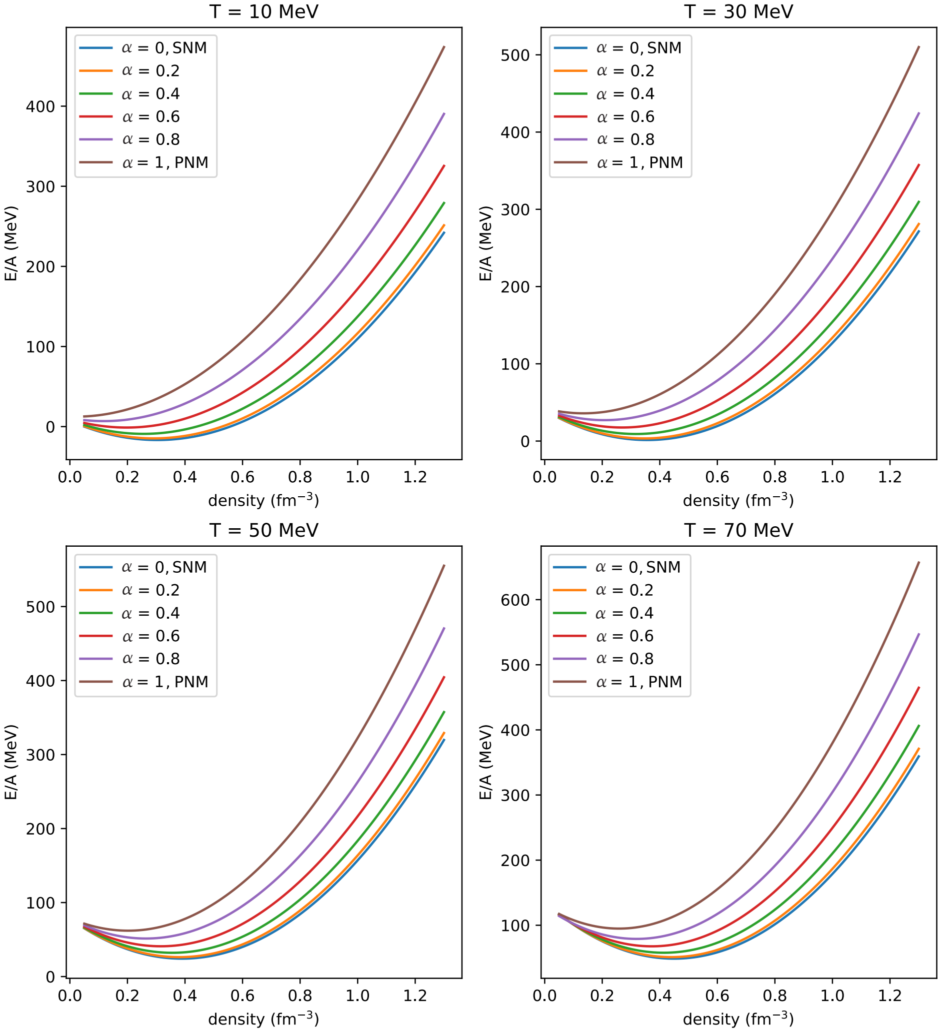

Figure 2.9: Energy per nucleon per nucleon E/A vs. density of asymmetric matter (ANM) calculated with the Bonn B potential for four different temperatures: 10, 30, 50, and 70 MeV. For each temperature, the asymmetry parameter α ranges from 0 (SNM) to 1 (PNM).

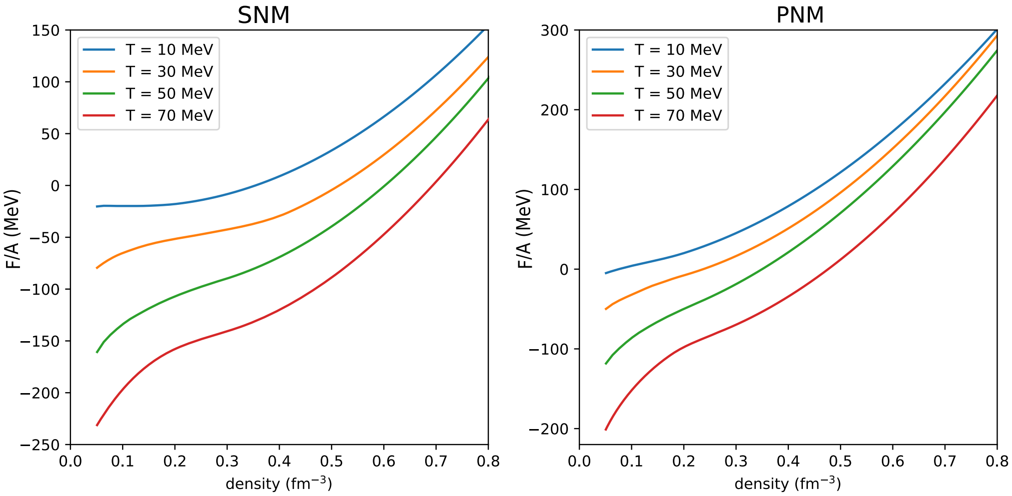

Figure 2.10: Free energy per nucleon F/A vs. density for SNM (left panel) and PNM (right panel) calculated with the Bonn B potential. The plots show results for four temperatures: 10, 30, 50, and 70 MeV.

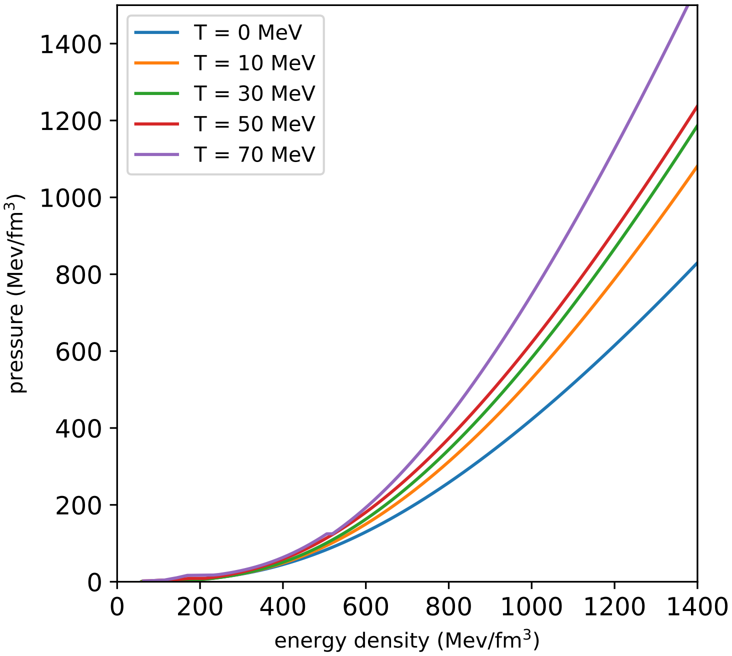

Figure 2.11: Pressure as a function of energy density calculated with the Bonn B potential for asymmetric nuclear matter with $\alpha = 0.8$. Shown are the zero-temperature EOS and four models at temperatures 10, 30, 50, and 70 MeV.

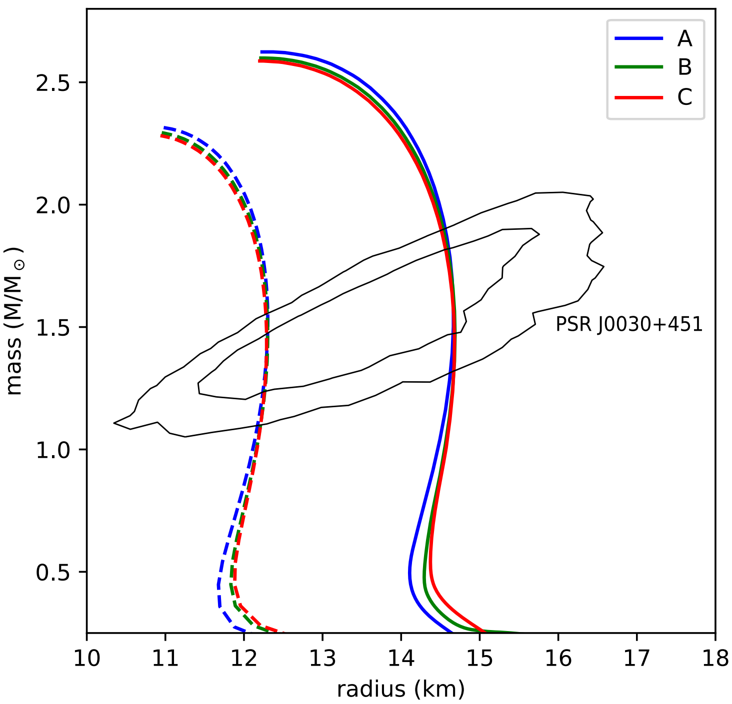

Figure 2.12: Mass-radius relations for rotating (solid lines) and non-rotating (dashed lines) neutron stars from EOS models computed with the RBHF approximation at zero temperature using the Bonn A, B, and C potentials. Computations use the full basis and a momentum-dependent self-energy (see text for more details). The black contours show the confidence intervals for the mass and radius of PSR J0030+451 [5], where the inner contour is the 95% and outer is 68%.

self-energy in the full basis for the Bonn A, B, and C potentials. For all three models, the rotating mass-radius relations are shown at their mass-shedding or Kepler limit ($\Omega = \Omega_K$). Additionally shown are the confidence intervals for the mass and radius of PSR J0030+451, observed by the Neutron Star Interior Composition Explorer (NICER) and analyzed in [5]. The outer contour is the 68% interval and the inner is 95%. Both the non-rotating and rotating mass-radius relations fall in the 95% confidence interval for all three potentials.

Bulk properties of non-rotating and rotating stars (at their mass-shedding limit) constructed with the zero-temperature EOS models are given in Table 2.2. For both non-rotating and rotating stars, the maximum mass $M_{\rm max}$ and corresponding radius $R_{\rm max}$ are shown. Ad-

Table 2.2: Non-rotating and rotating neutron star properties calculated with the zero-temperature EOS models from the RBHF approximation, using the three Bonn potentials. Results are shown for EOS models constructed with momentum-dependent and momentum-averaged self-energy Σ. Bulk properties include the maximum mass $M_{\max}$ and corresponding radius $R_{\max}$ for both non-rotating and rotating stars, as well as the Kepler frequency Ω_K and stability parameter $T/|W|$ for rotating stars.

		Non-rotating ($\Omega = 0$)		Rotating ($\Omega = \Omega_K$)			
Self-Energy Σ	Potential	$M_{\max}$ ($M_\odot$)	$R_{\max}$ (km)	$M_{\max}$ ($M_\odot$)	$R_{\max}$ (km)	Ω_K (Hz)	$T/\|W\|$
Momentum-Dependent	A	2.315	10.978	2.624	12.230	1916	0.116
	B	2.294	10.954	2.599	12.261	1908	0.115
	C	2.282	10.937	2.587	12.248	1900	0.115
Momentum-Averaged	A	2.237	10.861	2.538	12.186	1910	0.114
	B	2.225	10.855	2.525	12.140	1906	0.114
	C	2.203	10.824	2.501	12.117	1904	0.113

ditionally, the Kepler frequency Ω_K and stability parameter $T/|W|$ are provided for the rotating stellar models. The stability parameter is the ratio of rotational (T) to gravitational (W) energy; a more in-depth exploration into this parameter and instabilities that may arise in rotating neutron stars will be in Chapter 4. In brief, this parameter has been used to determine if different instability modes may be excited in rotating neutron stars. In the context of uniformly rotating neutron stars, stability studies have previously specified the limit of $T/|W| < 0.14$ for stars to remain stable against secular instabilities, which grow in the presence of a small dissipative mechanism like viscosity or gravitational radiation at lower rotation rates [162]. Previous work finds this parameter in the range $0.11 < T/|W| < 0.13$, just below the specified so-called "critical" limit of 0.14, for stars uniformly rotating at their respective Kepler frequencies [163, 164]. For the three Bonn potentials, both the momentum-dependent and momentum-averaged approximations fall within this range.

For finite temperatures, only models constructed using the momentum-averaged self-energy approximation are used, as discussed in Section 2.4.2. To solve for stellar models, the high-density, finite temperature EOS must also be fit to an EOS for the crust. Popular models for neutron star crusts, like the previously mentioned HW+NV, are all constructed at zero temperature, meaning there is a discontinuity in the temperature for the low-density and

Table 2.3: Non-rotating and rotating neutron star properties calculated with EOS models at finite temperatures from the RBHF approximation, using the Bonn B potential. Bulk properties include the maximum mass $M_{\max}$ and corresponding radius $R_{\max}$ for both non-rotating and rotating stars, as well as the Kepler frequency Ω_K and stability parameter $T/|W|$ for rotating stars.

	Non-rotating ($\Omega = 0$)		Rotating ($\Omega = \Omega_K$)			
Temperature (MeV)	$M_{\max}$ ($M_\odot$)	$R_{\max}$ (km)	$M_{\max}$ ($M_\odot$)	$R_{\max}$ (km)	Ω_K (Hz)	$T/|W|$
10	2.388	10.900	2.702	12.112	1967	0.120
30	2.461	10.973	2.776	12.238	1958	0.122
50	2.541	11.439	2.861	12.887	1844	0.119
70	2.650	11.819	2.963	13.277	1803	0.113

high-density regions of the star. In massive neutron stars, the crust regions are thin and contribute negligibly to the bulk properties like mass and radius [70]. For this reason, we focus only on higher-mass stars created by fitting the finite temperature EOS models constructed using the RBHF approximation to the zero-temperature HW+NV EOS for the crust.

Mass compared to central energy density ϵ_c for four temperatures (T = 10, 30, 50, and 70 MeV) are shown in Figure 2.13, calculated using the Bonn B potential. As mentioned previously, the low-density portion of the higher temperature EOS models, especially $T = 70$ MeV, do not have good agreement with the zero-temperature HW+NV EOS, which can be seen for the low mass stars in Figure 2.13. As with the zero-temperature constructed EOS models, the bulk properties of non-rotating and rotating neutron stars constructed with the finite temperature EOS models using the Bonn B potential are displayed in Table 2.3. Even with high temperatures, the stability parameter $T/|W|$ remains below the critical value $T/|W| < 0.14$ for stars rotating at their Kepler frequencies. Increasing the temperature leads to higher mass peaks, as shown in Table 2.3, but has an inverse effect on the Kepler frequency Ω_K. When compared to the zero-temperature EOS from the Bonn B potential using the momentum-averaged Σ in the RBHF approximation, the EOS at 70 MeV sees a 19.1% increase in mass for non-rotating stars and a 17.3% increase for rotating stars.

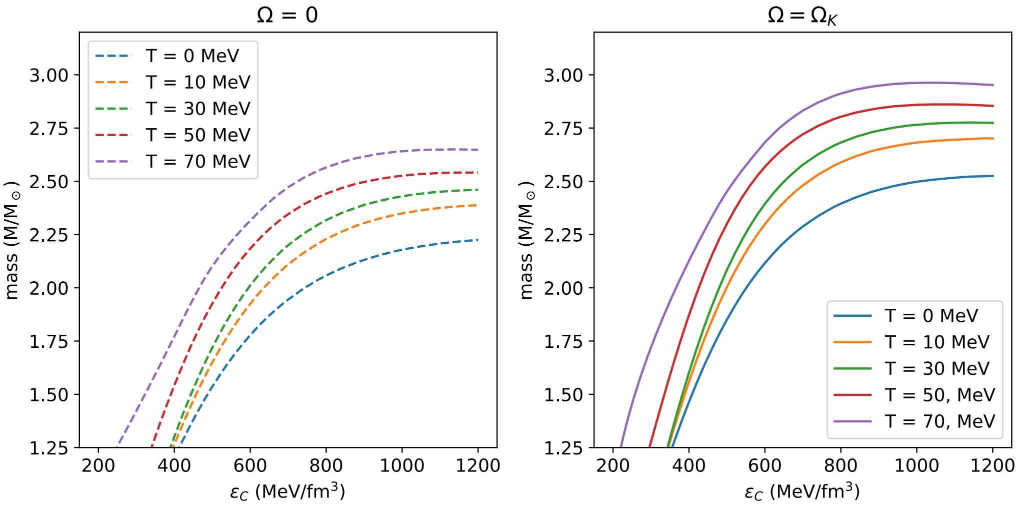

Figure 2.13: Mass vs. central density ϵ_C from EOS models computed with the RBHF approximation at a range of temperatures ($T = 10$, 30, 50, and 70 MeV) using the Bonn B potential. Non-rotating stellar models are shown on the left (dashed lines), and rotating models at the mass-shedding limit are shown on the left (solid lines).

2.5 Discussion and Conclusions

In this chapter, we present a comprehensive investigation into the properties of symmetric and asymmetric nuclear matter, employing self-consistent calculations utilizing the effective scattering matrix within the full Dirac space, following the methodology outlined in [83] and [70]. Specifically, we utilized the Bonn potentials (A, B, and C) for the OBE interaction. Our study begins with the examination of symmetric nuclear matter, where we conduct calculations of saturation properties at zero temperature, yielding results that align well with empirical values from diverse sources. Subsequently, our analysis extends to asymmetric nuclear matter, as detailed in Section 2.2.9, laying the groundwork for constructing equations of state (EOS) models pertinent to neutron star matter.

Expanding our investigation to include finite temperatures, we adapted the two-point Green's function within the RBHF scheme, as elucidated in Section 2.2.10. Here, employing the Bonn B potential, we derive results up to 70 MeV. Analogous to our zero-temperature analysis, the properties of asymmetric nuclear matter at finite temperatures serve as the foundation for constructing EOS models tailored to varying temperature regimes relevant to neutron stars. The incorporation of temperature is done in a self-consistent manner, as opposed to the common practice of adding a thermal contribution to models for the EOS of cold nuclear matter [165–167]. The integration of thermal effects into the RBHF framework ensures for a more comprehensive and accurate representation of the thermodynamic properties of dense nuclear matter.

Subsequently, we leveraged the zero and finite temperature EOS models to compute bulk properties of both non-rotating and rotating neutron stars, with the latter, computed up to the mass-shedding limit ($\Omega = \Omega_K$). Our investigation reveals that while the saturation properties of symmetric nuclear matter varied among the Bonn potentials at zero temperature, attributed to differences in the tensor force primarily provided by the pion, these variations did not markedly impact resulting neutron star properties, as evidenced in Figure 2.12.

Furthermore, the incorporation of finite temperature effects introduced additional contributions to the system's pressure, resulting in a discernible increase in the mass peak for both non-rotating and rotating stellar models, as illustrated in Figure 2.13. Comparing the maximum mass of the zero-temperature EOS utilizing the Bonn B potential to the corresponding EOS at 70 MeV, we observe a comparable increase in mass for both non-rotating (19.1%) and rotating (17.1%) stellar sequences. This underscores the significance of temperature effects in neutron star models, particularly in delineating their mass and associated properties.

It is noteworthy that the equations of state studied in this paper are sufficiently versatile to accommodate the mass of the most massive neutron star ever detected, PSR J0952–0607, estimated to be $2.35 \pm 0.17\, M_{\odot}$ [168, 169] and lead to masses and radii for PSR J0030+451 that are in agreement with the confidence intervals established for this pulsar [5].

As stated in Chapter 1, the finite temperature EOS models constructed in this Chapter will be used to construct models of differentially rotating stars. In the next chapter, we introduce the mathematical framework for the numerical scheme and provide example calculations at zero temperature. The finite temperature EOS models constructed in this Chapter are then used in Chapter 4.

Chapter 3

Differential Rotation in Compact Objects at Zero Temperature

This chapter presents text and results from previously published work (Ref. [99]) in collaboration with Fridolin Weber, Jia Jie Li, and Armen Sedrakian.

3.1 Introduction

As discussed in the previous chapter, extreme astrophysical events like core-collapse supernovae or binary neutron star mergers are characterized by extremely hot temperatures. Another feature that will influence the dynamics of the neutron stars involved in these events is the presence of a unique type of rotation called differential rotation, which is discussed in this chapter.

While the majority of rotating neutron stars are believed to be rotating uniformly, some neutron stars form with an appreciable amount of differential rotation, as discussed above. A newly formed proto-neutron star may experience some degree of differential rotation following a core-collapse supernova, but the phenomena would be short-lived, as hydrodynamical forces in the form of Ekman pumping and turbulent mixing will dampen any differential rotation in the star within a few days [70]. A more likely avenue for a star to experience differential rotation is following a binary neutron star (BNS) merger event. Binary neutron star mergers are likely to form differentially rotating remnants due to complicated hydrodynamic motions during the coalescence, evidenced in general relativistic numerical simulations.

The fate of the remnant of a BNS merger depends largely on the masses of the stars within the binary before coalescence. The mass of the remnant can be estimated as $M_0 = M_{1,0} + M_{2,0} - M_{\text{ejected},0}$, where $M_{1,0}$ and $M_{2,0}$ are the baryonic masses of the two stars before merging, and $M_{\text{ejected},0}$ is the mass ejected during the merger [170]. Depending on the remnant's mass in relation to the underlying EOS within the star, it may take the form of a massive, quasi-stable neutron star or promptly collapse into a black hole. As discussed in Chapter 2, there is an upper limit set on uniformly rotating stars by the Kepler or mass-shedding frequency. For the same EOS, a maximum mass can also be calculated for non-rotating stars. If the remnant mass falls between the Kepler mass and the non-rotating maximum mass, the remnant will likely take the form of a supramassive neutron star, which may find long-term stability or eventually collapse into a black hole depending on other dynamics within the star. If the remnant mass is instead over the Kepler limit, the remnant will either promptly collapse into a black hole, or form a hypermassive neutron star. A hypermassive star is stable only on short, dynamical timescales ($\lesssim 0.1$ s), where the short-term stability is likely due to differential rotation and thermal pressure. For the context of this chapter, we will focus solely on differential rotation; thermal effects paired with differential rotation are explored in Chapter 4.

In the case of hypermassive remnants, differential rotation provides stability which allows the star to sustain a total mass considerably higher than that of a uniformly rotating star [171], set by the Kepler or mass-shedding limit. A star will experience mass shedding when the rotational frequency at the star's equator surpasses the Kepler limit. In uniform rotation, the star rotates as a rigid body, meaning the maximum rotation rate at the equator restricts the overall rotational frequency. However, in the case of differential rotation, the star's core can rotate at frequencies beyond the Kepler frequency and maintain stability if the equator obeys the Kepler limit. The additional centrifugal force can therefore support the core from collapse while maintaining a considerably higher mass than uniform rotation, thus providing stability to hypermassive remnant stars.

Studies of differentially rotating neutron stars are of particular interest in the context of binary neutron star mergers following the first observation of a binary neutron star merger, GW170817 [172]. The BNS merger GW170817 was first detected by the gravitational wave detectors at LIGO and Advanced Virgo; the merger was followed rapidly by a short gamma-ray burst (GRB 170817A), detected by Fermi-GRB [173]. This particular event sparked a new era of multi-messenger astronomy and a revived interest in understanding the complex physics of BNS mergers. Understanding not only the inspiral phase but also the post-merger phase has the potential to provide further information on the equation of state of dense matter, neutron star properties, and the remnant's evolution.

In this chapter, numerical models for differentially rotating neutron stars are constructed for various equations of state at zero temperature to study the structure, deformation, and particle formation in hypermassive neutron stars. Models at finite temperatures will be explored in the following chapter. This chapter is organized as follows: Section 3.2 discusses the general relativistic theoretical framework for modeling differential rotation in neutron stars. For numerical models constructed under the assumption the densest portion of the star is in the center (discussed in further detail below), the results are shown in Section 3.3. Section 3.4 presents the summary and discussion of the work.

3.2 Theoretical Framework

The theoretical framework for modeling differential rotation in neutron stars described in this work follows from the framework laid out by Ref. [139], which was then modified in Ref. [104] (referred to as CST throughout the text). The equations shown in this section directly follow the modifications introduced in CST.

To model differentially rotating neutron stars, we begin with the definition of the line element [104]:

$$ds^2 = -e^{\gamma-\rho}dt^2 + e^{2\alpha}(dr^2 + r^2 d\theta) + e^{\gamma-\rho}r^2 \sin^2\theta(d\phi - \omega dt)^2, \tag{3.1}$$

which essentially has the same form as the line element for uniform rotation described in Chapter 2. As is for uniform rotation, the metric potentials, ρ, γ, α, and ω are dependent on both the radial r and polar θ coordinates, where θ is included to account for the physical deformation of the star from rotation described in Section 3.1. For both uniform and differential rotation, Eq. (3.1) models neutron stars as stationary, axisymmetric configurations of a (self-gravitating) perfect fluid [104]. Under the assumption of neutron star matter as a perfect fluid, sources of non-isotropic stresses such as magnetic fields or heat transport are ignored [102]. This assumption also allows neutron star matter to be described by the energy-momentum (or stress-energy) tensor given by:

$$T^{\kappa\sigma} = (\epsilon + P)\, u^{\kappa} u^{\sigma} + g^{\kappa\sigma} P, \tag{3.2}$$

where u is the fluid's 4-velocity, κ and σ are indices ranging from 0 to 3, and ϵ and P are given by the underlying EOS. Equilibrium models for neutron stars must obey the equation of hydrostatic equilibrium as Einstein's field equation, given as:

$$R^{\kappa\sigma} - \frac{1}{2}Rg^{\kappa\sigma} = 8\pi T^{\kappa\sigma}, \tag{3.3}$$

where $R^{\kappa\sigma}$ is the Ricci tensor, R is the curvature scalar, and $g^{\kappa\sigma}$ is the metric tensor.

3.2.1 Metric Potentials

Under the assumption of axisymmetry, the domain for the spherical coordinates r and θ are $0 \leq r \leq \infty$ and $0 \leq \theta \leq \pi/2$. The following coordinate transformations are introduced in CST to map the infinite radial domain into a finite domain to solve the problem numerically. The polar coordinate is transformed to μ:

$$\mu = \cos\theta, \tag{3.4}$$

and the radial coordinate is transformed to s:

$$\bar{r} = \bar{r}_e \left(\frac{s}{1-s}\right), \tag{3.5}$$

where $\bar{r}$ is a scaled version of the radius and $\bar{r}_e$ is the coordinate radius at the equator of the star [104]. Many quantities discussed throughout this text will be scaled following the definitions given in CST; an exhaustive list can be found in Appendix C.

The field equations for the metric potentials are a result of Einstein's field equation, Eq. (3.3). As described in CST, the metric potentials ρ, γ, and ω are written as [104]:

$$\begin{aligned} \rho(s,\mu) = -e^{-\gamma/2}\sum_{n=0}^{\infty} \mathrm{P}_{2n}(\mu) \Bigg[& \left(\frac{1-s}{s}\right)^{2n+1} \int_0^s \frac{ds' s'^{2n}}{(1-s')^{2n+2}} \int_0^1 d\mu' \mathrm{P}_{2n}(\mu') \tilde{S}_\rho(s',\mu') \\ & + \left(\frac{s}{1-s}\right)^{2n} \int_s^1 \frac{ds'(1-s')^{2n-1}}{s'^{2n+1}} \int_0^1 d\mu' \mathrm{P}_{2n}(\mu') \tilde{S}_\rho(s',\mu') \Bigg], \end{aligned} \tag{3.6}$$

$$\gamma(s,\mu) = \frac{2e^{-\gamma/2}}{\pi}\sum_{n=1}^{\infty}\frac{\sin[(2n-1)\theta]}{(2n-1)\sin\theta}$$
$$\Bigg[\left(\frac{1-s}{s}\right)^{2n}\int_0^s \frac{ds's'^{2n-1}}{(1-s')^{2n+1}}\int_0^1 d\mu' \sin[(2n-1)\theta']\tilde{S}_\gamma(s',\mu') \tag{3.7}$$
$$+\left(\frac{s}{1-s}\right)^{2n-2}\int_s^1 \frac{ds'(1-s'(^{2n-3}}{s'^{2n-1}}\int_0^1 d\mu' \sin[(2n-1)\theta']\tilde{S}_\gamma(s',\mu')\Bigg],$$

$$\hat{\omega}(s,\mu) = -e^{(2\rho-\gamma)/2}\sum_{n=1}^{\infty}\frac{\mathrm{P}^1_{2n-1}(\mu)}{2n(2n-1)\sin\theta}$$
$$\Bigg[\left(\frac{1-s}{s}\right)^{2n+1}\int_0^s \frac{ds's'^{2n}}{(1-s')^{2n+2}}\int_0^1 d\mu' \sin\theta' \mathrm{P}^1_{2n-1}(\mu')\tilde{S}_{\hat{\omega}}(s',\mu') \tag{3.8}$$
$$+\left(\frac{s}{1-s}\right)^{2n-2}\int_s^1 \frac{ds'(1-s')^{2n-3}}{s'^{2n-1}}\int_0^1 d\mu' \sin\theta' \mathrm{P}^1_{2n-1}\tilde{S}_{\hat{\omega}}(s',\mu')\Bigg],$$

where $\mathrm{P}_n(\mu)$ are Legendre polynomials, $\mathrm{P}^m_{2n}(\mu')$ are associated Legendre polynomials, and $\tilde{S}$ are the effective source terms for the three metric potentials [104]. The source terms are defined as:

$$\tilde{S}_\rho(s,\mu) = e^{\gamma/2}\Big[8\pi e^{2\alpha}\bar{r}_e^2(\bar{\epsilon}+\bar{P})\left(\frac{s}{1-s}\right)^2\frac{1+v^2}{1-v^2}+\left(\frac{s}{1-s}\right)^2(1-\mu)^2e^{-2\rho}$$
$$[(s(1-s)\hat{\omega}_{,s})^2+(w-\mu^2)\hat{\omega}^2_{,s}]+s(1-s)\gamma_{,s}-\mu\gamma_{,\mu}+\frac{\rho}{2}(16\pi e^{2\alpha}\,\bar{r}_e^2\bar{P}\left(\frac{s}{1-s}\right)^2 \tag{3.9}$$
$$-s(1-s)\gamma_{,s}\left[\frac{s(1-s)}{2}\gamma_{,s}+1\right]-\gamma_{,\mu}\left(\frac{1-\mu^2}{2}\gamma_{,\mu}-\mu\right)\Big)\Big],$$

$$\tilde{S}_\gamma(s,\mu) = e^{\gamma/2}\Big[16\pi e^{2\alpha}\bar{r}_e^2\bar{P}\left(\frac{s}{1-s}\right)^2+\frac{\gamma}{2}\Bigg(16\pi e^{2\alpha}\bar{r}_e^2\bar{P}\left(\frac{s}{1-s}\right)^2 \tag{3.10}$$
$$-\frac{s^2(1-s)^2}{2}\gamma^2_{,s}-\frac{1-\mu^2}{2}\gamma^2_{,\mu}\Big],$$

$$
\begin{aligned}
\tilde{S}_{\hat{\omega}}(s,\mu) = e^{(\gamma-2\rho)/2}\bigg(-16\pi e^{2\alpha}\frac{\hat{\Omega}-\hat{\omega}}{1-v^2}\bar{r}_e^2(\bar{\epsilon}+\bar{P})\left(\frac{s}{1-s}\right)^2 \\
+\hat{\omega}\left[-8\pi e^{2\alpha}\bar{r}_e^2\frac{(1+v^2)\bar{\epsilon}+2v^2\bar{P}}{2-v^2}\left(\frac{s}{1-s}\right)^2 - s(1-s)\left(2\rho_{,s}+\frac{1}{2}\gamma_{,s}\right)\right]+ \\
\hat{\omega}\left[\mu\left(2\rho_{,\mu}+\frac{1}{2}\gamma_{,\mu}\right)+\frac{s^2(1-s)^2}{4}(4\rho_{,s}^2-\gamma_{,\mu})\right] \\
+\hat{\omega}\left[+\frac{1-\mu^2}{4}(4\rho_{,\mu}^2-\gamma_{,\mu}^2)-(1-\mu^2)e^{-2\rho}\left(s^4\hat{\omega}_{,s}^2+\frac{s^2(1-\mu^2)}{(1-s)^2}\hat{\omega}_{,\mu}^2\right)\right]\bigg),
\end{aligned}
\tag{3.11}
$$

where v is the proper velocity of the matter and the quantities $\hat{\omega}$ and $\hat{\Omega}$ are scaled versions of the potential ω and the angular frequency Ω, given as:

$$
\begin{aligned}
&\hat{\omega} = \bar{r}_e\bar{\omega}, \\
&\hat{\Omega} = \bar{r}_e\bar{\Omega}.
\end{aligned}
\tag{3.12}
$$

The terms ending in $_{,s}$ or $_{,\mu}$ imply a derivative with respect to s or μ. The gravitational field for the fourth metric potential α can be reduced to a linear ordinary differential equation, given as:

$$
\begin{aligned}
\alpha_{,\mu} = -\frac{1}{2}(\rho_{,\mu}+\gamma_{,\mu}) - [(1-\mu^2)[1+s(1-s)\gamma_{,s}]^2+[-\mu+(1-\mu^2)\gamma_{,\mu}]^2]^{-1} \\
\times\Bigg[\frac{1}{2}(s(1-s)[s(1-s)\gamma_{,s}]_{,s}+s^2(1-s)^2\gamma_{,s}^2-[(1-\mu^2)\gamma_{,\mu}]_{,\mu} \\
-\gamma_{,\mu}[-\mu+(1-\mu^2)\gamma_{,\mu}])+\frac{1}{4}[s^2(1-s)^2(\rho_{,s}+\gamma_{,s})^2+(1-\mu^2)(\rho_{,\mu}+\gamma_{,\mu})^2] \\
[-\mu+(1-\mu^2)\gamma_{,\mu}]-s(1-s)(1-\mu^2)\Bigg[\frac{1}{2}(\rho_{,s}+\gamma_{,s})(\rho_{,\mu}+\gamma_{,\mu}) \\
+\gamma_{s\mu}+\gamma_{,s}\gamma_{,\mu}[1+s(1-s)\gamma_{,s}]+s(1-s)\mu\gamma_{,s}[1+s(1-s)\gamma_{,s}] \\
+\frac{1}{4}(1-\mu^2)e^{-2\rho}\Bigg[2\frac{s^3}{1-s}(1-\mu^2)\hat{\omega}_{,s}\hat{\omega}_{,\mu}[1+s(1-s)\gamma_{,s}] \\
-\left(s^4\hat{\omega}_{,s}^2-\frac{s^2}{(1-s)^2}(1-\mu^2)\hat{\omega}_{,\mu}^2\right)[-\mu+(1-\mu^2)\gamma_{,\mu}].
\end{aligned}
\tag{3.13}
$$

3.2.2 Rotational Frequency

While the definition of gravitational field equations for the metric potentials remains unchanged for uniform or differential rotation, the key difference separating the two rotation types will be discussed here. As mentioned previously, equilibrium models for neutron stars must obey the equation of hydrostatic equilibrium, which has the form:

$$h(P) - h_p = \int_{P_p}^{P} \frac{dP}{\epsilon + P} = \ln u^t - \ln u^t_p - \int_{\Omega_c}^{\Omega} F(\Omega) d\Omega, \tag{3.14}$$

where $h(P)$ is enthalpy as a function of the pressure and the subscripts p and c denote the variable's value at the pole or center, respectively. Additionally, u^t is the time-like component of the 4-velocity u^μ, defined as:

$$u^\mu = \frac{e^{-(\gamma+\rho)/2}}{(1-v^2)^{1/2}}[1, 0, 0, \Omega], \tag{3.15}$$

where the proper velocity v is:

$$v = (\Omega - \omega)\, r \sin\theta\, e^{-\rho}. \tag{3.16}$$

The integrand of the final integral term in Eq. (3.14), $F(\Omega)$, is the function that defines the rotation law of the matter in the case of differential rotation. Following CST, we define $F(\Omega)$ as a linear rotation law:

$$F(\bar{\Omega}) = A^2(\bar{\Omega}_c - \bar{\Omega}), \tag{3.17}$$

where A is a parameter that dictates the degree of differential rotation within the star. In the case of uniform rotation, Eq. (3.17) disappears as the value for the frequency at the center of the star is constant throughout (i.e. $\Omega_c = \Omega$). Using the specified rotation law in

Eq. (3.17), the equation of hydrostatic equilibrium can be integrated to give:

$$h(P) - h_p = \frac{1}{2}\left[\gamma_p + \rho_p - \gamma - \rho - \ln(1-v^2) + \hat{A}^2(\hat{\Omega} - \hat{\Omega}_c)^2\right], \tag{3.18}$$

where $\hat{A}$ is the rotation parameter scaled as $\hat{A} = A/\bar{r}_e$. The matrix of angular frequency $\hat{\Omega}$ can be derived using the following equation:

$$(\hat{\Omega}_c - \hat{\Omega}) = \frac{1}{\hat{A}^2}\left[\frac{(\hat{\Omega} - \hat{\omega})s^2(1-\mu^2)e^{-2\rho}}{(1-s)^2 - (\hat{\Omega} - \hat{\omega})^2 s^2(1-\mu^2)e^{-2\rho}}\right]. \tag{3.19}$$

The choice of rotation law directly impacts the maximum mass for a given EOS. Many other studies of differential rotation use the linear rotation law in Eq. (3.17) (see Refs. [104, 105, 107]), which is also referred to throughout the literature as the so-called "j-constant law". However, different studies of differential rotation have explored the impact of using modified versions of the linear law or completely different rotation laws. Ref. [174] explores the parameter space of a given rotation law using a generalized version of the "j-constant law", with Ref. [175] adopting a similar generalized version. Ref [176] instead carries out full simulations of BNS mergers and argues a linear rotation law cannot fully capture the complexity of a hypermassive remnant's rotation profile just after forming. For the context of this work, we will proceed with the linear rotation law in the form of Eq. (3.17), but interesting future work would entail implementing other rotation laws explored in the literature to see the impacts on calculated bulk properties.

To solve the numerical scheme for equilibrium models of differentially rotating stars, we begin with an ansatz for the metric potentials (ρ, γ, $\hat{\omega}$, and α) from a non-rotating solution of the TOV equation. These values are used to determine a value for the radius at the equator, r_e of the star:

$$\bar{r}_e^2 = \frac{2[h(\bar{P}(\bar{\epsilon}_c)) - h_p]}{\hat{\gamma} + p + \hat{\rho}_p - \hat{\gamma}_m - \hat{\rho}_m}, \tag{3.20}$$

which is equivalent to Eq. (3.18) evaluated at the location of the maximum (denoted by subscript m) density of the star, which is assumed to be the central value in CST. However, the equation for r_e changes when the maximum density within the star is not in the center, which is the case in very deformed configurations; see Figure 3.1 for a visual explanation of this phenomenon. Results in Section 3.3 use Eq. (3.20) to derive value for r_e (i.e. the traditional CST scheme), and Chapter 4 discusses how to update the numerical scheme when the central density is not the maximum density.

Returning to the CST scheme, Eq. (3.20) makes use of the following re-definitions:

$$\begin{aligned}
\hat{\rho} &= \frac{\rho}{\bar{r}_e^2}, \\
\hat{\gamma} &= \frac{\gamma}{\bar{r}_e^2}, \\
\hat{\alpha} &= \frac{\alpha}{\bar{r}_e^2}.
\end{aligned} \tag{3.21}$$

Next to be determined is the angular frequency $\hat{\Omega}$, which is dependent on the central value $\hat{\Omega}_c$. The central value is determined by evaluating Eqs. (3.18) and (3.19) at the equator, which take the form:

$$\bar{r}_e^2(\hat{\gamma}_2 + \hat{\rho}_e - \hat{\gamma}_p - \hat{\rho}_p) + \ln[1 - (\hat{\Omega}_e - \hat{\omega}_e)^2 \exp(-2\bar{r}_e^2\hat{\rho}_e)] = \hat{A}^2(\hat{\Omega}_e - \hat{\Omega}_c), \tag{3.22}$$

and:

$$\hat{A}^2(\hat{\Omega}_e - \hat{\Omega}_c) = \frac{1}{\hat{A}^2}\frac{(\hat{\Omega}_e - \hat{\omega}_e)^2 \exp(-4\bar{r}_e^2\hat{\rho}_e)}{[1 - (\hat{\Omega}_e - \hat{\omega}_e)^2 \exp(-2\bar{r}_e^2\hat{\rho}_e)]^2}, \tag{3.23}$$

where the subscript e denotes the value of the variable at the equator. To determine $\hat{\Omega}_c$, the value of $\hat{\Omega}_e$ is first determined from Eq. (3.23) using a root-finding algorithm; we implement Brent's method, which is described in Appendix C.0.2. After $\hat{\Omega}_e$ and $\hat{\Omega}_c$ are calculated, the full matrix for the angular velocity $\hat{\Omega}$ is determined using Eq. (3.19), solved for numerically

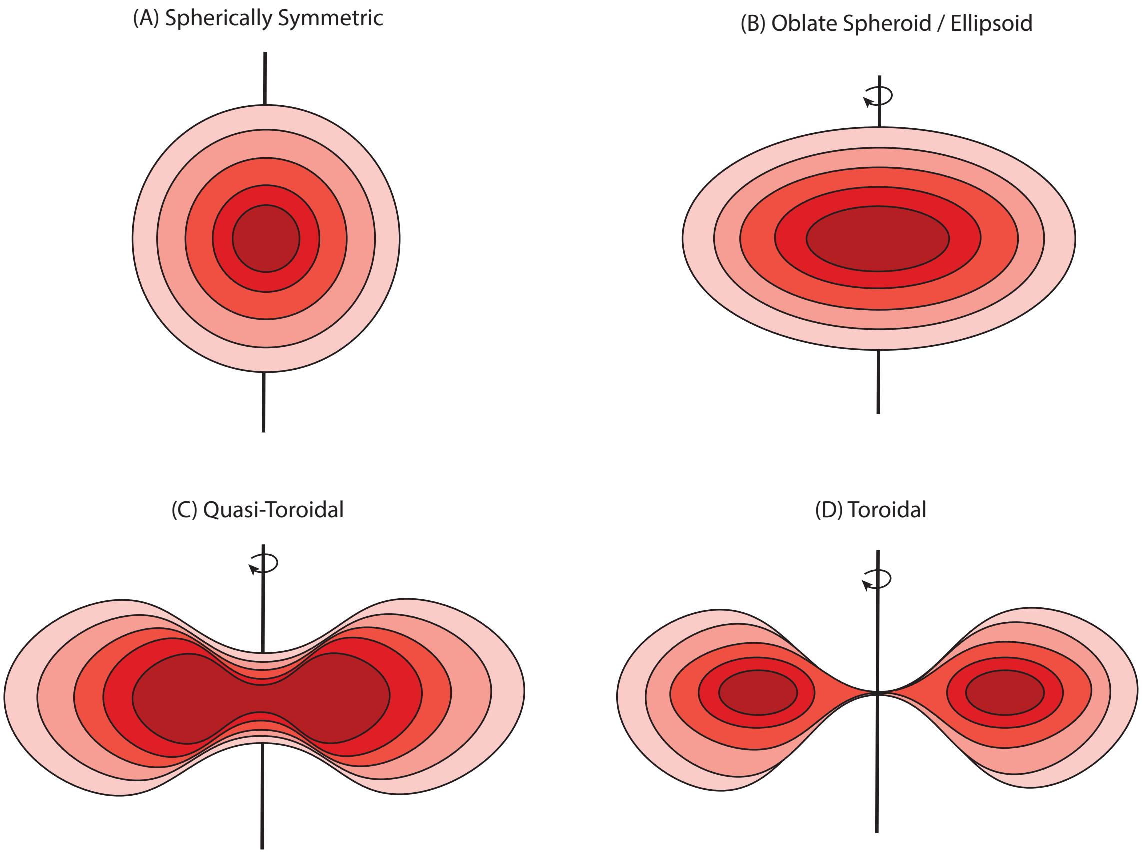

Figure 3.1: A schematic for the physical deformation seen in rotating neutron stars. In (A), the star is non-rotating and therefore spherically symmetric, and in (B) the star takes on an ellipsoid shape under extreme uniform or less extreme differential rotation. However, extreme differential rotation can result in (C) quasi-toroidal or (D) fully toroidal stars. For (A) and (B), the center of the star is the densest portion (signified by dark red), but in (C) and (D), the densest portion is no longer in the center of the star.

also using Brent's method. These values are then used to determine the enthalpy, velocity, and pressure of the system with Eqs. (3.18) and (3.16).

Finally, the effective source terms, defined in Eqs. (3.9), (3.10), and (3.11), are calculated and used to determine new values for the metric potentials. These new values start the iterative process over again, which is repeated until $\bar{r}_e$ converges. This process is shown schematically in Appendix C.

3.2.3 Stellar Properties

Once a set of self-consistent solutions are determined for the system, they are used to calculate the bulk properties of the star as described in CST. Some of these properties include the gravitational mass M:

$$M = \frac{4\pi\kappa^{1/2}c^2\bar{r}_e^3}{G}\int_0^1 \frac{s^2\,ds}{(1-s)^2}\int_0^1 d\mu\, e^{2\alpha+(\gamma+\rho)/2}\frac{\bar{\rho}_0}{(1-v^2)^{1/2}}, \tag{3.24}$$

the angular momentum J:

$$J = \frac{4\pi\kappa c^3\bar{r}_e^4}{G}\int_0^1 \frac{s^3\,ds}{(1-s)^5}\int_0^1 d\mu\,(1-\mu^2)^{1/2}e^{2\alpha+\gamma-\rho}(\bar{\epsilon}+\bar{P})\frac{v}{1-v^2}, \tag{3.25}$$

the rotational energy T:

$$T = \frac{2\pi\kappa^{1/2}c^2\bar{r}_e^3}{G}\int_0^1 \frac{s^3\,ds}{(1-s)^2}\int_0^1 d\mu\,(1-\mu^2)^{1/2}e^{2\alpha+\gamma-\rho}(\bar{\epsilon}+\bar{P})\frac{v\,\hat{\Omega}}{1-v^2}, \tag{3.26}$$

and the circumferential radius of the equator R_e:

$$R_e = \kappa^{1/2}\bar{r}_e e^{(\gamma_e-\rho_e)2}. \tag{3.27}$$

An exhaustive list of equations for the bulk properties can be found in CST (Ref. [104]).

3.3 Results for Maximum Density at the Center of the Star

Stellar models of differentially rotating neutron stars are constructed using the outlined numerical scheme. For the traditional CST algorithm, we fix three values to be constant: the central density ϵ_c, the ratio of polar to equatorial radii $r_{\rm ratio}$ (which dictates the deformation of the star), and the scaled rotation parameter, $\hat{A}$. More specifically, $\hat{A}^{-1}$ is fixed as it repeatedly appears in its inverse form in the equations described in Section 3.2. We follow the lead of previous work which parameterized sequences by values of $\hat{A}^{-1} = 0.3$, 0.5, 0.7, and 1.0 [104, 105, 174]. Uniform rotation is obtained in the limit $\hat{A}^{-1} \rightarrow 0$, and an upper bound of the scaled rotation parameter is $\hat{A}^{-1} = 1.0$. As differential rotation becomes more extreme in the star ($\hat{A}^{-1} \rightarrow 1.0$), the maximum mass and corresponding equatorial radius of a stellar sequence are expected to increase.

In this section, the traditional CST algorithm is used, which assumes the maximum density occurs at the center of the star. This assumption holds well for higher values of $r_{\rm ratio}$, or less extreme physical deformations (similar to what is observed in stars rotating uniformly at their Kepler frequency). The CST algorithm finds stable numerical results for $r_{\rm ratio}$ values of 1 (which is spherically symmetric) to ~ 0.55, so results shown in this section use values for $r_{\rm ratio}$ that fall within this range. More deformed configurations are explored in Chapter 4.

3.3.1 EOS Models using Relativistic Hartree-Fock (RHF) Theory

In this section, models for the EOS constructed using the RHF formalism at zero temperature are used as input to the numerical scheme. The four EOS models used in this section also include strange matter, which is hypothesized to occur in stable states at extreme densities. The high-density regime within a neutron star may include exotic degrees of freedom like deconfined quark matter, meson condensates, hyperons, and delta isobars (Δ). These additional degrees of freedom have been shown previously in numerical simulations to greatly impact properties like the mass and radius of neutron stars. In [177], the presence of Δ's was shown to soften the EOS in the low to intermediate-density region and stiffen it at high densities, resulting in a slightly increased maximum mass and considerably decreased radius for non-rotating compact objects.

The models of dense matter EOS used in this section are based on the framework of CDF theory, where meson-Δ coupling values are varied and the calculations are carried out with the relativistic Hartree-Fock (RHF) approximation. The Lagrangian of the model is given as

$$\mathcal{L} = \mathcal{L}_{\mathrm{B}} + \mathcal{L}_{\mathrm{m}} + \mathcal{L}_{\mathrm{int}} + \mathcal{L}_{\mathrm{l}}, \tag{3.28}$$

where $\mathcal{L}_{\mathrm{B}}$ represents free baryonic fields ψ_{B}, $\mathcal{L}_{\mathrm{m}}$ represents free meson fields ϕ_{m}, $\mathcal{L}_{\mathrm{int}}$ describes the interaction between baryons and mesons, and $\mathcal{L}_{\mathrm{l}}$ represents the contribution from free leptons. The baryons accounted for include the spin-1/2 octet of nucleons $N \in \{n, p\}$ and hyperons $Y \in \{\Lambda, \Xi^{0,-}, \Sigma^{+,0,-}\}$ and the spin-3/2 zero-strangeness quartet $\Delta \in \{\Delta^{++,+,0,-}\}$. The mesons accounted for include those regularly encountered in the RHF approximation including the isoscalar-scalar meson σ, the isoscalar-vector meson ω, the isovector-vector meson ρ, and the pseudo-vector meson π, as well as two hidden-strangeness mesons, σ^* and ϕ, which describe the interaction between hyperons. The leptons accounted for are electrons e^- and muons μ^-.

The standard procedure for obtaining the density functional begins with finding equations of motion from the Euler-Lagrange equations for each particle species. These take the form of the Dirac equations for the baryon octet and leptons, the Rarita-Schwinger equations for the Δ's, and the Klein-Gordon equations for the mesons. The solutions of these equations are used to generate the energy density functional by evaluating each of the baryon self energies, Σ, in the RHF approximation. In Dirac space, the self-energy can be defined as:

$$\Sigma(p) = \Sigma_S(p) + \gamma_0\, \Sigma_0(k) + \vec{\gamma} \cdot \hat{p}\, \Sigma_V(p)\,, \tag{3.29}$$

where Σ_S, Σ_0, and Σ_V denote the scalar self-energy, the time and space components of vector self-energy, respectively, γ_μ (μ = 0-3) are the Dirac matrices, and $\hat{p}$ is a unit vector along the 3-momentum $\vec{p}$. The self-energies, field equations, and the required charge neutrality condition are then used to determine EOS at zero temperature. The full self-consistent procedure is outlined in greater detail in [70, 177, 178].

The interaction between mesons and baryons, described by $\mathcal{L}_{\rm int}$ in Eq. ((3.3.1)), is parametrized by meson-baryon coupling constants g_{mB}. As discussed in Chapter 2, *ab initio* methods use values for the coupling constants from a given OBE model. But in the case of phenomenological methods like RHF, these values instead are determined by fitting to empirical data of nuclear and hypernuclear systems. For the hypernuclear sector, the coupling constant values are given by the SU(3) flavor symmetry quark model for vector mesons; for scalar mesons, the coupling constants are fitted to empirical hypernuclear potentials. The meson-Δ coupling is parametrized by Δ isoscalar potential V_Δ, which is measured in units of the nucleon isoscalar potential $\mathrm{V_N} = \Sigma_{0,\omega}(\omega) + \Sigma_{S,\sigma}(\sigma)$. Heavy-ion collision and scattering experiments provide approximate upper and lower bounds on V_Δ relating to $\mathrm{V_N}$, but there are no exact values defined for the isoscalar potential. Following [177], three potential depths V_Δ are chosen at nuclear saturation density ρ_0 as $\mathrm{V}_\Delta = 2/3\ \mathrm{V_N}$, $\mathrm{V_N}$, and $4/3\ \mathrm{V_N}$. These are consistent with inferences of Δ potentials from terrestrial experiments and are compatible with the lower limit on the maximum mass of static compact stars $M_{\rm TOV} \geq 2M_\odot$. For comparison, we also include a hypernuclear EOS constructed from the framework of CDF theory which does not include Δ particles, labeled "npY" throughout the text. The three mixed Δ-hyperon EOS models parametrized by V_Δ and the purely hypernuclear EOS model npY are shown in Fig. 3.2.

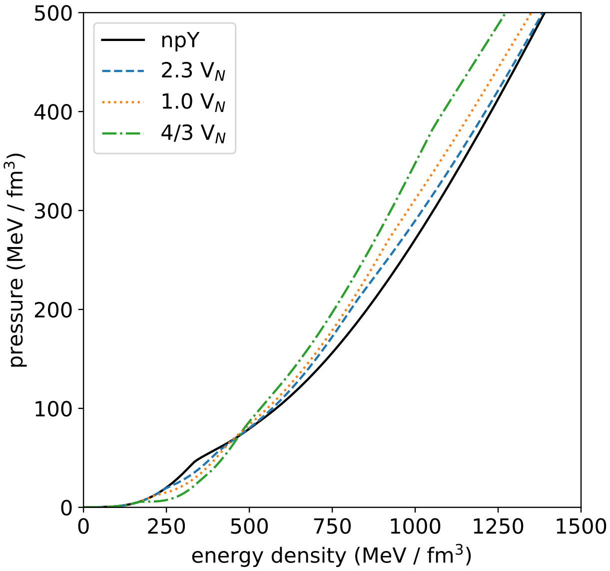

Figure 3.2: Pressure vs. energy density for four EOS models constructed using RHF theory at zero temperature. The black curve, denoted “npY”, describes hypernuclear matter that does not contain Δ isobars. The other three curves contain both hyperons and Δ’s, parametrized by different values of the potential depth V_Δ (see text for more details).

3.3.2 Stellar Sequences

We first show results for stellar sequences with a constant central density range to demonstrate the expected increase in mass due to differential rotation. Figures 3.3 and 3.4 show mass-radius (equatorial) relations for four degrees of differential rotation, parameterized by $\hat{A}^{-1}$, compared to the non-rotating curves calculated with the Tolman-Oppenheimer-Volkoff (TOV) equation; Figure 3.3 uses the hyperonic EOS model and Figure 3.4 uses the EOS model with largest potential depth value of $V_\Delta = 4/3\ V_N$ [177].

They highlight that the inclusion of Δ in the EOS composition softens the EOS at lower densities and stiffens it at higher densities. This impacts the corresponding mass-radius relations for non-rotating stars by decreasing the radius but increasing the maximum mass. When comparing the mass-radius curves under differential rotation resulting from the hyperonic EOS in Figure 3.3 to those resulting from the largest value of V_Δ in Figure 3.4,

Table 3.1: Maximum gravitational mass (in units of $M_\odot$) of four RHF EOS models which account for hyperons (npY) or hyperons and Δ particles (given as values of the V_Δ potential):

EOS model	TOV	$\hat{A}^{-1} = 0.3$	$\hat{A}^{-1} = 0.5$	$\hat{A}^{-1} = 0.7$	$\hat{A}^{-1} = 1.0$
npY	2.011	2.183	2.253	2.319	2.356
2/3 V_N	2.034	2.200	2.270	2.334	2.366
1.0 V_N	2.054	2.216	2.287	2.355	2.386
4/3 V_N	2.103	2.262	2.339	2.418	2.461

the same trend is observed. For the highest degree of differential rotation ($\hat{A}^{-1} = 1.0$), the canonical 1.4 $M_\odot$ star containing Δ's has a radius of 15.46 km for the EOS with $V_\Delta = 4/3$ V_N, compared to a radius of 17.65, reflecting the same decrease in radius observed with the non-rotating curves in [177].

The maximum masses of the hyperonic EOS and the three EOS models containing both hyperons and Δ's are given in Table 3.1 for non-rotating (TOV) and differentially rotating stars. For values of parameter $\hat{A}^{-1}$ corresponding to different degrees of differential rotation are used. Both Table 3.1 and Figures 3.3 and 3.4 reflect calculated values for stellar models at a fixed value of the ratio between the polar and equatorial radius, $r_{\mathrm{ratio}} = 0.7$. For all employed EOS models, we observe a similar 16-17% increase in the maximum mass of a maximally differentially rotating star when compared to the maximum mass of a static (TOV) star. This shows that the difference in particle compositions that were accounted for has no significant impact on how much the maximum mass will increase as the rotation parameter $\hat{A}^{-1} \to 1.0$.

3.3.3 Particle Composition

In this section, density distributions of massive, differentially rotating stars are used to demonstrate where in the star different particle species appear.

Individual stellar models are constructed with a series of set parameters: the central density,

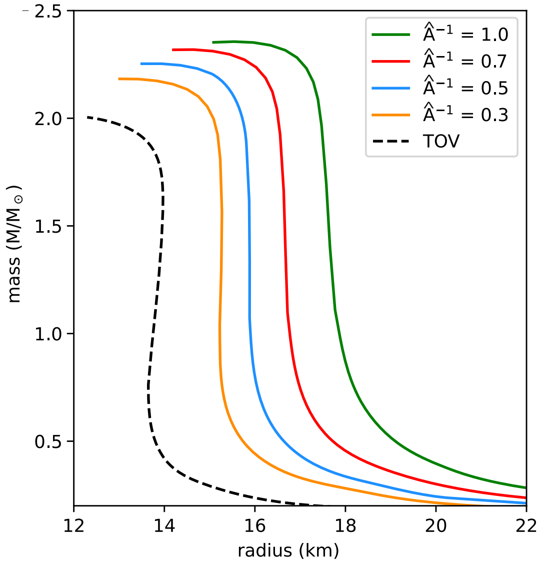

Figure 3.3: Mass-radius relations for the hyperonic EOS npY constructed using RHF theory at zero temperature. The dashed black line shows the non-rotating curve resulting from the TOV equation, while the solid-colored lines are curves under different degrees of differential rotation. Differential rotation is parameterized by values of the rotation parameter, $\hat{A}^{-1}$ (see text for more details).

the ratio between the polar and equatorial radius $\mathrm{r}_{\mathrm{ratio}}$, and the rotation parameter $\hat{A}^{-1}$ which specifies the degree of differential rotation. The parameter $\mathrm{r}_{\mathrm{ratio}}$ reflects the structural deformation observed with rapid rotation, which has been extensively showed through numerical simulation [70, 179, 180] to result in a lengthening of the radius at the equator and shortening at the pole. In the case of differential rotation, more extreme structural deformations can occur as $\mathrm{r}_{\mathrm{ratio}} \to 0$, in some cases leading to the formation of toroidally shaped objects [105, 155]. In this section, we fix $\mathrm{r}_{\mathrm{ratio}}$ at a value of 0.6, slightly lower than that used to create stellar sequences in the previous section, resulting in massive, rapidly rotating, ellipsoid-shaped stars.

We construct density distribution maps for the hyperonic EOS model and the $\mathrm{V}_\Delta = 4/3$ V_N EOS model additionally containing Δ's. Particle fractions for both EOS models can be found in Figure 3.5. For the hyperonic EOS model, the three hyperon species accounted for

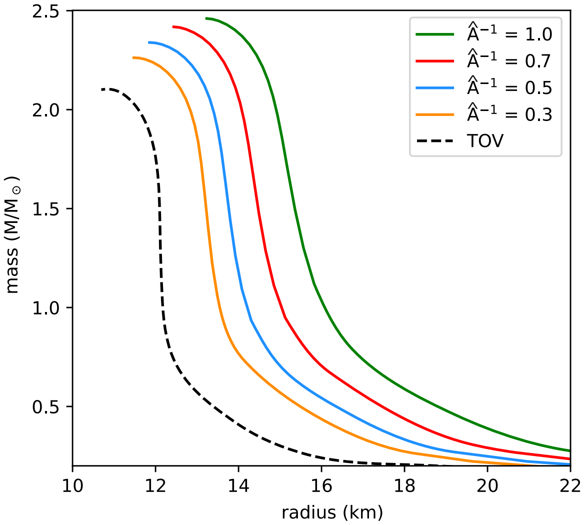

Figure 3.4: Mass-radius relations for the mixed hyperon-Δ EOS with $V_\Delta = 4/3\ V_N$ constructed using RHF theory at zero temperature. The dashed black line shows the non-rotating curve resulting from the TOV equation, while the solid-colored lines are curves under different degrees of differential rotation. Differential rotation is parameterized by values of the rotation parameter, $\hat{A}^{-1}$ (see text for more details).

are the Λ, the Ξ^-, and the Σ^- hyperons, which appear in that order. Figure 3.6 shows the density map of a 2.48 $M_\odot$ star constructed from the npY EOS model, with the following set parameters: central density $\epsilon_c = 900$ MeV, $r_{ratio} = 0.6$, and rotation parameter $\hat{A}^{-1} = 0.7$. The Λ hyperon first appears at an equatorial radius, r_e, of $\sim$5 km and a density of 329.4 MeV/fm^3 (shown in cyan); the Λ hyperon would be present from this depth until the center of the star. The Σ^- and Ξ^- both appear at $r_e \approx 3$ km and densities of 479.1 and 510.9 MeV/fm^3, respectively (shown in green). The Σ^- only appear briefly due to their repulsive potential at nuclear saturation density [177], but the Ξ^- would be populated throughout the star up to its center.

The density distribution map for a 2.55 $M_\odot$ star constructed with the mixed hyperon and Δ EOS with a potential depth of $V_\Delta = 4/3\ V_N$ is shown in Figure 3.7. The same values for the central density, r_{ratio}, and rotation parameter $\hat{A}^{-1}$ were used as in Figure 3.6. As shown in both Figure 3.5 and Figure 2 of [177], a larger value of the potential V_Δ results in a lowered onset threshold for Δ's, and their threshold density is much lower than the one for the first hyperon. For the largest potential depth V, the same-charge Δ^- isobar effectively replaces the Σ^- hyperons in the star. In this case, only the Λ and Ξ^- hyperons appear. The same-charge Δ^- isobar effectively replaces the Σ^- hyperon, as it is energetically more favorable due to its large negative potential. In Figure 3.7, the Δ^- appears at a density of 168.66 MeV/fm^3, corresponding to an r_e of $\sim$8 km (shown in royal blue). The next species to appear, Δ^0, appears at a density of 344.1 MeV/fm^3 corresponding to an r_e of $\sim$8 km (shown in cyan). The Λ and Δ^+ become present at densities of 465.9 and 486.3 MeV/fm^3 respectively, shown in green at a radius of $\sim$ 5 km. The particle species to appear is the Δ^{++}, at a density of 763.6 MeV/fm^3 and radius of $<$ 3 km shown in red. All particles would be present from the density they appear through to the star's center.

It is important to note here that neutrons, protons, electrons, and muons are additionally present within the stellar models discussed above but not shown explicitly in Figures 3.6 and 3.7.

3.4 Discussion and Conclusions

In Section 3.3.1, we extended the previous work of [177] and [181] that studied static and uniformly rotating stellar configurations of hyperonic and Δ-admixed stars to stellar models that support differential rotation. Specifically, we examined how the inclusion of Δ isobars in the EOS of dense matter impacts the corresponding stellar properties like mass and equatorial radius for non-vanishing differential rotations. Computation of stellar sequences using the RHF EOS models demonstrated that the inclusion of Δ's in hypernuclear EOS results in the reduction of the equatorial radius of the differentially rotating star and an increase in its maximum mass. These trends are consistent with analogous findings for uniformly rotating and static compact stars. An interesting finding is that when comparing the maximum masses from the highest degree of differential rotation (where the rotation parameter $\hat{A}^{-1} = 1.0$) to the lowest ($\hat{A}^{-1} = 0.3$), the magnitude of the increase in mass remained constant for all four EOS models considered. In particular, the inclusion of Δ's in the hypernuclear EOS does not change the total amount of mass increase once the differential rotation is allowed. In Section 3.2, density distribution maps of massive, differentially rotating stars were shown to demonstrate at what radial depth different particle species appear. The competition between the nucleation of Σ^- hyperon and Δ^- isobar was demonstrated, whose outcome depends on the value of the Δ^- potential in nuclear matter.

As mentioned in Section 3.2.2, the results shown in this chapter use a simple, linear rotation law (the so-called "j-constant law"), but other studies like Ref. [176] argue a more complex law is necessary to describe remnant stars following BNS mergers. While the implementation of other rotation laws is not explored in the context of this work, future work should explore if the same findings hold using hyperonic and Δ-admixed EOS models. Particularly, the specified rotation law may impact the emergence of Δ particles.

The stellar models presented in this chapter are constructed at zero temperature, which is standard for traditional neutron stars. In the next chapter, we explore how temperature impacts the structure and bulk properties of differentially rotating stars, and focus on more deformed stellar configurations.

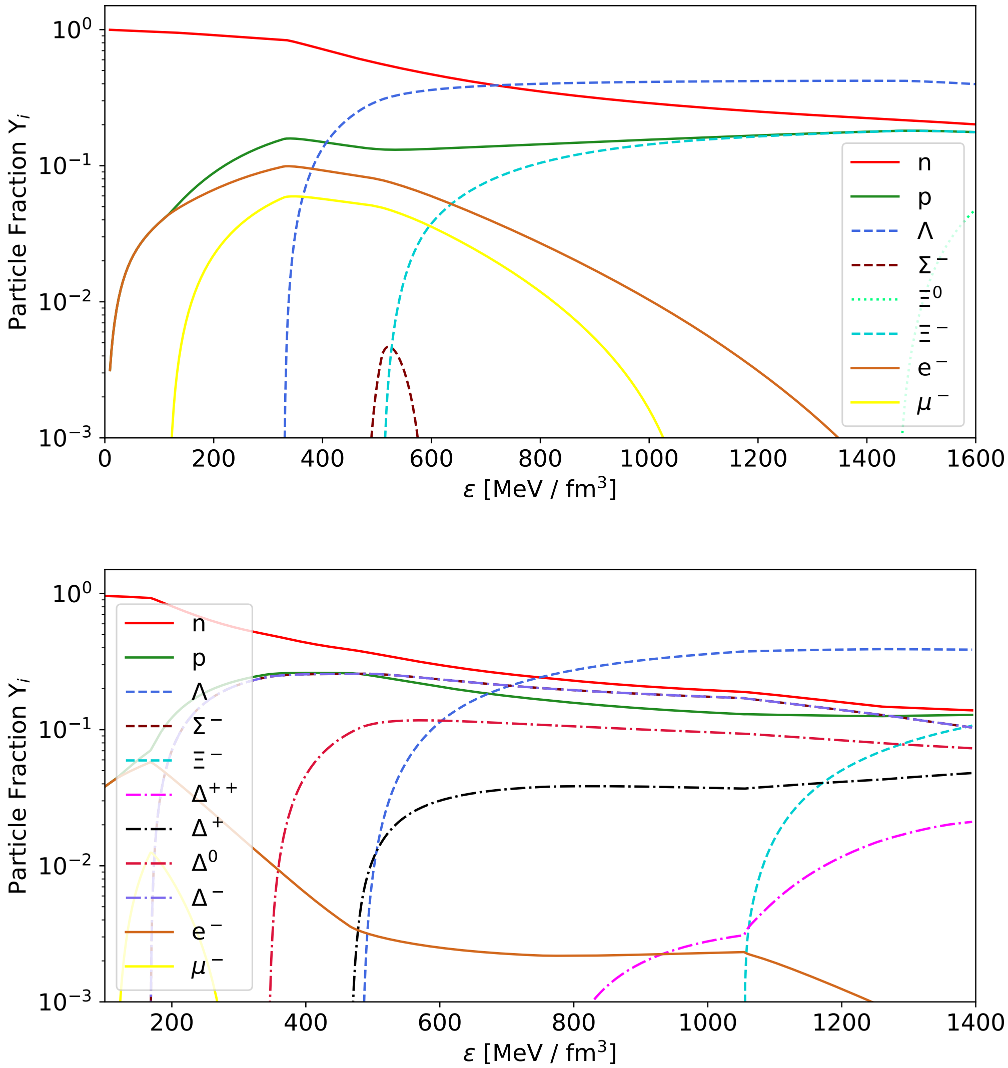

Figure 3.5: Relative particle fractions Y$_i$ for the hypernuclear EOS npY (top panel) and the hyperon-Δ admixed EOS with a potential depth of 4/3 V$_\mathrm{N}$ (bottom panel).

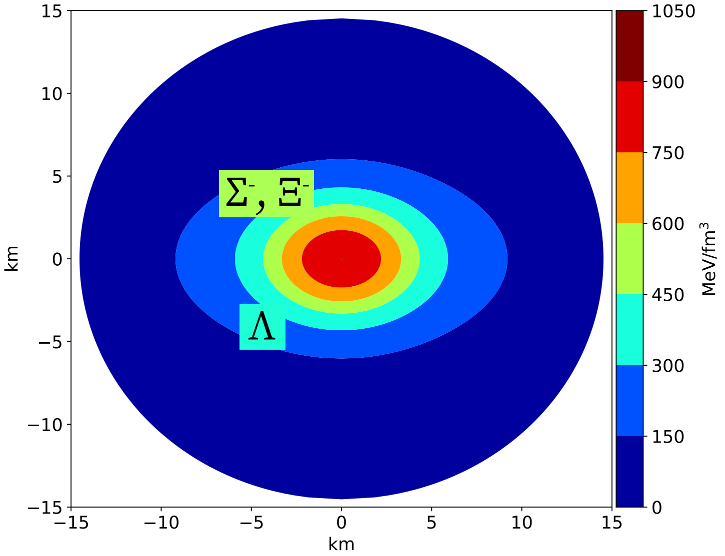

Figure 3.6: Energy density map of a 2.48 $M_\odot$ differentially rotating star constructed with hyperonic EOS npY. The star has an $r_{ratio} = 0.6$ and rotation parameter $\hat{A}^{-1} = 0.7$.

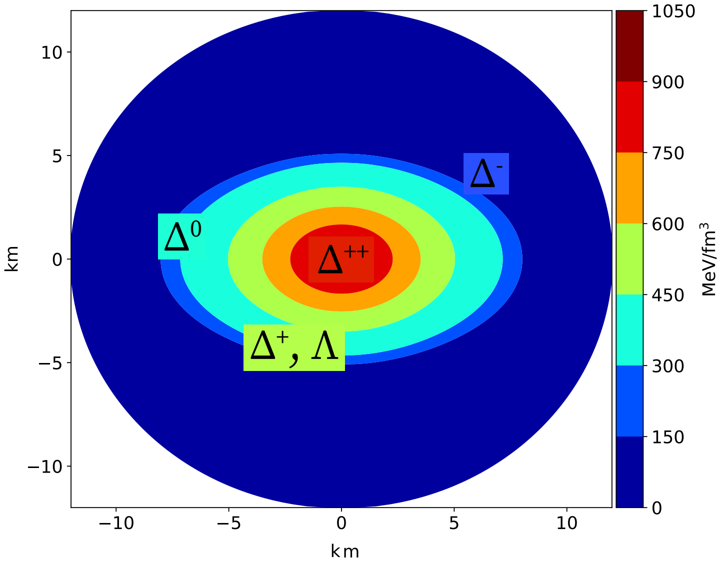

Figure 3.7: Energy density map of a 2.55 $M_\odot$ differentially rotating star constructed with hyperon-Δ admixed EOS with a potential depth of 4/3 V_N. The star has an $r_{ratio} = 0.6$ and rotation parameter $\hat{A}^{-1} = 0.7$.

Chapter 4

Differential Rotation in Hot, Hypermassive Stars

4.1 Introduction

The coalescence of two of the densest objects in the Universe, a binary neutron star (BNS) merger, is a volatile event. If the resulting remnant star does not promptly collapse into a black hole, it may take the form of a hypermassive neutron star. This hypermassive remnant would be very hot (up to 100 MeV) and is likely to find equilibrium by distributing the angular momentum from the collision differentially rather than uniformly. The thermal pressure and differential rotation stabilize these stars in otherwise unstable physical configurations on short, dynamical timescales.

Up to now, this thesis has independently explored features found in a hot, hypermassive neutron star remnant. In Chapter 2, models for the EOS of hot, superdense neutron star matter at varying temperatures were constructed using the RBHF formalism. In Chapter 3, the traditional numerical scheme for modeling differential rotation in neutron stars, "CST"

[104], was introduced and used to model differentially rotating objects at zero temperature. This chapter combines the ideas presented in the previous two chapters to numerically model hot, differentially rotating compact objects.

An important note discussed in Chapter 3 is the limitation of the traditional CST algorithm when constructing models for very deformed stars, as the original algorithm assumes the densest portion of the star is at the center. While the CST algorithm was shown to produce deformed stars at zero temperature in the previous chapter, modeling stars that take a quasi-toroidal or fully-toroidal shape is beyond the breadth of the traditional algorithm. This chapter modifies the traditional CST algorithm to allow for greater physical deformation and heavier stars.

This chapter is organized as follows: Section 4.2 discusses the mathematical and numerical modifications to the CST algorithm necessary to construct models where the maximum density is no longer at the center of the star. Section 4.3 shows results of differentially rotating stars constructed using the four EOS models constructed in Chapter 2. In this section, we show stellar sequences and individual stellar models while also discussing the stability of such models. Section 4.4 presents the summary and discussion of the work.

4.2 Modifications to the CST Algorithm

The theoretical framework for modeling differential rotation in neutron stars follows directly from the previous chapter, which assumes the density at the star's center is the maximum density throughout. However, this assumption limits the physical deformation possible, as shown in extreme configurations like (C) or (D) in Fig. 3.1. This section introduces a modification to the original CST algorithm to model stars whose maximum density is not at its center.

Stars that adopt a quasi- and fully-toroidal shape have a ratio of polar to equatorial radii within the star, r_{ratio}, that tends towards 0. Our implementation of the original CST algorithm becomes numerically unstable and thus fails to find solutions for small values of r_{ratio}; other implementations of the same algorithm discuss a similar issue, like those in Refs. [105, 182]. Specifically, Ref. [182] mentions that differentially rotating sequences can be split into two branches, one with the maximum density at the center of the star and spheroidal geometry, and one with an off-center location of the maximum density and quasi-toroidal shape. They argue the CST algorithm in its traditional form will generally fail to converge to a solution at values of r_{ratio} before mass shedding and, therefore, possibly before the maximum mass for a given configuration is reached [182]. The first branch of sequences described in Ref. [182] is representative of the (A) and (B) configurations in Fig. 3.1, where the maximum density occurs at the star's center. The second branch of sequences, where the maximum density is off-center, is representative of the (C) and (D) configurations in Fig. 3.1. As described in Section 3.2.2, the original CST algorithm therefore must be modified to achieve the second branch of sequences as described by Ref. [182].

As presented in the last chapter, the equation of hydrostatic equilibrium is given as:

$$h(P) - h_p = \frac{1}{2}\left[\gamma_p + \rho_p - \gamma - \rho - \ln(1 - v^2) + \hat{A}^2(\hat{\Omega} - \hat{\Omega}_c)^2\right], \tag{4.1}$$

which can be written in terms of the scaled metric potentials as:

$$h(P) - h_p = \frac{1}{2}\left[(\hat{\gamma}_p + \hat{\rho}_p - \hat{\gamma} - \hat{\rho})r_e^2 - \ln(1 - v^2) + \hat{A}^2(\hat{\Omega} - \hat{\Omega}_c)^2\right]. \tag{4.2}$$

In the original CST algorithm, this equation is evaluated at the maximum density of the star (i.e. the center) and rearranged to determine the radius at the equator of the star, r_e, defined as:

$$\bar{r}_e^2 = \frac{2[h(\bar{P}(\bar{\epsilon}_c)) - h_p]}{\hat{\gamma} + p + \hat{\rho}_p - \hat{\gamma}_m - \hat{\rho}_m}, \tag{4.3}$$

where the subscript m denotes the location of the maximum density of the star. The last two terms on the right side of Eq. (4.1) disappear as the velocity at the center of the star goes to 0 and $\hat{\Omega} = \hat{\Omega}_c$. If the assumption is instead that the densest regions of the star are not at the center, Eq. (4.3) must be redefined accordingly and the following updates are introduced to our algorithm.

In the updated version, the iterative process to solve for metric potentials is employed twice for each stellar model. The first run follows the original CST algorithm where r_e is determined using Eq. (4.3). Once convergence is reached, the coordinate values (s, μ) of the maximum density of the star are determined; this can be implemented succinctly using the built-in function `maxloc` in modern Fortran, or an equivalent argmax function. The coordinate values from the maximum density are then used to determine the corresponding maximum pressure, enthalpy, and scaled metric potentials $\hat{\gamma}$ and $\hat{\rho}$ (given as $\hat{\gamma}_m$ and $\hat{\rho}_m$). Resolving for r_e using Eq. (4.2) gives the following:

$$r_e^2 = \frac{2(h(P_m) - h_p) + \ln(1 - v_m^2) - \hat{A}^2(\hat{\Omega}_m - \hat{\Omega}_c)^2}{[\hat{\gamma}_p + \hat{\rho}_p - \hat{\gamma}_m - \hat{\rho}_m]}, \tag{4.4}$$

where the subscript m denotes the quantity's value at the coordinates of the maximum density. When using Eq. (4.4) instead of Eq. (3.20) to update r_e, the program is no longer restricted to the assumption that the maximum density is at the center of the star. The iterative process to determine values for the metric potentials is employed for a second time using these substitutions, and these values are then used to calculate the bulk properties of the star.

The final modification to our implementation of the original CST algorithm is regarding the root-finding methods used to determine the angular frequency Ω. In the previous chapter, Brent's method is used to determine the rotational frequency at the equator Ω_e, which subsequently is used to determine its value at the center Ω_c. As r_{ratio} becomes small, finding the supposed window containing the root using Brent's method becomes increasingly difficult, so we found it to be more numerically stable to instead solve for Ω_e and Ω_c simultaneously using the Levenberg-Marquardt algorithm. Brent's method is still however employed to find the matrix values of the full rotational frequency Ω.

4.3 Results for Maximum Density not at the Center of the Star

Results in this section use the above substitutions, and we present stable solutions for more extreme configurations of differentially rotating stars. The stellar models constructed with the modified CST algorithm use the finite temperature EOS models from Chapter 2 to model hot, hypermassive neutron stars. Because the updated method used in this chapter allows for a wider range of r_{ratio} values, we present results that examine how this parameter impacts the mass for each EOS.

4.3.1 EOS Models using Relativistic Brueckner-Hartree-Fock (RBHF) Theory

In this section, EOS models constructed using the RBHF formalism at finite temperatures are used as an input to construct differentially rotating stellar models. The inclusion of finite temperatures into the EOS more accurately depicts a remnant star following a BNS merger, and temperature likely plays an important role in the stability of the remnant. As discussed in Chapter 1, lone neutron stars (or those in binary systems before coalescence) are relatively cold; neutron stars are considered to be zero temperature on the nuclear scale, or less than 10^{10} K. A quasi-stable hypermassive neutron star remnant, however, would be incredibly hot - on the order of several hundred billion degrees or up to 100 MeV [183]. Because temperature adds to the complex calculations required to derive a nuclear EOS model, most EOS models are constructed at zero temperature. As shown in Chapter 2, the inclusion of temperature complicates the treatment of nucleons and the many-body system when calculating pressure and density. Due to the restricted number of publicly available and constraint-fulfilling finite-temperature EOS models, many simulations of binary neutron star mergers and remnant stars used a "hybrid-EOS", where a cold, zero-temperature EOS model is combined with a thermal contribution [183]. The thermal contribution obeys an ideal fluid and is parameterized in terms of a simple adiabatic index assumed to be constant [165]. Unfortunately, this treatment of the adiabatic index does not accurately describe the behavior of nuclear matter at finite temperatures [184]. In Chapter 2, nuclear many-body calculations were carried out at finite temperatures in a self-consistent fashion using the RBHF formalism, which more accurately describes hot nuclear matter than hybrid-EOS models. We use the EOS models from Chapter 2 as input to the differential rotation scheme to construct models of hot, differentially rotating neutron stars.

4.3.2 Stellar Sequences Varying the Ratio of Polar to Equatorial Radius

In the previous chapter, stellar sequences over a range of central density values were constructed with a fixed rotation parameter $\hat{A}^{-1}$ and fixed r_{ratio}. When assuming the maximum density of the star is no longer in the center, more extreme configurations with lower values of r_{ratio} can be calculated. Results are presented in this section for a range of r_{ratio} values to demonstrate the parameter's impact on the maximum mass for a given EOS.

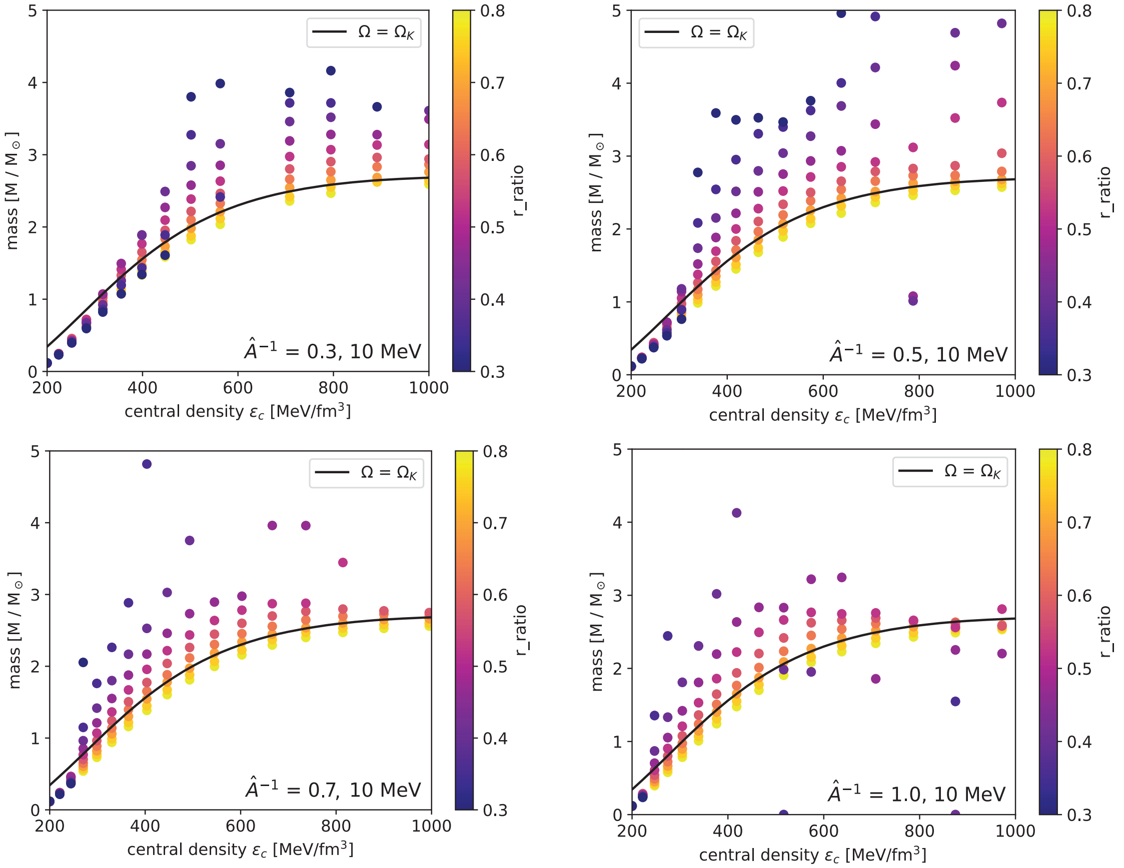

Figure 4.1: Mass vs. central density of differentially rotating neutron stars constructed using the EOS model from the Bonn B potential at $T = 10$ MeV. The four panes show values for four instances of the rotation parameter $\hat{A}^{-1}$ for a range of r_{ratio} values.

Table 4.1: The ratio of polar to equatorial radii, r_{ratio}, corresponding to the uniformly rotating maximum mass of the four finite temperature EOS models constructed with the Bonn B potential.

EOS	$r_{\text{ratio}} = r_p/r_e$
$T = 10$ MeV	0.739
$T = 30$ MeV	0.740
$T = 50$ MeV	0.739
$T = 70$ MeV	0.752

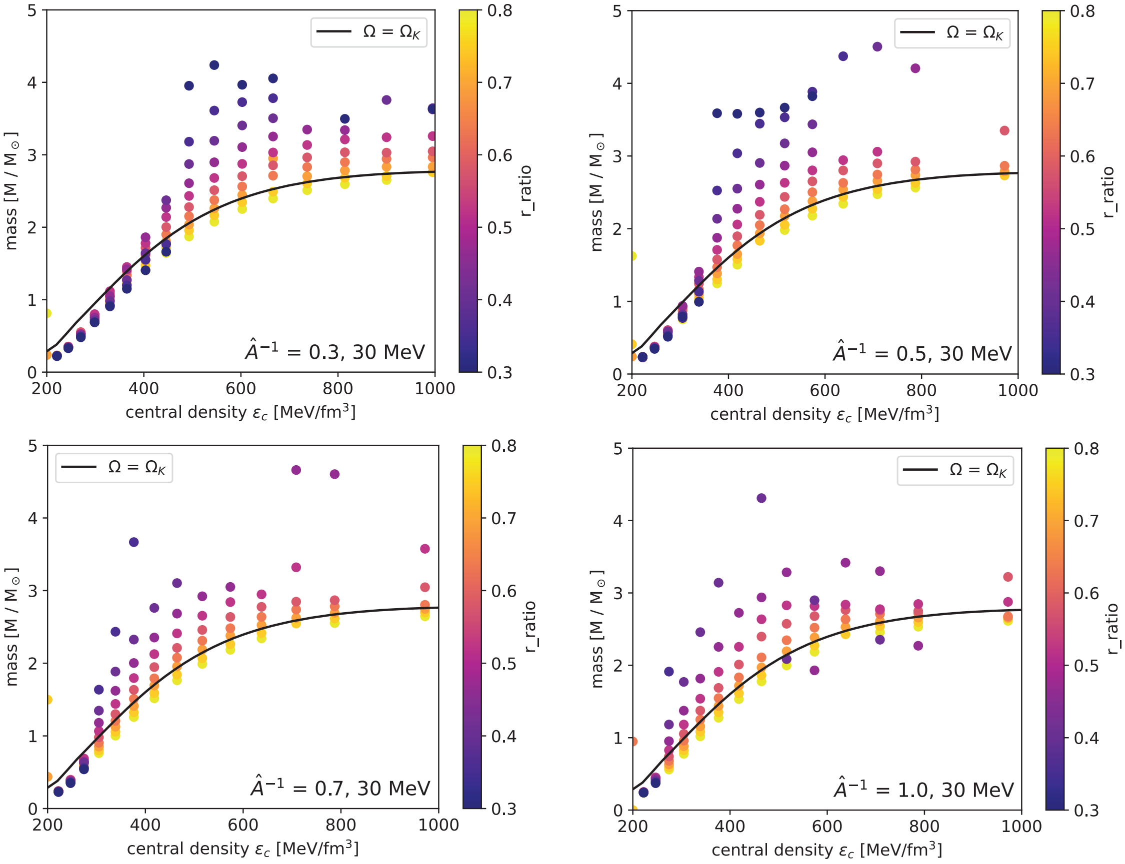

Figure 4.2: Mass vs. central density of differentially rotating neutron stars constructed using the EOS model from the Bonn B potential at $T = 30$ MeV. The four panes show values for four instances of the rotation parameter $\hat{A}^{-1}$ for a range of r_{ratio} values.

In Chapter 2, four EOS models at temperatures of 10, 30, 50, and 70 MeV are used to determine mass values for non-rotating stars and for stars uniformly rotating at their Kepler frequencies. The uniformly rotating stars exhibit some level of structural deformation, which can be observed by calculating the ratio of polar to equatorial radii in the star ($r_{\rm ratio}$). For the four EOS models, the corresponding $r_{\rm ratio}$ values at the mass peak for uniform rotation are given in Table 4.1; the maximum mass at each of the four temperatures exhibits an average $r_{\rm ratio}$ of 0.7425.

When using the modifications to the CST algorithm described in Section 4.2, a wider range of $r_{\rm ratio}$ can be used. While Chapter 3 presented stellar sequences for a given EOS over a range of central densities, this chapter will present results over both a range of central densities and a range of $r_{\rm ratio}$ values. Specifically, sequences over a range of central densities are calculated at varying values of $r_{\rm ratio}$, where only the rotation parameter $\hat{A}^{-1}$ is kept constant. For each EOS model at a given temperature, we provide stellar sequences of this form for four degrees of differential rotation that follow directly from the previous chapter: $\hat{A}^{-1} = 0.3$, 0.5, 0.7, and 1.0. For the EOS model with temperature $T = 10$ MeV, the resulting stellar sequences are shown in Fig. 4.1, $T = 30$ MeV are shown in Fig. 4.2, $T = 50$ MeV are shown in Fig. 4.3, and $T = 70$ MeV are shown in Fig. 4.4. For all four temperatures, the general trend follows that more extreme differential rotation ($\hat{A}^{-1} \to 1.0$) paired with more extreme structural deformation ($r_{\rm ratio} \to 0.0$) results in higher masses at lower central densities, which then taper off to the Kepler limit at higher central densities. This trend is also encountered in Ref. [105], who make similar modifications to the original CST algorithm. Additionally, the stellar models computed with $r_{\rm ratio}$ similar to the $r_{\rm ratio}$ values seen in uniform rotation closely follow the Kepler curve, indicating that even high levels of differential rotation may have less of an impact on the mass of the system when compared to the overall structure of the star.

At higher temperatures (i.e. $T = 50$ and 70 MeV), the numerical scheme fails to find stable solutions at high central densities, usually over 700 MeV/fm^3. One explanation for this phenomenon is the linking of a finite temperature EOS for the dense regions of the star to a zero-temperature EOS for the crust. The numerical scheme requires a full EOS as an input, meaning a model for the crust must be added to the high-density portion of the EOS. As mentioned in Chapter 2, the conventionally used EOS models for the inner and outer crusts are all constructed at zero temperature. Results in this chapter, as well as the previous chapter, use BPS+BBP for the crust. When including temperature in the full EOS, there exists a substantial discontinuity between the highest-density portion of the cold crust and the lowest-density region of the hot core, which grows as temperature increases and impacts the resulting bulk properties of the star. In Fig. 4.4 (at 70 MeV), calculated mass values dip below the Kepler curve at lower densities for low degrees of differential rotation, which is likely due to the different crust EOS models used for this chapter and in Chapter 2. This issue may be rectified by adding a thermal contribution to the EOS of the crust, but this is not conventionally done in the literature.

Alternatively, the lack of stellar models at higher central densities, shown in Figs. 4.3 and 4.4, could be because there exist no physical solutions for hot stars at those central densities.

4.3.3 Dynamical Bar-Mode Instability

The ratio of rotational (T) to gravitational (W) energy within the star $T/|W|$, referred to as the stability parameter, was introduced for uniformly rotating stars in Chapter 2. This parameter commonly appears as β throughout the literature. In this section, we explore how this parameter determines the stability of differentially rotating models against the dynamic bar-mode instability.

Rotating neutron stars formed from a CCSN or binary stellar merger may experience nonaxisymmetric instabilities that directly impact their rotation rate and overall stability. Previous

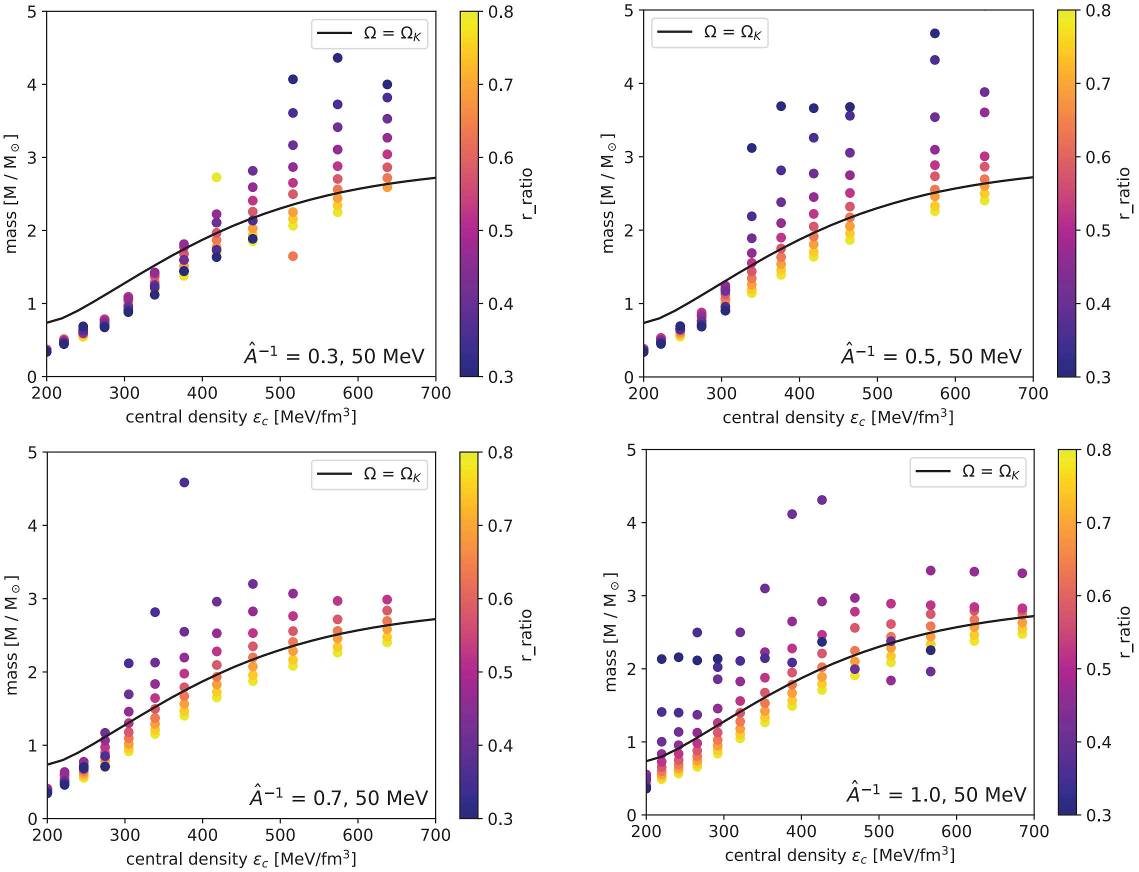

Figure 4.3: Mass vs. central density of differentially rotating neutron stars constructed using the EOS model from the Bonn B potential at $T = 50$ MeV. The four panes show values for four instances of the rotation parameter $\hat{A}^{-1}$ for a range of r_{ratio} values.

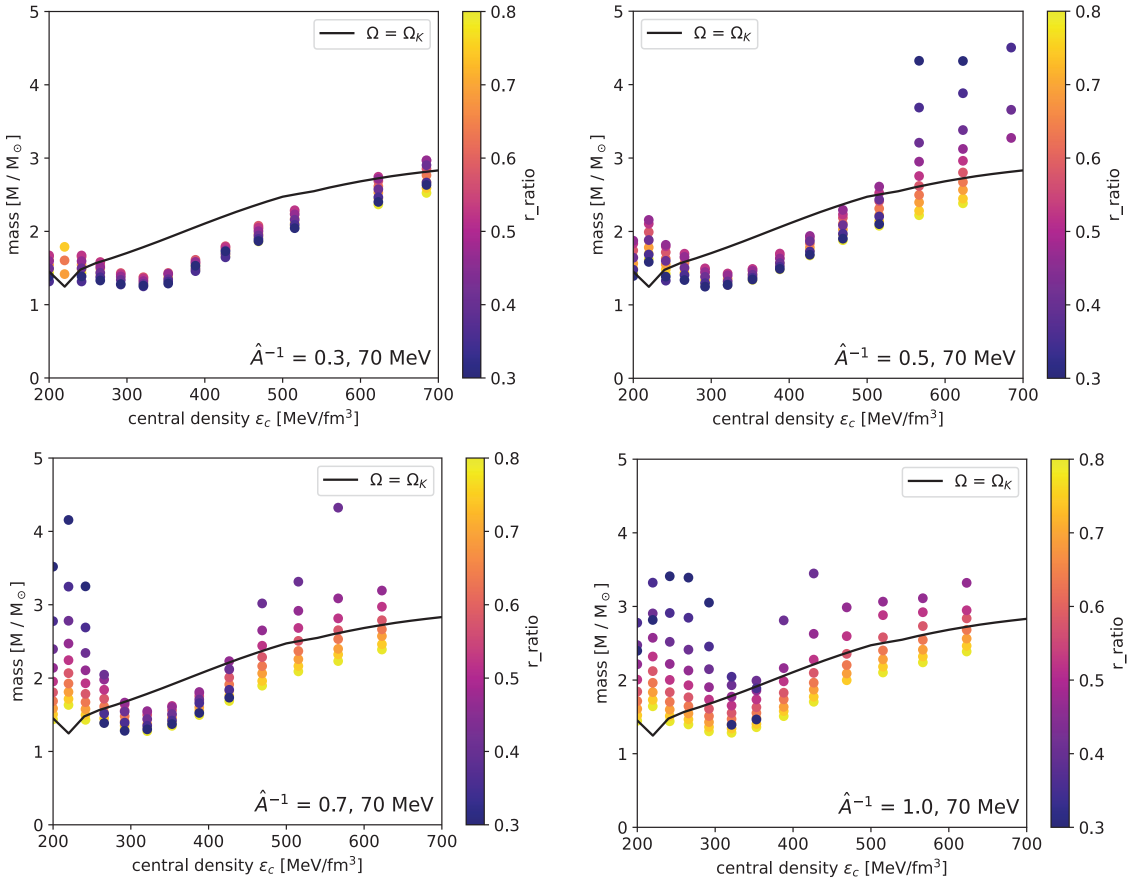

Figure 4.4: Mass vs. central density of differentially rotating neutron stars constructed using the EOS model from the Bonn B potential at $T = 70$ MeV. The four panes show values for four instances of the rotation parameter $\hat{A}^{-1}$ for a range of r_{ratio} values.

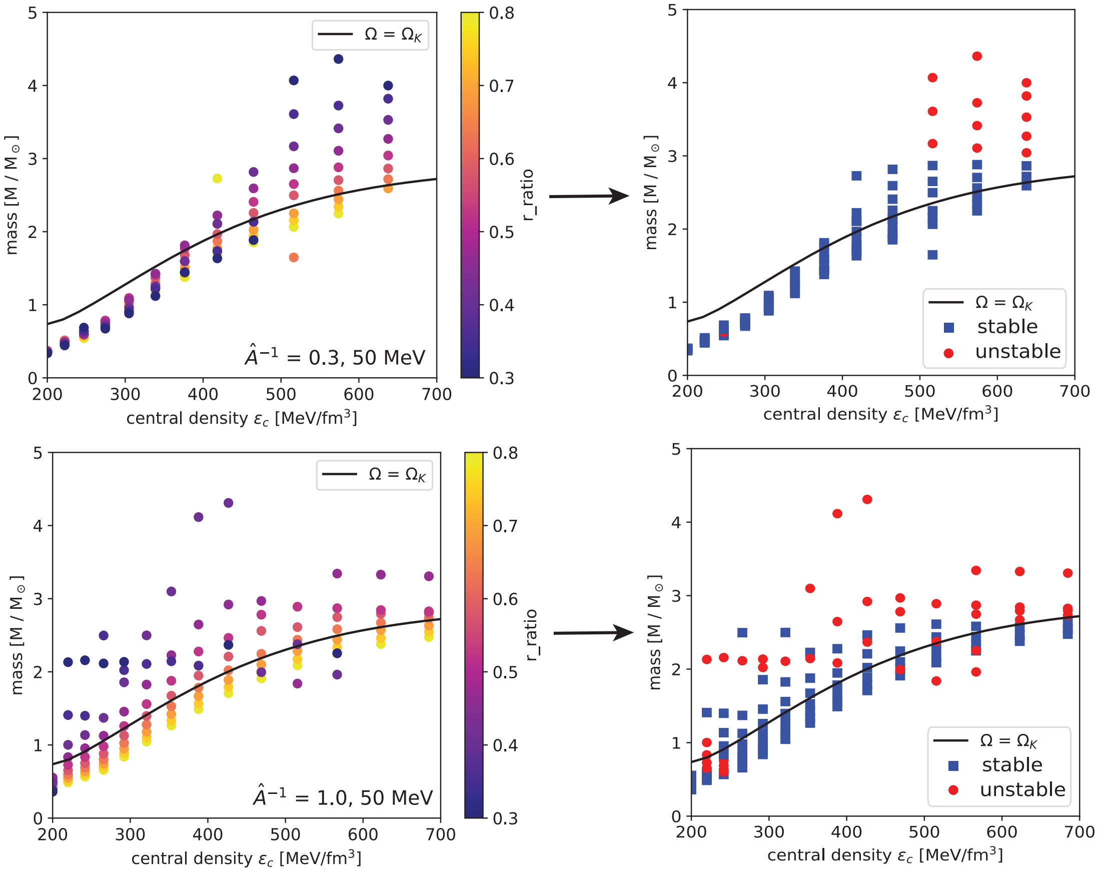

Figure 4.5: Mass vs. central density of for two cases of differential rotation ($\hat{A}^{-1} = 0.3$ for the top panes, $\hat{A}^{-1} = 1.0$ for the bottom) at $T = 50$ MeV. The left plots show mass vs. central density for various values of r_{ratio} as shown in Fig. 4.3, while the right plots show the same values color-coded based on their stability parameter $\beta = T/|W|$. Stars are deemed "unstable" if $\beta \geq 0.25$, see text for more details.

studies (see Refs. [185, 186]) in Newtonian gravity have shown rotational instabilities arise from non-radial toroidal modes, i.e. $e^{im\phi}$ $(m = \pm 1, 2, ...)$, which result in the stability parameter exceeding some critical value β_c. These rotational instabilities are likely to impact a star's gravitational radiation signal, making the study of such instabilities an important topic in the wake of new gravitational wave detectors. In this section, we will focus on the so-called bar-mode instability where $m = \pm 2$, which is expected to be the fastest-growing mode and the subject of many instability studies for both uniformly and differentially rotating neutron stars.

Two mechanisms cause rotating stars to be unstable to bar-mode deformation: secular and dynamical instabilities. In Newtonian theory, uniformly rotating incompressible neutron stars become secularly unstable to bar-mode deformation at a critical value $\beta_c \geq 0.14$ with similar findings in studies of post-Newtonian theories [187]. In general, the secular instability grows only in the presence of a small dissipative mechanism like viscosity or gravitational radiation at lower rotation rates [162]. The secular instability usually has a longer growth time when compared to the dynamic timescale of the system. A similar critical value of β_c has been observed in numerical studies of relativistic stars but is also dependent on the compaction (M/R) of the star and the dissipative mechanism. For example, viscosity-driven secular instability has been shown to occur at $\beta_c > 0.14$ in more compact configurations with higher rotation rates, but gravitational radiation-driven instabilities occur at $\beta_c < 0.14$ at lower rotation rates; a more in-depth review of this topic is given in Ref. [188].

The dynamical bar-mode instability occurs independent of any dissipative mechanism and with a growth rate determined by the dynamical timescale of the system, which is generally faster than the timescale of growth for secular instabilities. Therefore, numerical simulations of hydrodynamical equations are necessary to determine the onset threshold of the dynamical bar-mode instability. Many simulations have been carried out in Newtonian theory, the consensus of which gives the critical value $\beta_c \geq 0.27$ [189]. Simulations of the dynamical bar-mode instability in general relativity are less common, as solving the nonlinear hydrodynamical equations in full relativity is more complex. However, there have been reliable studies carried out by Refs. [189, 190] for uniformly rotating stars and Refs. [191–195] for differentially rotating stars.

The relativistic simulation of differentially rotating stars carried out in [194] finds that the critical value of the stability parameter for the dynamic bar-mode instability is $\beta_c \approx 0.24 - 0.25$, slightly lower than the Newtonian limit. These simulations were carried out using the same linear rotation law as in this chapter (and the proceeding one) for similar values of r_{ratio}. Therefore, we adhere to their specified threshold of β to determine whether differentially rotating stars are stable or unstable to the dynamical bar-mode deformation. Specifically, we use the upper limit for the critical threshold, so stars deemed unstable in this section will have a stability parameter $\beta_c \geq 0.25$.

A visual representation of stable and unstable models using this criterion at $T = 50$ MeV for two degrees of differential rotation is shown in Fig. 4.5. The two panels in each row show the same information, mass vs. central density for a range of r_{ratio} values, where the figures in the right column categorize each stellar model as stable with a blue square or unstable with a red dot. The top row presents a lesser degree of differential rotation ($\hat{A}^{-1} = 0.3$), where 81.6% of calculated stellar models are considered stable against dynamical bar-mode deformation. In contrast, the bottom row has the highest degree of differential rotation ($\hat{A}^{-1} = 1.0$), and the increase in differential rotation decreases the percentage of stable models to 67.2%. For both cases of differential rotation, the majority of the unstable configurations have small values for r_{ratio}, a trend that will be echoed in the next section.

Table 4.2 gives the percentage of unstable models and the average r_{ratio} of those unstable models for four degrees of differential rotation for each temperature: 10, 30, 50, and 70 MeV. The general trend appears to be as temperature increases, the percentage of unstable models decreases. However, this trend requires more context: the numerical scheme fails to

Table 4.2: The percentage of unstable models and the average $r_{\rm ratio}$, $\bar{r}_{\rm ratio}$, of unstable models for four degrees of differential rotation for each temperature EOS: 10, 30, 50, and 70 MeV.

EOS	$\hat{A}^{-1}$	% unstable	$\bar{r}_{\rm ratio}$
$T = 10$ MeV	0.3	23.2	0.47
	0.5	27.6	0.46
	0.7	25.5	0.51
	1.0	27.0	0.52
$T = 30$ MeV	0.3	27.4	0.50
	0.5	30.2	0.48
	0.7	30.5	0.50
	1.0	31.6	0.54
$T = 50$ MeV	0.3	18.4	0.43
	0.5	21.4	0.43
	0.7	21.7	0.49
	1.0	32.8	0.47
$T = 70$ MeV	0.3	1.7	0.49
	0.5	9.1	0.40
	0.7	9.7	0.43
	1.0	12.2	0.49

find solutions at high central densities for higher temperatures ($T = 50$ and 70 MeV), so the percentages may be skewed. A more important figure to look at is the average $r_{\rm ratio}$, $\bar{r}_{\rm ratio}$, of the unstable models. A small correlation could be made where $\bar{r}_{\rm ratio}$ decreases as temperature increases, but for all four temperatures, the average values generally tend to fall between 0.4 to 0.5. Stars with $r_{\rm ratio} \leq 0.5$ are extremely deformed and thus likely to be vulnerable to dynamical instabilities. These findings imply temperature plays little role when compared to the star's deformation on its stability against dynamical bar-mode excitation.

4.3.4 Structural Deformation

In this section, we examine density and frequency maps of individual stellar models at two temperatures, $T = 10$ MeV and $T = 50$ MeV. For each temperature, two models are computed: the first with a lesser degree of differential rotation ($\hat{A}^{-1} = 0.3$) and the second with a larger degree of differential rotation ($\hat{A}^{-1} = 1.0$). All four models are computed with an $r_{\mathrm{ratio}} = 0.4$, which is a significant degree of structural deformation. Information on the stars' masses, radii, and stability parameters are given in Table 4.3.

The density and frequency maps for $T = 10$ MeV are shown in Fig. 4.6, where the top row shows results for $\hat{A}^{-1} = 0.3$ and the bottom for $\hat{A}^{-1} = 1.0$. The lesser degree of differential rotation is shown very clearly in the frequency map, where the difference of frequency values in the star only spans 320 Hz. In contrast, the star with a higher degree of differential rotation sees a span of 5,600 Hz from the highest to lowest frequency values. The density maps show an interesting depiction of the overall structural deformation. For $\hat{A}^{-1} = 0.3$, the star takes an ellipsoid-like shape, but for $\hat{A}^{-1} = 1.0$, the star instead takes a quasi-toroidal shape, as was demonstrated schematically in Fig. 3.1. While each star was initialized with the same central density of 400 MeV/fm^3, the star with $\hat{A}^{-1} = 1.0$ experiences much higher densities outside of the center of the star. A similar story is seen for $T = 50$ MeV in Fig. 4.7 but with even higher densities observed at the higher temperature.

As shown in the previous section, the stability of the star depends not only on the deformation characterized by r_{ratio} but also on the degree of differential rotation. In Table 4.3, all four models have the same value of r_{ratio}. For both temperatures, the stars computed with $\hat{A}^{-1} = 0.3$ have stability parameters $T/|W|$ well below the critical limit of 0.25. However, the stars with $\hat{A}^{-1} = 1.0$ are well above the critical limit for β, where the stability parameter is 0.64 for $T = 10$ MeV and 0.75 for $T = 50$ MeV. These stars are well beyond the threshold for the dynamical bar-mode instability and thus likely unphysical.

The timescale over which the dynamical bar-mode instability develops, also known as the dynamical timescale, is proportional to $\mathrm{R}^{3/2}/\mathrm{M}^{1/2}$. While this is not a definite indication of the growth time of the instability, which would instead require a full simulation in both time and space (see Ref. [194] for a good example), for extremely unstable configurations the dynamical timescale can provide some idea of how long these stars may exist with the bar-mode instability excited before collapse. For the unstable configuration at $T = 10$ MeV,

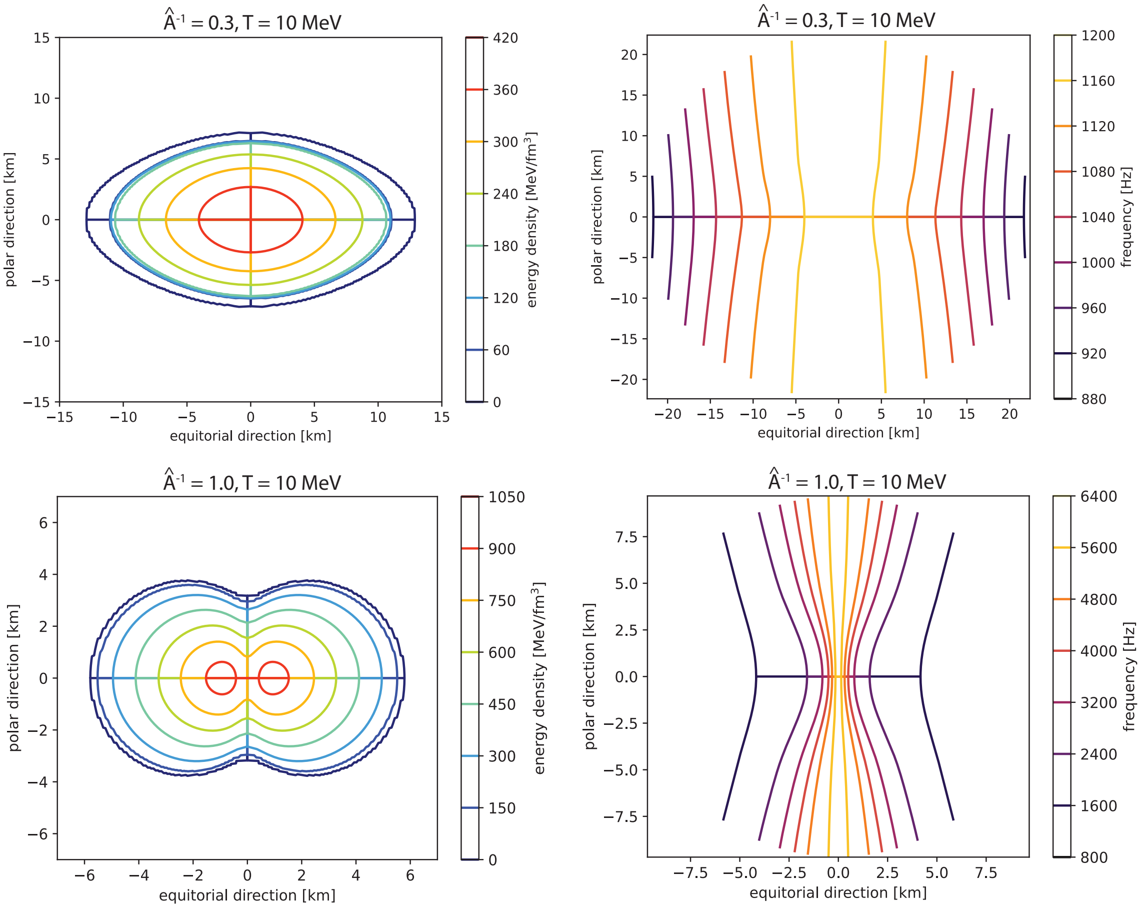

Figure 4.6: Energy density (left) and frequency (right) contours for individual stellar models at two degrees of differential rotation, constructed using the EOS model from the Bonn B potential at $T = 10$ MeV. The top row has a lower degree of differential rotation ($\hat{A}^{-1} = 0.3$) and the bottom has a higher degree ($\hat{A}^{-1} = 1.0$). The corresponding masses, radii, and stability parameters are given in Table 4.3.

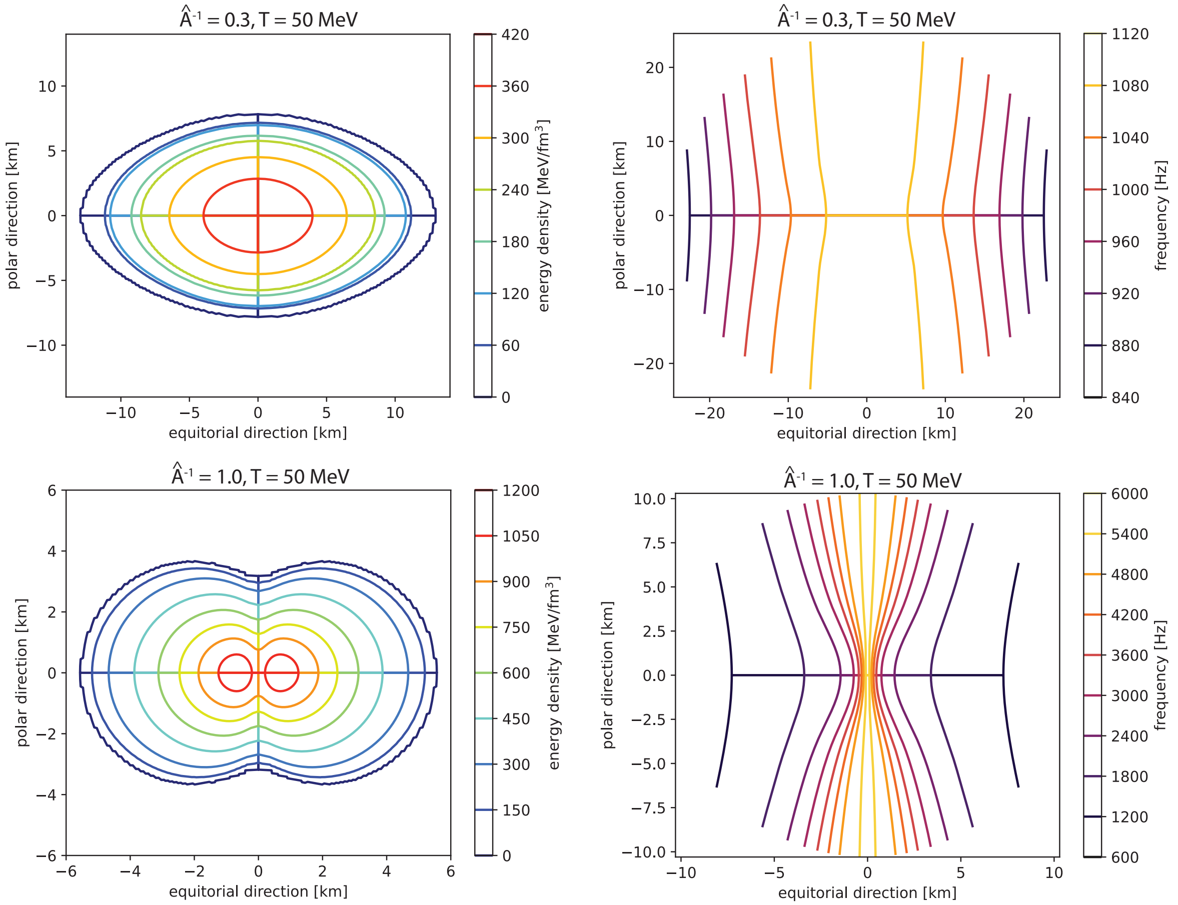

Figure 4.7: Energy density (left) and frequency (right) contours for individual stellar models at two degrees of differential rotation, constructed using the EOS model from the Bonn B potential at $T = 50$ MeV. The top row has a lower degree of differential rotation ($\hat{A}^{-1} = 0.3$) and the bottom has a higher degree ($\hat{A}^{-1} = 1.0$). The corresponding masses, radii, and stability parameters are given in Table 4.3.

Table 4.3: Bulk properties of highly deformed neutron stars, all with $r_{\text{ratio}} = 0.4$, at two temperatures: 10 MeV and 50 MeV. For both temperatures, results are presented for a small degree of differential rotation ($\hat{A}^{-1} = 0.3$) and a large degree of differential rotation ($\hat{A}^{-1} = 1.0$). Calculated properties include the gravitational mass M_G, baryonic mass M_B, equatorial radius r_e, polar radius r_p, the ratio of central to equatorial frequency Ω_c/Ω_e, and stability parameter $T/|W|$. The $T = 10$ MeV entries correspond to Fig. 4.6 and the $T = 50$ MeV entries correspond to Fig. 4.7; see text for more details.

EOS	$\hat{A}^{-1}$	r_{ratio}	M_G ($\text{M}_\odot$)	M_B ($\text{M}_\odot$)	r_e (km)	r_p (km)	Ω_c/Ω_e	$T/\|W\|$
$T = 10$ MeV	0.3	0.4	1.69	1.84	20.41	8,16	1.13	0.01
	1.0	0.4	1.91	2.61	12.94	5.18	5.88	0.63
$T = 50$ MeV	0.3	0.4	1.78	1.93	22.25	8.90	1.13	0.01
	1.0	0.4	2.08	2.84	13.65	5.19	5.95	0.75

the dynamical timescale is $\propto$ 35.8 seconds, and for the unstable configuration at $T = 50$ MeV, the dynamical timescale is $\propto$ 34.9 seconds.

4.4 Discussion and Conclusions

In this chapter, we present results that differ from the previous chapter in two ways. The first is that the numerical scheme is modified to allow for more deformed stars, by changing the criteria previously in place where the central density of the star was its maximum. The second differentiation comes from the type of EOS models used as input to the numerical scheme that models differential rotation. In this chapter, we use the finite temperature EOS models constructed from the RBHF formalism as described in Chapter 2, where the temperatures span 10, 30, 50, and 70 MeV. The inclusion of temperature is pertinent to the realistic modeling of extreme astrophysical events where differential rotation may occur like BNS mergers or core-collapse supernovae.

The modifications to the numerical scheme allow for solutions in a wider range of r_{ratio} values, or the ratio between the polar and equatorial radius of the star. In Section 4.3.2, we calculate stellar sequences with varying r_{ratio} values (0.8 to 0.3) over a range of central densities for all four finite temperature EOS models. The general trend echos what has previously been shown in literature at zero temperature, where a higher degree of differential rotation ($\hat{A}^{-1} \to 1.0$) results in higher mass stars at lower central densities when compared to lower values of $\hat{A}^{-1}$, especially as r_{ratio} decreases. For all four temperatures, the numerical scheme struggled to find physical solutions as $\hat{A}^{-1}$ increased and r_{ratio} decreased, especially at higher densities. This was especially true for $T = 50$ MeV and 70 MeV, where no solutions were found beyond a central density of 700 MeV/fm^3.

The calculated stellar models' stability against rotational instabilities, specifically the dynamical bar-mode instability, is explored in Section 4.3.3. At a temperature of 10 MeV, the average r_{ratio} value of stars unstable against dynamical bar-mode excitement is 0.49, for 30 MeV the average is 0.50, for 50 MeV the average is 0.455, and for 70 MeV the average is 0.452. The results presented in this section emphasize that the deformation, characterized r_{ratio}, has a greater impact on the star's stability than temperature against dynamical instabilities.

Finally, individual stellar maps of density and frequency distributions were shown in Section 4.3.4 for two temperatures, 10 and 50 MeV, and two degrees of differential rotation. As expected, the frequency range for higher degrees of differential rotation (and higher values of $\hat{A}^{-1}$) was much wider. Higher values of $\hat{A}^{-1}$ also resulted in a shift in the overall shape of the star, from ellipsoid to quasi-toroidal. However, the two quasi-toroidal models computed had stability parameters well beyond the critical limit of 0.25, making them unstable to the bar-mode instability and likely unphysical configurations.

In the next chapter, we turn our attention back to the inference of the EOS of neutron star matter. Instead of theoretical modeling as done in Chapter 2, we implement novel numerical techniques using machine learning to decipher a link between the observation of neutron stars and the underlying EOS.

Chapter 5

Equation of State Inference from Simulated X-ray Spectra using Machine Learning

This chapter presents text and results from previously published work (Ref. [10]) in collaboration with Pierre Baldi, Jordan Ott, Aishik Ghosh, Andrew W. Steiner, Atharva Kavitkar, Lee Lindblom, Daniel Whiteson, and Fridolin Weber.

5.1 Introduction

While the work presented thus far has focused on modeling neutron star matter theoretically and, in turn, determining macroscopic properties, the next chapters instead explore the inference of the equation of state (EOS) from simulated observable neutron star data. Previous chapters have given the mathematical framework where the EOS of a star in static gravitational equilibrium determines stellar properties such as its mass and radius. These

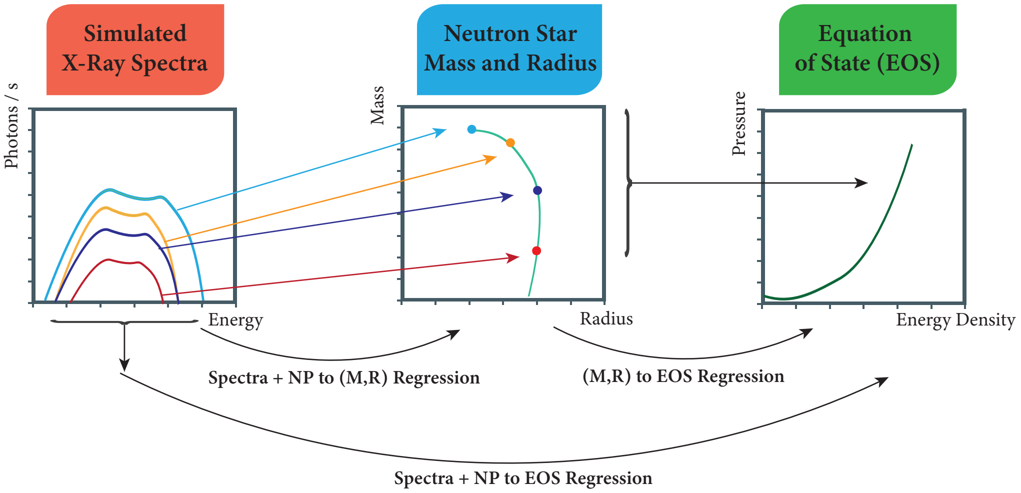

Figure 5.1: Overview of the regression task, which involves either inferring stellar summary quantities such as mass and radius, which can then be used to deduce the equation of state as in earlier work [6–9] or inference of EOS directly from stellar spectra, as is demonstrated in this study.

same properties can also be determined from thermal, X-ray, or gravitational wave emission of neutron stars; for the context of this work, we will focus on X-ray emission. Spectral emission can therefore, in principle, allow inference of the EOS from inference of mass and radius, which has been demonstrated in the literature [113–118], though inversion of this second step is numerically very difficult. Additional challenges are due to the small number of neutron star observations, $\mathcal{O}(10)$, and the significant uncertainty of individual measurements. It is therefore vital that as much information as possible is extracted from each star, and that the uncertainties be propagated accurately, to provide the most complete information possible about the EOS.

While traditional inference methods include statistical methods like Bayesian inference, other numerical methods can be well-suited for this task. In recent years, there has recently been a dramatic burst of progress in artificial intelligence, specifically deep learning [132], a modern re-branding of neural networks. This progress has led to breakthroughs not only in traditional areas such as natural language processing and computer vision but also in the natural sciences, including particle physics, often increasing the statistical power of difficult-to-collect data [133] while allowing robust handling of uncertainties [134]. Where earlier neural networks were limited in size, computing progress, especially in the form of Graphical Processing Units (GPUs), has enabled the deployment of larger and deeper networks that can handle more complex and higher-dimensional data [135, 136], allowing direct analysis of data without requiring dimensional reduction, or other preprocessing steps, that can often sacrifice useful information. The full power of these techniques has not yet been brought to bear on many astrophysical tasks.

In the context of the inference of neutron star EOS, recent work by Fujimoto *et al.* [6, 7] demonstrated the ability of deep networks to regress the EOS directly from a set of stellar mass-radius pairs, without the need to extract the functional relationship between mass and radius. Their analysis used a toy model to describe the uncertainties in mass and radius, assuming uncorrelated Gaussian errors randomly drawn from ad-hoc priors. Real measurements, of course, do not often obey these simplifying assumptions, and show complex correlations between mass and radius [196]. Related work [8] has demonstrated similar regression, again assuming Gaussian uncertainty on mass and radius values, but with clever efforts to reduce dependence on EOS parameterization. An alternative approach [9] uses both neural networks and support vector machines to regress the EOS from stellar radii and tidal deformations.

More realistic characterization of the uncertainties in the mass-radius plane can be extracted using the state-of-the-art tool XSPEC [197], which assumes a theoretical model for the star and telescope response, allowing for explicit calculation of the likelihood of X-ray telescope spectra for various mass and radius values. The likelihood can be used in the standard way to extract the best estimates and uncertainty contours of any shape in the mass-radius plane. However, these complex mass-radius likelihoods cannot be trivially incorporated into the existing EOS inference schemes, motivating the simplifying assumptions of uncorrelation normal distributions which can be described by two width values. An additional concern is that XSPEC's contours rely on the simplifying assumptions of the theoretical model.

What has received less attention in the literature are likelihood-free methods to infer the EOS directly from the telescope spectra, without the intermediate stepping stone of the mass-radius determination and the challenges of its representation. This would allow for the full propagation of realistic uncertainties and the relaxation of assumptions about the theoretical model.

In this chapter, a technique of EOS inference that allows for the full propagation of the uncertainties in the X-ray spectra is presented, without making simplifying assumptions about the shape of the contours in the mass-radius plane. The work presented in this chapter follows directly from Ref. [10]. We proceed in three steps, beginning from an approach similar to the state of the art but with realistic uncertainty propagation, and moving towards end-to-end inference. In the first step, our neural network model infers the neutron star EOS from a set of stellar masses and radii extracted from XSPEC, but rather than making simplifying assumptions of extracting uncertainty contours from XSPEC, we vary the assumed nuisance parameters (NPs) which are the source of the uncertainty to produce new best-estimate mass-radius points. The EOS inference can then be performed on many sets, each corresponding to varied NP values, producing a variation in the inferred which represents the propagated uncertainty. In the second step, we investigate a more flexible method of inferring the mass and radius that does not explicitly rely on XSPEC's specific theoretical model. We introduce a network capable of directly analyzing high-dimensional neutron star spectra, performing inference of stellar mass and radii from telescope spectra, a demonstration of the impressive capacity of modern deep networks. Finally, we perform a first-of-its-kind inference of the EOS parameters directly from a multi-star *set* of stellar spectra, without requiring the intermediate step of collapsing the information into mass and radius; see Figure 5.1. In both cases, we allow for full propagation of uncertainties by conditioning the networks on the stellar nuisance parameters. As this is – to our knowledge – the first attempt at full propagation of these uncertainties for this task, there are no direct benchmarks in prior work. Instead, we show comparisons between our three methods and visualize the impact on the EOS inference of variation of the nuisance parameters for a fixed X-ray spectrum.

The chapter is organized as follows. In Section 5.2, the background on the physics of the connection between the nuclear equation of state and the stellar observations is given. Section 5.3 describes the fundamentals of the machine learning concepts on which our studies rely. Details of the samples of simulated data are given in Section 5.4. Section 5.5 demonstrates inference of the EOS parameters from mass and radius, while Section 5.6 describes how mass and radius parameters can be inferred directly from stellar spectra, and Section 5.7 shows end-to-end inference of EOS parameters from a set of neutron star spectra.

5.2 Background

The theoretical connection between the EOS of dense matter and the mass and radius of neutron stars is discussed extensively in previous chapters. For non-rotating stars, numerically solving the TOV equations (Eqs. 2.67 and 2.68) for M and R is straightforward given an EOS. These equations create a one-to-one map from the EOS to the $M-R$ relation [118]; the inverse form of this map can therefore provide constraints on the EOS from observable properties. To mathematically invert the TOV equation, at least two stars' mass and radius must be known exactly, a feat that is not possible with current observational technology. Solving the inverse problem is therefore much more complicated, potentially even intractable without making significant numerical assumptions.

5.2.1 X-Ray Spectroscopy for Neutron Stars

Many reliable observations of neutron stars come from X-ray emission, either from electromagnetic radiation from pulsars or thermal emission in quiescent low-mass X-ray binaries (qLMXBs). qLMXBs are particularly desirable to place strong constraints on neutron star structure as they are likely to have low magnetic fields (10^{8-9} G), resulting in minimal effects on the radiation transport or temperature distribution on the star's surface [196, 198, 199]. Additionally, these binaries are identified in globular clusters where distances, ages, and reddening are well-constrained [200]. The distinctive soft thermal spectra from these sources come from a long-lived thermal glow resulting from heat stored in the deep crust of the neutron stars within the binary system during accretion, which is then re-radiated from the whole surface when accretion stops [201]. For the context of this work, the inference of EOS will come from simulated thermal spectra from qLMXBs.

Observation of neutron star emission, whether X-ray or gravitational wave, has long served as a way to constrain mass and radius for neutron stars (eg. [202, 203]), but uncertainties arise in the inference of these properties for a variety of reasons. In the case of X-ray radiation from qLMXBs, constraints on mass and radius are determined by fitting the emitted spectrum with an appropriate atmosphere model (where the surface composition is known or can be determined by the X-ray spectrum) and combining the spectroscopic measurements with the distance of the source. Models for thermal X-ray radiation are based on a light-element atmosphere, as the lightest element that is present in the atmosphere floats to the top due to rapid gravitational settling on neutron star surfaces [196]. Atmospheric models used on X-ray spectra from qLMXBs gave the first broad constraints on neutron star radius, and more modern analyses of X-ray spectra have provided tighter constraints on both radius and EOS.

The high-resolution imaging and spectroscopy of NASA's *Chandra X-ray Observatory* have provided powerful insight into neutron star properties like cooling [204, 205], mass and radius [196], and binary mergers of exotic stars [206]. *Chandra*'s telescope contains a system of four pairs of mirrors that focus incoming X-ray photons to the Advanced CCD Imaging Spectrometer (ACIS), which measures the energy of each incoming X-ray. The observed spectrum, along with a corresponding instrument response, is then fit to a well-motivated parameterized model. Many such models for spectral fitting exist in XSPEC [197], an X-ray spectral fitting package distributed and maintained by the aegis of the GSFC High Energy Astrophysics Science Archival Research Center (HEASARC). These parameterized models differ for different types of X-ray sources, as well as assumptions about the source's atmosphere, magnetic field, and temperature (a full list of models can be found in the XSPEC manual [197]). XSPEC has been used numerous times in the past to analyze data from *Chandra* as well as other spectrometers like *NICER*, *Nustar*, and *XMM-Newton*, making it a valuable resource for inference of neutron star properties.

5.3 Machine Learning

Machine learning methods, in particular deep learning, aim to extract useful knowledge from data automatically and are rapidly being applied across many data-rich fields of science [132]. In regression tasks such as EOS inference, one is interested in constructing a function f whose inputs are the observed data and whose outputs are an estimate of some parameter of interest. The optimal function f is not known initially, but an approximation can be learned from a set of input-output example pairs.

To approximate f, machine learning methods first begin with a suitable class C of parameterized functions (e.g. polynomials of a certain degree, neural networks of a certain architecture) and then seek to find the best approximation to f within the class C. This is typically done through a stochastic gradient descent procedure that seeks to iteratively minimize the approximation error on the training set.

The well-known technique of linear regression is the most elementary form of regression and can be viewed as a form of shallow learning (no hidden layers). Deep learning generalizes linear regression by using multi-layer neural networks as the class C thus enabling the construction of sophisticated and flexible non-linear approximations. With sufficient training data and computing power, deep learning methods can handle large-scale problems with high-dimensional data and avoid heuristic simplifications that lose information. It is not uncommon to deal with problems with input sizes in the range of up to 10^9 examples, each with dimensions of 10^{3-4}, with neural networks that can have up to 10^{11} free parameters. Training sets can range in size from 10^1 to 10^{10} or more. Unlike shallow learning and linear regression, deep learning does not require that the number of parameters be equal to the number of training examples [207]. More recent, attention-based architectures, such as transformers [208, 209], allow networks to take advantage of structures and symmetries in the data and are applied in the sections below.

When the interpretation of data depends on external unmeasured or poorly-known parameters, such as neutron star temperature or distance, it can be useful to apply *parameterized networks* [135]. Such networks learn a task as a function of the external parameter, allowing for the evaluation of a fixed dataset under varying assumptions about the parameter [134].

5.4 Training Samples

Samples of simulated neutron stars, used to train networks and evaluate their performance, are described below.

Each simulated star is described by two high-level summary quantities, the mass and radius, which are drawn from the mass-radius relation determined by the EOS, as well as three nuisance parameters that are independent of the EOS and can vary from star to star. These five parameters are sufficient to determine the expected simulated Chandra telescope spectrum in the chosen neutron star theoretical model. In the case of EOS inference, sets of stars with consistent EOS are grouped to form training and testing sets. Details of each step of the generation are provided below.

5.4.1 Equation of State

The equation of state of the hadronic matter within the core is modeled with the relativistic non-linear mean field model GM1L [11]. The version used here only accounts for protons and neutrons but can be extended to include hyperons and Δ baryons [210]. The corresponding saturation properties of symmetric nuclear matter for the GM1L parametrization are shown in Table 5.1 [210, 211]. These properties include the nuclear saturation density n_0, energy per nucleon E_0, nuclear compressibility K_0, effective nucleon mass m_N^*/m_N, asymmetry energy J, asymmetry energy slope L_0, and the value of the nucleon potential U_N. The value of L_0 listed in Table 5.1 is in agreement with the value of the slope of the symmetry energy deduced from nuclear experiments and astrophysical observations [212].

The most commonly used constraints on K_0 come from experimental values of the giant monopole resonance, which lie in the range of 220 to 260 MeV [213, 214]. The analysis of [215], however, suggests a higher range of 250 to 315 MeV. The value of $K_0 = 300$ MeV considered in our paper falls into the latter category, but this will not dramatically impact the neutron-rich equation of state appropriate for neutron star interiors. The GM1L equation of state for the core is paired with two models for the crust. For the outer crust, which falls in the density range $10^4 - 10^{11}$ g/cm^3, we use the Baym-Pethick-Sutherland (BPS) model [216]. For the inner crust, with densities in the range $10^{11} - 10^{14}$ g/cm^3, we use the Baym-Bethe-Pethick (BBP) model [217].

Table 5.1: Parameters of the model used to select example equations of state for the generation of simulated data samples. Shown are properties of the symmetric nuclear matter at saturation density for the GM1L parametrization of neutron star interiors[11]; see text for details.

Saturation Property	Value	Units
n_0	0.153	fm^{-3}
E_0	-16.3	MeV
K_0	300.0	MeV
m_N^*/m_N	0.70	-
J	32.5	MeV
L_0	55.0	MeV
U_N	-65.5	MeV

To limit the number of parameters the networks must learn, the essential features of the high-density portion of the EOS needed to be represented efficiently by just a few values. This can be done accurately by constructing parametric representations based on spectral fits, formed as generalizations of the Fourier series used to represent periodic functions [116]. An EOS, defined as $P = P(\epsilon)$ or $\epsilon(P) = \epsilon$, can be represented as a linear combination of basis functions $\epsilon_k(\phi)$:

$$\epsilon(p) = \sum_k \epsilon_k \Phi_k(p) \tag{5.1}$$

where $\phi_k(p)$ can be any complete set of functions. The EOS is therefore determined by the spectral coefficients ϵ_k, making $\epsilon_k = \epsilon(p, \epsilon_k)$. There are two important conditions that a physical EOS must satisfy to ensure microscopic stability. The first is that the EOS must be non-negative, or $p(\epsilon) \geq 0$, and the second is that pressure must be monotonically increasing with density [116]. Because these conditions are not naturally respected by arbitrary basis functions in a spectral representation, representing an EOS with a straightforward spectral expansion will likely produce data that violates microscopic stability and is therefore erroneous. To ensure these two conditions are met, we instead turn to a faithful construction of spectral representations of the EOS; the process for constructing these is outlined in detail in [218] and [116].

The spectral representation of GM1L is formed from representing the EOS in terms of the relativistic enthalpy, h, where the EOS can be rewritten as a pair of equations $P = P(h)$ and $\epsilon = \epsilon(h)$. The enthalpy can be defined as

$$h(P) = \int_0^P \frac{dP'}{\epsilon(P')c^2 + P'} \tag{5.2}$$

where c is the speed of light [218]. Inverting Eq. (5.2) obtains the equation $P = P(h)$, which can recover the EOS $\epsilon(P)$ as $\epsilon(h) = \epsilon[P(h)]$. The pair of equations $P = P(h)$ and $\epsilon = \epsilon(h)$ can be expressed from a reduction to quadrature:

$$P(h) = P_0 + (\epsilon_0 c^2 + P_0) \int_{h_0}^{h} \mu(h')dh', \tag{5.3}$$

$$\epsilon(h) = -P(h)c^{-2} + (\epsilon_0 + p_0 c^{-2})\mu(h). \tag{5.4}$$

The function $\mu(h)$ is defined as

$$\mu(h) = \exp\left\{\int_{h_0}^{h} [2 + \Gamma(h')]dh'\right\} \tag{5.5}$$

which is dependent on the sound speed or velocity function $\Gamma(h)$ and constants $P_0 = P(h_0)$ and $\epsilon_0 = \epsilon(h_0)$ [218]. Similar to Eq. (5.1), the velocity function can be represented as a spectral expansion:

$$\Gamma(h, \nu_k) = \exp\left[\sum_k \nu_k \Phi_k(h)\right] \tag{5.6}$$

where $\Phi_k(h)$ is any complete set of basis functions on the domain $[h_0, h_{max}]$.

We constructed enthalpy-based causal spectral fits for the GM1L EOS with up to 10 parameters. Figure 5.2 shows that just two spectral parameters produce parameterizations with a mean relative error of only 10%, and additional parameters can reduce the error to 5% or lower. A small number of parameters is preferred due to the increased complexity of learning multiple parameters, and the danger of Runge's phenomenon when applying our networks to current neutron star observations with accurate readings of mass and radius, which are still relatively few. Runge's phenomenon arises when attempting to fit equispaced data points with polynomials of a high degree; increasing the order of the polynomial interpolation can result in issues with convergence or divergence rates for certain functions [219]. When applied to neutron star observation, attempting to fit a small number of data points (with varying accuracy in observation method) with a model having many parameters may result in fits that accurately fit the data, but are very poor representations of the actual physics. Based on the reasons listed above, we chose to use two spectral parameters to represent the EOS, hereafter referred to as λ_1 and λ_2.

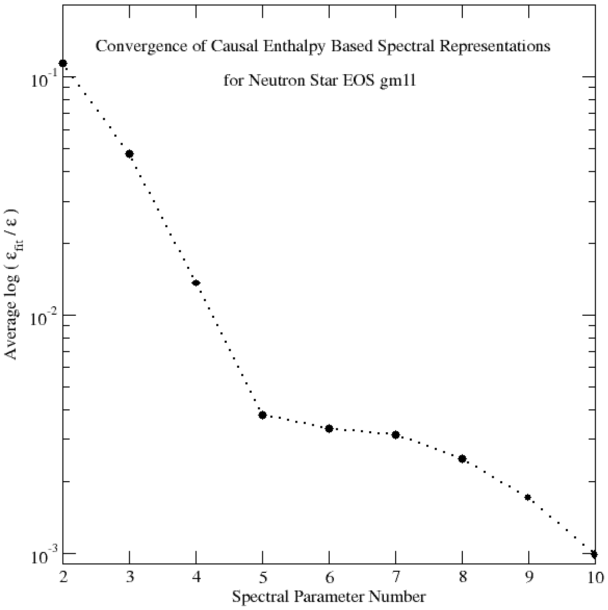

Figure 5.2: Relative error in the spectral parameterization of the equation of state, shown as a function of the number of parameters used.

To create many samples needed for training and testing, spectral parameters were then constructed from the expression:

$$\lambda_{\text{generated}} = \lambda_{\text{true}} \cdot (1 + 2 \cdot \mathit{scale}(-0.5 + \mathit{ran2})), \tag{5.7}$$

where $\lambda_{\text{generated}}$ represents the newly constructed spectral parameter, λ_{true} is the best fit (true) spectral parameter of GM1L, and *scale* is a scaling parameter set to 0.05. *ran2* are uniformly distributed random numbers in the range 0 to 1 generated by the *ran2* function given in [220]. This process was repeated to create 10^4 different EOS variations. Each EOS variation was used to generate a coinciding $M - R$ relation using equations (Eqs. 2.67 and 2.68), examples of which are seen in Figure 5.3, from which 100 (M, R) pairs are selected, each representing stellar parameters consistent with that EOS. Due to the random component of our EOS generation, some models have a mass peak below the current observed mass limit, 2.1 $M_\odot$. All models have a minimum mass of at least 1 $M_\odot$. The physicality of predicted results will be discussed in further detail Section 5.8.

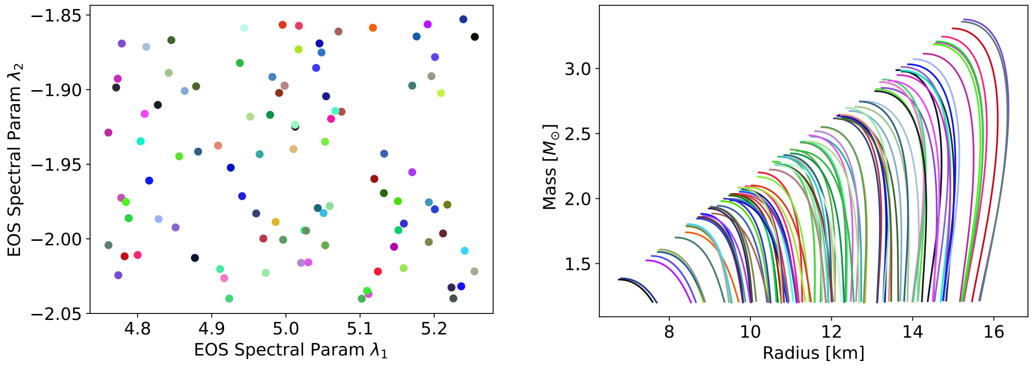

Figure 5.3: Examples of training data. On the left: 100 samples in EOS spectral parameter space (λ_1, λ_2) randomly selected from the full set of 10,000 EOS spectral pairs. On the right: neutron star mass-radius curves determined by the selected EOS parameters.

5.4.2 Modeling X-ray Spectra

The relation between stellar parameters (M, R) is determined by the EOS and samples from the allowed curve are used as input to generate simulated X-ray Chandra spectra, such as the Chandra observation of the quiescent low-mass X-ray binary (qLMXB) X7 in the globular cluster 47 Tuc [196].

The XSPEC program [197], which can be used for spectral fitting, is also capable of generation of simulated spectra, via the `fakeit` command when a neutron star model and telescope response matrix are provided.

The neutron star theoretical model `NSATMOS` [221] selected includes a hydrogen atmosphere model with electron conduction and self-irradiation. The Chandra telescope response specified in Ref. [221] was also used to describe the instrument response and telescope effective area.

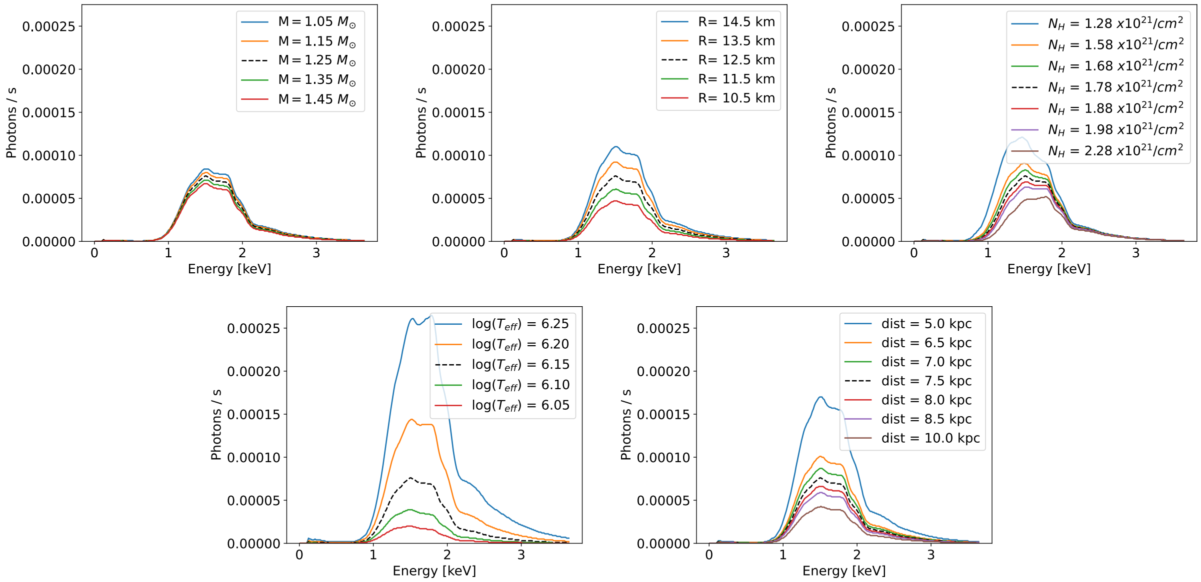

Figure 5.4: Examples of simulated stellar spectra expected for several values of stellar parameters. Each pane shows the expected rate of photons in Chandra per energy bin, for variations of the parameters of interest (mass M, radius R) as well as for variations of the nuisance parameters (N_H, $\log(T_{\text{eff}})$, distance). The dashed black line has the same parameters in each pane.

5.4.3 Nuisance Parameters

The `NSATMOS` model has five parameters to describe each star: gravitational mass M in units of $M\odot$, radius R in units of km, and three additional parameters related to observation. For the context of $M - R$ and subsequent EOS inference, only M and R are parameters of interest, whose values come from those generated by the GM1L EOS and so provide information relevant to the physical question. The remaining three nuisance parameters are the effective temperature of the surface, T_{eff}, the distance to the star, d, and the hydrogen column, N_H which parameterizes the reddening of the spectrum by the interstellar medium. These parameters influence the observed spectrum of a given neutron star. Lack of knowledge of these values is a leading source of uncertainty in the inference of mass and radius, and hence EOS.

Using Table 1 in Ref. [203] as a guide, we find that distances typically range between 2 and 10 kpc, and hydrogen columns lie between 0.2 and 5×10^{21} cm^{-2}. While neutron stars with larger distances and larger hydrogen columns exist, they are sufficiently distant to be difficult to obtain spectral information. From Table 3 in Ref. [222], effective temperatures at the surface typically lie between 50 and 200 eV, or from 6×10^5 and 2.4×10^6 K. Note that core temperatures are typically a few orders of magnitude larger. Again colder neutron stars most certainly exist but are more difficult to observe.

Examples of generated spectra for varying stellar parameters are shown in Figure 5.4. The generated spectra are very sensitive to the effective surface temperature, with lesser sensitivity to other parameters. The dependence of the curves in Figure 5.4 to the changing nuisance parameters is not surprising: roughly proportional to radius and distance squared, but higher power in temperature.

The networks detailed below provide estimates of either the neutron star mass and radius or the EOS parameters, conditioned on NP values. Uncertainty in regressed parameters of

Table 5.2: Description of “true”, “tight”, and “loose” nuisance parameter (NP) scenarios. Shown are the width of each Gaussian distribution representing the prior knowledge of each NP. For distance and N_H, width is relative; for $\log(T_{\text{eff}})$, it is absolute. See text for details and references.

Nuis. Param.	True	Tight	Loose
Distance	exact	5%	20%
Hydrogen Column N_H	exact	30%	50%
$\log(T_{\text{eff}})$	exact	±0.1	±0.2

interest due to uncertainties in the NP can then be fully propagated via variation of the NPs used during regression. To demonstrate the impact of NP uncertainties, we define three example scenarios of uncertainties, dubbed “true”, “tight”, and “loose”, which describe the quality of prior information on the NP values for each star.

In the “true” scenario, the NPs are set to the true value used to generate the spectra, such that the NP prior is essentially a delta function. In the “tight” scenario, the uncertainty is described as a narrow Gaussian for each NP, with distance having a width of 5%, hydrogen column having a width of 30%, and $\log(T_{\text{eff}})$ having a width of 0.1. In the “loose” scenario, the uncertainties are described by a wider Gaussian, with distance having a width of 20%, hydrogen column having a width of 50%, and $\log(T_{\text{eff}})$ having a width of 0.2. These ranges are shown in Table 5.2. The sensitivity to NP values is reflected in the performance of the networks below.

5.5 Inference of EOS from Mass and Radius

Previous applications of machine learning to the task of inferring the equation of state have begun from the stellar mass and radii [6–8], or equivalent parameters [9], though with simple ad-hoc descriptions of the uncertainty on stellar mass and radius values, often modeled as two-dimensional uncorrelated Gaussians rather than fully propagating the underlying uncertainties. In this section, we tackle the same problem, but where the stellar data are more realistic and the underlying uncertainties are fully propagated to the EOS estimation. Specifically, the best estimates of stellar mass and radius are derived using state-of-the-art tools that extract them from realistic stellar spectra, which include the impact of stellar nuisance parameters and limited observation time. In addition, this mass-radius estimation is conditioned on the nuisance parameters, such that variations in those nuisance parameters lead to variations in the mass and radius estimates. This connects directly to the neural network regression of EOS parameters from mass-radius values parameterized in the nuisance parameters, allowing for the direct propagation of the underlying uncertainties to give a measure of the resulting uncertainty on the regressed EOS parameters.

Below, we describe the extraction of realistic mass and radius values with XSPEC, and their subsequent use in NN regression of the EOS parameters and the estimation of the uncertainty. For comparison, we also provide a demonstration of the regression of EOS parameters using polynomial regression. In subsequent sections, we consider an alternative extraction of mass and radius using a NN, as well as end-to-end regression of EOS directly from stellar spectra.

5.5.1 Mass and Radius inference by XSPEC

Sample stellar spectra are generated as described above, including Poisson noise corresponding to an observation time of 100 ks, and nuisance parameters variations as specified in Table 5.2.

Given a sample observed X-ray spectrum, the XSPEC code scans the mass and radius parameter space, searching for values that best describe it. For each mass-radius pair, the expected spectrum is calculated using the chosen model and telescope response function, identical to those used to generate the sample spectra being fit. The fitted values are those that minimize a bin-wise χ^2, and reported errors are those that generate a fixed increase in the χ^2 metric.

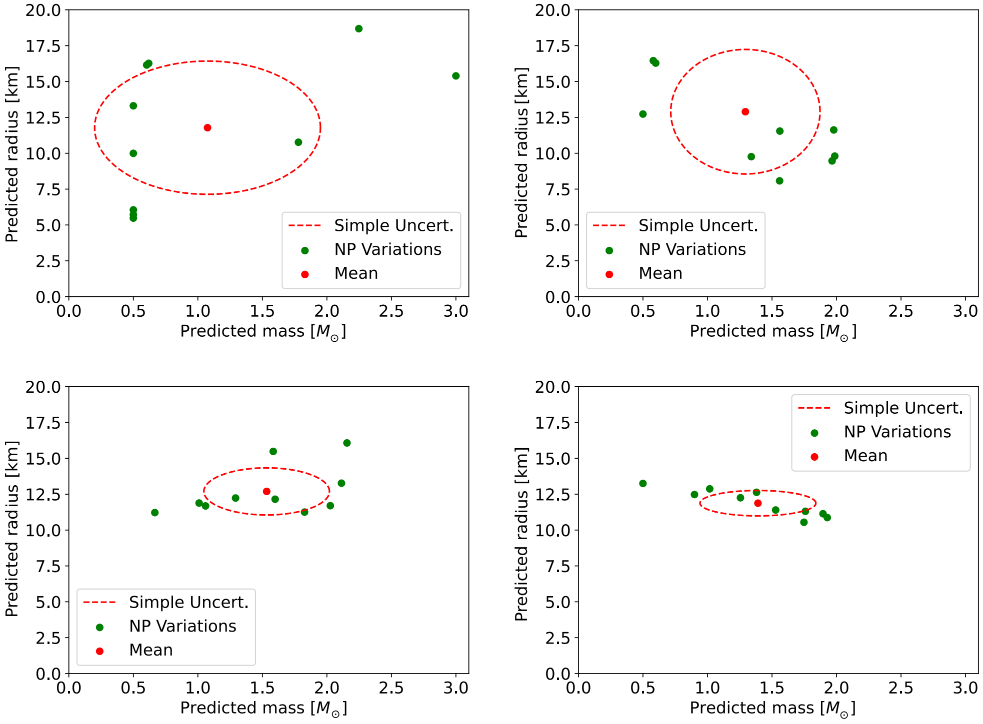

Figure 5.5: Estimation of the mass and radius of a neutron star from the underlying stellar spectra, by XSPEC. Each pane represents one star, and shown (green) are estimates for several independent values of the nuisance parameters drawn from the associated priors, and the mean value (red). Top two cases have loose priors, bottom two have tight. The dashed ellipse, whose widths are set to the standard deviation of the mass and radius estimates, is a demonstration of the inadequacy of a simple uncertainty model.

To propagate the uncertainty due to the lack of knowledge of the NP values, the fit on a given spectrum is performed several times with varying assumed values of the NPs drawn from the appropriate prior. The variation in the resulting fitted values then describes the impact of uncertainty on the NPs. For this reason, during each single XSPEC fit, the NP values are not allowed to vary but are frozen. Figure 5.5 shows examples for individual stars, demonstrating the variation of the stellar parameter estimates with varying NP values. For illustrative comparison to ad-hoc models of uncertainty, the standard deviation in mass and radius are used to define the widths of a 2d error ellipse, though it is clear that this fails to capture the complex nature of the impacts of the underlying uncertainties; these simple error models are not used in our analysis.

XSPEC is also capable of *floating* the nuisance parameters, varying their values to improve an individual fit, and reporting an uncertainty envelope in the mass-radius plane. This can be helpful in the case where the mass and radius and their envelope are the final targets. However, to propagate the uncertainty downstream requires that we have the full posterior in the mass-radius plane or samples from it. An estimate and envelope do not provide that capacity, though they can allow for ad-hoc parameterizations of the prior as have been performed previously. We condition the nuisance parameters to allow full propagation of the NP uncertainty through to EOS estimation, as we do below.

Performance of XSPEC regression of mass and radius is shown in Figure 5.6, where the residuals increase as expected with wider priors on the nuisance parameters. In addition, note that in the case of the "loose" priors, there is a small fraction of cases where XSPEC fails to converge on an estimate, as the nuisance parameters are fixed to a value far from the value used to generate the spectrum.

One important note regarding XSPEC's performance is that the same theoretical model, `NSATMOS`, is used in data generation and regression. Because of this, the regression models discussed in the next section can, at best, match XSPEC's performance for the evaluation dataset. Nonetheless, it is an important step in demonstrating the capacity of these methods to perform such inference without explicitly relying on a single theoretical model.

5.5.2 Inference of EOS from mass and radius

In this section, we demonstrate the inference of EOS parameters from the stellar mass and radius data, using neural network regression parameterized in the NPs to allow propagation of the uncertainty. In addition, we build polynomial regression models which serve as a benchmark, following Ref. [6].

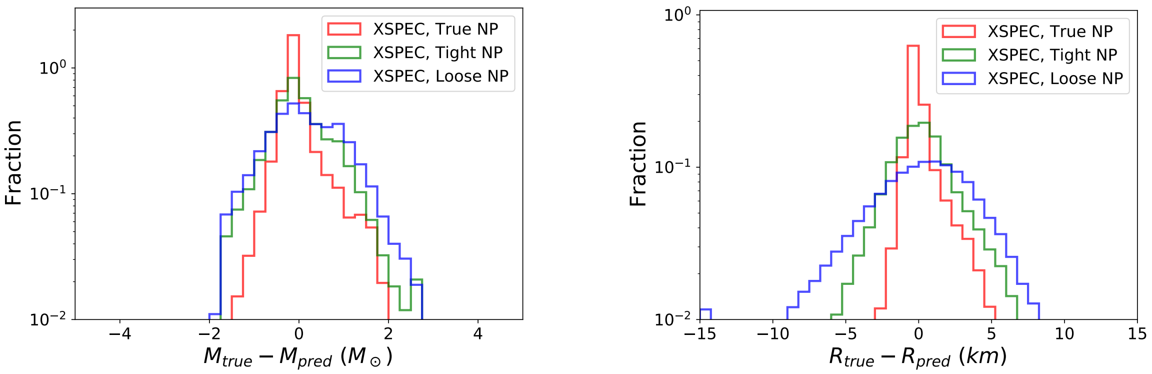

Figure 5.6: Performance of XSPEC inference of neutron star mass and radius, as measured by residuals between the fitted (”pred”) and true values under three treatments of the nuisance parameters (NPs). In the “true” case, the NPs are fixed to their true values; in the “tight” and “loose” cases, they are drawn from narrow or wide priors, respectively; see text for details. Cases in which XSPEC fails to converge are shown as large negative residuals.

Neural Network regression

Deep feed-forward neural networks are trained to provide the EOS parameters given a collection of ten stars, each represented by their mass and radius. Each network has two outputs, λ_1 and λ_2.

We train three networks, one for each of the true, tight, and loose NP scenarios. All networks have identical architecture, 10 hidden layers with 32 nodes each followed by an output layer with 2 nodes. Rectified linear units (ReLU) are used as activation functions for the hidden layers while linear activations are used for the output layers. They were trained up to 1000 epochs with a mean squared error (MSE) loss and an Adam optimizer [223], and the performance is evaluated on independent validation data. The performance was not found to be highly sensitive to hyper-parameter tuning, so permutation symmetry-preserving architectures were not explored. The networks were implemented using `Tensorflow 2.7.0` on a single `NVIDIA RTX A5000` GPU.

Polynomial regression

Following the example of Ref [6], as a performance benchmark we also construct a polynomial regression model to regress EOS parameters λ_1 and λ_2 from stellar mass and radius information. The input for each model is a 20 x 1 vector containing the following information from each of the ten stars: mass M, radius R.

Each 20 x 1 input to the polynomial regression network represents a set of stars, all of which are chosen from the same EOS. We construct two multivariate polynomial regression models of degree two, following the general form:

$$\lambda = \beta_0 + \sum_{i=1,2}^{N} \beta_i x^i \tag{5.8}$$

where each β are coefficients and $N = 20$ to represent the cluster size or 10 mass-radius pairs. Polynomial features were created using the machine learning toolbox scikit-learn [224], and subsequently fit to a linear regression model. This model uses optimization in the form of ordinary least squares, which takes the form:

$$\min_\beta ||X\beta - y||_2^2 \tag{5.9}$$

where X is the $N = 20$ input vector, and y is the target EOS parameter, either λ_1 or λ_2.

Estimation of Uncertainty

The uncertainty in the underlying neutron star nuisance parameters has a significant impact on the estimation of EOS parameters. Because the mass and radius estimation is conditioned on the NPs, leading to variations in the mass and radius, (eg see Figure 5.5), those variations can be propagated through the EOS estimation. The significant uncertainties in stellar

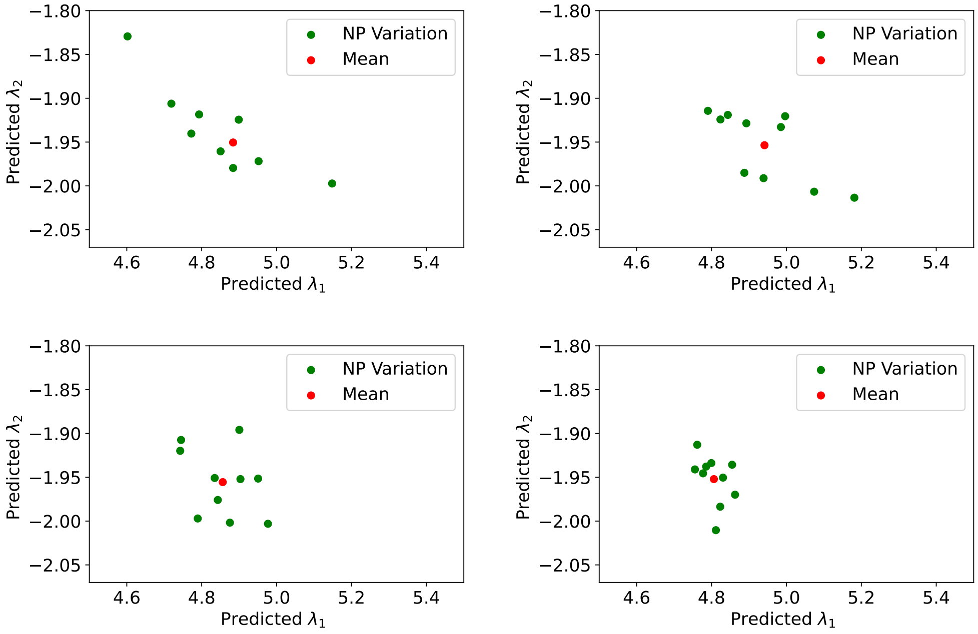

Figure 5.7: Neural network regression of the EOS parameters λ_1 and λ_2 of a set of 10 neutron stars from their masses and radii as estimated by XSPEC from each star's spectrum. Each pane represents an example dataset of 10 simulated stars, and shown (green) are EOS estimates for several independent values of the stellar nuisance parameters drawn from the associated priors, and the mean value (red). Top two cases have loose priors, bottom two have tight.

nuisance parameters and the small number of stars observed to date make the treatment of those uncertainties vital. The validity of the final result is only as powerful as the validity of its uncertainties. In Figure 5.7, examples of the variation of the EOS estimates are shown, where the underlying stellar spectra are fixed. Thus, this provides a measure of the uncertainty in the EOS due to the uncertainty in the NPs.

Performance

Performance of neural network regression of the EOS parameters λ_1 and λ_2 are compared to polynomial regression of the same quantities using identical datasets via comparison of the residuals, the difference between the true and regressed values. As seen in Figures 5.8 and 5.9, while PR can achieve narrower residuals in the true case, the network regression is more robust in cases with larger uncertainties.

This result confirms what has been seen in earlier studies of NN regression from mass-radius pairs [6], but our study extends previous work by using realistic values of the mass and radius inferred from realistic simulated spectra, as well as by demonstrating uncertainty quantification, via full propagation of the underlying uncertainties due to nuisance parameters.

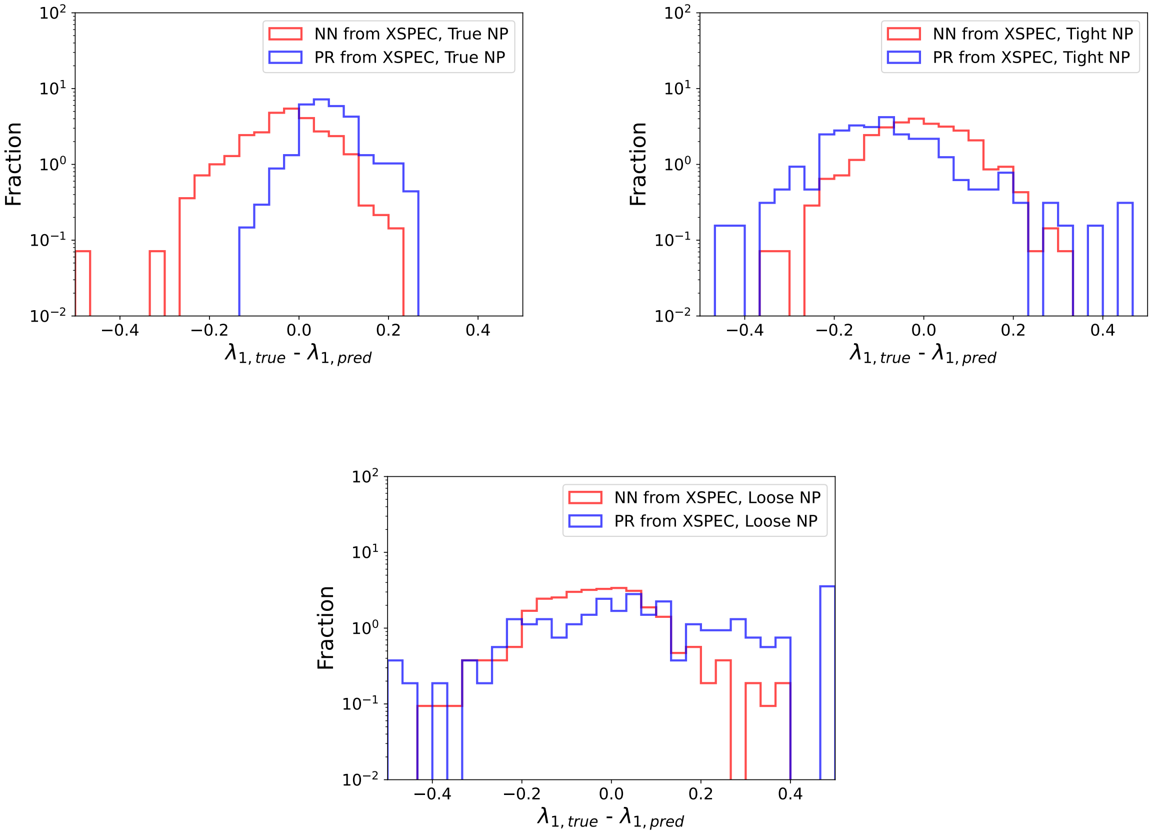

Figure 5.8: Comparison of the performance of NN regression and polynomial regression of EOS parameter λ_1 from mass-radius pairs inferred by XSPEC from stellar spectra. Shown is the residual, the difference between the predicted and true values for each of the three treatments of the stellar nuisance parameters. In the “true” case, the NPs are fixed to their true values; in the “tight” and “loose” cases, they are drawn from narrow or wide priors, respectively; see text for details.

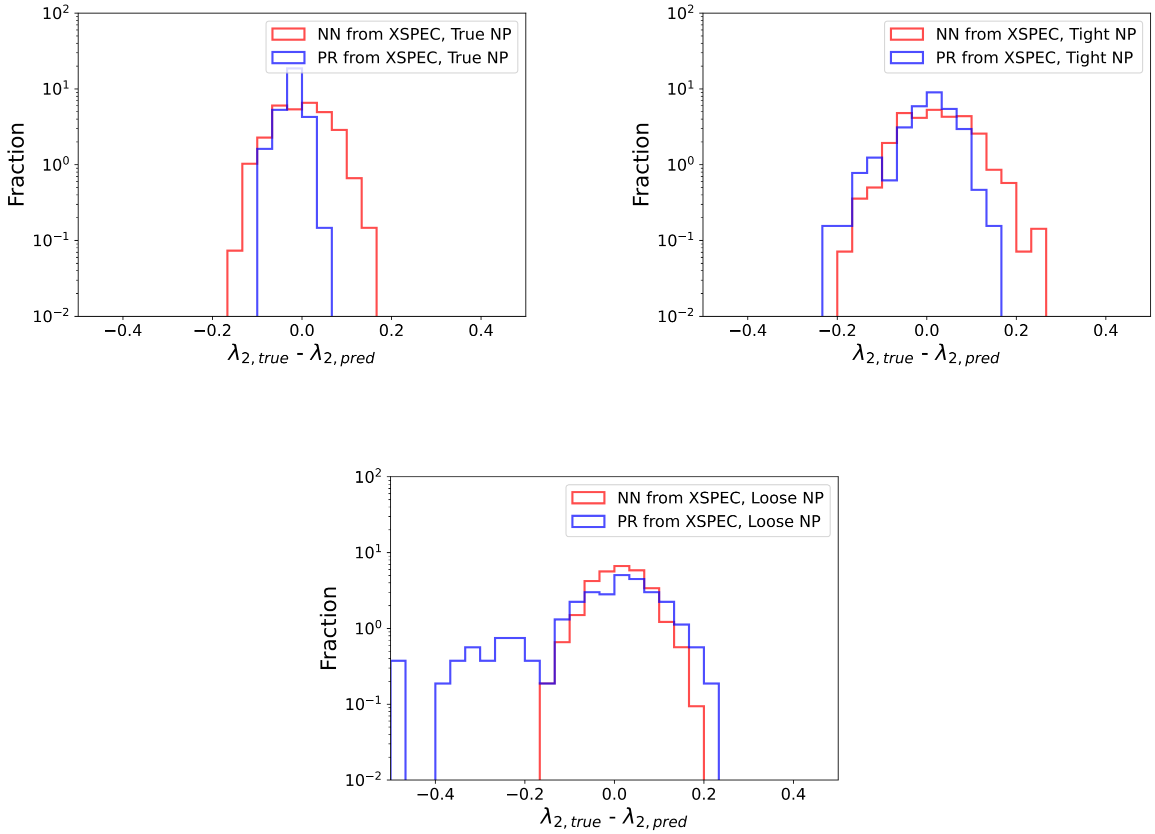

Figure 5.9: Comparison of the performance of NN regression and polynomial regression of EOS parameter λ_2 from mass-radius pairs inferred by XSPEC from stellar spectra. Shown is the residual, the difference between the predicted and true values for each of the three treatments of the stellar nuisance parameters. In the "true" case, the NPs are fixed to their true values; in the "tight" and "loose" cases, they are drawn from narrow or wide priors, respectively; see text for details.

5.6 Inference of Mass and Radius from Spectra

Previous applications of machine learning to neutron star datasets focus on the analysis of mass-radius pairs, as demonstrated above, rather than the direct analysis of the stellar spectra by neural networks.

A potential obstacle to direct analysis of spectra by neural networks is that the spectra are high-dimensional, often with $\mathcal{O}(10^3)$ bins of photon energy. However deep learning methods combined with GPUs have no trouble analyzing data with similarly high dimensionality [135], opening up new opportunities to tackle this important topic. While the mass and radius are powerful summaries of the information in the lower-level spectra which is relevant to the equation of state, direct ML analysis of the spectra themselves may allow for the extraction of additional information or provide more robust propagation of uncertainties. As an initial step, we begin by estimating the stellar mass and radius from a single stellar spectrum before moving on to end-to-end inference of EOS parameters directly from a set of spectra in the next section.

In this section, we apply machine learning to the task of extracting the mass and radius from the stellar spectra, training a network we refer to as MR_Net. This serves as a demonstration of the capabilities of ML to grapple with high-dimensional datasets, allows us to harmonize the treatment of nuisance parameters end-to-end from spectra to EOS, and potentially extract more relevant information.

5.6.1 MR_Net Method

We build a network whose inputs correspond to the bins of the stellar X-ray spectrum, and whose outputs are the estimates of the star's mass and radius. In addition, the mass and radius regressor is parameterized on the stellar nuisance parameters (distance, N_H, $\log(T_{\mathrm{eff}})$), which allows the results to be conditioned on the nuisance parameters.

This architecture is composed of two input branches, one to process the star's spectra and another to process the corresponding nuisance parameters. Each branch contains a series of layers that process its inputs in isolation. Following these initial layers, the output from the branches is combined, forming a single vector containing all the information. This vector is then passed to a final series of layers to predict the star's mass and radius. Each segment of the network, both the branches and the main trunk of the network, contains four layers, giving the network eight layers in total. All fully connected layers contain 275 nodes and utilize a dropout probability of 0.25. The network employs skip connections between alternate layers. This stabilizes the training process and adds robustness to the network overall. The network is trained with an MSE loss and an Adam optimizer with an initial learning rate of 0.00017 which is slowly decayed over the course of training.

Mass-radius regression is formulated as a supervised learning problem, where the network learns to minimize the error between the true mass and radius and its predictions. The network weights are updated by stochastic gradient descent using backpropagation. The Huber loss function [225] is used and the Adam optimizer computes gradients and schedules the backward passes.

5.6.2 MR_Net Performance in Mass and Radius

We begin with the best-case scenario in which the nuisance parameters are known with zero uncertainty, referred to as "true NP" above. Figure 5.10 shows the performance of MR_Net given neutron star spectra with statistical noise corresponding to 100,000 seconds (100 ks) of observation time, as well as for spectra without statistical noise. This demonstrates the contribution of statistical noise to the residual and demonstrates the network's ability to digest the spectral information and understand the dependence on mass and radius.

What is clear is that MR_Net is capable of extracting the mass and radius values of the star directly from the spectrum. We emphasize that the network is trained on examples, but does not benefit from the knowledge of the theoretical model used to generate these stars, while XSPEC requires precise specification of the theoretical model. This lack of requirement of a theoretical model opens new possibilities, such as training MR_Net to interpolate smoothly between theoretical models by providing a mixed or parameterized training set.

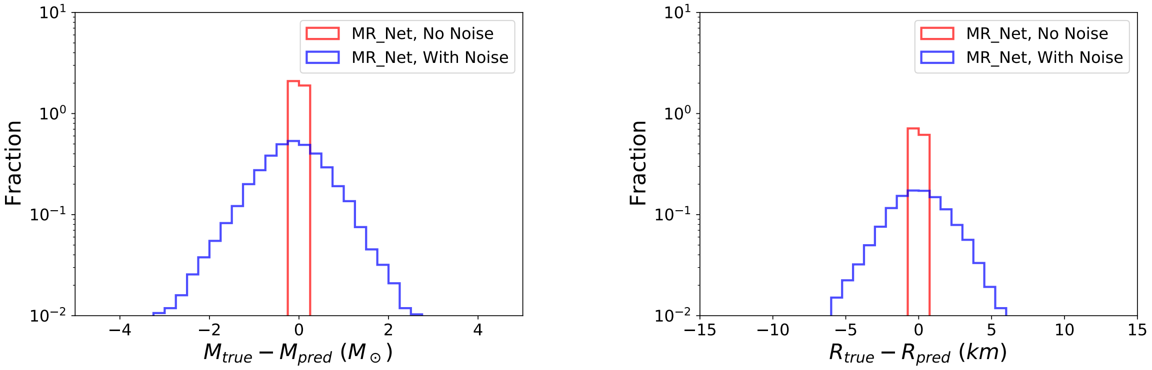

Figure 5.10: Performance of the MR_Net regression of a neutron star mass (top) and radius (bottom) from its stellar X-ray spectrum. Shown is the residual, the difference between the true and predicted values, for spectra with statistical noise (blue) corresponding to an observation time of 100ks, and for spectra without statistical noise (red), which demonstrates the network's capacity. Nuisance parameters are fixed to their true values.

The MR_Net is conditioned on the nuisance parameters, allowing for propagation of the NP uncertainties through to the regression target as was done with XSPEC estimates. To assess the impact of NP uncertainty, we draw from priors on the NPs under the "Tight" and "Loose" scenarios defined earlier. The residuals widen, as expected. Figures 5.11 and 5.12 show the mass and radius residuals, respectively, under each NP scenario for MR_Net and XSPEC. Table 5.3 shows the mean and width of each residual distribution, as well as the combined width. As an additional comparison, Figure 5.13 shows the ratio of predicted values from MR_Net to true values subtracted from 1.

MR_Net is capable of analyzing the stellar spectrum directly and extracting stellar parameters in a robust manner that allows for the propagation of NP uncertainties.

5.6.3 Network Uncertainty on Mass and Radius

Conditioning the extraction of M and R on the nuisance parameters allows for the natural propagation of the corresponding uncertainties. As was done for XSPEC mass and radius

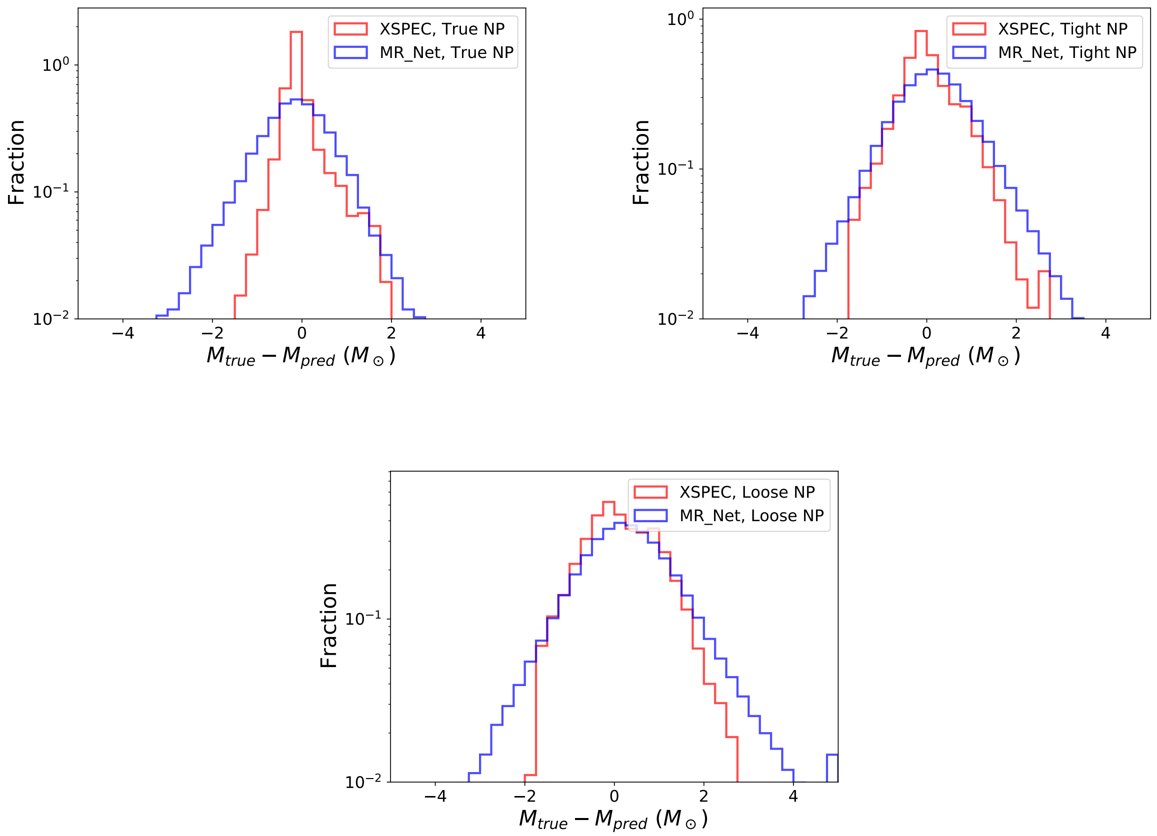

Figure 5.11: Performance of the MR_Net regression of a neutron star mass from its stellar X-ray spectrum, compared to regression using XSPEC. Shown is the residual, the difference between the true and predicted values, for three scenarios of nuisance parameter uncertainties. In the "true" case, the NPs are fixed to their true values; in the "tight" and "loose" cases, they are drawn from narrow or wide priors, respectively; see text for details.

estimates, we propagate the NP uncertainty through to mass and radius uncertainty by sampling from the stellar NP priors several times for a given stellar spectrum, performing the mass and radius regression multiple times. Figure 5.14 demonstrates this for several example stars. Note that the variation of NP values does not produce variation in M and R which can be accurately summarized by 2D uncorrelated Gaussians, as has been assumed in previous studies [6] with ad-hoc datasets.

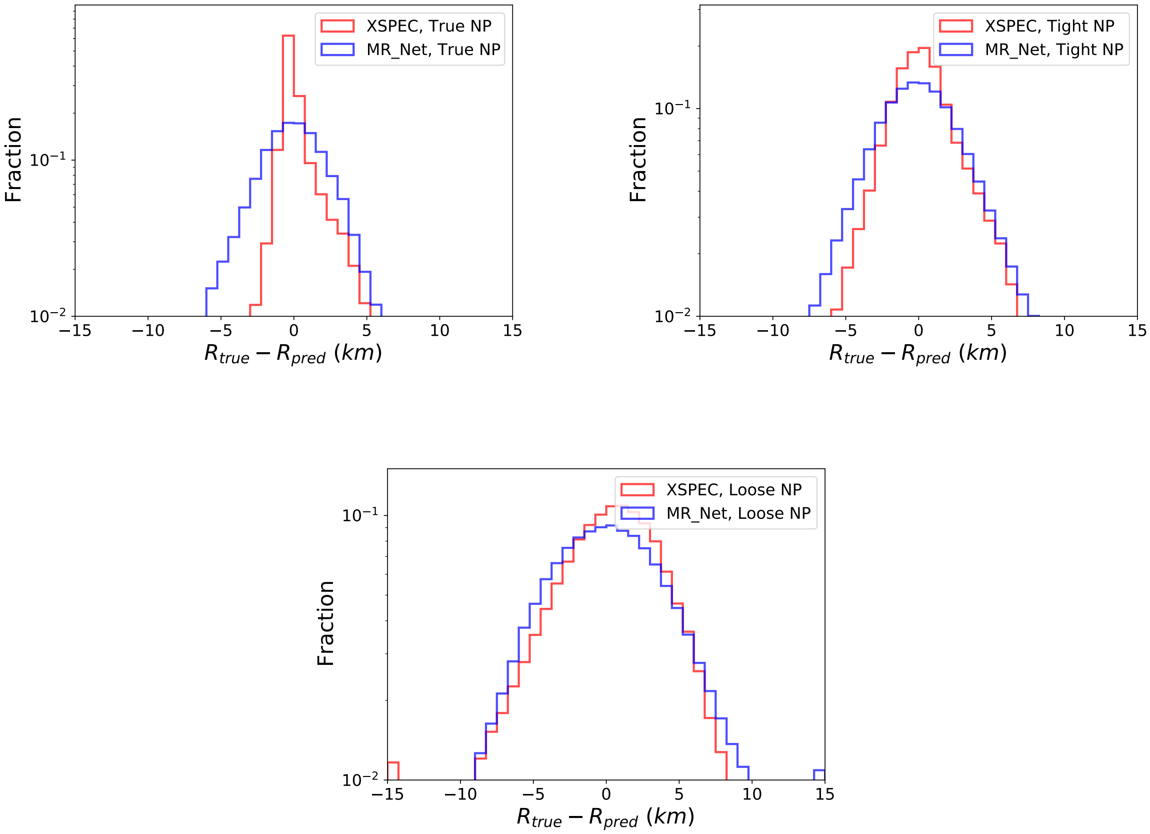

Figure 5.12: Performance of the MR_Net regression of a neutron star radius from its stellar X-ray spectrum, compared to regression using XSPEC. Shown is the residual, the difference between the true and predicted values, for three scenarios of nuisance parameter uncertainties. In the "true" case, the NPs are fixed to their true values; in the "tight" and "loose" cases, they are drawn from narrow or wide priors, respectively; see text for details.

5.6.4 Revisiting EOS Regression

The question driving the analysis of neutron star spectra is not a desire to measure their masses and radii, but to use those to determine the equation of state parameters. In this section, we push the results of MR_Net through our NN regression of EOS parameters to analyze the performance of spectra→ (M, R) →EOS regression. In later sections, we remove the intermediate step and perform direct spectra→EOS regression.

Performance of the EOS regression using stellar mass and radius information from MR_Net is

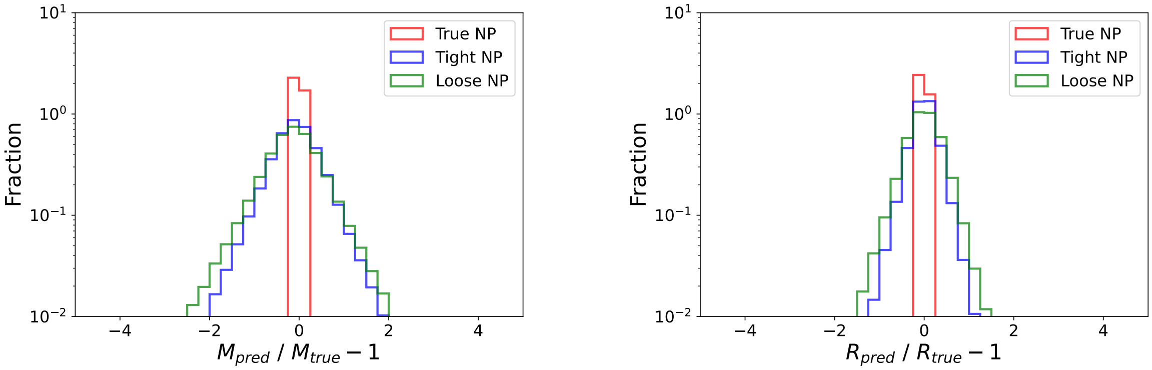

Figure 5.13: Performance of the MR_Net regression of a neutron star mass (top) and radius (bottom) from its stellar X-ray spectrum. Shown is the ratio of predicted (”pred”) to true values minus one for three scenarios of nuisance parameter uncertainties. In the “true” case, the NPs are fixed to their true values; in the “tight” and “loose” cases, they are drawn from narrow or wide priors, respectively; see text for details.

Table 5.3: Performance of the regression of neutron star mass and radius for XSPEC as well as our neural network regression, MR_Net, which lacks any knowledge of the theoretical model. Shown are the mean (μ) and standard deviation (σ) of the residuals under three scenarios of nuisance parameter uncertainties. In the “true” case, the NPs are fixed to their true values; in the “tight” and “loose” cases, they are drawn from narrow or wide priors, respectively; see text for details. The combined column is a quadrature sum of the standard deviations of radius and mass.

	Nuis.	Mass		Radius		Combined
Method	Params	μ	σ	μ	σ	σ
XSPEC	True	−0.01	0.50	0.23	1.44	1.51
MR_Net	True	−0.14	0.93	−0.07	2.80	2.99
XSPEC	Tight	−0.06	0.73	0.24	2.61	2.69
MR_Net	Tight	0.17	1.06	0.06	3.52	2.76
XSPEC	Loose	0.18	0.86	−0.06	4.32	4.40
MR_Net	Loose	0.28	1.29	0.14	4.93	5.10

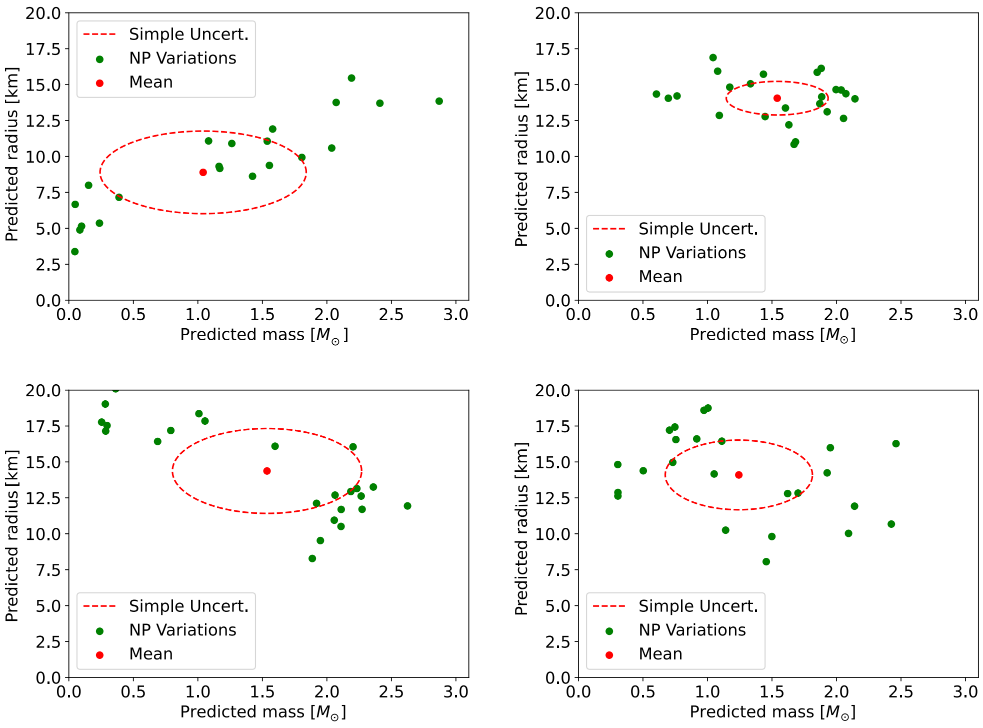

Figure 5.14: Estimation of the mass and radius of a neutron star from the underlying stellar spectra, by MR_Net. Each pane represents one star, and shown (green) are estimates for several independent values of the nuisance parameters drawn from the associated priors, and the mean value (red). Top two cases have loose priors, bottom two have tight. The dashed ellipse, whose widths are set to the standard deviation of the mass and radius estimates, is a demonstration of the inadequacy of a simple uncertainty model.

shown in Figures 5.18 and 5.19, and compared to regression from mass and radius information by XSPEC. Examples of uncertainty propagation through to EOS estimates are shown in Figure 5.15.

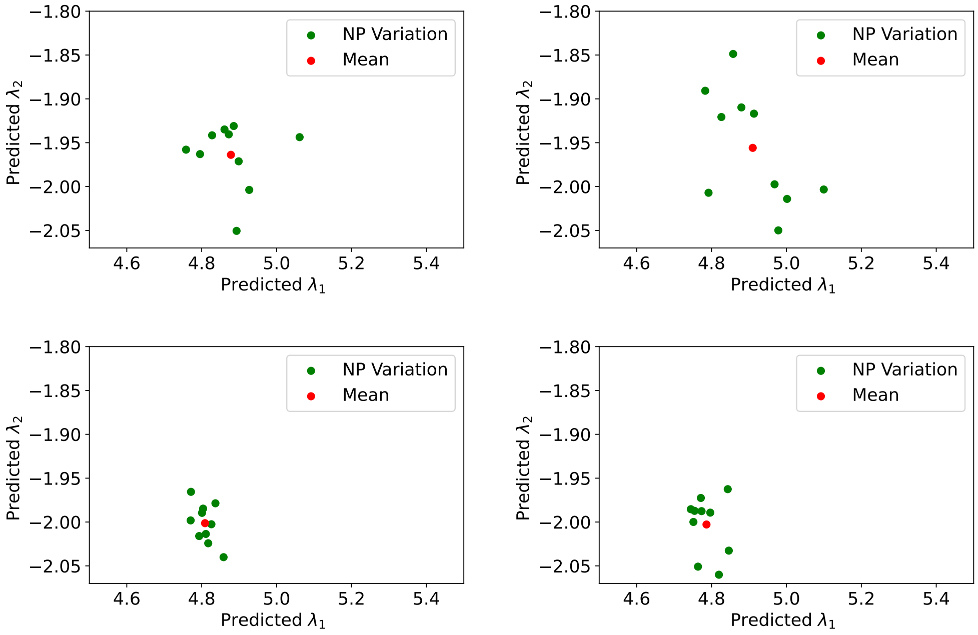

Figure 5.15: Neural network regression of the EOS parameters λ_1 and λ_2 of a set of 10 neutron stars from their masses and radii as estimated by MR_Net from each star's spectrum. Each pane represents an example dataset of 10 simulated stars, and shown (green) are EOS estimates for several independent values of the stellar nuisance parameters drawn from the associated priors, and the mean value (red). Top two cases have loose priors, bottom two have tight.

5.7 Inference of EOS from Spectra

In the previous section, we connected the two ML models, MR_Net(spectra $\rightarrow M, R$) and our EOS regression NN ($M, R \rightarrow$ EOS). This required the collapse of the full information and dependence on nuisance parameters into these two physical quantities. At the same time, MR_Net demonstrated that it is possible to regress physics quantities directly from high-dimensional stellar spectra. In this section, rather than connecting two networks via mass and radius, we use a single network to perform end-to-end regression of EOS parameters from a set of stellar spectra, avoiding the information collapse, keeping the full information, and allowing for robust propagation of the stellar nuisance parameters into uncertainty quantification for the EOS parameters of interest.

In addition to a demonstration of the power of networks to directly analyze low-level data, this allows us to probe the question of whether the mass and radius are sufficient statistics, and whether they contain *all* of the information relevant to the problem. There are many examples in the literature in which such well-motived high-level heuristics fail to capture the complete information contained in lower-level data. In this case, while in principle the mass and radius are all that are required to infer the EOS in the context of a fixed theoretical stellar model, such information is never without uncertainty. Full propagation of the dependence on nuisance parameter uncertainty may allow for more accurate and robust estimates.

Furthermore, there are properties of neutron stars that can be deciphered from spectra beyond simply mass and radius. Quantities like temperature inhomogeneities [226] may impact a star's equation of state but are not captured by the mass and radius.

5.7.1 Architecture

Many neural network architectures operate on sequences of vectors, rather than a set of vectors. For instance, in natural language processing, the input may be a sentence where each word is converted to a vector and the ordering of the vectors matters. However, in the case of neutron stars and other problems, we need neural networks that operate on sets of vectors, such as the independent spectra observations for multiple stars.

One architecture with invariant properties with respect to permutations of the input vectors is the transformer architecture [209, 227]. Perhaps surprisingly, transformers were originally developed for problems in natural language processing, thus requiring the addition of positional information bits to the vector encoding each word to recover the sequential dimension. More recently they have been used in other areas, including physics [228, 229] to leverage their permutation invariance properties. Transformer architectures typically consist of stacks of encoder modules followed by decoder modules. The structure of each encoder module and each decoder module is similar, thus we describe only a typical encoder module. A transformer encoder module accepts an unordered set of inputs and produces a set of outputs. The transformer employs a mechanism called *self-attention*, which allows it to compare each element in the set against every other. This mechanism allows the network to attend to important features in the set while computing an output prediction. Briefly, self-attention (Equation 5.10) operates on an input matrix X, with N rows and D columns. Three matrices are produced from the projection of X with differing, trainable, weight matrices: $Q = XW_Q, K = XW_K, V = XW_V$ (termed Query, Key, and Value respectively).

$$S = D(Q, K, V) = \text{softmax}\left(\frac{QK^T}{\sqrt{d_q}}\right)V \tag{5.10}$$

Thus in short each output corresponds to a different convex combination of the Value vectors, where each convex combination depends on the degree of similarity between the corresponding Query and Key vectors. The similarity is computed by taking dot products between corresponding Query and Key vectors and then applying a softmax to yield a convex combination (see [209, 227] for additional details).

In the neutron star application, the transformer architecture takes input spectra and corresponding nuisance parameters for each star in the set. In the results shown below, the network is given a set of 10 stars, though the structure of the network allows it to accept larger or smaller datasets with minimal modification. The final output of the network is the two EOS parameters. This is shown schematically in Figure 5.16.

The network is composed of six consecutive transformer blocks. Each block processes the input through multi-head attention (with eight heads), followed by dropout ($p = 0.15$), normalization, and fully connected layers. Following these blocks the output is processed by one final fully connected layer to regress the EOS coefficients λ_1 and λ_2. All fully connected layers, with the exception of the final one, use the ReLU activation function. The Adam optimizer was used to provide gradient updates with an initial learning rate of 0.000075, which was a slow decade over the course of training.

5.7.2 Training the Network

The parameters of the network architecture and the learning algorithm, the hyperparameters, were optimized with Sherpa [230], a Python library for hyperparameter tuning. The algorithm used is based on a random search and has the advantage of making no assumptions about the structure of the hyperparameter search problem and thus is well suited for exploring a variety of parameter settings. An initial exploratory search was conducted on a subset of the data to find appropriate hyperparameters.

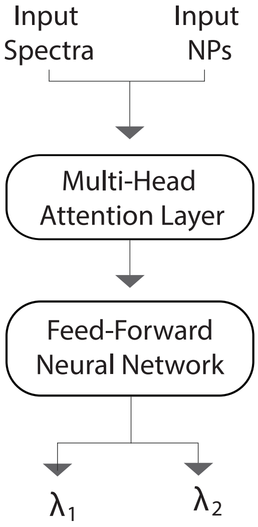

Figure 5.16: Schematic diagram of the transformer neural network used to determine EOS coefficients λ_1 and λ_2 from an input of spectra and NPs.

Following this exploratory phase, the network is trained for 1,000 epochs on the full dataset. The Adam optimizer [223] is used for gradient descent, with early stopping monitoring of the validation loss to prevent overfitting.

5.7.3 Results

Figure 5.17 shows the performance of spectra→EOS regression in the best-case scenario, where the nuisance parameters are perfectly known. Shown is the performance with statistical noise corresponding to 100 ks of observation time per star, as well as for spectra without statistical noise. While there is significant width to the residuals, this is dominated by the statistical uncertainty, not the network's ability to digest the spectral information and understand the dependence on mass and radius. This clearly demonstrates the network's capacity is sufficient for the regression task.

We next analyze the performance of the direct regression in cases where the nuisance pa-

Table 5.4: Performance of the regression of neutron star EOS parameters λ_1 and λ_2 using direct regression from spectra, as compared to NN regression from mass and radius (M, R) information extracted via MR_Net or XSPEC. Shown are the mean (μ) and standard deviation (σ) of the residuals under three scenarios of nuisance parameter uncertainties; distributions are given in Figures 5.18 and 5.19. In the "true" case, the NPs are fixed to their true values; in the "tight" and "loose" cases, they are drawn from narrow or wide priors, respectively; see text for details. The combined column is a quadrature sum of the standard deviations of λ_1 and λ_2.

	Nuis.	λ_1		λ_2		Combined
Method	Params.	μ	σ	μ	σ	σ
NN(Spectra)	True	-0.02	0.066	0.01	0.075	0.099
NN(M, R via MR_Net)	True	-0.03	0.089	-0.02	0.068	0.112
NN(M, R via XSPEC)	True	-0.03	0.065	0.01	0.055	0.085
NN(Spectra)	Tight	0.02	0.085	-0.02	0.077	0.115
NN(M, R via MR_Net)	Tight	0.00	0.104	0.02	0.072	0.126
NN(M, R via XSPEC)	Tight	-0.03	0.081	0.01	0.056	0.098
NN(Spectra)	Loose	-0.03	0.131	-0.01	0.078	0.152
NN(M, R via MR_Net)	Loose	-0.01	0.135	-0.02	0.078	0.156
NN(M, R via XSPEC)	Loose	-0.03	0.123	0.01	0.058	0.136

rameters are not perfectly determined. Figures 5.18 and 5.19 show the residuals in the EOS parameters for the end-to-end regression, as compared to regression from mass and radius information provided by MR_Net or XSPEC from the stellar spectra. Table 5.4 summarizes the performance for each method.

As the full network is again conditioned on the NPs, we can propagate this uncertainty directly through our regression. Figure 5.20 demonstrates how variations of the NPs, drawn from the appropriate priors, provide a measure of the uncertainty of the final result.

5.8 Discussion

The performance of the three methods is measured in simulated stellar samples generated with the same theoretical stellar model that is assumed by XSPEC, which makes it a valuable

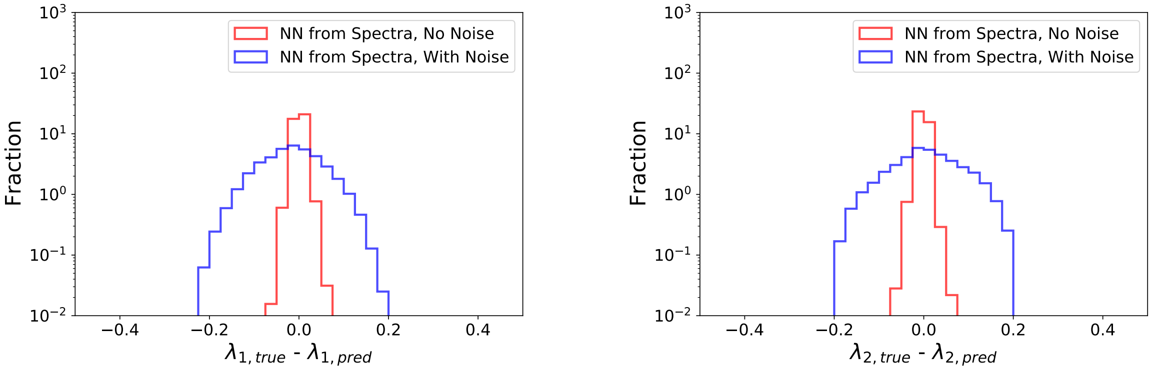

Figure 5.17: Performance of the neural network regression of the neutron star EOS parameters λ_1 (top) and λ_2 (bottom) directly from a set of stellar X-ray spectra, without intermediate prediction of the mass and radius. Shown is the residual, the difference between the true and predicted values, for spectra with statistical noise (blue) corresponding to an observation time of 100k seconds per star, and for spectra without statistical noise (red), which demonstrates the capacity of the network. Nuisance parameters are fixed to their true values.

upper limit for the two fully neural network-based methods, which must infer the relationships. The three approaches perform comparably, and the end-to-end method slightly but consistently outperforms the two-step method using MR_Net. Once trained, the end-to-end network can handle any prior on the nuisance parameters, whereas the networks that rely on XSPEC fits or MR_Net predictions need first to be trained on data with the desired prior.

When the data are simulated and drawn from a known theoretical model, one cannot achieve more statistical power than directly calculating the likelihood. However, even powerful theoretical models for spectral fitting still rely on a variety of assumptions about the spectrum's source. The flexibility of these fully neural network-based approaches is an important advantage, opening the door to interpolating between theoretical models [134], or even learning directly from observational data [231, 232]. An inference approach with this flexibility and the capacity for robust propagation of uncertainties is vital.

As a further visualization, Figure 5.21 shows several example curves in the mass-radius

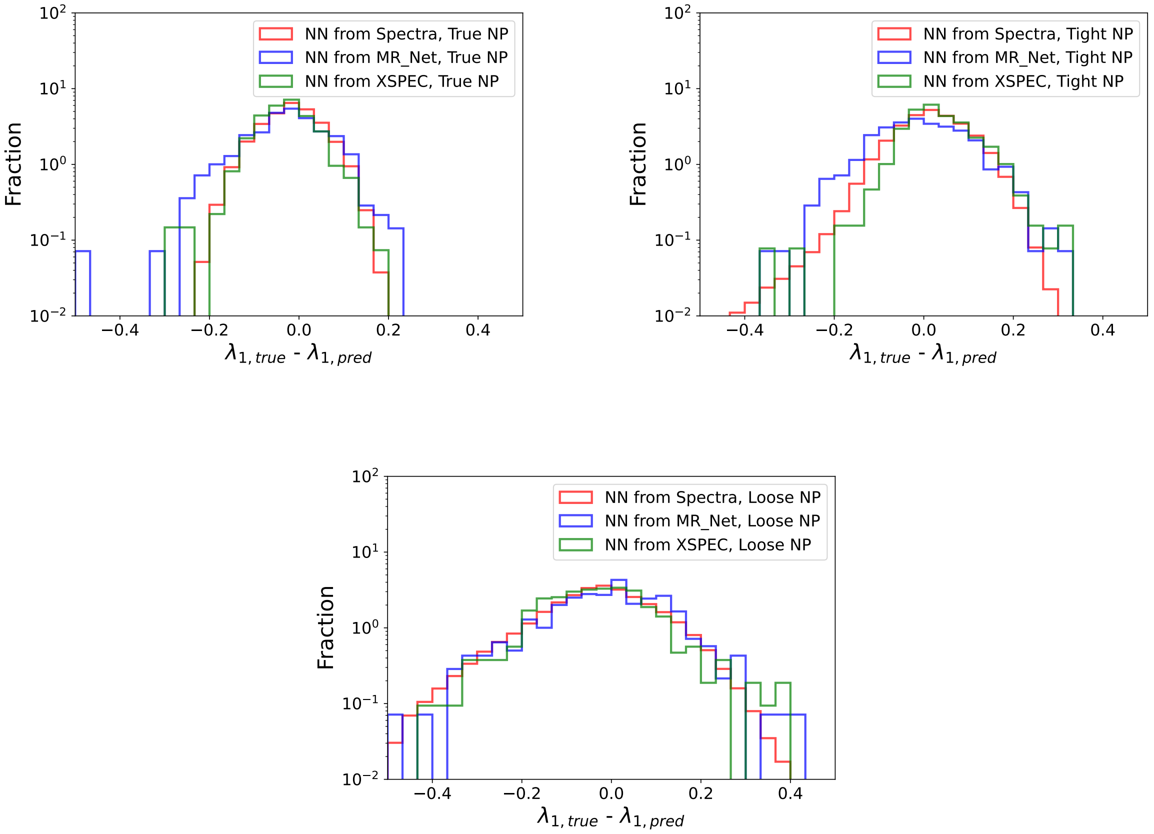

Figure 5.18: Performance of the regression of neutron star EOS parameter λ_1 using direct regression from spectra, as compared to regression from mass and radius information extracted via MR_Net or XSPEC. Shown are the residual distributions, the difference between the true and predicted values, under three scenarios of nuisance parameter uncertainties. See Table 5.4 for quantitative analysis. In the "true" case, the NPs are fixed to their true values; in the "tight" and "loose" cases, they are drawn from narrow or wide priors, respectively (see text for details).

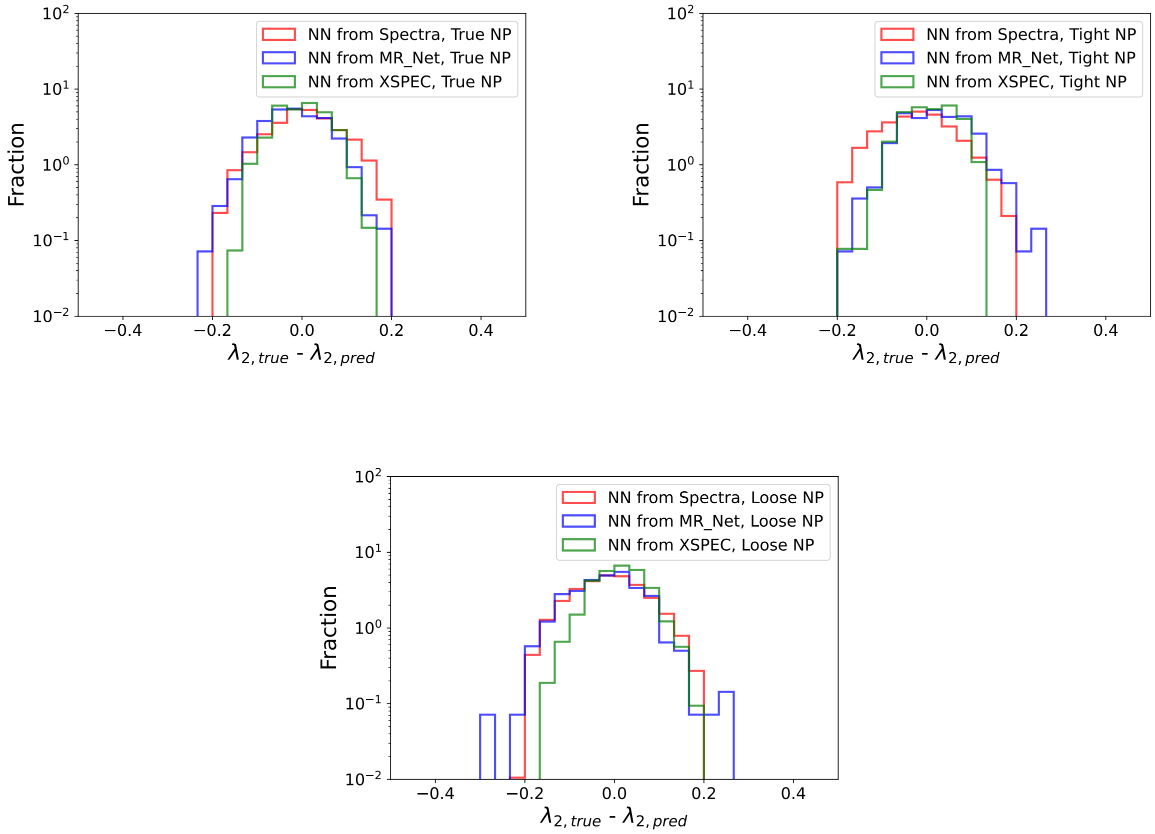

Figure 5.19: Performance of the regression of neutron star EOS parameter λ_2 using direct regression from spectra, as compared to regression from mass and radius information extracted via MR_Net or XSPEC. Shown are the residual distributions, the difference between the true and predicted values, under three scenarios of nuisance parameter uncertainties. See Table 5.4 for quantitative analysis. In the "true" case, the NPs are fixed to their true values; in the "tight" and "loose" cases, they are drawn from narrow or wide priors, respectively (see text for details).

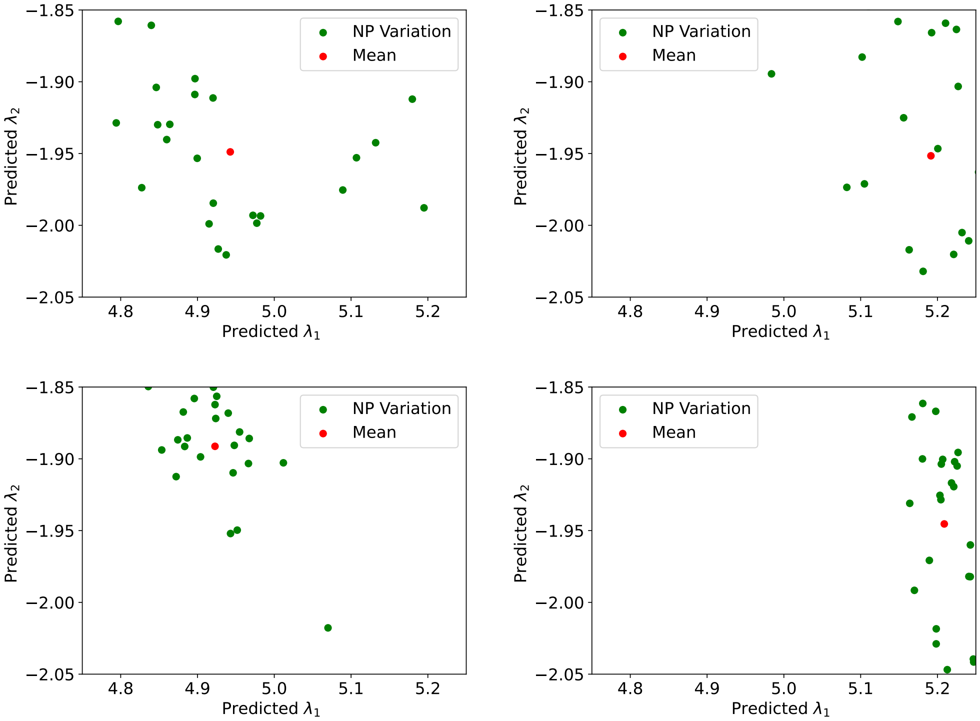

Figure 5.20: Neural network regression of the EOS parameters λ_1 and λ_2 of a set of 10 neutron stars directly from the set of stellar spectra. Each pane represents an example dataset of 10 simulated stars, and shown (green) are EOS estimates for several independent values of the stellar nuisance parameters drawn from the associated priors, and the mean value (red). Top two cases have loose priors, bottom two have tight.

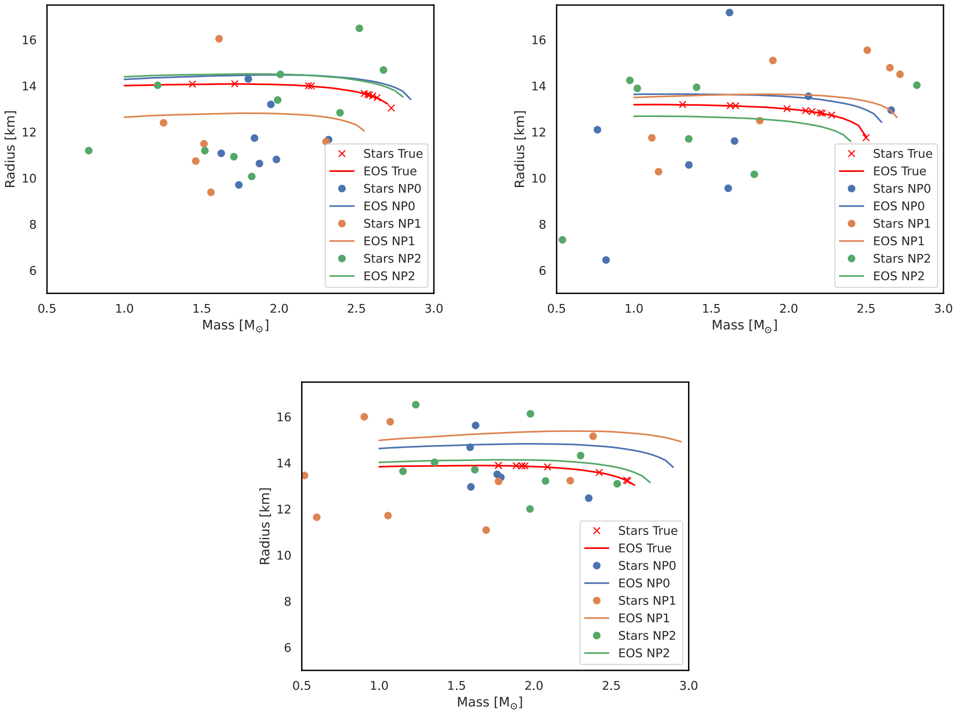

Figure 5.21: Demonstration of the impact of nuisance parameters on the regression of EOS parameters for three sets of observed stellar spectra. In red are the true mass and radius of the stars, drawn from the mass-radius curve determined by the true EOS parameters. In blue dots are the values of the mass and radius deduced by MR_Net for each star given a set of stellar NPs drawn from the priors; the blue line shows the mass-radius curve corresponding to the EOS parameters deduced directly from the stellar spectra and NPs by the proposed end-to-end regression. The results of MR_Net are not used in the EOS regression and only appear to aid the visualization. Brown and green are similar to blue but for independent draws of the NPs from the same stellar priors.

plane fitted to the same stellar spectra with varying nuisance parameters.

5.9 Conclusions

We have demonstrated the network regression of EOS parameters from realistic neutron star mass and radius estimates drawn from simulated stellar spectra. Our approach of conditioning each step on nuisance parameters allows us to fold in the NP uncertainty via multiple sampling from priors and permits full propagation of the uncertainty through to the final regression targets. The full propagation is important because variation in NPs does not produce variations in the mass and radius of neutron stars that can be accurately summarised as two-dimensional uncorrelated Gaussians (see Figure 5.14), as has been assumed in previous studies. In addition, we have shown that networks can analyze high-dimensional telescope data directly, including sets of multiple stars, and achieve comparable performance to methods that assume perfect knowledge of the theoretical model used to generate the simulated samples. In realistic cases where the nuisance parameter uncertainties are significant, the proposed end-to-end network regression achieves comparable precision in EOS regression to the network using XSPEC fits or MR_Netpredictions.

These results suggest many future directions. Our networks are parameterized in the nuisance parameters, allowing for the propagation of prior uncertainties which are implicity derived from auxiliary data. However, the stellar spectra may also offer information that constrains the NP uncertainty. Profiling over the nuisance parameters could reduce this uncertainty, though it may be computationally very expensive without neural likelihood estimation techniques [233].

Alternatively, rather than employing regression to directly produce estimates of the EOS parameters, one might train a generative model to operate as a surrogate of the likelihood [234], allowing for fast evaluation of the likelihood as a function of the EOS parameters and potentially direct profiling.

To reduce the impact on one particular set of theoretical assumptions, such networks may be trained on a collection of theoretical models, and in the future when more telescope data becomes available, even trained directly from observed spectra.

Other future directions for the networks described in this paper would be to test more exotic neutron star equations of state, including those with 1st order (i.e., constant pressure) phase transitions. Including additional parameters will play a key role in conducting similar research using alternative models in XSPEC that rely on different nuisance parameters, like a Helium atmospheric model. Even more interesting would be extending this type of EOS inference to other compact objects like white dwarfs.

Chapter 6

Equation of State Inference from Simulated X-ray Spectra using Machine Learning Derived Likelihoods

This chapter presents text and results from previously published work (Ref. [235]) in collaboration with Pierre Baldi, Jordan Ott, Aishik Ghosh, Andrew W. Steiner, Atharva Kavitkar, Lee Lindblom, Daniel Whiteson, and Fridolin Weber.

6.1 Introduction

In this chapter, we extend the premise of inference of EOS from X-ray spectra beyond regression using the same dataset from Chapter 5; the work presented in this chapter is the same as it appears in Ref. [235]. This chapter introduces a different novel approach to the inference of EOS parameters from neutron star X-ray spectra using likelihood estimation, in which the likelihood is made tractable by replacing the intractable elements with neural networks trained on samples of simulated stars. Rather than directly learning the entire likelihood [236] in one step, we leverage our knowledge of the problem by replacing only the crucial missing pieces, which focuses on the learning task and allows the interpretation of network outputs as physically meaningful quantities. The resulting *machine-learning-derived likelihood* of observing a set of stellar spectra given EOS parameters allows for estimation of the EOS parameters via Bayesian *maximum a posteriori* and use of standard error estimation techniques. The derivation of this machine-learning-derived likelihood is shown schematically in Figure 6.1.

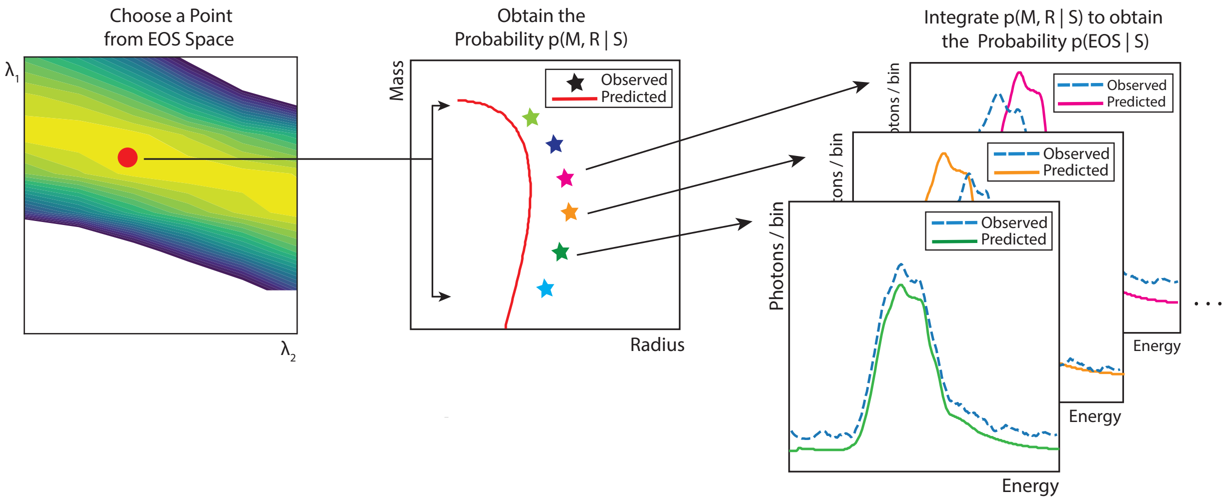

Figure 6.1: Schematic diagram depicting the evaluation of the likelihood of producing a set of observed stellar spectra by comparing it to the predicted spectra along the mass-radius curve determined by EOS parameters λ_1, λ_2. Each value of the EOS parameters determines a curve in the mass-radius plane. Integrating along the curve, the probability of observing each star is evaluated as in Fig. 6.2.

This chapter is outlined as follows. The strategy for machine-learning-derived likelihoods is described in Section 6.2. Sections 6.3 and 6.4 demonstrate the likelihood calculation and extraction of parameter estimates for mass-radius information and EOS parameters, respectively. Section 6.5 presents a discussion of the results, conclusions, and future directions.

6.2 Machine-Learning Derived Likelihood Calculation

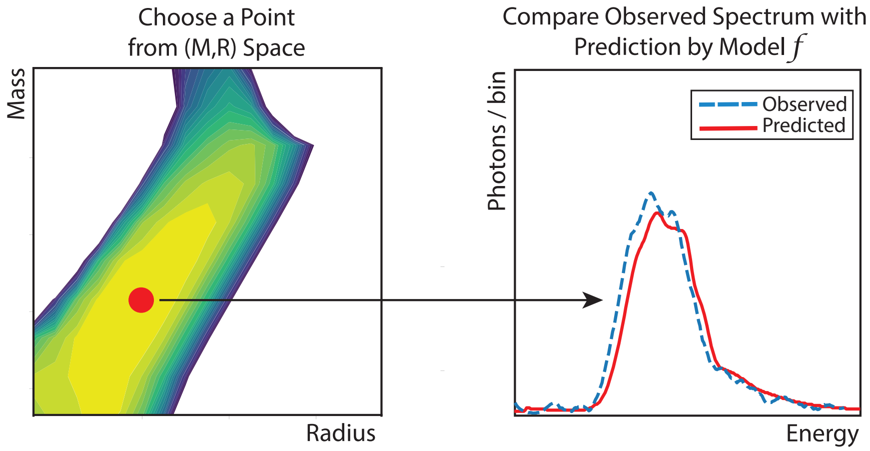

Figure 6.2: Schematic diagram depicting the evaluation of the likelihood of producing on the observed stellar spectrum by comparing it to the predicted spectrum for assumed values of stellar mass and radius. Varying the assumed mass and radius allows for an evaluation of the likelihood across the (M, R) parameter space.

If the likelihood $p(x|\theta)$ of observing some data x for given values of the theoretical model parameters θ were known, estimating the value of θ for a given x would be a straightforward task. In a Bayesian approach, one would use *maximum a posteriori* (MAP) to find $\hat{\theta}$, the value of θ which maximizes the product of the likelihood and the prior $p(\theta)$.

In the case of neutron star EOS estimation, the likelihood $p(S|\lambda_1, \lambda_2)$ of observing a set of stellar spectra S for a given choice of EOS parameters λ_1, λ_2 is not tractable. Instead, simulation-based inference [137] techniques often circumvent the need for a closed-form likelihood by approximating $p(S|\lambda_1, \lambda_2)$ using density estimation with simulated samples. But accurately estimating the density in high-dimensional spaces such as those for stellar spectra, with dimensionality of $\approx \mathcal{O}(1000)$, would require prohibitively large samples of simulated events. Instead, we use machine learning to estimate the likelihood. But rather than estimating the entire likelihood in one step, our machine-learning-derived likelihood calculation focuses on the statistical power where it is most needed for a given set of observations by combining the available analytic components with neural networks to replace the intractable components.

For the estimation of parameters such as EOS or mass and radius, many elements of the likelihood calculation are known, such as the Poisson fluctuations within each energy bin of a stellar spectrum. However, there are two elements without closed-form expressions that require machine-learning assistance. We overview those intractable components here briefly and provide more detail below.

The first missing piece is a prediction for the expected photon rates observed in a telescope given stellar parameters M and R and nuisance parameters ν. Below, we train a neural network to estimate this quantity and demonstrate its application by doing MAP estimates of M and R, in which we integrate over the nuisance parameters ν.

The second missing piece is a prediction for the mass-radius values allowed by given EOS parameters λ_1, λ_2. We train a neural network to output the allowed radius for a given stellar mass when provided with the EOS parameters. This allows integration over the $M-R$ curve defined by the EOS.

Together, these two machine-learned elements allow for a tractable calculation of the likelihood $p(S|\lambda_1, \lambda_2)$ and provide a MAP estimate of λ_1, λ_2 for a given set of spectra S. We describe each piece in turn below.

6.3 Stellar Mass and Radius Inference

The mass and radius of a neutron star can be estimated from its spectrum s if one can calculate and maximize $p(s|M, R)p(M, R)$ for a fixed s. This requires access to $p(s|M, R)$, which depends on $p(s|M, R, \nu)$, the likelihood to produce this spectrum s given the full set of stellar parameters including the nuisance parameters ν:

$$p(s|M,R) = \int d\nu \; p(s|M,R,\nu) \; p(\nu), \tag{6.1}$$

If the spectra consist of a set of energy bins of telescope photon counts,

$$s = (N_1^\gamma, N_2^\gamma, ..., N_{n_{\text{bins}}}^\gamma), \tag{6.2}$$

then the joint likelihood $p(s|M,R,\nu)$ over the bins can be written as:

$$p(s|M,R,\nu) = \prod_j^{n_{\text{bins}}} \text{Pois}(N_j^\gamma, \mu_j(M,R,\nu)), \tag{6.3}$$

where Pois refers to the Poisson distribution and μ_j is the expected number $\langle N_j^\gamma \rangle$ of photons in bin j of n bins:

$$\mu(M,R,\nu) = (\langle N_1^\gamma \rangle, \langle N_2^\gamma \rangle, ..., \langle N_{n_{\text{bins}}}^\gamma \rangle), \tag{6.4}$$

determined by M, R, ν via complex physics of the stellar emission model as well as the telescope response. In principle, for this specific scenario, this function is contained within XSPEC, but is not exposed to the user in a convenient fashion which would allow for a rapid evaluation of many points, as needed for this application. More generally, one may want to learn a function in scenarios where no function is available, or where the training sample contains examples generated from a mixture of models where no single simple function can describe all samples.

When we do not have access to a simple expression for $\mu(M,R,\nu)$, it is possible to train a neural network to learn a function $f[M,R,\nu]$:

$$f[M,R,\nu] \rightarrow (\frac{dN_1^\gamma}{dt}, \frac{dN_2^\gamma}{dt}, ..., \frac{dN_{n_{\text{bins}}}^\gamma}{dt}), \tag{6.5}$$

such that $\mu(M, R, \nu)$ can be estimated from $f(M, R, \nu)$ scaled by the observation time Δt:

$$\mu(M, R, \nu) \approx f[M, R, \nu]\Delta t. \tag{6.6}$$

The likelihood $p(s|M, R, \nu)$ can then be estimated as:

$$p(s|M, R, \nu) = \prod_{j}^{n_{\text{bins}}} \text{Pois}(N_j^\gamma, \mu_j = f[M, R, \nu]_j \Delta t), \tag{6.7}$$

where the final likelihood can be obtained by marginalizing over the nuisance parameters:

$$p(s|M, R) = \int d\nu \; p(s|M, R, \nu) \; p(\nu) = \int d\nu \prod_{j}^{n_{\text{bins}}} \text{Pois}(N_j^\gamma, \mu_j = f[M, R, \nu]_j \Delta t) p(\nu). \tag{6.8}$$

This estimate allows for a scan of the M, R plane for the values that maximize $p(s|M, R)p(M, R)$ to find the MAP estimate for (M, R) given a fixed s. Schematically, this process is shown in Fig 6.2.

6.3.1 Learning the Model f to Model Stellar Spectra

The estimated likelihood requires learning a function $f[M, R, \nu]$ which produces the expected stellar spectrum in each bin. This function is modeled by a deep neural network with five inputs (M, R, and the three components of ν: effective temperature, distance, and N_H) and 250 outputs, one for each of the spectral bins.

The network architecture includes two input branches, one to process the mass and radius, and another to process the nuisance parameters. Each branch contains a series of nine layers, with 2048 nodes and leaky Rectified linear units (ReLU) activation, that process its inputs in isolation. Following these initial layers, the output from the branches is combined together, forming a single volume with all information. This grouping is then passed to another successive set of nine layers which produce the generated spectra. The choice of hyperparameters has a significant impact on the performance of this network. A complete list of hyperparameters tried is given in Appendix D; the architecture used for model f was the configuration with the best performance on the validation set.

Generating the spectra is formulated as a supervised learning problem, where the network learns to minimize the error between the true spectra and its predictions for a set of simulated examples generated by XSPEC. The weights are updated with gradient descent via backpropagation. The Huber loss function [225] is used, which is a standard loss function for regression robust to outliers, and the Adam optimizer [223] computes gradients and schedules the backward passes.

Figure 6.3 shows several examples of generated spectra. Each subplot contains generated results using various values of mass, radius, and nuisance parameters. The predictions are shown with their corresponding version from XSPEC. The predictions track the XSPEC values remarkably well across a range of parameter values. In general, we notice a slight overprediction by the network; below, we estimate the potential bias due to this overprediction and find it to be negligible compared to statistical uncertainties and other systematic uncertainties.

6.3.2 Results

The machine-learning-derived likelihood is tractable, allowing for a scan of $p(s|M, R)$ for individual stars. Fig. 6.4 shows examples of two individual simulated stars under the three nuisance parameter scenarios.

The likelihood can then be used to produce estimated values of neutron star mass and radius for a given spectrum, after marginalizing over the nuisance parameters. The mass-radius plane is scanned using adaptive optimization to find values that maximize the product

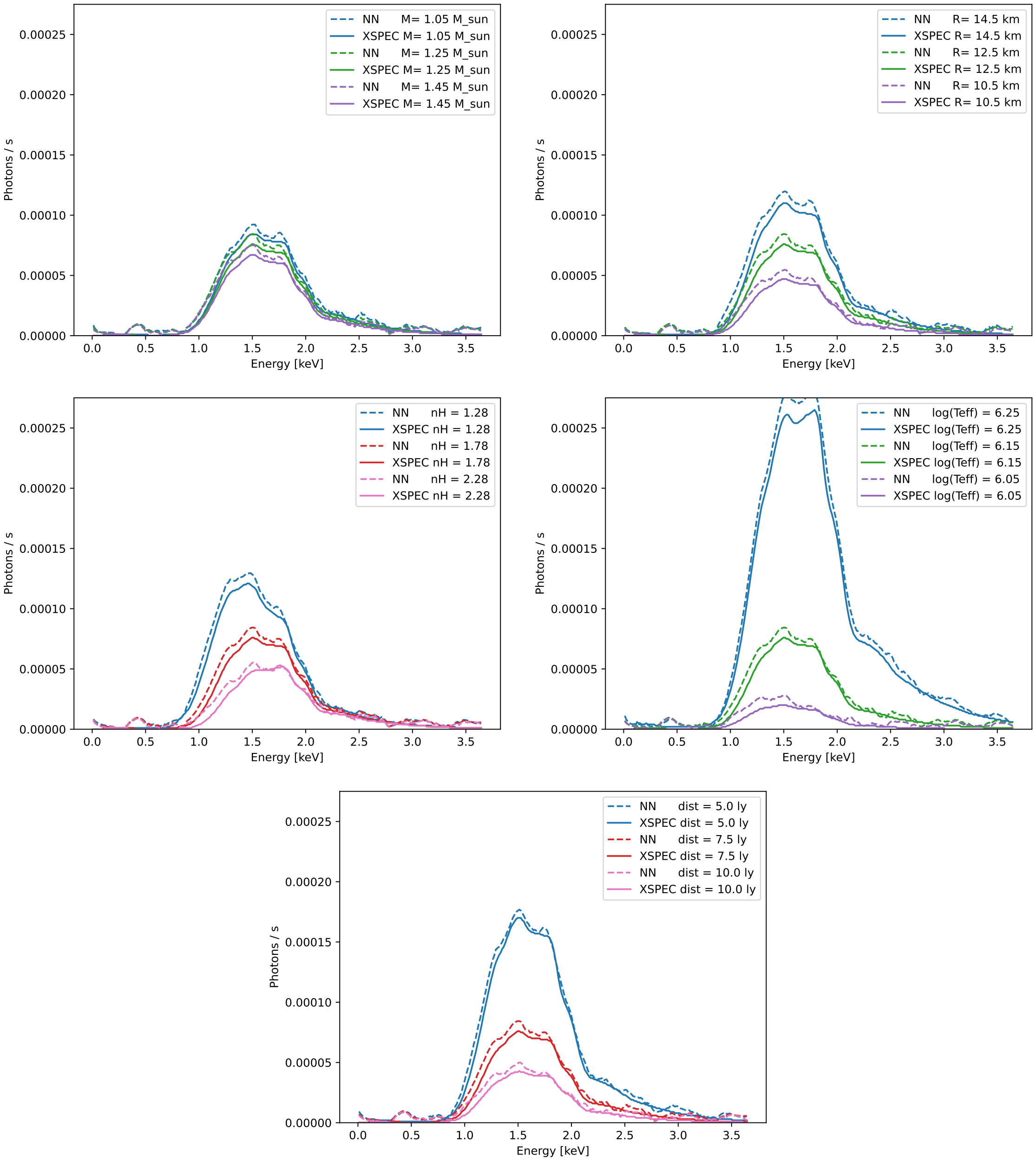

Figure 6.3: Comparison of neutron star X-ray spectra predictions (dashed) from our network $f[M, R, \nu]$ described in the text, as compared to training data generated by XSPEC (solid). Each pane shows the expected rate of photons ($\frac{dN_1^\gamma}{dt}$) in Chandra per energy bin, for variations of the parameters of interest (mass M, radius R) as well as for variations of the nuisance parameters ν (n_H, $\log(T_{\text{eff}})$, distance).

of the likelihood and the prior.

We assess the performance of this method to produce likelihood estimates, $\text{ML-Likelihood}_{\text{M,R}}$,

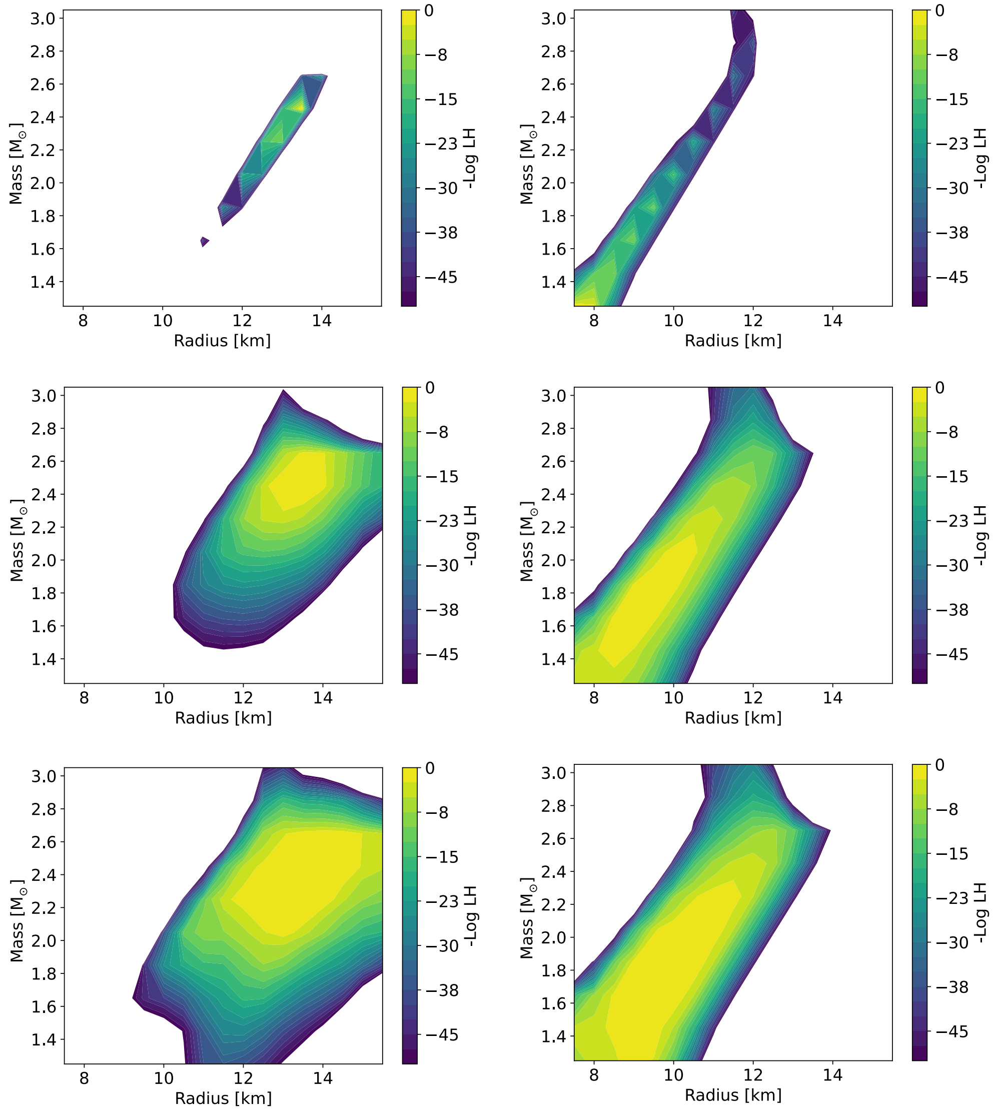

Figure 6.4: Scans of the likelihood for two example stellar spectra s (left, right) versus stellar mass and radius. Top demonstrates the ideal nuisance parameter (NP) conditions where the NPs are fixed to their true values. For the same simulated observed spectra, the center shows a more realistic "tight" scenario, and bottom shows a "loose" scenario in which the NPs are not well constrained by priors. In the "loose" and "tight" scenarios, dependence on the nuisance parameters has been integrated out as described in the text.

by calculating the residual between the true values of the mass and radius and the estimates produced by our method. As benchmarks, we compare the residuals to those generated by XSPEC itself, which has access to the true likelihood used to generate the simulated samples, as well as a regression-based method, MR_Net, described in Ref. [10]. Figure 6.5 and Table 6.1 shows a comparison of the results.

It is striking that ML-Likelihood$_{\mathrm{M,R}}$ outperforms MR_Net dramatically, despite being trained on the same dataset. ML-Likelihood$_{\mathrm{M,R}}$ benefits from the physics knowledge encoded in the approximate likelihood, which requires ML solutions only for a specific sub-task, rather than having to blindly learn the entire problem, as MR_Net must. ML-Likelihood$_{\mathrm{M,R}}$ performs essentially as well as XSPEC, even having smaller residuals when nuisance parameters have the most uncertainty, despite not having access to the explicit likelihood used to generate the data, as XSPEC does. Note that the performance comparison here highlights a *practical* difference between our method and use of XSPEC, rather than a *principled* difference in the methods. That is, our method of replacing the difficult calculational step with a learned ML model allows for convenient and rapid evaluation of the likelihood over many values of the nuisance parameters, enabling us to marginalize over them, which explains the improved relative performance. While in principle one could perform the same operation with XSPEC, its lack of a convenient programmable interface makes this impractical. The practical distinction is crucial, however, as it allows for greater general flexibility, such as interpolation across several models, or in application to the broader EOS inference problem described below, where likelihoods are not just hidden behind inconvenient interfaces, but completely unavailable.

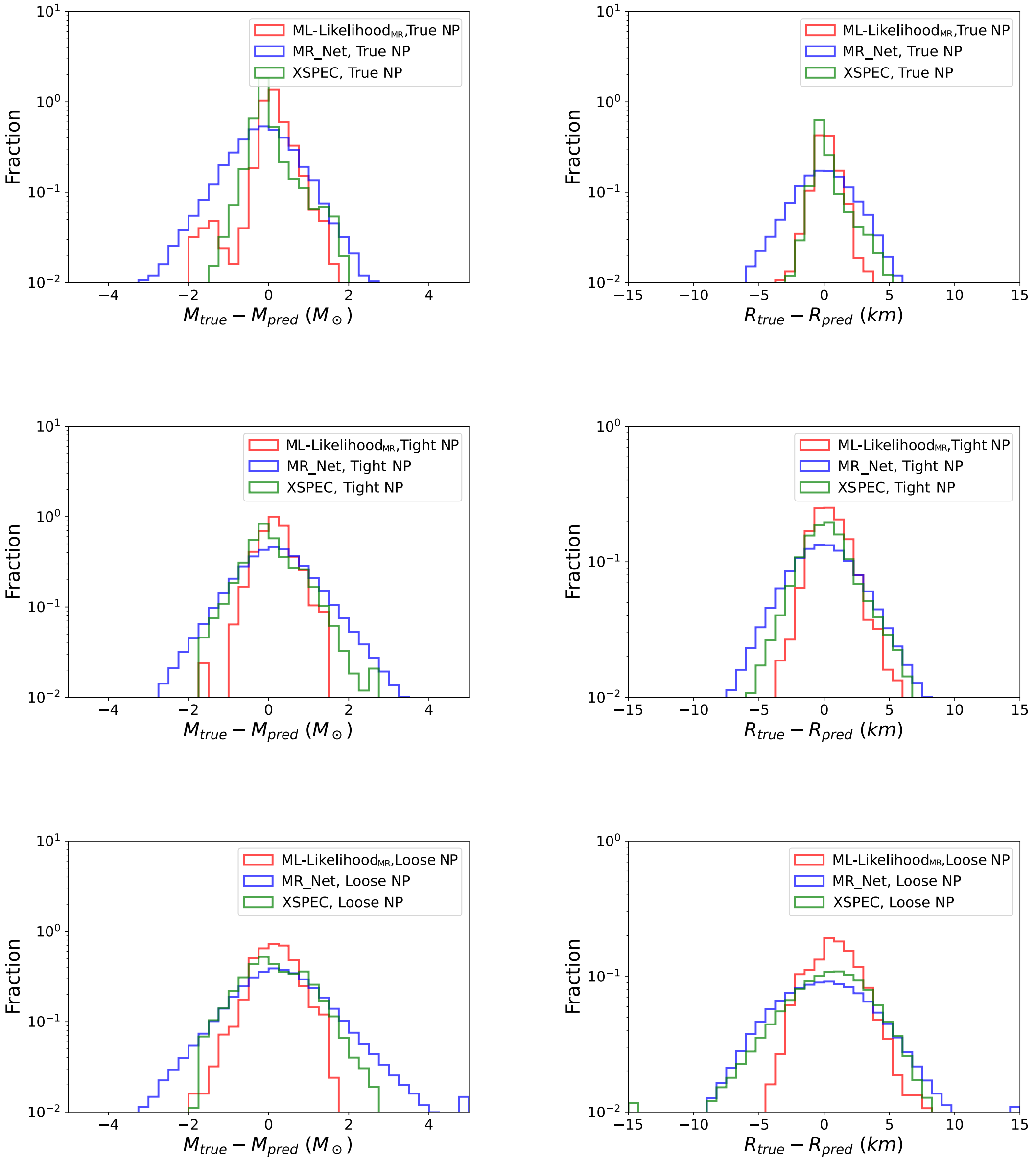

Figure 6.5: Performance of our estimation of neutron star mass (left) and radius (right) using an approximate likelihood which incorporates neural networks, ML-Likelihood$_{\mathrm{M,R}}$, in comparison to the performance of a pure regression network, MR_Net [10] and the XSPEC tool. Shown is the residual, the difference between the true and predicted values, for three scenarios of nuisance parameter uncertainties. In the "true" case, the NPs are fixed to their true values; in the "tight" and "loose" cases, they are drawn from narrow or wide priors, respectively; see text for details.

Table 6.1: Performance of our estimation of neutron star mass (left) and radius (right) using an approximate likelihood which incorporates neural networks, ML-Likelihood$_{\mathrm{M,R}}$, in comparison to the performance of a pure regression network, MR_Net [10] and the XSPEC tool. Shown are the mean (μ) and standard deviation (σ) of the residual distributions under three scenarios of nuisance parameter uncertainties. In the "true" case, the NPs are fixed to their true values; in the "tight" and "loose" cases, they are drawn from narrow or wide priors, respectively; see text for details.

	Nuis.	Mass		Radius	
Method	Params	μ	σ	μ	σ
ML-Likelihood$_{\mathrm{M,R}}$	True	0.11	0.47	0.28	1.43
XSPEC	True	-0.01	0.50	0.23	1.44
MR_Net	True	-0.14	0.93	-0.7	2.80
ML-Likelihood$_{\mathrm{M,R}}$	Tight	0.15	0.50	0.57	1.87
XSPEC	Tight	0.06	0.73	0.24	2.61
MR_Net	Tight	0.17	1.06	0.06	3.52
ML-Likelihood$_{\mathrm{M,R}}$	Loose	0.15	0.58	0.91	2.42
XSPEC	Loose	0.18	0.86	-0.15	4.32
MR_Net	Loose	0.28	1.29	0.14	4.93

6.4 Equation of State Inference

The ultimate goal is to estimate the EOS parameters (λ_1, λ_2) given a set of spectra $S = (s_1, s_2..., s_{n_{\mathrm{stars}}})$. In principle, this would be straightforward if one could evaluate $p(S|\lambda_1, \lambda_2)p(\lambda_1, \lambda_2)$, which would allow for maximization to find an estimate for λ_1, λ_2 for a fixed S.

We begin with the assumption that the EOS parameters have a uniform prior within their physical boundaries of $\lambda_1 \in [4.75, 5.25], \lambda_2 \in -[1.85, -2.05]$ (see Fig 3 of Ref. [10]). The remaining step is evaluating $p(S|\lambda_1, \lambda_2)$.

First, we express the probability over the entire set S as the joint probability for each star s_i:

$$p(S|\lambda_1, \lambda_2) = \prod_{i}^{n_{\mathrm{stars}}} p(s_i|\lambda_1, \lambda_2). \tag{6.9}$$

The obstacle is that we do not know how to evaluate $p(s|\lambda_1, \lambda_2)$, only $p(s|M, R)$, which depends on stellar parameters M and R. Linking these expressions is not trivial, as the EOS parameters λ_1, λ_2 do not uniquely determine stellar parameters M and R, instead they only determine the M-R relation. That is, each point in (λ_1, λ_2) space specifies a curve in M-R space. The solution is to integrate over the M-R curve allowed by the EOS parameters λ_1, λ_2. This is most directly accomplished by expressing the integral over the mass-radius plane, constrained by a delta function which traces out the M-R curve determined by the EOS parameters λ_1, λ_2:

$$p(s|\lambda_1, \lambda_2) = \int dMdR \; p(M, R|\lambda_1, \lambda_2) p(s|M, R) \,, \tag{6.10}$$

where $p(M, R|\lambda_1, \lambda_2)$ describes the allowed M-R relation given the EOS specified by λ_1, λ_2, as:

$$p(M, R|\lambda_1, \lambda_2) = \delta(h_\lambda[M] - R) \;\; p(M|\lambda_1, \lambda_2), \tag{6.11}$$

where $h_\lambda[M] \to R$ is a function that gives the allowed value of R for a value of M, determined by the EOS parameters λ_1, λ_2. The function $h_\lambda[M]$ encodes all of the physics which translates the EOS into stellar mass and radius, and is not available analytically or tractable numerically. It is possible, however, to train a neural network to learn this function, as we do below. Assuming $h_\lambda[M]$ is available, we choose to integrate over mass, as each mass is mapped to a unique R; the same is not true for scanning in R, as shown in Fig. 6.6.

The delta function reduces the double integral in M and R to a single integral over mass:

$$p(s|\lambda_1, \lambda_2) = \int dM \; p(M|\lambda_1, \lambda_2) \; p(s|M, R = h_\lambda[M]), \tag{6.12}$$

where the range of the mass integral is limited to the physical region, from $1.2M_\odot$ to $1.6 - 3.25M_\odot$, depending on the radius, as shown in Fig. 6.6. This allows us to write an expression for the joint probability over the set of stars:

$$p(S|\lambda_1, \lambda_2) = \prod_{i}^{n_{\text{stars}}} \int dM_i \; p(M_i|\lambda_1, \lambda_2) \; p(s_i|M_i, R_i = h_\lambda[M_i]). \tag{6.13}$$

We have now expressed the likelihood $p(S|\lambda_1, \lambda_2)$ in terms of the likelihood $p(s|M, R)$, which we previously learned to calculate. The equation for $p(s|M, R)$ now allows for the expression of a joint likelihood over the stars and the bins:

$$\begin{aligned} L_S(\lambda_1, \lambda_2) = p(S|\lambda_1, \lambda_2) = \prod_{i}^{n_{\text{stars}}} \int dM_i \; p(M|\lambda_1, \lambda_2) \\ \int d\nu \prod_{j}^{n_{\text{bins}}} \text{Pois}(N^{\gamma}_{ij}, \mu_{ij}(M_i, R_i = h_\lambda[M_i], \nu) p(\nu), \end{aligned} \tag{6.14}$$

where we can replace each of the μ_{ij} as we did above with $f[M, R, \nu]\Delta t$:

$$\begin{aligned} L_S(\lambda_1, \lambda_2) = p(S|\lambda_1, \lambda_2) = \prod_{i}^{n_{\text{stars}}} \int dM_i \; p(M|\lambda_1, \lambda_2) \\ \int d\nu \prod_{j}^{n_{\text{bins}}} \text{Pois}(N^{\gamma}_{ij}, \mu_{ij} = f[M_i, h_\lambda[M_i], \nu]_j \Delta t) p(\nu). \end{aligned} \tag{6.15}$$

This expression can be evaluated, assuming one can learn a function $h_\lambda[M] \rightarrow R$. The determination of the likelihood $L_S(\lambda_1, \lambda_2)$ is shown schematically in Fig. 6.1.

6.4.1 Learning the Model h to Model Stellar Radius

The approximate likelihood above requires learning a function $h_\lambda[M]$ which estimates the stellar radius for a given stellar mass as determined by the EOS parameters λ_1, λ_2. Note that one could equivalently estimate the mass from the radius, but this has the additional complication of degenerate outputs for some radii, as shown in Fig. 6.6. It is important here to note that model $h_\lambda[M]$ is trained on M-R relations created by equations of state

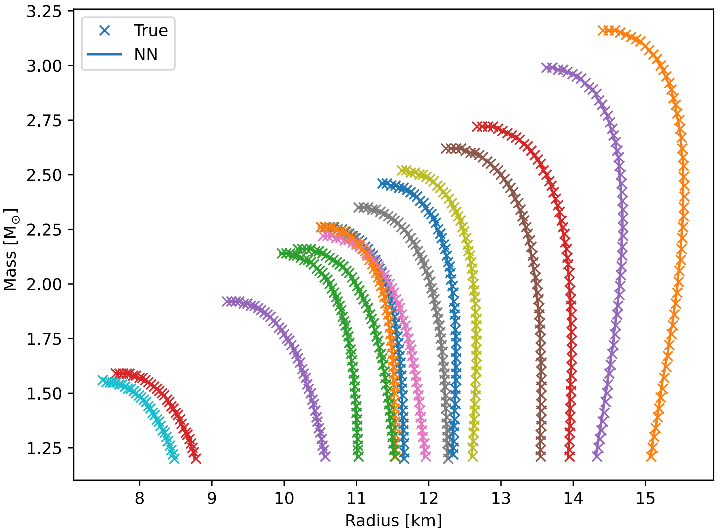

Figure 6.6: Relationship between neutron star mass and radius, as determined by equation of state parameters λ_1, λ_2. Each color represents a single choice of EOS parameters, which determine a curve in the mass-radius plane. Individual calculations as described in the text are shown (crosses), as compared with the output of a neural network function $h_\lambda[M]$ (solid line), which estimates the radius corresponding to an input value of M as determined by the EOS parameters.

that do not feature a phase transition; parameterizing the M-R relation as a function of $R = h_\lambda[M]$ may miss details stemming from more exotic features, like those caused by a strong, first-order phase transition, in the EOS.

We model $h_\lambda[M]$ with a deep neural network comprising 10 hidden layers with 32 nodes each and ReLU activation. The output layer is a single node with linear activation, which is standard for regression. The number of hidden layers, their widths, and activation functions were optimized for the functionality of $h_\lambda[M]$; the relatively small width of 32 nodes and ReLU activation were found to perform well. The network was trained with Mean Squared Error (MSE) loss and the Adam optimizer. Figure 6.6 demonstrates how the network $h_\lambda[M_i] \to R$ performs for a few example values of the EOS parameters λ. Generation of the training data as described above required approximately 24 hours of CPU time for 10^6 stars; in comparison, evaluation of the network $h_\lambda[M]$ generates 10^6 stellar radii in 400 ms, a relative speed enhancement of 10^5.

6.4.2 Results

The two networks that model the missing functions f and h allow for an approximate evaluation of the likelihood, Eq. (6.15) as a function of the EOS parameters. Figure 6.7 shows examples of two individual sets of simulated stars under the three nuisance parameter scenarios.

To estimate the EOS parameters from a fixed set of stellar spectra, the likelihood is maximized via a course scan over EOS parameter space followed by the use of an optimization algorithm for a more refined location of the optimal EOS parameters. Each evaluation of the likelihood involves nested loops over the stars, an integral over possible masses, and a loop over the spectral bins. Performance of ML-Likelihood$_{\mathrm{EOS}}$ and comparison with benchmarks are shown in Fig. 6.8 and Table 6.2. We note that the data used in evaluations are generated via XSPEC, not from the models f and h, allowing for a test of the fidelity of the machine-learned models. Experiments in which simulated spectra are generated using the models f and h show equivalent performance, indicating that any bias due to mis-estimation by f or h is negligible in this context.

6.5 Discussion

The results in this chapter demonstrate that machine-learning-derived likelihoods are useful statistical tools, allowing for traditional inference such as parameter estimation for quantities of interest (eg stellar M and R) as well as profiling over nuisance parameters (eg stellar distances and temperatures).

In the case of M,R-estimation for an individual star, the performance of the ML-Likelihood$_{\mathrm{M,R}}$ method matches the performance of XSPEC when the nuisance parameters are known. This is an important validation of the technique, as the simulated samples are generated by

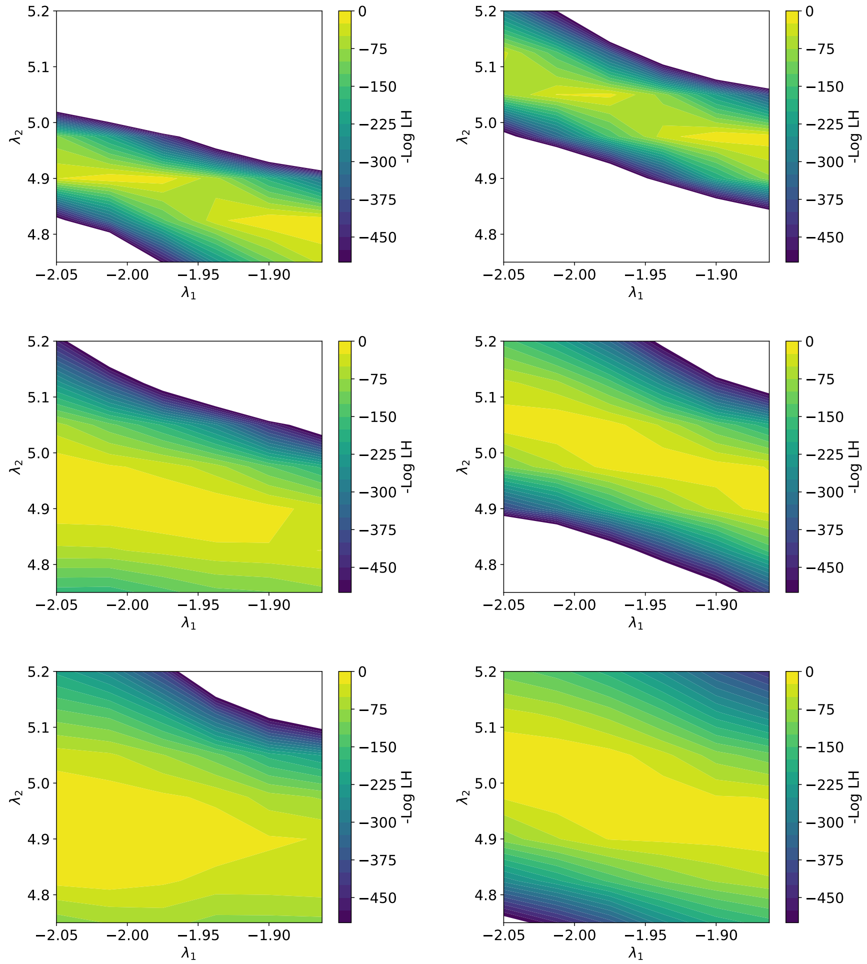

Figure 6.7: Scans of the likelihood for two example sets of stellar spectra s (left, right) versus EOS parameters λ_1 and λ_2. Top demonstrates the ideal nuisance parameter (NP) conditions where the NPs are fixed to their true values. For the same simulated observed spectra, the center shows a more realistic “tight” scenario, and the bottom shows a “loose” scenario in which the NPs are not well constrained by priors. In the “loose” and “tight” scenarios, dependence on the nuisance parameters has been integrated out as described in the text.

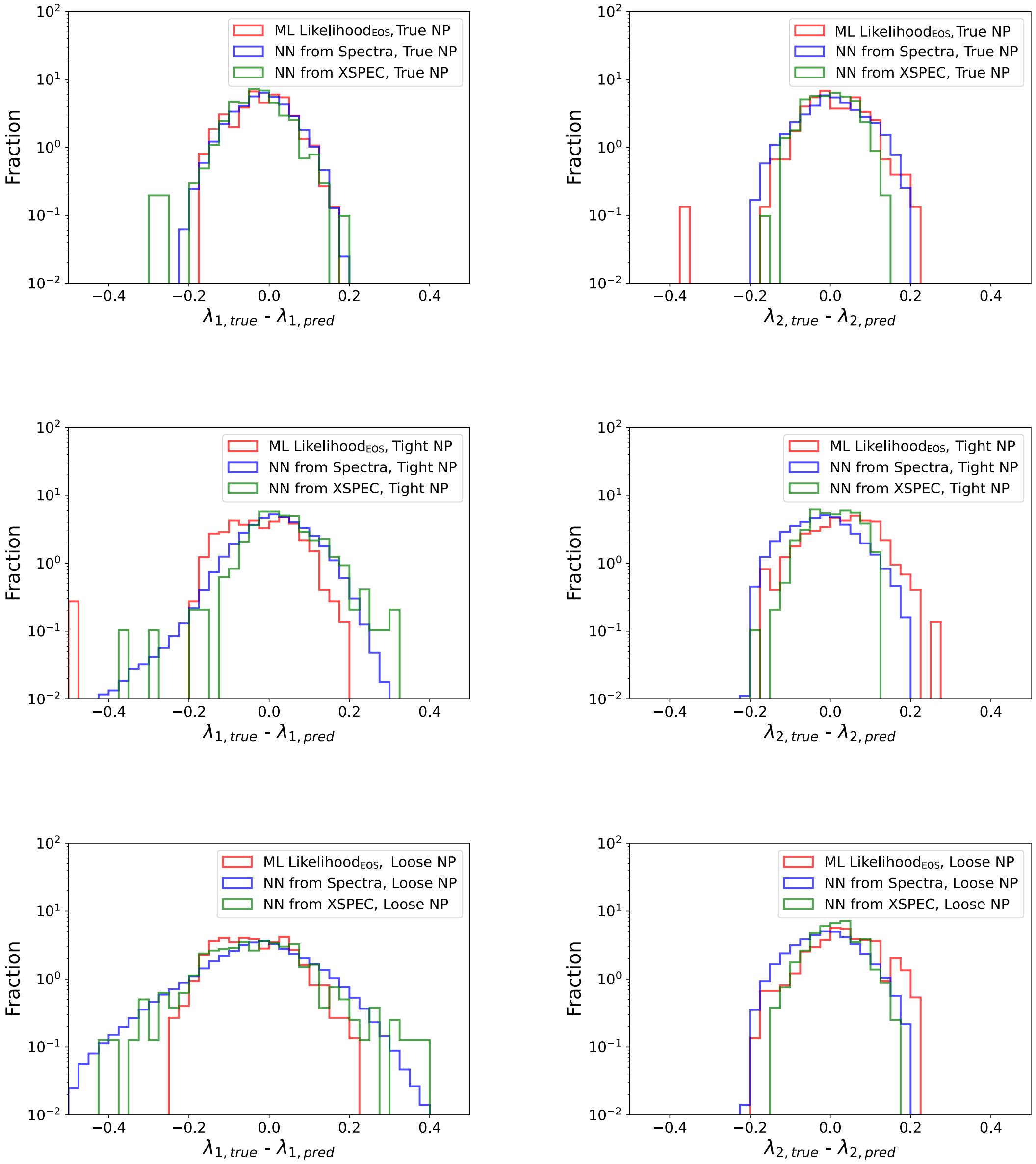

Figure 6.8: Performance of our estimation of neutron star EOS parameters λ_1 (left) and λ_2 (right) using an approximate likelihood that incorporates a neural network, ML-Likelihood$_{\mathrm{EOS}}$, in comparison to the performance of a spectra-to-EOS regression network and network which regresses EOS parameters from M, R values estimated by XSPEC, both from Ref. [10]. Shown are the residual distributions, the difference between the true and predicted values, under three scenarios of nuisance parameter uncertainties. See Table 6.2 for quantitative analysis. In the "true" case, the NPs are fixed to their true values; in the "tight" and "loose" cases, they are drawn from narrow or wide priors, respectively; see text for details

Table 6.2: Performance of our estimation of neutron star EOS parameters λ_1 (left) and λ_2 (right) using an approximate likelihood that incorporates a neural network, ML-Likelihood$_{\mathrm{EOS}}$, in comparison to the performance of a spectra-to-EOS regression network and network which regresses EOS parameters from M, R values estimated by XSPEC, both from Ref. [10]. Shown are the mean (μ) and standard deviation (σ) of the residual distributions under three scenarios of nuisance parameter uncertainties. See Fig 6.8 for distributions. In the "true" case, the NPs are fixed to their true values; in the "tight" and "loose" cases, they are drawn from narrow or wide priors, respectively; see text for details

		λ_1		λ_2		Combined
Method	Nuis. Params.	μ	σ	μ	σ	σ
ML-Likelihood$_{\mathrm{EOS}}$	True	-0.02	0.066	0.01	0.070	0.096
NN(Spectra)	True	-0.02	0.066	0.01	0.075	0.099
NN(M, R via XSPEC)	True	-0.03	0.065	0.01	0.055	0.085
ML-Likelihood$_{\mathrm{EOS}}$	Tight	-0.02	0.078	0.03	0.081	0.112
NN(Spectra)	Tight	0.02	0.085	-0.02	0.077	0.115
NN(M, R via XSPEC)	Tight	-0.03	0.081	0.01	0.056	0.098
ML-Likelihood$_{\mathrm{EOS}}$	Loose	-0.04	0.089	0.03	0.081	0.120
NN(Spectra)	Loose	-0.03	0.131	-0.01	0.078	0.152
NN(M, R via XSPEC)	Loose	-0.03	0.123	0.01	0.058	0.136

XSPEC and so its internal likelihood estimation represents something of an upper bound on possible performance. Though XSPEC can provide point estimates and other analysis, ML-Likelihood$_{\mathrm{M,R}}$ in this case is valuable as a building block for further analysis, as XSPEC does not provide an efficient interface to its internal calculations. For example, in the cases where nuisance parameters weaken the inference, ML-Likelihood$_{\mathrm{M,R}}$ can improve on XSPEC's performance by marginalizing over the stellar nuisance parameters. Given access to the full likelihood, one could also choose to profile over the nuisance parameters. In addition, while XSPEC's inference is linked to a particular theoretical model, ML-Likelihood$_{\mathrm{M,R}}$ can be trained on a variety or mixture of models, providing a smooth interpolation between otherwise distinct conceptual approaches [232].

The M, R-likelihood estimation is a building block toward the estimation of EOS parameters for sets of stars. In this case, as well, the likelihood provides for reliable inference of the EOS parameters, as demonstrated by the performance of ML-Likelihood$_{\mathrm{EOS}}$. The residuals in this case again are narrower than the pure regression approach, nearly matching the performance of XSPEC in the true case, and exceeding its unmarginalized estimates in the realistic case where nuisance parameter uncertainty is important.

Our method uses machine learning to enable what is typically termed a *forward* process, in that it aids the calculation of the likelihood of experimental data from the parameters, rather than *backward* inference of the parameters from the data. In this sense, it can be considered a fast and flexible simulation tool. The neural networks developed for this work effectively enable end-to-end, fast, and convenient simulation of neutron star spectra for a range of EOS parameters and nuisance parameters, including the intermediate step of generating plausible neutron star properties (mass and radius) for a given set of EOS parameters. In the case where the true likelihood exists but is not made conveniently accessible, our approach provides a powerful and flexible new interface, even without speed enhancements. In the more general case, such as for EOS inference, the approach additionally allows for more rapid generation of simulated stellar masses and radii for specific EOS parameters without solving the complex sets of equations underlying the physical model.

Once released, this framework will serve as a convenient simulation tool that can be used by the larger machine learning research community to generate neutron star samples without the expert knowledge required to run XSPEC or solve the TOV equations, and spur further innovation, such as in simulator-based inference techniques that can handle a large number of nuisance parameters, or to setup ML challenges where participants are given access to the simulator.

6.6 Conclusions

In this work, we demonstrate an alternative approach to deducing neutron star mass, radius, and EOS from simulated stellar X-ray spectra using machine learning. The alternative approach employs a technique novel to neutron star astrophysics, machine-learning-derived likelihoods, in which intractable elements of the calculation are replaced with machine-learned functions. This allows for an approximate likelihood calculation with increased interpretability. Our forward neural network model allows us to predict the X-ray spectra given a value of nuisance parameters, the equation of state parameters, and the neutron star mass. Forward modeling of this kind demonstrates how these networks are interpretable, testable, and often with the assumptions being explicit rather than implicit when compared to inverse models [203, 237]. The ML-Likelihood$_{\mathrm{EOS}}$ model outperforms our previous best-performing regression model, demonstrating the power of such a technique for point estimation. Note that it additionally provides access to the full likelihood, which can inform uncertainty estimation.

While the studies shown in this work demonstrate the power of the method to provide a tractable likelihood for stellar spectra generated from a specific model, the natural ability of neural networks to interpolate allows for the treatment of inherent model uncertainties, by training on samples with mixed or varying models [134].

The machine learning-driven calculations lend themselves to various future directions. As mentioned in the previous chapter, training data could be modified, either by using EOS models with different parametrizations or by using a different response matrix (e.g. from NuStar, NICER, or XMM-Newton as described in [238]) in XSPEC to generate simulated X-ray spectra. In addition, this technique can be rapidly applied to the analysis of X-ray spectra from recent observations. The networks developed for this work will become a convenient tool for fast simulation of neutron star spectra which can be run without the expert knowledge required to run XSPEC or to solve the TOV equations.

Chapter 7

Conclusions and Final Remarks

The work presented in this thesis employed different theoretical and computational techniques to study the equation of state (EOS) of dense nuclear matter and the structure of neutron stars. The topics investigated in this thesis align with NASA's roadmap and the long-range plans of NSF and DOE for nuclear science [239, 240], which emphasize the significance of extracting information about dense nuclear matter properties from astrophysical observations. The thesis aims to contribute to this goal by providing advanced models for the equation of state of hot and dense nuclear matter, specifically for use in simulations of binary neutron star mergers [241].

In Chapter 2, the properties of symmetric and asymmetric nuclear matter were investigated by performing self-consistent, relativistic Brueckner-Hartree-Fock (RBHF) calculations paired with the Bonn potentials for the OBE interaction, following the methodology outlined in [70] and [83]. The saturation properties of SNM are first determined at zero temperature with good agreement to empirical values from a wide variety of sources, and results are then used to calculate the properties of ANM and thus the EOS of neutron star matter at zero temperature. The methodology is extended to finite temperatures, and EOS models are produced up to a temperature of 70 MeV. The nuclear equations of state studied in this work incorporate finite temperatures in a self-consistent manner. This means that the effects of finite temperatures are not merely added on to models of cold nuclear matter, as has been commonly practiced in previous studies [165–167]. Instead, the finite-temperature effects are integrated into the fundamental framework of the equations of state, ensuring a more comprehensive and accurate representation of the thermodynamic properties of dense nuclear matter. At zero and finite temperatures, bulk properties of non-rotating and uniformly rotating neutron stars are computed up to the mass-shedding limit ($\Omega = \Omega_K$).

In Chapter 3, the numerical scheme for modeling differential rotation in neutron stars is introduced, following the methodology outlined in [104]. The bulk properties of differentially rotating hyperonic and Δ-admixed stars at zero temperature, modeled using the RHF formalism, are calculated to examine how the inclusion of Δ isobars in the EOS of dense matter impacts the corresponding stellar properties like mass and equatorial radius. Previous work [177] demonstrated that inclusion of Δ populations in hyperonic EOS models softens the EOS at low to intermediate densities but stiffens it at high densities due to the additional degrees of freedom, which slightly increases the maximum mass for a given EOS and decreases the radius significantly. For computed stellar sequences, it was shown that the inclusion of Δ's in the hypernuclear EOS does not change the total amount of mass increase once the differential rotation is allowed, meaning increasing the degree of differential rotation resulted in a similar percentage increase in mass for hyperonic and Δ-admixed stars. Additionally, density distribution maps of massive, differentially rotating stars were shown to demonstrate at what radial depth different particle species appear. The competition between the nucleation of Σ^- hyperon and Δ^- isobar was demonstrated, whose outcome depends on the value of the Δ^- potential in nuclear matter.

In Chapter 4, the ideas presented in the two previous chapters are combined to more closely describe a hypermassive remnant from a BNS merger, characterized by finite temperatures and differential rotation. This chapter modifies the numerical scheme from the previous chapter to be able to calculate stellar configurations more massive and deformed, demonstrated with stellar sequences calculated over a range of stellar deformation. These sequences are tested for stability against dynamical bar-mode excitation, where it was determined that the stars' deformation has a greater impact on stability than temperature against rotational instabilities. Density and frequency distribution maps were constructed for two temperatures, 10 and 50 MeV, where it was demonstrated that increasing the degree of differential rotation shifted the shape of the star from ellipsoid to quasi-toroidal.

While the topic of determining the EOS of neutron star matter theoretically is discussed in Chapter 2, the EOS is instead determined from observable properties using machine learning techniques in Chapters 5 and 6. In Chapter 5, EOS parameters are regressed from realistic neutron star mass and radius estimates drawn from simulated stellar spectra, a novel approach to the problem. This chapter used different neural network architectures in the regression task, where each step in the process is conditioned on so-called nuisance parameters, and nuisance parameter uncertainty is folded in via multiple sampling from priors; this technique permits full propagation of the uncertainty through to the final regression targets, improving upon similar implementations in the literature where uncertainty is collapsed into two-dimensional uncorrelated Gaussians.

The problem is expanded upon in Chapter 6, where machine-learning-derived likelihoods for bulk properties of neutron stars and the corresponding EOS are constructed and the intractable pieces of the likelihood are replaced using neural networks. Like in the previous chapter, the technique outlined in this chapter is used to determine the EOS for a set of stellar spectra, but can also be used in the reverse direction to determine either mass and radius or stellar spectra from a given EOS, thus making it a fast and flexible simulation tool. The model used to determine the EOS in this chapter outperforms the best-performing regression model from Chapter 5 and provides access to the full likelihood, demonstrating the power of forward modeling.

7.1 Future Directions

The projects described in this thesis open various directions for future work.

In modeling differential rotation, results presented in Chapters 3 and 4 use the linear, "j-constant" rotation law. While this law has widely been used in the literature, more recent studies of binary neutron star merger events suggest a linear rotation law can not fully capture the complexities of the rotation profile of the remnant object, especially immediately after formation. An interesting extension of the numerical scheme presented in this work would be to test how the bulk properties of differentially rotating stars are modified when using non-linear rotation laws.

I will also highlight that the numerical scheme for modeling differential rotation is not parallelized in its current form. This is perfectly fine when computing a sequence of stars over a central density range with a specified rotation parameter and r_{ratio}. When fixing these parameters, a sequence of 15 stars can be computed in approximately 2 minutes, which can increase or decrease depending on how "good" the initial guesses for the metric potentials and root-finding windows are. When computing sequences over a range of central densities and r_{ratio} values, as shown in Chapter 4, the runtime increases dramatically. For each star, the iteration process is run twice - the first to determine the densest portion of the star, fixing those coordinates as the maximum, and re-running to solve for the metric potentials. If r_{ratio} was kept fixed, this would simply double the runtime for each central density. However, the runtime increases exponentially when computing multiple stars with different r_{ratio} values at each central density. Future work could entail parallelizing the iteration loop over central density.

Concerning the application of machine learning techniques to the determination of the EOS of neutron star matter, potential future directions are very broad. For the specific work presented in this thesis, Chapters 5 and 6 bring up specific future directions regarding training data creation. The spectral representation used for the EOS can be extended to include more parameters, which may complicate the learning process but would be able to capture other features in the EOS like a phase transition. Additionally, the original EOS parametrization used to generate training data was the GM1L parametrization, only including protons and neutrons; another interesting future direction may be the inclusion of other particles like hyperons or Δ isobars as shown in Chapter 3. The Chandra response matrix was used to generate simulated X-ray spectra in XSPEC, but this could also be altered to use a newer observatory like NICER.

Beyond training data, ML techniques not discussed in this thesis could be employed that might be better suited for high-dimensional data like simulated X-ray spectra. A recent collaboration (not explicitly discussed in the thesis) I participated in with Len Brandes, Chirag Modi, Aishik Ghosh, Lee Lindblom, Lukas Heinrich, Andrew Steiner, Fridolin Weber, and Daniel Whiteson used a simulation-based inference technique, neural likelihood estimation, to determine the EOS from simulated X-ray spectra; in this work, a normalizing flow used samples of simulated spectra to learn the likelihood of observation as a function of the EOS and NPs [242]. The architecture and capability of ML grow rapidly, often outpacing scientific applications, meaning there will likely continue to be a better, more accurate, and more efficient way to approach determining EOS of neutron star matter from observable spectra.

Bibliography

[1] Anna L. Watts, Nils Andersson, Deepto Chakrabarty, Marco Feroci, Kai Hebeler, Gianluca Israel, Frederick K. Lamb, M. Coleman Miller, Sharon Morsink, Feryal Ozel, Alessandro Patruno, Juri Poutanen, Dimitrios Psaltis, Achim Schwenk, Andrew W. Steiner, Luigi Stella, Laura Tolos, and Michiel van der Klis. Colloquium: Measuring the neutron star equation of state using x-ray timing. *Rev. Mod. Phys.*, 88:021001, Apr 2016.

[2] Milva G Orsaria, Germán Malfatti, Mauro Mariani, Ignacio F Ranea-Sandoval, Federico García, William M Spinella, Gustavo A Contrera, Germán Lugones, and Fridolin Weber. Phase transitions in neutron stars and their links to gravitational waves. *Journal of Physics G: Nuclear and Particle Physics*, 46(7):073002, 2019.

[3] Mei Huang. Qcd phase diagram at high temperature and density. *arXiv preprint arXiv:1001.3216*, 2010.

[4] A Akmal, VR Pandharipande, and DG and Ravenhall. Equation of state of nucleon matter and neutron star structure. *Physical Review C*, 58(3):1804, 1998.

[5] MC Miller, Frederick K Lamb, AJ Dittmann, Slavko Bogdanov, Zaven Arzoumanian, Keith C Gendreau, S Guillot, AK Harding, WCG Ho, JM Lattimer, et al. Psr j0030+ 0451 mass and radius from nicer data and implications for the properties of neutron star matter. *The Astrophysical Journal Letters*, 887(1):L24, 2019.

[6] Yuki Fujimoto, Kenji Fukushima, and Koichi Murase. Mapping neutron star data to the equation of state using the deep neural network. *Phys. Rev. D*, 101(5):054016, 2020.

[7] Yuki Fujimoto, Kenji Fukushima, and Koichi Murase. Extensive Studies of the Neutron Star Equation of State from the Deep Learning Inference with the Observational Data Augmentation. *JHEP*, 03:273, 2021.

[8] Filip Morawski and Michał Bejger. Neural network reconstruction of the dense matter equation of state derived from the parameters of neutron stars. *Astron. Astrophys.*, 642:A78, 2020.

[9] Márcio Ferreira and Constança Providência. Unveiling the nuclear matter EoS from neutron star properties: a supervised machine learning approach. 10 2019.

[10] Delaney Farrell, Pierre Baldi, Jordan Ott, Aishik Ghosh, Andrew W Steiner, Atharva Kavitkar, Lee Lindblom, Daniel Whiteson, and Fridolin Weber. Deducing neutron star equation of state parameters directly from telescope spectra with uncertainty-aware machine learning. *Journal of Cosmology and Astroparticle Physics*, 2023(02):016, 2023.

[11] S. Typel, G. Röpke, T. Klähn, D. Blaschke, and H. H. Wolter. Composition and thermodynamics of nuclear matter with light clusters. *Phys. Rev. C*, 81:015803, Jan 2010.

[12] Lyndon Evans and Philip Bryant. Lhc machine. *Journal of instrumentation*, 3(08):S08001, 2008.

[13] H Hahn, E Forsyth, H Foelsche, M Harrison, J Kewisch, G Parzen, S Peggs, E Raka, A Ruggiero, A Stevens, et al. The rhic design overview. *Nuclear Instruments and Methods in Physics Research Section A: Accelerators, Spectrometers, Detectors and Associated Equipment*, 499(2-3):245–263, 2003.

[14] Subhasis Chattopadhyay. Facility for antiproton and ion research. *Current Science*, 100(5):598, 2011.

[15] VD Kekelidze. Nica project at jinr: status and prospects. *Journal of Instrumentation*, 12(06):C06012, 2017.

[16] M. Alford. Ann. rev. nucl. part. sci. **51** (2001) 131. *Annual Review of Nuclear and Particle Science*, 51:131, 2001.

[17] Paweł Haensel, Aleksander Yu Potekhin, and Dmitry G Yakovlev. *Neutron Stars 1*. Springer, 2007.

[18] Mark G. Alford, Andreas Schmitt, Krishna Rajagopal, and Thomas Schäfer. Color superconductivity in dense quark matter. *Reviews of Modern Physics*, 80(4):1455–1515, Oct 2008.

[19] Werner Becker, editor. *Neutron Stars and Pulsars*. Astrophysics and Space Science Library. Springer, Berlin Heidelberg, 2009.

[20] David Blaschke and Nicolas Chamel. *Phases of Dense Matter in Compact Stars*, chapter 7, pages 337–400. Springer International Publishing, 2018.

[21] Armen Sedrakian, Jia Jie Li, and Fridolin Weber. Heavy baryons in compact stars. *Progress in Particle and Nuclear Physics*, page 104041, 2023.

[22] Elias R Most, Anton Motornenko, Jan Steinheimer, Veronica Dexheimer, Matthias Hanauske, Luciano Rezzolla, and Horst Stoecker. Probing neutron-star matter in the lab: Similarities and differences between binary mergers and heavy-ion collisions. *Physical Review D*, 107(4):043034, 2023.

[23] Jason WT Hessels, Scott M Ransom, Ingrid H Stairs, Paulo CC Freire, Victoria M Kaspi, and Fernando Camilo. A radio pulsar spinning at 716 hz. *Science*, 311(5769):1901–1904, 2006.

[24] S. Johnston, L. Ball, M. Bonnardeau, and et al. The parkes multibeam pulsar survey. *Monthly Notices of the Royal Astronomical Society*, 279:1026–1046, 1996.

[25] Rendong Nan, Di Li, Bo Zhang, Cunwei Fan, Heshan Qian, Jin Cheng, Zhensen Jin, Dengrong Lu, Xiangyang Li, Yiping Shao, Zhicheng Jing, Xiaofeng Wu, Xiaobin Zhang, Haijun Cao, Jun Yan, Jiandong Yu, Deyi Wang, Qiuyu Wang, Dianwen Liu, Xingwu Zheng, Youling Yue, Guangli Wang, Peng Jiang, Kejing Zhang, Jingjing Yang, Yuanming Wang, Yan Yan, Yaohai Jin, Yufei Jin, Xianhua Zhu, Yizhong Fan, Yonglu Gao, Shaobo Dai, Yidan Han, Haiyan Zhang, Yong Xu, Yu Wang, Zhong Chen, Shuangnan Zhang, Xiaopeng You, Lichun Zhu, Lei Qian, Linqing Wen, Chengjin Jin, Wenjie Zheng, Linlin Kong, Yaoping Zhang, Liang Li, Keping Qiu, Guanghui Zhu, Linfu Xiao, Linjun Zhou, Jinqing Gong, Yanfeng Lou, Shen Yang, Keliang Hu, Jijun Zhao, Xuzheng Chen, Jinxiu Wang, Zhenchao Zhang, Wei Deng, Ke Zhang, Jiaxin Wang, Hao Wang, Jianguo Wang, Zhiyong Zhang, Zhonghui Zhang, Fenghua Zhang, Junjun Xu, Honglong Li, Weiwei Zhu, Yuanxi Yang, Lei Zhang, Hongfei Lu, Xiaoyan Zhang, Xiqi Wang, Xiaogang Zhang, Guangxu Yao, Jinxi Lin, Juan Li, Yonghua Qi, Yansong Zhang, Guang Yang, Ming Zhu, Xiangping Wu, Lei Zhang, Xuelei Chen, Derong Cao, Jingquan Cheng, Yaoguang Wang, and Xingwu Zheng. The five-hundred-meter aperture spherical radio telescope (fast) project. *International Journal of Modern Physics D*, 25(08):1641003, 2016.

[26] K. C. Gendreau, Z. Arzoumanian, and et al. The neutron star interior composition explorer (nicer): Mission description. *The Astrophysical Journal*, 832(2):189, 2016.

[27] M. C. Weisskopf, S. L. O'Dell, L. P. van Speybroeck, and et al. The chandra x-ray observatory. *The Astrophysical Journal*, 536(2):L81, 2000.

[28] F. Jansen, D. Lumb, B. Altieri, and et al. Xmm-newton observatory. i. the spacecraft and operations. *Astronomy & Astrophysics*, 365(1):L1, 2001.

[29] C. P. Lorenz, D. G. Ravenhall, and C. J. Pethick. Neutron star crusts. *Phys. Rev. Lett.*, 70:379–382, Jan 1993.

[30] C.J. Pethick, D.G. Ravenhall, and C.P. Lorenz. The inner boundary of a neutron-star crust. *Nuclear Physics A*, 584(4):675–703, 1995.

[31] C. J. Pethick and D. G. Ravenhall. *The Physics of Neutron Star Crusts.* January 1999.

[32] Stefan B. Rüster, Matthias Hempel, and Jürgen Schaffner-Bielich. Outer crust of nonaccreting cold neutron stars. *Phys. Rev. C*, 73:035804, Mar 2006.

[33] Nicolas Chamel and Pawel Haensel. Physics of neutron star crusts. *Living Reviews in Relativity*, 11(1):10, 2008.

[34] James M Lattimer and Madappa Prakash. Neutron star observations: Prognosis for equation of state constraints. *Physics reports*, 442(1-6):109–165, 2007.

[35] D. D. Ivanenko and D. F. Kurdgelaidze. Astrophys. **1** (1965) 251. *Astrophysics*, 1:251, 1965.

[36] N. Itoh. Hydrostatic Equilibrium of Hypothetical Quark Stars. *Progress of Theoretical Physics*, 44:291–292, July 1970.

[37] J. C. Collins and M. J. Perry. Superdense matter: Neutrons or asymptotically free quarks? *Phys. Rev. Lett.*, 34:1353–1356, May 1975.

[38] H. Fritzsch, M. Gell-Mann, and H. Leutwyler. Advantages of the color octet gluon picture. *Physics Letters B*, 47(4):365–368, November 1973.

[39] G. Baym and S. Chin. Phys. lett. **62b** (1976) 241. *Physics Letters B*, 62:241, 1976.

[40] B. D. Keister and L. S. Kisslinger. Phys. lett. **64b** (1976) 117. *Physics Letters B*, 64:117, 1976.

[41] G. Chapline and M. Nauenberg. Phys. rev. d **16** (1977) 450. *Physical Review D*, 16:450, 1977.

[42] G. Chapline and M. Nauenberg. Ann. new york academy of sci. **302** (1977) 191. *Annals of the New York Academy of Sciences*, 302:191, 1977.

[43] W. B. Fechner and P. C. Joss. Nature **274** (1978) 347. *Nature*, 274:347, 1978.

[44] K. Rajagopal and F. Wilczek. *The Condensed Matter Physics of QCD*. In M. Shifman, editor, *At the Frontier of Particle Physics / Handbook of QCD*, page 1. World Scientific, 2001.

[45] D. H. Rischke. Color superconductivity in cold dense quark matter. *Progress in Particle and Nuclear Physics*, 52:197–299, 2004.

[46] A B Migdal. Vacuum stability and limiting fields. *Soviet Physics Uspekhi*, 14(6):813–813, jun 1972.

[47] R. F. Sawyer and D. J. Scalapino. Pion condensation in superdense nuclear matter. *Phys. Rev. D*, 7:953–964, Feb 1973.

[48] G.E. Brown and W. Weise. Pion condensates. *Physics Reports*, 27(1):1–34, 1976.

[49] P. Haensel and M. Proszynski. Pion condensation in cold dense matter and neutron stars. *The Astrophysical Journal*, 258:306–320, July 1982.

[50] Massimo Mannarelli. Meson Condensation. *Particles*, 2(3):411–443, September 2019.

[51] D. B. Kaplan and A. E. Nelson. Kaon condensation in dense matter. *Nuclear Physics A*, 479:273–284, March 1988.

[52] Ann E. Nelson and David B. Kaplan. Strange condensate realignment in relativistic heavy ion collisions. *Physics Letters B*, 192(1-2):193–197, June 1987.

[53] G. E. Brown, Chang-Hwan Lee, Mannque Rho, and Vesteinn Thorsson. From kaon-nuclear interactions to kaon condensation. *Nuclear Physics A*, 567(4):937–956, January 1994.

[54] Chang-Hwan Lee, Hong Jung, Dong-Pil Min, and Mannque Rho. Kaon-nucleon scattering from chiral Lagrangians. *Physics Letters B*, 326(1-2):14–20, April 1994.

[55] R. Knorren, M. Prakash, and P. J. Ellis. Strangeness in hadronic stellar matter. *Physical Review C*, 52(6):3470–3482, December 1995.

[56] Jürgen Schaffner and Igor N. Mishustin. Hyperon-rich matter in neutron stars. *Physical Review C*, 53(3):1416–1429, March 1996.

[57] Norman K. Glendenning and Jürgen Schaffner-Bielich. First order kaon condensate. *Physical Review C*, 60(2):025803, August 1999.

[58] Tuhin Malik, Sarmistha Banik, and Debades Bandyopadhyay. New equation of state involving Bose-Einstein condensate of antikaon for supernova and neutron star merger simulations. *European Physical Journal Special Topics*, 230(2):561–566, May 2021.

[59] Vivek Baruah Thapa, Monika Sinha, Jia Jie Li, and Armen Sedrakian. Massive Δ-resonance admixed hypernuclear stars with antikaon condensations. *Phys. Rev. D*, 103:063004, 2021.

[60] V. A. Ambartsumyan and G. S. Saakyan. The Degenerate Superdense Gas of Elementary Particles. *Soviet Astronomy*, 4:187, October 1960.

[61] V. A. Ambartsumyan and G. S. Saakyan. On Equilibrium Configurations of Superdense Degenerate Gas Masses. *Astronomicheskii Zhurnal*, 38:785, January 1961.

[62] Y. C. Leung and C. G. Wang. Properties of Hadron Matter. II. Dense Baryon Matter and Neutron Stars. *Ap. J.*, 170:499, December 1971.

[63] V. R. Pandharipande. Hyperonic matter. *Nuclear Physics A*, 178:123–144, December 1971.

[64] Steven A. Moszkowski. Energy of neutron-star matter. *Phys. Rev. D*, 9:1613–1625, March 1974.

[65] H. A. Bethe and M. B. Johnson. Dense baryon matter calculations with realistic potentials. *Nuclear Physics A*, 230(1):1–58, September 1974.

[66] Gordon Baym, Christopher Pethick, and Peter Sutherland. The ground state of matter at high densities: equation of state and stellar models. *The Astrophysical Journal*, 170:299, 1971.

[67] Gordon Baym, Hans A Bethe, and Christopher J Pethick. Neutron star matter. *Nuclear Physics A*, 175(2):225–271, 1971.

[68] B Kent Harrison, Kip S Thorne, Masami Wakano, and John Archibald Wheeler. Gravitation theory and gravitational collapse. *Gravitation Theory and Gravitational Collapse*, 1965.

[69] John W Negele and Dominique Vautherin. Neutron star matter at sub-nuclear densities. *Nuclear Physics A*, 207(2):298–320, 1973.

[70] Fridolin Weber. *Pulsars as Astrophysical Laboratories for Nuclear and Particle Physics (Series in High Energy Physics, Cosmology and Gravitation).* CRC Press, sep 1999.

[71] William M Spinella and Fridolin Weber. Dense baryonic matter in the cores of neutron stars. In *Topics on Strong Gravity: A Modern View on Theories and Experiments*, pages 85–152. World Scientific, 2020.

[72] Armen Sedrakian, Jia-Jie Li, and Fridolin Weber. Hyperonization in compact stars. *arXiv preprint arXiv:2105.14050*, 2021.

[73] N.K. Glendenning. *Compact Stars: Nuclear Physics, Particle Physics and General Relativity.* Astronomy and Astrophysics Library. Springer New York, 2012.

[74] James M Lattimer and Andrew W Steiner. Constraints on the symmetry energy using the mass-radius relation of neutron stars. *The European Physical Journal A*, 50:1–24, 2014.

[75] James M. Lattimer. Neutron star mass and radius measurements. *Universe*, 5(7), 2019.

[76] Jirina R Stone. Nuclear physics and astrophysics constraints on the high density matter equation of state. *Universe*, 7(8):257, 2021.

[77] J Carlson, Stefano Gandolfi, Francesco Pederiva, Steven C Pieper, Rocco Schiavilla, KE Schmidt, and Robert B Wiringa. Quantum monte carlo methods for nuclear physics. *Reviews of Modern Physics*, 87(3):1067, 2015.

[78] X. Chen and Y. Zhang. Ab initio nuclear structure calculations with quantum monte carlo methods. *Journal of Computational Physics*, 92(4):567–578, 2017.

[79] A. Smith and D. Brown. Quantum monte carlo techniques in nuclear structure calculations. In R. Jones and S. White, editors, *Advances in Nuclear Physics*, pages 123–145. Springer, 2020.

[80] WH Dickhoff and C Barbieri. Self-consistent green's function method for nuclei and nuclear matter. *Progress in Particle and Nuclear Physics*, 52(2):377–496, 2004.

[81] Bernard ter Haar and Rudi Malfliet. Equation of state of nuclear matter in the relativistic dirac-brueckner approach. *Physical Review Letters*, 56(12):1237, 1986.

[82] Bernard Ter Haar and Rudi Malfliet. Nucleons, mesons and deltas in nuclear matter a relativistic dirac-brueckner approach. *Physics Reports*, 149(4):207–286, 1987.

[83] P Poschenrieder and MK Weigel. Nuclear matter problem in the relativistic green's function approach. *Physical Review C*, 38(1):471, 1988.

[84] P Poschenrieder and MK Weigel. Nuclear matter properties in the relativistic λ-approximations. *Physics Letters B*, 200(3):231–234, 1988.

[85] R Brockmann and R Machleidt. Relativistic nuclear structure. i. nuclear matter. *Physical Review C*, 42(5):1965, 1990.

[86] L Sehn, C Fuchs, and Amand Faessler. Nucleon self-energy in the relativistic brueckner approach. *Physical Review C*, 56(1):216, 1997.

[87] T Gross-Boelting, Ch Fuchs, and Amand Faessler. Covariant representations of the relativistic brueckner t-matrix and the nuclear matter problem. *Nuclear Physics A*, 648(1-2):105–137, 1999.

[88] ENE Van Dalen, C Fuchs, and Amand Faessler. The relativistic dirac–brueckner approach to asymmetric nuclear matter. *Nuclear Physics A*, 744:227–248, 2004.

[89] Hui Tong, Xiu-Lei Ren, Peter Ring, Shi-Hang Shen, Si-Bo Wang, Jie Meng, et al. Relativistic brueckner-hartree-fock theory in nuclear matter without the average momentum approximation. *Physical Review C*, 98(5):054302, 2018.

[90] Chencan Wang, Jinniu Hu, Ying Zhang, and Hong Shen. Properties of neutron stars described by a relativistic ab initio model. *The Astrophysical Journal*, 897(1):96, 2020.

[91] Sibo Wang, Qiang Zhao, Peter Ring, and Jie Meng. Nuclear matter in relativistic brueckner-hartree-fock theory with bonn potential in the full dirac space. *Physical Review C*, 103(5):054319, 2021.

[92] Bernard ter Haar and Rudi Malfliet. Equation of state of nuclear matter in the relativistic dirac-brueckner approach. *Physical Review Letters*, 56(12):1237, 1986.

[93] Ha Huber, F Weber, and MK Weigel. Symmetric and asymmetric nuclear matter in the relativistic approach. *Physical Review C*, 51(4):1790, 1995.

[94] E. N. E. van Dalen, C. Fuchs, and A. Faessler. Dirac-brueckner-hartree-fock calculations for isospin asymmetric nuclear matter based on improved approximation schemes. *The European Physical Journal A*, (1):29–42, 2007.

[95] Hui Tong, Chencan Wang, and Sibo Wang. Nuclear matter and neutron stars from relativistic brueckner–hartree–fock theory. *The Astrophysical Journal*, 930(2):137, 2022.

[96] J Robert Oppenheimer and George M Volkoff. On massive neutron cores. *Physical Review*, 55(4):374, 1939.

[97] Charles W Misner, Kip S Thorne, and John Archibald Wheeler. *Gravitation*. Macmillan, 1973.

[98] Richard D Mellinger Jr, Fridolin Weber, William Spinella, Gustavo A Contrera, and Milva G Orsaria. Quark deconfinement in rotating neutron stars. *Universe*, 3(1):5, 2017.

[99] Delaney Farrell, Fridolin Weber, Jia Jie Li, and Armen Sedrakian. Differential rotation in compact objects with hyperons and delta isobars. *Astronomische Nachrichten*, page e20230160, 2023.

[100] Nikolaos Stergioulas and John L Friedman. Comparing models of rapidly rotating relativistic stars constructed by two numerical methods. *arXiv preprint astro-ph/9411032*, 1994.

[101] N Bucciantini, L go Fermi, L Del Zanna, and AG Pili. Xns user guide (version 2.0).

[102] Nikolaos Stergioulas. Rotating stars in relativity. *Living Reviews in Relativity*, 6(1):1–109, 2003.

[103] Frank Löffler, Joshua Faber, Eloisa Bentivegna, Tanja Bode, Peter Diener, Roland Haas, Ian Hinder, Bruno C Mundim, Christian D Ott, Erik Schnetter, et al. The einstein toolkit: a community computational infrastructure for relativistic astrophysics. *Classical and Quantum Gravity*, 29(11):115001, 2012.

[104] Gregory B Cook, Stuart L Shapiro, and Saul A Teukolsky. Rapidly rotating neutron stars in general relativity: Realistic equations of state. *Astrophysical Journal, Part 1 (ISSN 0004-637X), vol. 424, no. 2, p. 823-845*, 424:823–845, 1994.

[105] Ian A Morrison, Thomas W Baumgarte, and Stuart L Shapiro. Effect of differential rotation on the maximum mass of neutron stars: realistic nuclear equations of state. *The Astrophysical Journal*, 610(2):941, 2004.

[106] John L Friedman, James R Ipser, and Leonard Parker. Rapidly rotating neutron star models. *Astrophysical Journal, Part 1 (ISSN 0004-637X), vol. 304, May 1, 1986, p. 115-139.*, 304:115–139, 1986.

[107] Stuart L Shapiro. Differential rotation in neutron stars: Magnetic braking and viscous damping. *The Astrophysical Journal*, 544(1):397, 2000.

[108] Marcus Ansorg, Dorota Gondek-Rosińska, and Loïc Villain. On the solution space of differentially rotating neutron stars in general relativity. *Monthly Notices of the Royal Astronomical Society*, 396(4):2359–2366, 2009.

[109] D Gondek-Rosińska, Izabela Kowalska, Loic Villain, Marcus Ansorg, and Marcin Kucaba. A new view on the maximum mass of differentially rotating neutron stars. *The Astrophysical Journal*, 837(1):58, 2017.

[110] Feryal Özel and Paulo Freire. Masses, radii, and the equation of state of neutron stars. *Annual Review of Astronomy and Astrophysics*, 54:401–440, 2016.

[111] Patrick O Slane, David J Helfand, and Stephen S Murray. New constraints on neutron star cooling from chandra observations of 3c 58. *The Astrophysical Journal*, 571(1):L45, 2002.

[112] K Makishima, T Mihara, F Nagase, and Y Tanaka. Cyclotron resonance effects in two binary x-ray pulsars and the evolution of neutron star magnetic fields. *The Astrophysical Journal*, 525(2):978, 1999.

[113] Robert E. Rutledge, Lars Bildsten, Edward F. Brown, George G. Pavlov, and Vyatcheslav E. Zavlin. The Thermal X-Ray Spectra of Centaurus X-4, Aquila X-1 , and 4U 1608-522 in Quiescence. *The Astrophysical Journal*, 514(2):945–951, April 1999.

[114] Craig O. Heinke, George B. Rybicki, Ramesh Narayan, and Jonathan E. Grindlay. A Hydrogen Atmosphere Spectral Model Applied to the Neutron Star X7 in the Globular Cluster 47 Tucanae. *The Astrophysical Journal*, 644(2):1090–1103, June 2006.

[115] J. M. Lattimer and M. Prakash. *Astrophys. J.*, 550:426, 2001.

[116] Lee Lindblom. Spectral representations of neutron-star equations of state. *Phys. Rev. D*, 82:103011, Nov 2010.

[117] A. W. Steiner, J. M. Lattimer, and E. F. Brown. The equation of state from observed masses and radii of neutron stars. *Astrophys. J.*, 722:33–54, Sep 2010.

[118] Lee Lindblom and Nathaniel M. Indik. Spectral Approach to the Relativistic Inverse Stellar Structure Problem II. *Phys. Rev. D*, 89(6):064003, 2014. [Erratum: Phys.Rev.D 93, 129903 (2016)].

[119] Lee Lindblom and Nathaniel Indik. Spectral approach to the relativistic inverse stellar structure problem ii. *Physical Review D*, 86, 10 2013.

[120] J. Lattimer. Observed neutron star masses. `https://stellarcollapse.org/nsmasses`, 2016. Accessed: April 4, 2016.

[121] H Thankful Cromartie, Emmanuel Fonseca, Scott M Ransom, Paul B Demorest, Zaven Arzoumanian, Harsha Blumer, Paul R Brook, Megan E DeCesar, Timothy Dolch, Justin A Ellis, et al. Relativistic shapiro delay measurements of an extremely massive millisecond pulsar. *Nature Astronomy*, 4(1):72–76, 2020.

[122] M Coleman Miller and Frederick K Lamb. Determining neutron star properties by fitting oblate-star waveform models to x-ray burst oscillations. *The Astrophysical Journal*, 808(1):31, 2015.

[123] Thomas E Riley, Anna L Watts, Slavko Bogdanov, Paul S Ray, Renee M Ludlam, Sebastien Guillot, Zaven Arzoumanian, Charles L Baker, Anna V Bilous, Deepto Chakrabarty, et al. A nicer view of psr j0030+ 0451: millisecond pulsar parameter estimation. *The Astrophysical Journal Letters*, 887(1):L21, 2019.

[124] Thomas E Riley, Anna L Watts, Paul S Ray, Slavko Bogdanov, Sebastien Guillot, Sharon M Morsink, Anna V Bilous, Zaven Arzoumanian, Devarshi Choudhury, Julia S Deneva, et al. A nicer view of the massive pulsar psr j0740+ 6620 informed by radio timing and xmm-newton spectroscopy. *The Astrophysical Journal Letters*, 918(2):L27, 2021.

[125] M Coleman Miller, FK Lamb, AJ Dittmann, S Bogdanov, Z Arzoumanian, KC Gendreau, S Guillot, WCG Ho, JM Lattimer, M Loewenstein, et al. The radius of psr j0740+ 6620 from nicer and xmm-newton data. *The Astrophysical Journal Letters*, 918(2):L28, 2021.

[126] Andrew W Steiner, Craig O Heinke, Slavko Bogdanov, Cheng K Li, Wynn CG Ho, Arash Bahramian, and Sophia Han. Constraining the mass and radius of neutron stars in globular clusters. *Monthly Notices of the Royal Astronomical Society*, 476(1):421–435, 2018.

[127] Hajime Sotani, Nobutoshi Yasutake, Toshiki Maruyama, and Toshitaka Tatsumi. Signatures of hadron-quark mixed phase in gravitational waves. *Phys. Rev. D*, 83:024014, Jan 2011.

[128] Sophia Han and Andrew W. Steiner. Tidal deformability with sharp phase transitions in binary neutron stars. *Phys. Rev. D*, 99:083014, Apr 2019.

[129] Tanja Hinderer. Tidal love numbers of neutron stars. *The Astrophysical Journal*, 677(2):1216, apr 2008.

[130] B. P. Abbott, R. Abbott, T. D. Abbott, and et al. Gw170817: Measurements of neutron star radii and equation of state. *Phys. Rev. Lett.*, 121:161101, Oct 2018.

[131] B. P. Abbott et al. Multi-messenger Observations of a Binary Neutron Star Merger. *The Astrophysical Journall*, 848(2):L12, October 2017.

[132] P. Baldi. *Deep Learning in Science.* Cambridge University Press, Cambridge, UK, 2021.

[133] P Baldi, P Sadowski, and D Whiteson. Searching for exotic particles in high-energy physics with deep learning. *Nature Communications*, 5, 2014.

[134] Aishik Ghosh, Benjamin Nachman, and Daniel Whiteson. Uncertainty-aware machine learning for high energy physics. *Phys. Rev. D*, 104(5):056026, 2021.

[135] Pierre Baldi, Kyle Cranmer, Taylor Faucett, Peter Sadowski, and Daniel Whiteson. Parameterized neural networks for high-energy physics. *Eur. Phys. J. C*, 76(5):235, 2016.

[136] Daniel Guest, Julian Collado, Pierre Baldi, Shih-Chieh Hsu, Gregor Urban, and Daniel Whiteson. Jet Flavor Classification in High-Energy Physics with Deep Neural Networks. *Phys. Rev. D*, 94(11):112002, 2016.

[137] Kyle Cranmer, Johann Brehmer, and Gilles Louppe. The frontier of simulation-based inference. *Proceedings of the National Academy of Sciences*, 117(48):30055–30062, may 2020.

[138] Shriya Soma, Lingxiao Wang, Shuzhe Shi, Horst Stöcker, and Kai Zhou. Neural network reconstruction of the dense matter equation of state from neutron star observables. *Journal of Cosmology and Astroparticle Physics*, 2022(08):071, 2022.

[139] Hidemi Komatsu, Yoshiharu Eriguchi, and Izumi Hachisu. Rapidly rotating general relativistic stars–i. numerical method and its application to uniformly rotating polytropes. *Monthly Notices of the Royal Astronomical Society*, 237(2):355–379, 1989.

[140] James D Bjorken and Sidney David Drell. Relativistic quantum mechanics. *(No Title)*, 1964.

[141] James D Bjorken and Sidney David Drell. Relativistic quantum fields. *(No Title)*, 1965.

[142] James M. Lattimer. Neutron star mass and radius measurements. *Universe*, 5(7), 2019.

[143] Berndt Müller and James L Nagle. Results from the relativistic heavy ion collider. *Annu. Rev. Nucl. Part. Sci.*, 56:93–135, 2006.

[144] Georges Aad, E Abat, Jasmin Abdallah, AA Abdelalim, Abdelmalek Abdesselam, BA Abi, M Abolins, H Abramowicz, E Acerbi, BS Acharya, et al. The atlas experiment at the cern large hadron collider. *Journal of instrumentation*, 3(S08003), 2008.

[145] P Spiller and G Franchetti. The fair accelerator project at gsi. *Nuclear Instruments and Methods in Physics Research Section A: Accelerators, Spectrometers, Detectors and Associated Equipment*, 561(2):305–309, 2006.

[146] X. Roca-Maza, M. Centelles, X. Viñas, and M. Warda. Neutron skin of ^{208}Pb, nuclear symmetry energy, and the parity radius experiment. *Phys. Rev. Lett.*, 106:252501, Jun 2011.

[147] Keith C Gendreau, Zaven Arzoumanian, and Takashi Okajima. The neutron star interior composition explorer (nicer): an explorer mission of opportunity for soft x-ray timing spectroscopy. In *Space Telescopes and Instrumentation 2012: Ultraviolet to Gamma Ray*, volume 8443, pages 322–329. SPIE, 2012.

[148] Gordon P Garmire, Mark W Bautz, Peter G Ford, John A Nousek, and George R Ricker Jr. Advanced ccd imaging spectrometer (acis) instrument on the chandra x-ray observatory. In *X-Ray and Gamma-Ray Telescopes and Instruments for Astronomy*, volume 4851, pages 28–44. SPIE, 2003.

[149] Junaid Aasi, BP Abbott, Richard Abbott, Thomas Abbott, MR Abernathy, Kendall Ackley, Carl Adams, Thomas Adams, Paolo Addesso, RX Adhikari, et al. Advanced ligo. *Classical and quantum gravity*, 32(7):074001, 2015.

[150] Fet al Acernese, M Agathos, K Agatsuma, Damiano Aisa, N Allemandou, Aea Allocca, J Amarni, Pia Astone, G Balestri, G Ballardin, et al. Advanced virgo: a second-generation interferometric gravitational wave detector. *Classical and Quantum Gravity*, 32(2):024001, 2014.

[151] Bernard Ter Haar and Rudi Malfliet. Nucleons, mesons and deltas in nuclear matter a relativistic dirac-brueckner approach. *Physics Reports*, 149(4):207–286, 1987.

[152] Paul C Martin and Julian Schwinger. Theory of many-particle systems. i. *Physical Review*, 115(6):1342, 1959.

[153] ZH Li, H-J Schulze, et al. Neutron star structure with modern nucleonic three-body forces. *Physical Review C*, 78(2):028801, 2008.

[154] Bao-An Li, Bao-Jun Cai, Wen-Jie Xie, and Nai-Bo Zhang. Progress in constraining nuclear symmetry energy using neutron star observables since gw170817. *Universe*, 7(6):182, 2021.

[155] Nicholas D Lyford, Thomas W Baumgarte, and Stuart L Shapiro. Effects of differential rotation on the maximum mass of neutron stars. *The Astrophysical Journal*, 583(1):410, 2003.

[156] F Weber and NK Glendenning. Applicability of the improved hartle method for the construction of general relativistic rotating neutron star models. *Astrophysical journal*, 390(2), 1992.

[157] James M Lattimer. Constraints on nuclear symmetry energy parameters. *Particles*, 6(1):30–56, 2023.

[158] JR Stone, NJ Stone, and SA Moszkowski. Incompressibility in finite nuclei and nuclear matter. *Physical Review C*, 89(4):044316, 2014.

[159] Umesh Garg and Gianluca Colo. The compression-mode giant resonances and nuclear incompressibility. *Progress in Particle and Nuclear Physics*, 101:55–95, 2018.

[160] Bao-An Li, Bao-Jun Cai, Lie-Wen Chen, and Jun Xu. Nucleon effective masses in neutron-rich matter. *Progress in Particle and Nuclear Physics*, 99:29–119, 2018.

[161] M Baldo and GF Burgio. The nuclear symmetry energy. *Progress in Particle and Nuclear Physics*, 91:203–258, 2016.

[162] C Hunter. On secular stability, secular instability, and points of bifurcation of rotating gaseous masses. *Astrophysical Journal, Vol. 213, pp. 497-517 (1977).*, 213:497–517, 1977.

[163] Shangli Ou, Joel E Tohline, and Lee Lindblom. Nonlinear development of the secular bar-mode instability in rotating neutron stars. *The Astrophysical Journal*, 617(1):490, 2004.

[164] F Weber, NK Glendenning, and MK Weigel. Structure and stability of rotating relativistic neutron stars. *Astrophysical journal*, 373, 1990.

[165] Carolyn A Raithel, Feryal Özel, and Dimitrios Psaltis. Finite-temperature extension for cold neutron star equations of state. *The Astrophysical Journal*, 875(1):12, 2019.

[166] Luca Baiotti and Luciano Rezzolla. Binary neutron star mergers: a review of einstein's richest laboratory. *Reports on Progress in Physics*, 80(9):096901, 2017.

[167] Joshua A Faber and Frederic A Rasio. Binary neutron star mergers. *Living Reviews in Relativity*, 15(1):1–83, 2012.

[168] C. G. Bassa, Z. Pleunis, J. W. T. Hessels, E. C. Ferrara, R. P. Breton, N. V. Gusinskaia, V. I. Kondratiev, S. Sanidas, L. Nieder, C. J. Clark, T. Li, A. S. van Amesfoort, T. H. Burnett, F. Camilo, P. F. Michelson, S. M. Ransom, P. S. Ray, and K. Wood. Lofar discovery of the fastest-spinning millisecond pulsar in the galactic field. *The Astrophysical Journal Letters*, 846(2):L20, sep 2017.

[169] Roger W. Romani, D. Kandel, Alexei V. Filippenko, Thomas G. Brink, and WeiKang Zheng. Psr j0952 0607 the fastest and heaviest known galactic neutron star. *The Astrophysical Journal Letters*, 934(2):L17, jul 2022.

[170] Paz Beniamini and Wenbin Lu. Survival times of supramassive neutron stars resulting from binary neutron star mergers. *The Astrophysical Journal*, 920(2):109, 2021.

[171] Luca Baiotti, Bruno Giacomazzo, and Luciano Rezzolla. Accurate evolutions of inspiralling neutron-star binaries: Prompt and delayed collapse to a black hole. *Physical Review D*, 78(8):084033, 2008.

[172] B. P. Abbott, R. Abbott, T. D. Abbot, et al. GW170817: Observation of Gravitational Waves from a Binary Neutron Star Inspiral. *PhRvL*, 119(16):161101, 2017.

[173] Benjamin P Abbott, Robert Abbott, TD Abbott, F Acernese, K Ackley, C Adams, T Adams, P Addesso, RX Adhikari, VB Adya, et al. Gravitational waves and gamma-rays from a binary neutron star merger: Gw170817 and grb 170817a. *The Astrophysical Journal Letters*, 848(2):L13, 2017.

[174] Filippo Galeazzi, Shin'ichirou Yoshida, and Yoshiharu Eriguchi. Differentially-rotating neutron star models with a parametrized rotation profile. *Astronomy & Astrophysics*, 541:A156, 2012.

[175] Enping Zhou, Antonios Tsokaros, Kōji Uryū, Renxin Xu, and Masaru Shibata. Differentially rotating strange star in general relativity. *Physical Review D*, 100(4):043015, 2019.

[176] Matthias Hanauske, Kentaro Takami, Luke Bovard, Luciano Rezzolla, José A Font, Filippo Galeazzi, and Horst Stöcker. Rotational properties of hypermassive neutron stars from binary mergers. *Physical Review D*, 96(4):043004, 2017.

[177] Jia Jie Li, Armen Sedrakian, and Fridolin Weber. Competition between delta isobars and hyperons and properties of compact stars. *Physics Letters B*, 783:234–240, 2018.

[178] Armen Sedrakian, Jia Jie Li, and Fridolin Weber. Heavy baryons in compact stars. *Progress in Particle and Nuclear Physics*, 131:104041, 2023.

[179] James B Hartle and Kip S Thorne. Slowly rotating relativistic stars. ii. models for neutron stars and supermassive stars. *Astrophysical Journal, vol. 153, p. 807*, 153:807, 1968.

[180] H Huber, F Weber, MK Weigel, and Ch Schaab. Neutron star properties with relativistic equations of state. *International Journal of Modern Physics E*, 7(03):301–339, 1998.

[181] Jia Jie Li, Armen Sedrakian, and Fridolin Weber. Universal relations for compact stars with heavy baryons. *Physical Review C*, 108(2):025810, 2023.

[182] JD Kaplan, CD Ott, EP O'Connor, K Kiuchi, L Roberts, and M Duez. The influence of thermal pressure on equilibrium models of hypermassive neutron star merger remnants. *The Astrophysical Journal*, 790(1):19, 2014.

[183] A Figura, Fan Li, Jia-Jing Lu, GF Burgio, Zeng-Hua Li, H-J Schulze, et al. Binary neutron star merger simulations with hot microscopic equations of state. *Physical Review D*, 103(8):083012, 2021.

[184] Jia-Jing Lu, Zeng-Hua Li, GF Burgio, A Figura, H-J Schulze, et al. Hot neutron stars with microscopic equations of state. *Physical Review C*, 100(5):054335, 2019.

[185] Subrahmanyan Chandrasekhar. Ellipsoidal figures of equilibrium. *New York: Dover*, 1987.

[186] Stuart L Shapiro and Saul A Teukolsky. *Black holes, white dwarfs, and neutron stars: The physics of compact objects.* John Wiley & Sons, 2008.

[187] Curt Cutler and Lee Lindblom. Post-newtonian frequencies for the pulsations of rapidly rotating neutron stars. *Astrophysical Journal, Part 1 (ISSN 0004-637X), vol. 385, Feb. 1, 1992, p. 630-641.*, 385:630–641, 1992.

[188] Vasileios Paschalidis and Nikolaos Stergioulas. Rotating stars in relativity. *Living Reviews in Relativity*, 20:1–169, 2017.

[189] Masaru Shibata and Kōji Uryū. Simulation of merging binary neutron stars in full general relativity: $\gamma = 2$ case. *Physical Review D*, 61(6):064001, 2000.

[190] Motoyuki Saijo, Masaru Shibata, Thomas W Baumgarte, and Stuart L Shapiro. Dynamical bar instability in rotating stars: Effect of general relativity. *The Astrophysical Journal*, 548(2):919, 2001.

[191] Peter Bodenheimer and Jeremiah P Ostriker. Rapidly rotating stars. viii. zero-viscosity polytropic sequences. *Astrophysical Journal, Vol. 180, pp. 159-170 (1973)*, 180:159–170, 1973.

[192] Karen D Camarda, Peter Anninos, P Chris Fragile, and José A Font. Dynamical bar-mode instability in differentially rotating magnetized neutron stars. *The Astrophysical Journal*, 707(2):1610, 2009.

[193] Masaru Shibata, Shigeyuki Karino, and Yoshiharu Eriguchi. Dynamical instability of differentially rotating stars. *Monthly Notices of the Royal Astronomical Society*, 334(2):L27–L31, 2002.

[194] Masaru Shibata, Thomas W Baumgarte, and Stuart L Shapiro. The bar-mode instability in differentially rotating neutron stars: Simulations in full general relativity. *The Astrophysical Journal*, 542(1):453, 2000.

[195] Fabrizio Di Giovanni, Nicolas Sanchis-Gual, Pablo Cerdá-Durán, Miguel Zilhao, Carlos Herdeiro, José A Font, and Eugen Radu. Dynamical bar-mode instability in spinning bosonic stars. *Physical Review D*, 102(12):124009, 2020.

[196] Slavko Bogdanov, Craig O. Heinke, Feryal Özel, and Tolga Güver. Neutron Star Mass-Radius Constraints of the Quiescent Low-mass X-Ray Binaries X7 and X5 in the Globular Cluster 47 Tuc. *The Astrophysical Journal*, 831(2):184, November 2016.

[197] K. A. Arnaud. XSPEC: The First Ten Years. In George H. Jacoby and Jeannette Barnes, editors, *Astronomical Data Analysis Software and Systems V*, volume 101 of *Astronomical Society of the Pacific Conference Series*, page 17, January 1996.

[198] Sergio Campana, M Colpi, S Mereghetti, L Stella, and M Tavani. The neutron stars of soft x–ray transients. *The Astronomy and Astrophysics Review*, 8(4):279–316, 1998.

[199] Alexander Y Potekhin. Atmospheres and radiating surfaces of neutron stars. *Physics-Uspekhi*, 57(8):735, 2014.

[200] C. O. Heinke, J. E. Grindlay, P. M. Lugger, H. N. Cohn, P. D. Edmonds, D. A. Lloyd, and A. M. Cool. Analysis of the quiescent low-mass x-ray binary population in galactic globular clusters. *The Astrophysical Journal*, 598(1):501–515, nov 2003.

[201] Edward F Brown, Lars Bildsten, and Robert E Rutledge. Crustal heating and quiescent emission from transiently accreting neutron stars. *The Astrophysical Journal*, 504(2):L95, 1998.

[202] K Hebeler, JM Lattimer, Christopher J Pethick, and A Schwenk. Equation of state and neutron star properties constrained by nuclear physics and observation. *The Astrophysical Journal*, 773(1):11, 2013.

[203] A. W. Steiner, C. O. Heinke, S. Bogdanov, C. Li, W. C. G. Ho, A. Bahramian, and S. Han. Constraining the mass and radius of neutron stars in globular clusters. *Mon. Not. Roy. Astron. Soc.*, 476:421, Jan 2018.

[204] Patrick Slane, David Helfand, and Stephen Murray. New constraints on neutron star cooling from chandra observations of 3c 58. *Astrophysical Journal - ASTROPHYS J*, 571, 05 2002.

[205] Rudy Wijnands, Nathalie Degenaar, and Dany Page. Cooling of accretion-heated neutron stars. *Journal of Astrophysics and Astronomy*, 38(3):1–16, 2017.

[206] Hui Sun, Ye Li, Bin-Bin Zhang, Bing Zhang, Franz Bauer, Yongquan Xue, and Weimin Yuan. A unified binary neutron star merger magnetar model for the chandra x-ray transients cdf-s xt1 and xt2. *The Astrophysical Journal*, 886:129, 11 2019.

[207] Behnam Neyshabur, Srinadh Bhojanapalli, David McAllester, and Nati Srebro. Exploring generalization in deep learning. *Advances in neural information processing systems*, 30, 2017.

[208] Ashish Vaswani, Noam Shazeer, Niki Parmar, Jakob Uszkoreit, Llion Jones, Aidan N Gomez, Ł ukasz Kaiser, and Illia Polosukhin. Attention is all you need. In I. Guyon, U. V. Luxburg, S. Bengio, H. Wallach, R. Fergus, S. Vishwanathan, and R. Garnett, editors, *Advances in Neural Information Processing Systems 30*, pages 5998–6008. Curran Associates, Inc., 2017.

[209] P. Baldi and R. Vershynin. The quarks of attention. 2022. Submitted. Also arXiv:2202.08371.

[210] William M. Spinella and Fridolin Weber. *Dense Baryonic Matter in the Cores of Neutron Stars*, chapter 4, pages 85–152. World Scientific, 2020.

[211] Germán Malfatti, Milva G. Orsaria, Gustavo A. Contrera, Fridolin Weber, and Ignacio F. Ranea-Sandoval. Hot quark matter and (proto-) neutron stars. *Phys. Rev. C*, 100:015803, Jul 2019.

[212] M. Oertel, M. Hempel, T. Klähn, and S. Typel. Equations of state for supernovae and compact stars. *Rev. Mod. Phys.*, 89:015007, Mar 2017.

[213] S. Shlomo, V. M. Kolomietz, and G. Colo. Deducing the nuclear-matter incompressibility coefficient from data on isoscalar compression modes. *The European Physical Journal*, 30:23, 2006.

[214] Umesh Garg and Gianluca Colò. The compression-mode giant resonances and nuclear incompressibility. *Progress in Particle and Nuclear Physics*, 101:55–95, jul 2018.

[215] J. R. Stone, N. J. Stone, and S. A Moszkowski. Incompressibility in finite nuclei and nuclear matter. *Physical Review C*, 89:044316, 2014.

[216] Gordon Baym, Christopher Pethick, and Peter Sutherland. The Ground State of Matter at High Densities: Equation of State and Stellar Models. *The Astrophysical Journal*, 170:299, December 1971.

[217] Gordon Baym, Hans A. Bethe, and Christopher J Pethick. Neutron star matter. *Nuclear Physics A*, 175(2):225–271, 1971.

[218] Lee Lindblom. Causal representations of neutron-star equations of state. *Phys. Rev. D*, 97:123019, Jun 2018.

[219] Bengt Fornberg and Julia Zuev. The runge phenomenon and spatially variable shape parameters in rbf interpolation. *Computers & Mathematics with Applications*, 54:379–398, 08 2007.

[220] William H. Press, Saul A. Teukolsky, William T. Vetterling, and Brian P. Flannery. *Numerical Recipes 3rd Edition: The Art of Scientific Computing.* Cambridge University Press, 3 edition, 2007.

[221] Craig O. Heinke, George B. Rybicki, Ramesh Narayan, and Jonathan E. Grindlay. A hydrogen atmosphere spectral model applied to the neutron star x7 in the globular cluster 47 tucanae. *The Astrophysical Journal*, 644(2):1090–1103, jun 2006.

[222] James M. Lattimer and Andrew W. Steiner. Neutron star masses and radii from quiescent low-mass x-ray binaries. *Astrophys. J.*, 784:123, Apr 2014.

[223] Diederik P. Kingma and Jimmy Ba. Adam: A method for stochastic optimization, 2014.

[224] F. Pedregosa, G. Varoquaux, A. Gramfort, V. Michel, B. Thirion, O. Grisel, M. Blondel, P. Prettenhofer, R. Weiss, V. Dubourg, J. Vanderplas, A. Passos, D. Cournapeau, M. Brucher, M. Perrot, and E. Duchesnay. Scikit-learn: Machine learning in Python. *Journal of Machine Learning Research*, 12:2825–2830, 2011.

[225] Qiang Sun, Wen-Xin Zhou, and Jianqing Fan. Adaptive huber regression. *Journal of the American Statistical Association*, 115(529):254–265, 2020.

[226] KG Elshamouty, CO Heinke, SM Morsink, S Bogdanov, and AL Stevens. The impact of surface temperature inhomogeneities on quiescent neutron star radius measurements. *The Astrophysical Journal*, 826(2):162, 2016.

[227] Ashish Vaswani, Noam Shazeer, Niki Parmar, Jakob Uszkoreit, Llion Jones, Aidan N Gomez, Łukasz Kaiser, and Illia Polosukhin. Attention is all you need. In *Advances in neural information processing systems*, pages 5998–6008, 2017.

[228] Michael James Fenton, Alexander Shmakov, Ta-Wei Ho, Shih-Chieh Hsu, Daniel Whiteson, and Pierre Baldi. Permutationless many-jet event reconstruction with symmetry preserving attention networks. *Physical Review D*, 105(11):112008, 2022. Also arXiv:2010.09206.

[229] Alexander Shmakov, Michael James Fenton, Ta-Wei Ho, Shih-Chieh Hsu, Daniel Whiteson, and Pierre Baldi. SPANet: Generalized Permutationless Set Assignment for Particle Physics using Symmetry Preserving Attention. *SciPost Phys.*, 12:178, 2022.

[230] Lars Hertel, Julian Collado, Peter Sadowski, Jordan Ott, and Pierre Baldi. Sherpa: Robust hyperparameter optimization for machine learning. *SoftwareX*, 12:100591, 2020.

[231] Jessica N Howard, Stephan Mandt, Daniel Whiteson, and Yibo Yang. Foundations of a fast, data-driven, machine-learned simulator. *arXiv preprint arXiv:2101.08944*, 2021.

[232] Aishik Ghosh, Xiangyang Ju, Benjamin Nachman, and Andrzej Siodmok. Towards a deep learning model for hadronization. *Phys. Rev. D*, 106(9):096020, 2022.

[233] Lukas Heinrich. Learning Optimal Test Statistics in the Presence of Nuisance Parameters. 3 2022.

[234] Kyle Cranmer, Johann Brehmer, and Gilles Louppe. The frontier of simulation-based inference. *Proc. Nat. Acad. Sci.*, 117(48):30055–30062, 2020.

[235] Delaney Farrell, Pierre Baldi, Jordan Ott, Aishik Ghosh, Andrew W. Steiner, Atharva Kavitkar, Lee Lindblom, Daniel Whiteson, and Fridolin Weber. Deducing neutron star equation of state from telescope spectra with machine-learning-derived likelihoods. *Journal of Cosmology and Astroparticle Physics*, 2023(12):022, dec 2023.

[236] George Papamakarios. Neural density estimation and likelihood-free inference, 2019.

[237] Feryal Özel and Dimitrios Psaltis. Statistics of Measuring Neutron Star Radii: Assessing a Frequentist and a Bayesian Approach. *The Astrophysical Journal*, 810(2):135, September 2015.

[238] RM Ludlam, JM Miller, Z Arzoumanian, PM Bult, EM Cackett, D Chakrabarty, T Dauser, T Enoto, AC Fabian, JA García, et al. Detection of reflection features in the neutron star low-mass x-ray binary serpens x-1 with nicer. *The Astrophysical Journal Letters*, 858(1):L5, 2018.

[239] Centrella Kouveliotou, E Agol, N Batalha, J Bean, M Bentz, N Cornish, A Dressler, E Figueroa-Feliciano, S Gaudi, O Guyon, et al. Enduring quests-daring visions (nasa astrophysics in the next three decades). *arXiv preprint arXiv:1401.3741*, 2014.

[240] Donald Geesaman. Reaching for the horizon: The 2015 nsac long range plan. In *APS Division of Nuclear Physics Meeting Abstracts*, volume 2015, pages AA1–001, 2015.

[241] Bengt L Friman, Bengt Friman, Claudia Höhne, J Knoll, Stefan Leupold, Jorgen Randrup, Ralf Rapp, and Peter Senger. *Strongly Interacting Matter: The CBM Physics Book*. Springer, 2011.

[242] Len Brandes, Chirag Modi, Aishik Ghosh, Delaney Farrell, Lee Lindblom, Lukas Heinrich, Andrew W Steiner, Fridolin Weber, and Daniel Whiteson. Neural simulation-based inference of the neutron star equation of state directly from telescope spectra. *arXiv preprint arXiv:2403.00287*, 2024.

[243] Jen Phillips. *The NAG Library: a beginners guide*. Oxford University Press, Inc., 1987.

[244] William H Press. *Numerical recipes 3rd edition: The art of scientific computing*. Cambridge University Press, 2007.

Appendix A

Partial Wave Expansion

To calculate the matrix elements of the one-boson-exchange (OBE) interaction V and the scattering T-matrix as shown in Chapter 2, a useful simplification is the partial wave expansion or decomposition. This process is fully outlined in Chapter 10 of [70], but this Appendix will provide a basic explanation.

Figure A.1 depicts two particles, denoted by their momenta p_1 and p_2, scattering in the $x-z$ plane with the scattering angle ϕ. Following this setup, an expansion for the OBE potential V into angular momentum states can be written as:

$$\langle\Phi_{\lambda_1'}(p')\Phi_{\lambda_2'}(p')|\, V\, |\Phi_{\lambda_1}(p)\Phi_{\lambda_2}(p)\rangle = \frac{1}{4\pi}\sum_j (2j+1) d^j_{\lambda\lambda'}(\phi)\langle\lambda_1'\lambda_2'|\, V^j(p',p)\, |\lambda_2\lambda_2\rangle, \tag{A.1}$$

where $\lambda = \lambda_1 - \lambda_2$. This relation can be inverted and the quantities $d^j_{\lambda\lambda'}(\phi)$ can be represented in terms of Legendre polynomials $P_j(\cos\phi)$. Taking into account parity and spin conservation, V^j is reduced to six amplitudes for symmetric nuclear matter (SNM) and eight for asymmetric nuclear matter (ANM). While this process is done for all meson types, the

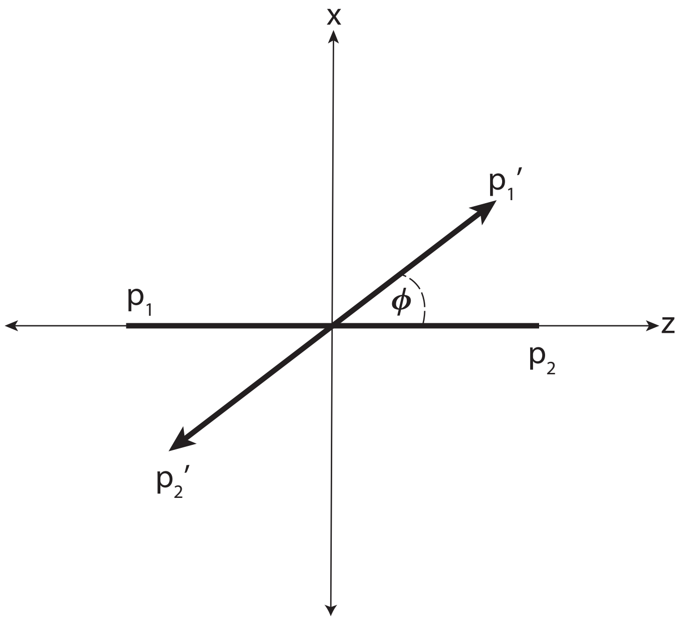

Figure A.1: Two particle scattering in a center-of-mass system in the x-z plane, where ϕ is the scattering angle between p_1 and p_2.

six amplitudes V^j for SNM and scalar coupling are given as:

$$^{0}V_s^j(p',p) = g_s^2 \frac{\pi}{m'^* m^*}\left[p'^* p^* \frac{\tilde{Q}_j^{(1)}}{|p'||p|} - (m^{*\prime} m^* + W'W)\frac{\tilde{Q}_j}{|p'||p|}\right], \tag{A.2}$$

$$^{12}V_s^j(p',p) = g_s^2 \frac{\pi}{m'^* m^*}\left[p'^* p^* \frac{\tilde{Q}_j}{|p'||p|} - (m^{*\prime} m^* + W'W)\frac{\tilde{Q}_j^{(1)}}{|p'||p|}\right], \tag{A.3}$$

$$^{1}V_s^j(p',p) = g_s^2 \frac{\pi}{m'^* m^*}\left[p'^* p^* \frac{\tilde{Q}_j^{(2)}}{|p'||p|} - (m^{*\prime} m^* + W'W)\frac{\tilde{Q}_j}{|p'||p|}\right], \tag{A.4}$$

$$^{34}V_s^j(p',p) = g_s^2 \frac{\pi}{m'^* m^*}\left[p'^* p^* \frac{\tilde{Q}_j}{|p'||p|} - (m^{*\prime} m^* + W'W)\frac{\tilde{Q}_j^{(2)}}{|k'||k|}\right], \tag{A.5}$$

$$^{5}V_s^j(p',p) = g_s^2 \frac{\pi}{m'^* m^*} \left[(m^* W' + m^{*\prime} W) \frac{\tilde{Q}_j}{|p'||p|} \right], \tag{A.6}$$

and $^{6}V_s^j(p',p) =^5 V_s^j(p',p)$ from time-reversal invariance [70]. Here g_s^2 is the scalar coupling constant (see Table B.1). The functions $\tilde{Q}_j$, $\tilde{Q}_j^{(1)}$, and $\tilde{Q}_j^{(2)}$ are calculated by integrating the Legendre polynomials $P_j(\cos\phi)$. These same processes are carried out for the other types of mesons and the particle-antiparticle matrix elements, defined in Eqs. (2.41) - (2.44).

A similar decomposition is used for the T-matrix. For SNM, the T-matrix elements can be written as:

$$^{0}T^j =^0 V^j +^0 V^j \bar{\Lambda}^0 T^j, \tag{A.7}$$

$$^{12}T^j =^{12} V^j +^{12} V^j \bar{\Lambda}^{12} T^j + 4\,^{5}V^j \bar{\Lambda}^{6} T^j, \tag{A.8}$$

$$^{1}T^j =^1 V^j +^1 V^j \bar{\Lambda}^1 T^j, \tag{A.9}$$

$$^{34}T^j =^{34} V^j +^{34} V^j \bar{\Lambda}^{34} T^j + 4\,^{6}V^j \bar{\Lambda}^{5} T^j, \tag{A.10}$$

$$^{5}T^j =^5 V^j +^{12} V^j \bar{\Lambda}^5 T^j +^5 V^j \bar{\Lambda}^{34} T^j, \tag{A.11}$$

$$ {}^6T^j ={}^6 V^j +{}^6 V^j\bar{\Lambda}^{12}T^j +{}^{34} V^j\bar{\Lambda}^6T^j, \tag{A.12} $$

where $\bar{\Lambda}$ is the angle-averaged propagator. For ANM, the mixed particle-antiparticle amplitudes of the scattering matrix can be defined in shorthand notation as:

$$ \langle\lambda_1'\lambda_2'p'|\overset{1}{R}|\lambda_1\lambda_2p\rangle = \langle\theta^p_{\lambda_1'}(p_1')\Phi^n_{\lambda_2'}(p_2')|\,T\,|\Phi^n_{\lambda_1}(p_1)\Phi^n_{\lambda_2}(p_2)\rangle, \tag{A.13} $$

$$ \langle\lambda_1'\lambda_2'p'|\overset{2}{R}|\lambda_1\lambda_2p\rangle = \langle\theta^p_{\lambda_1'}(p_1')\Phi^p_{\lambda_2'}(p_2')|\,T\,|\Phi^n_{\lambda_1}(p_1)\Phi^p_{\lambda_2}(p_2)\rangle, \tag{A.14} $$

$$ \langle\lambda_1'\lambda_2'p'|\overset{3}{R}|\lambda_1\lambda_2p\rangle = \langle\theta^p_{\lambda_1'}(p_1')\Phi^p_{\lambda_2'}(p_2')|\,T\,|\Phi^p_{\lambda_1}(p_1)\Phi^n_{\lambda_2}(p_2)\rangle, \tag{A.15} $$

$$ \langle\lambda_1'\lambda_2'p'|\overset{4}{R}|\lambda_1\lambda_2p\rangle = \langle\theta^n_{\lambda_1'}(p_1')\Phi^p_{\lambda_2'}(p_2')|\,T\,|\Phi^p_{\lambda_1}(p_1)\Phi^p_{\lambda_2}(p_2)\rangle, \tag{A.16} $$

$$ \langle\lambda_1'\lambda_2'p'|\overset{5}{R}|\lambda_1\lambda_2p\rangle = \langle\theta^n_{\lambda_1'}(p_1')\Phi^n_{\lambda_2'}(p_2')|\,T\,|\Phi^n_{\lambda_1}(p_1)\Phi^p_{\lambda_2}(p_2)\rangle, \tag{A.17} $$

$$ \langle\lambda_1'\lambda_2'p'|\overset{6}{R}|\lambda_1\lambda_2p\rangle = \langle\theta^n_{\lambda_1'}(p_1')\Phi^n_{\lambda_2'}(p_2')|\,T\,|\Phi^p_{\lambda_1}(p_1)\Phi^n_{\lambda_2}(p_2)\rangle, \tag{A.18} $$

$$\langle\lambda_1'\lambda_2'p'|\overset{1}{S}|\lambda_1\lambda_2p\rangle = \langle\theta^p_{\lambda_1'}(p_1')\Phi^n_{\lambda_2'}(p_2')|\,T\,|\Phi^n_{\lambda_1}(p_1)\theta^p_{\lambda_2}(p_2)\rangle, \tag{A.19}$$

$$\langle\lambda_1'\lambda_2'p'|\overset{2}{S}|\lambda_1\lambda_2p\rangle = \langle\theta^p_{\lambda_1'}(p_1')\Phi^p_{\lambda_2'}(p_2')|\,T\,|\Phi^p_{\lambda_1}(p_1)\theta^n_{\lambda_2}(p_2)\rangle, \tag{A.20}$$

$$\langle\lambda_1'\lambda_2'p'|\overset{3}{S}|\lambda_1\lambda_2p\rangle = \langle\theta^p_{\lambda_1'}(p_1')\Phi^p_{\lambda_2'}(p_2')|\,T\,|\Phi^p_{\lambda_1}(p_1)\theta^p_{\lambda_2}(p_2)\rangle, \tag{A.21}$$

$$\langle\lambda_1'\lambda_2'p'|\overset{4}{S}|\lambda_1\lambda_2p\rangle = \langle\theta^n_{\lambda_1'}(p_1')\Phi^n_{\lambda_2'}(p_2')|\,T\,|\Phi^n_{\lambda_1}(p_1)\theta^n_{\lambda_2}(p_2)\rangle, \tag{A.22}$$

$$\langle\lambda_1'\lambda_2'p'|\overset{1}{P}|\lambda_1\lambda_2p\rangle = \langle\theta^p_{\lambda_1'}(p_1')\Phi^p_{\lambda_2'}(p_2')|\,T\,|\theta^p_{\lambda_1}(p_1)\Phi^p_{\lambda_2}(p_2)\rangle, \tag{A.23}$$

$$\langle\lambda_1'\lambda_2'p'|\overset{2}{P}|\lambda_1\lambda_2p\rangle = \langle\theta^n_{\lambda_1'}(p_1')\Phi^n_{\lambda_2'}(p_2')|\,T\,|\theta^n_{\lambda_1}(p_1)\Phi^n_{\lambda_2}(p_2)\rangle, \tag{A.24}$$

$$\langle\lambda_1'\lambda_2'p'|\overset{3}{P}|\lambda_1\lambda_2p\rangle = \langle\theta^p_{\lambda_1'}(p_1')\Phi^n_{\lambda_2'}(p_2')|\,T\,|\theta^p_{\lambda_1}(p_1)\Phi^n_{\lambda_2}(p_2)\rangle, \tag{A.25}$$

$$\langle \lambda_1' \lambda_2' p' | \overset{4}{P} | \lambda_1 \lambda_2 p \rangle = \langle \theta^n_{\lambda_1'}(p_1') \Phi^p_{\lambda_2'}(p_2') | \, T \, | \theta^n_{\lambda_1}(p_1) \Phi^p_{\lambda_2}(p_2) \rangle. \tag{A.26}$$

where each R, S, and P can be broken down into angular momentum states as with V for various amplitudes. Once the partial wave decomposition has been done for both the matrix elements of V and T, they are used to calculate the three self-energy components in the self-consistent basis: $\Sigma_{\Phi\Phi}$, $\Sigma_{\theta\theta}$, and $\Sigma_{\theta\Phi}$.

Appendix B

Numerical Scheme for T-matrix Calculation: *Lambt*

The numerical scheme for calculating properties of a relativistic many-body system at finite temperatures, described in Chapter 2, is called *Lambt*. The original framework for this code was created by P. Poschenrieder, M. K. Weigel, F. Weber, H. Huber, and others at Ludwig Maximilian University of Munich. The original code calculated the bulk properties of nuclear and neutron matter at zero temperature in the relativistic Hartree-Fock (RHF) or relativistic Brueckner-Hartree-Fock (RBHF) approximations, the latter of which can also be referred to as the Λ approximation. The Λ approximation is generalized to use various propagators or Λ's; the RBHF approximation is simply the Λ approximation with the Brueckner propagator, as discussed in Chapter 2. Apart from the RBHF propagator, *Lambt* is capable of also employing the Λ^{00} and Λ^{10} propagators.

In this section, we describe the numerical scheme and all relevant routines involved in *Lambt*, which extends the previous work to finite temperatures.

B.0.1 Numerical Scheme

A schematic diagram of the code *Lambt*, which calculates properties of nuclear matter using the RBHF approximation, is shown in Figure B.1. This code is written using Fortran90 and contains modules from the NAG numerical library [243].

The numerical scheme works well up to densities up to 0.5 fm^{-3}. To reach higher densities (i.e. for neutron star matter), we extrapolate quantities necessary to calculate the equation of state: the energy per nucleon E/A for calculations at zero temperature, and also the free energy per nucleon F/A at finite temperatures. The extrapolation, done in Python, is carried out by first fitting the calculated data to a curve using a least squares polynomial fit using Numpy's `polyfit` and `poly1d` functions. Once extrapolated to higher densities, the energy per nucleon and free energy per nucleon are then used to calculate the asymmetry energy, pressure, and energy density of the system.

B.0.2 Input Data

The user must provide initial data to *Lambt*. The first several lines of the input file specify parameters for the one-boson-exchange (OBE) interaction, for which we use the three Bonn potentials (A, B, or C). For each meson α, these parameters include the coupling factor $g_\alpha^2/4\pi$ and cut-off mass Λ_α, which are given in Table B.1 and taken from Table VI in [85]. In older works, these OBE interactions are also referred to as the Brockmann potentials. An example of an input file, complete with the values from the Bonn A potential, is shown below.

```
'PARAMETERSATZ A BROCKMANN'
'Bonn A'
'SIGM0',.550,8.3141,4,2.0,2*0.
```

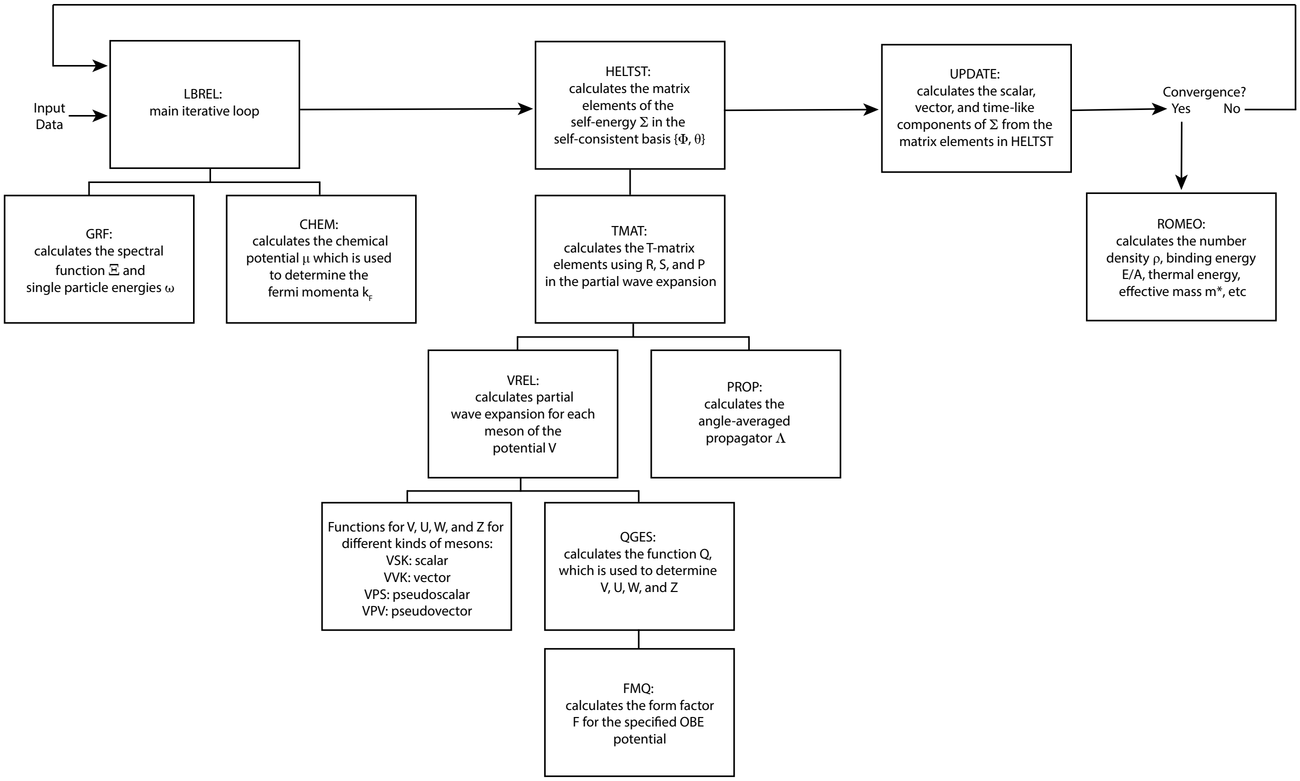

Figure B.1: The numerical scheme of *Lambt*, which calculates properties of nuclear matter using the RBHF formalism.

Table B.1: Parameters for the three relativistic Bonn OBE potentials (A, B, and C). For each meson α, the mass m_α, coupling factor $g_\alpha^2/4\pi$, and cut-off mass Λ_α are given. Additionally, for the ρ meson the parameter $f_\rho/g_\rho = 6.1$. This table is adapted from Table VI in [85].

Meson Parameters		Potential A		Potential B		Potential C	
Meson α	m_α (MeV)	$g_\alpha^2/4\pi$	Λ_α (GeV)	$g_\alpha^2/4\pi$	Λ_α (GeV)	$g_\alpha^2/4\pi$	Λ_α (GeV)
σ	550.0	8.3141	2.0	8.0769	2.0	8.0279	1.8
ω	782.6	20.0	1.5	20.0	1.5	20.0	1.5
π	138.03	14.9	1.05	14.6	1.2	14.6	1.3
ρ	769.0	0.99	1.3	0.95	1.3	0.95	1.3
δ	983.0	0.7709	2.0	3.1155	1.5	5.0742	1.5
η	548.8	7.0	1.5	5.0	1.5	3.0	1.5

```
'SIGM1',.550,8.3141,4,2.0,2*0.
'OMEGA',.7826,20.,4,1.50,2*0.
'OMEG2',0.,0.,0,3*0.
'PI   ',.138,14.9,4,1.05,2*0.
'RO   ',.769,0.99,4,1.3,2*0.,6.1
'PHI  ',1.020,7.,0,1.950,2*0.
'DELTA',.983,0.7709,4,2.0,2*0.
'ETA  ',.5488,7.,-4,1.50,2*0.
'AMNUC',0.9389
'UMRFA',0.197329
'NSTEU',0,1,0,1,5,3,0,1
'IGEL ',1.250,.025,1.,10,4,8,4,5,1,1,2,2,2,1,1,1,1,1,1
'EPS  ',.001,.025,.001,1.E-4,10.7,25,150
'START',-.18,0.,.15
'DICHTE',0.1,.2,.02
'TEMPERATUR MeV',20.,20.,5.
'RELAX',.3,.3,.3,.3,.3,.3
'RELEN',0.,0.,0.,0.,0.,0.,0.,0.,0.,0.
'CHEM POT.',.9
'ENDRUN'
```

After information for the η meson, the nucleon mass (in GeV) is given by “AMNUC”, followed by a conversion factor “UMFRA” from fm^{-3} to GeV^3. The next line “NSTEU” gives a series of eight control parameters (NS1, NS2, NS3, NS4, NS5, NS6, NTEST, and IFOCK). The relevant parameters to the RBHF approximation are:

- NS2: inclusion of retardation (= 1 do not include, = 2 include),

- NS4: treatment of π meson ($= 1$ pseudovector, $= 2$ pseudoscalar),
- NS5: type of calculation, takes values 1 to 5 ($1 =$ HF, $2 = \Lambda^{00}$, $3 = \Lambda^{10}$, $4 = \Lambda^{11}$, $5 =$ BHF),
- IFOCK: inclusion of the exchange term ($= 0$ direct term only, $\neq 0$ include direct and exchange term).

A second set of control parameters is listed on the next line "IGEL", of which the last 12 parameters are stored in the code as ISTEU(1:12). For the RBHF approximation, the relevant parameters are:

- ISTEU(2): inclusion of temperature in the calculation of boson-exchange matrix elements ($= 1$ include, $= 2$ ignore),
- ISTEU(3): breakdown by meson ($= 1$ do not, $= 2$ do),
- ISTEU(6): specifies the type of basis ($= 1$ vacuum-basis, $= 2$ self-consistent spinor-antispinor basis),
- ISTEU(7): carry out a relativistic ($= 1$) or nonrelativistic ($= 2$) calculation,
- ISTEU(8): inclusion of the vector components of the self-energy Σ ($= 1$ do not, $= 2$ do),
- ISTEU(9): type of matter ($= 1$ symmetric nuclear matter, $= 2$ pure neutron matter),
- ISTEU(12): momentum-averaging self-energy Σ ($= 1$ full calculation, $= 2$ momentum-averaging).

The other parameters included are specific to the numerical calculation (integration, extrapolation, etc). The following line "EPS" includes information about convergence criteria and values for the maximum number of iterations.

The next lines give initial conditions for the calculations. “START” provides the starting values for the scalar, vector, and time-like components of the self-energy Σ. “DICHTE” gives the starting and ending values for the density along with the step size, respectively. “TEMPERATUR MeV” gives the same information as “DICHTE” but for the temperature (in MeV). Finally, “RELAX” and “RELEN” are the relaxation factors for the self-energy Σ and single-particle energy, and “CHEM POT.” is the chemical potential.

Appendix C

Numerical Scheme for Differential Rotation: *DRNS*

The numerical method to solve bulk properties of differentially rotating neutron stars follows an open-source code that models uniformly rotating stars called *RNS* (for Rapidly Rotating Neutron Stars) written by Nikolaos Stergioulas, and an updated and expanded version of *RNS* written by Rodrigo Negreiros. The open-source version of the original *RNS* code is available freely online, which solves Einstein's field equations for uniformly rotating stars using the scheme laid out by CST [104]. This appendix will give more general details about the numerical scheme and explicitly provide our modifications to extend its capability to differentially rotating stars.

Under the assumption that the maximum density occurs at the center of the star (see Chapter 3 for more details), the user must supply the following when computing equilibrium models for a single star or sequence of stars:

- A equation of state (EOS) model that includes the energy density ϵ, pressure P, enthalpy h, and number density n in CGS units,

- A central density, or range of central densities for a given number of stellar models,
- The ratio of polar to equatorial radius, $r_{\rm ratio}$,
- The inverse of the scaled rotation parameter, $\hat{A}^{-1}$.

Alternatively, *DRNS* has the option to assume the maximum density is not at the center of the star (discussed in Chapter 4), which is the case for more deformed configurations. If this option is chosen, the numerical models can be calculated using smaller values of $r_{\rm ratio}$, or the user can specify a range of values for $r_{\rm ratio}$ for which the code will find solutions over.

Once the input data is loaded, bulk properties of differentially rotating stars are calculated using an iterative scheme, shown schematically in Figure C.1. The schematic shows the process for a single star with a set central density, but a sequence of stars can be solved by completing the scheme for a range of densities.

C.0.1 Parameter Scaling

While describing equations throughout this body of text, geometrized units are adopted ($G = c = 1$). However, these variables are still present throughout calculations within the *DRNS* code. The physical parameters within the calculation like the metric functions, rotational frequency, EOS, and more are scaled both within the CST numerical scheme and the *DRNS* code. The scaled variables are given in Appendix A of CST [104] but are also listed here for convenience.

The fundamental length scale chosen in CST is $\kappa^{1/2}$, which is used to scale physical parameters and is defined as:

$$\kappa^{1/2} = \left(\frac{c^2}{G\epsilon_0}\right)^{1/2}, \tag{C.1}$$

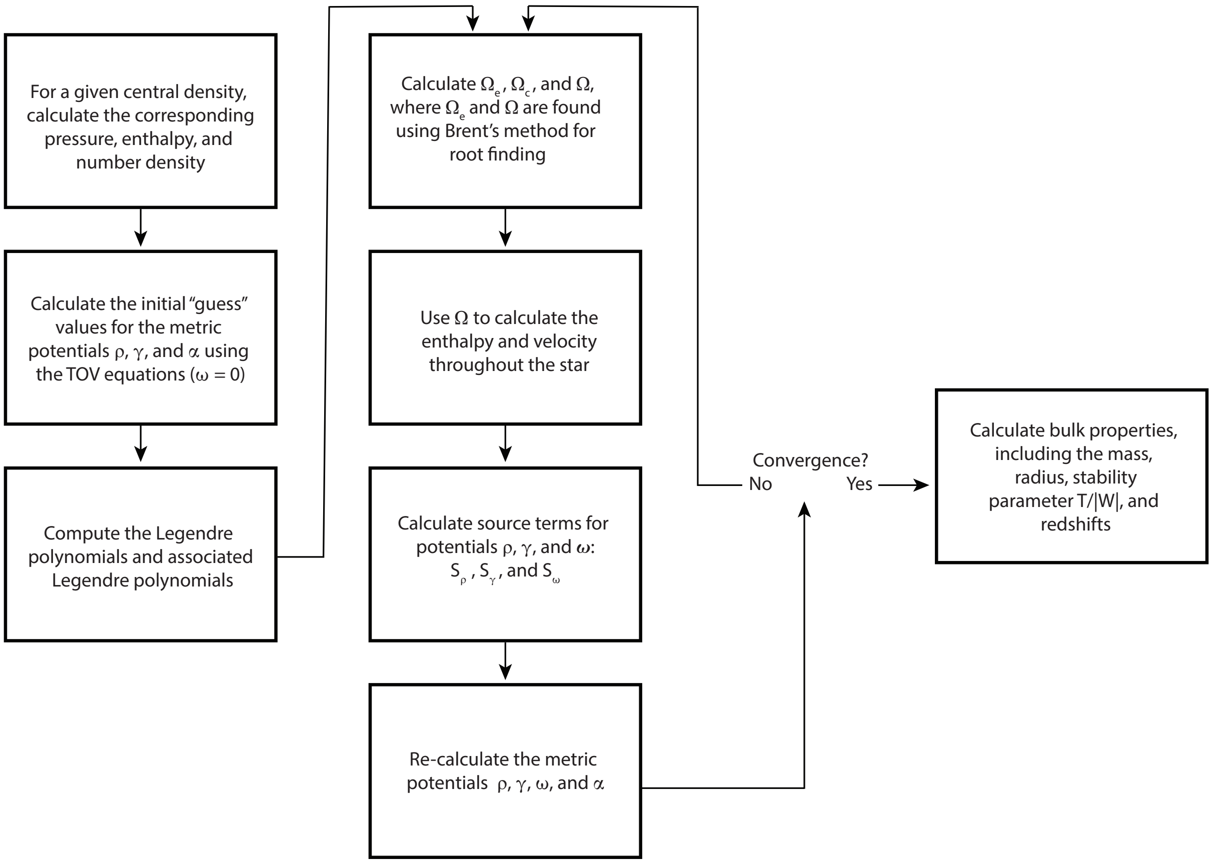

Figure C.1: The numerical scheme of *DRNS*, which calculates bulk properties differentially rotating neutron stars.

where c is the speed of light, G is the gravitational constant, and ϵ_0 is 10^{15} g/cm^3. The following variables are then scaled (denoted by a bar over the variable) using κ as:

$$\bar{r} = \kappa^{-1/2}\, r, \tag{C.2}$$

$$\bar{t} = \kappa^{-1/2}\, ct, \tag{C.3}$$

$$\bar{\omega} = \kappa^{1/2} \frac{\omega}{c}, \tag{C.4}$$

$$\bar{\Omega} = \kappa^{1/2} \frac{\Omega}{c}, \tag{C.5}$$

$$\bar{\rho}_0 = \kappa \frac{G\rho_0}{c^2}, \tag{C.6}$$

$$\bar{\epsilon} = \kappa \frac{G\epsilon}{c^2}, \tag{C.7}$$

$$\bar{P} = \kappa \frac{GP}{c^4}, \tag{C.8}$$

$$\bar{J} = \kappa^{-1}\frac{GJ}{c^3}, \tag{C.9}$$

$$\bar{M} = \kappa^{1/2}\frac{GM}{c^2}. \tag{C.10}$$

C.0.2 Root Finding: Brent's Method

To determine the frequency at the equator Ω_e and then the star's total frequency Ω, Eqs. (3.23) and (3.19) must be solved using a root-finding algorithm. In *DRNS*, this is done using Brent's method, more formally known as the van Wijngaarden-Deker-Brent method. This root-finding method combines root bracketing, bisection, and inverse quadratic interpolation; the reader is directed to Ref. [244] for a full description and the source code. The basic idea of the algorithm is as follows: for three points $[a, f(a)]$, $[b, f(b)]$, and $[c, f(c)]$, a polynomial interpolation for point x is given as:

$$x = \frac{[y - f(a)][y - f(b)]c}{[f(c) - f(a)][f(c) - f(b)]} + \frac{[y - f(b)][y - f(c)]a}{[f(a) - f(b)][f(a) - f(c)]} + \frac{[y - f(c)][y - f(a)]b}{[f(b) - f(c)][f(b) - f(a)]}. \tag{C.11}$$

For root-finding, y is set to 0, giving:

$$x = b + P/Q, \tag{C.12}$$

where P is defined as:

$$S[T(R - T)(c - b) - (1 - R)(b - a)], \tag{C.13}$$

and Q is defined as:

$$Q = (T - 1)(R - 1)(S - 1). \tag{C.14}$$

The auxiliary variables R, S, and T are defined in terms of f as:

$$\begin{aligned} R &= f(b)/f(c), \\ S &= f(b)/f(a), \\ T &= f(a)/f(c). \end{aligned} \tag{C.15}$$

Appendix D

Supplemental Information for Machine-Learning-Derived Likelihoods

D.1 Integration and Optimization

This section describes the numerical integration and optimization methods used in Chapter 6.

D.1.1 Integration

Integration is performed by a Monte Carlo method. In order to ensure convergence, four independent sets of 100 samples are made, leading to four estimates of the value of the integral. Additional sets of 100 samples are performed until the uncertainty on the mean over the sets is reduced to less than 3% relative. The mean value over all sets is then used as the estimate.

D.1.2 Optimization

Optimization is performed in two stages. First, the rough location of the maximum is located, followed by the use of a maximization algorithm for fine-tuning.

The first stage performs a simple grid scan of the parameter space, dividing the space into N tiles centered on the full parameter range. The process is repeated, but now centered over the expectation value calculated from the previous round, and with a search space the width of three grid tiles, again divided into N smaller tiles. The process is repeated M times. In the results shown in Chapter 6, $N = 4$ and $M = 3$.

The second stage runs an algorithm to find a minimum. The `scipy.minimize` function with Nelder-Mead and conjugate-gradient algorithms. In addition, a method that performs two one-dimensional parabolic fits through the center of the region was explored. The results shown in Chapter 6 use the Nelder-Mead algorithm.

The two-stage method performed more reliably than running the algorithm over the full parameter space.

D.2 Hyperparameter Optimization

This section describes the hyperparameter optimization methods for model f, which generates simulated X-ray spectra from mass, radius, and the nuisance parameters ν.

The network has two input branches, the first to process the mass and radius values and the second to process ν. The output of the two branches is combined and processed through the remaining layers to predict the X-ray spectra. In both the input branches as well as the secondary portion of the network, we trained models with random combinations of the following parameters:

1. Number of layers: one to fifteen,
2. Number of hidden nodes: 64 to 2048,
3. Dropout: 0 to 1,
4. Learning rate: 0.0001 to 0.005,
5. Activation functions,
6. Skip connections,
7. Loss functions: mean squared error (MSE), mean absolute percentage error (MAPE), and the Huber loss function,
8. Data scalers for both the input and the output: zero-mean, log, min-max, and standard scaler. The scalers preprocess the data before it enters the network, meaning scaled input values (mass, radius, and ν) with a scaled output (spectra) are used for training. After training, the scaling procedure is inverted for the predicted spectra to produce meaningful values.

The hyperparameters chosen were the combination that had the best performance on the validation data set, described in Section 6.2.